ProQuest Number: 10183411

ProQuest 10183411

ProQuest LLC.
789 East Eisenhower Parkway
P.O. Box 1346
Ann Arbor, MI 48106 – 1346

Structure-function relationships for basic zeolites

Maurits Wilhm Engelbert van den Berg

A thesis submitted in partial fulfilment of the requirements of The Nottingham Trent University for the degree of Doctor of Philosophy

May 2004

Abstract

Lewis basicity in zeolitic materials is thought to be a property of framework oxygen atoms. Zeolitic basicity is amongst other factors governed by Si/Al ratio, framework type and guest cation. It was speculated that lead(II) introduced into the zeolite through ion exchange would enhance the basic properties.

Three zeolite types (zeolite X, Y and Beta) were ion-exchanged with lead(II) acetate in a watery solution. As reference basic catalysts several potassium and caesium-exchanged zeolites were prepared. All ion exchanges resulted in crystalline zeolites. The amount of lead(II) introduced in Pb-Na-X zeolites varied from ~4 to ~42 wt%. Thermal treatment at high temperatures (973 K) of the zeolites in vacuum or in a helium atmosphere led to the emergence of a metallic lead phase in some Pb-Na-X zeolites, where a high lead loading (~42 wt%) resulted in the emergence of a metallic lead phase even at 773 K.

The dehydrogenation of isopropanol yielding acetone is thought to be catalysed by basic catalytic sites, whereas acidic sites catalyse the dehydration of isopropanol, yielding propene. Adsorption of probe molecules carbon dioxide, ammonia and nitromethane monitored by infrared spectroscopy was employed as further means of examining acido-basic character of the zeolites.

Results indicate for Pb-Na-X samples that at a temperature of ~523 K a selectivity to acetone of about 70 molar% was achieved in the dehydrogenation of isopropyl alcohol, at conversion levels of 1-2 molar%. In infrared spectra of adsorbed carbon dioxide, carbonate formation has been found over these samples, whilst with ammonia adsorption at 423 K very little acid sites were seen. In the infrared spectra of adsorbed nitromethane at room temperature, bands were found which might be assigned to isocyanate species. According to literature, the above results point to presence of basic sites in Pb-Na-X.

When comparing the Pb-Na-X samples to conventional basic materials such as K-Na-X, K-Na-Y and Cs-Na-X, in the isopropyl alcohol dehydrogenation it was noticed that most of these traditional catalysts produce acetone at a higher

temperature than the Pb-Na-X materials. On Pb-Na-Y and Pb-H-Beta samples no (substantial) formation of acetone was detected. Known acidic materials, such as H-Y, produced propene only. It was found that washing K-Na-Y zeolites with water after the ion exchange had a negative effect on acetone production.

Acknowledgements

I would like to thank my supervisors, Dr. Michael Stockenhuber and Prof. Richard Joyner for their help and support. I also would like to thank the following people for their contribution to the investigation, by providing knowledge, encouragement, and friendship.

Dr. F. Karpowitz

A. Richards

S. Turner

M. Aklaqul-ambea

G. Burgess

Dr. G. Paine

Dr. J. Dixon

Dr. M. J. Duggan

O. Sonntag

M.L.M. Bonati

Table of contents

1 Introduction

1.1 Aims and scope of this thesis

Historically, solid acid catalysis using porous materials, has received more attention than solid base catalysis. The success of for example acidic Faujasite catalysts in fuel cracking is well documented [1]. In fact, it was estimated that in the late nineteen nineties only ~10% of industrial acid-base processes relied on solid base catalysts [2].

There are however, reasons why basic catalysts can be useful in industrial catalytic reactions. Many industrially relevant (organic) processes require formation of carbanion intermediates through proton abstraction, for which liquid bases are often used in stoichiometric or greater quantities [3]. Disadvantageous to the use of these liquid bases is their corrosive nature. This, and waste processing issues resulting from stoichiometric use, has prompted the search for solid base catalysts. Some reactions that can be successfully performed using solid base catalysts are: double bond isomerization of olefins, side-chain alkylation of aromatics, dehydrogenation of alcohols and the Knoevenagel condensation of aldehydes [4, 5].

Much of the early work on basicity concentrated on catalytic materials such as bulk oxides and zeolites. In the nineteen seventies, Yashima and co-workers explored the basicity of zeolites X and Y [6]. They observed, that alkali metal exchanged zeolites were active in the dehydrogenation of isopropropyl alcohol (IPA) to give acetone. This reaction was believed to be initiated by proton abstraction, which would be achieved by zeolite framework oxygen. A further observation regarding the behaviour of alkali zeolites in the IPA dehydrogenation was the increase in selectivity to acetone (*i.e.* the base-catalysed product) when the electropositivity of the charge-compensating cation increased. Thus, Cs-X was believed to be more basic than K-X, which in turn would be more basic than Na-X. This observation was incorporated into the developing theory of zeolite basicity by assuming that framework oxygen atoms are the basic sites, active in the target reaction. Proton abstraction ability would be related the negative charge on the framework oxygen atom, which in turn

would be modified by the electropositivity of the charge-compensating cation in the zeolite.

Strong basic materials were sought by many researchers. Oxide species dispersed in zeolite cavities have received a lot of attention. Carrier materials for basic oxides were explored, and a new range of materials were proven to be active in basic reactions [7]. Problems with the basicity concept remained though, leaving this topic not without controversy. For instance, Weiss and co-workers hinted at a redox mechanism in the oxidative coupling of methane [8]. The same reaction was also used to investigate basic sites [9]. Clearly, strong conclusions about basicity of a catalyst solely based on reaction data cannot be tenable, as difficulties often arise when a reaction mechanism is not completely understood.

Thus, other experimental techniques can be required to complement reactor data, *e.g.* adsorption of probe molecules. Conclusions can be drawn from the nature of the interactions between the probe molecule and the substrate. These interactions can be monitored by *e.g.* infrared spectroscopy. However, similar problems arise with adsorbed probe molecule approach as with reaction experiments. If the adsorption of a probe molecule can take place on several sites on the substrate, which are of a different nature, conclusions drawn from the observed phenomena can be rather ambiguous. Again, the mechanism of the adsorption needs to be understood well enough for conclusions about basicity to hold. Often a combination of reactor data and data obtained from other experimental techniques is desirable.

Basicity in catalysis continues to receive less attention in scientific literature than acid catalysed processes, with interest now and again flaring up. Some catalysts were designed to incorporate both acidic and basic sites in close proximity. These are so called bi-functional catalysts [2, 10], and seem to be quite promising for industrial applications [2].

For investigation of basic porous materials, we decided to concentrate on zeolites. Zeolites offer advantages over bulk materials such as oxides, as will be explained in § 1.2.

We speculated for this work, that a possible candidate to increase the basicity of a zeolite could be lead (II). As lead (II) is an electron rich element, and its ionic radius is rather large, it might be feasible that lead, if it were located in close vicinity of zeolite framework oxygen, would be able to enhance the basic character of these framework oxygen atoms.

From the literature available presently, the following becomes clear about the investigations into acido-basic character of zeolites:

- Basicity of zeolites seems to be related to partial charge of zeolite framework oxygen atoms [4, 5, 11]. The more negative the charge on the framework oxygen, the better the zeolite is able to act as a proton abstractor.

- Among the factors influencing basicity of a zeolite are: the framework type, the Si/Al ratio and the charge compensating cations [4, 12]. Zeolites with low Si/Al ratio (such as zeolite X and Y) have been able to act as a proton abstractor. Materials whereby alkali metals such as caesium and potassium have replaced sodium in zeolites X and Y displayed enhanced ability to abstract a proton from a target molecule [13].

- Lead (II) has been successfully ion exchanged into Faujasite-Y [14-17]. The ability of zeolites to take up lead (II) was a useful property in the treatment of (industrial) waste-water [18].

- Lead (II) exchanged zeolites have been used in a reaction where basic catalysis is thought to be involved, namely the oxidative coupling of methane [9, 19]. As has been explained (*vide supra*), this involvement of basicity in this reaction is not without controversy.

- A standard test reaction used in basic catalysis is the dehydrogenation of IPA to give acetone [20-22]. Dehydration of IPA yielding propene is thought to be indicative for acidic sites [20, 23].

- Carbon dioxide adsorption monitored by infrared spectroscopy has been used to investigate basic sites in solids [24-26]. On zeolite framework oxygen atoms, adsorption of carbon dioxide can lead to the emergence of (pseudo) carbonates, which is thought to be evidence for basicity [24].

- Ammonia adsorption investigated by infrared spectroscopy was used as a tool for investigation of acidic sites in zeolites. Ample examples can be found in literature of ammonia adsorption, on for example H-forms of zeolites [27, 28]

- Adsorption of nitromethane monitored by infrared spectroscopy is a relatively new tool in the investigation of basicity of oxides [29]. These investigations centre on cyanide and cyanate species, however, it seems the mechanism of adsorption is not yet fully explained.

The aim is to investigate the acido-basic character of lead (II) exchanged zeolites X, Y and Beta. These are zeolites with a Si/Al-ratio that ranges from roughly 1.5 (zeolite X) to 2.5 (zeolite Y) to 12.5 (zeolite Beta). The investigations into the acido-basic nature of ion-exchanged materials shall be done by means of reactor studies (IPA dehydrogenation) and the adsorption of probe molecules ammonia, carbon dioxide and nitromethane. In the next paragraphs of this chapter, a brief theoretical background will be given to the research. The following questions are central to this work:

1) Is it possible to exchange ion-exchange lead(II) into zeolites X, Y and Beta, yielding crystalline materials?

2) What is the bulk composition of the materials obtained through ion exchange?

3) How do the lead(II) exchanged zeolites respond to thermal treatment?

4) What products are seen when isopropyl alcohol is reacted over the lead(II) zeolites?

5) Does the adsorption of probe molecules carbon dioxide, ammonia and nitromethane give evidence for existence of basic sites?

6) On the above, how do the lead(II) zeolites compare to other zeolite materials which are known to be basic?

7) On the above, how do the lead(II) zeolites compare to other zeolite materials which are known to be acidic?

8) Do the data found in probe molecule adsorption experiments agree with reactor data?

9) What is the relation between the structure of the zeolite and its acido-basic function?

In § 1.2, zeolites, their naming, (chemical) structure and usage will be discussed, with particular emphasis on zeolites that are used for this work. Ion exchange is an important and useful phenomenon in zeolites, which will be exploited in this work. Activation of zeolites with low Si/Al-ratios is worth some attention, as structural changes in the zeolite may result from activation.

In § 1.3, the concept of basicity will be explored. Current concepts and understanding of basicity in relation to zeolites will be given. There are several experimental methods available to investigate basicity in zeolites. The ones that were chosen for this work will be discussed.

In section 2, the experimental approach used in this work will be presented. Theoretical basis of the experimental techniques, as well as the practical application will be given.

Section 3 is reserved for results of the experimental work discussed in section 2. Conclusions and discussion of the results can be found in that chapter.

In section 4 some overall conclusions will be given.

Section 5 deals with future work.

1.2 Zeolites

1.2.1 Abstract

Zeolites are metastable crystalline porous aluminosilicates. They consist of [SiO$_2$] and [AlO$_2$]$^-$ units which are connected at their oxygen atoms, building tetrahedra known as TO$_4$ units. Acidic catalytic sites are formed by OH groups in the Al(OH)Si unit. For this work, Faujasite X (Si/Al-ratio ~1.5), Faujasite Y (Si/Al ratio ~2.55) and Beta (Si/Al-ratio ~12.5) were used.

A useful property of zeolites is ion exchange. Ion exchange in watery phase can be described in the form of an equilibrium, for which isotherms can be drawn. From literature isotherms it is known that it is possible to introduce lead into zeolite Na-Y.

Activation of zeolites is often a prerequisite for *e.g.* catalysis. A problem of structural degradation may arise if activation temperature is too high, whereas a low activation temperature may lead to species remaining adsorbed on the zeolite.

Zeolites can be synthesised under hydrothermal conditions, through precipitation from aluminosilicate solutions in basic media. They have a widespread use as catalysts, detergent additives and adsorbents.

1.2.2 Definition of the term 'zeolite'

The Swedish mineralogist Crønstedt (1722-1765) [30, 31] was the first to give zeolites their name, for which he used ancient Greek. "Zeolite" is a composite of the words ζειν (to boil) and λυθος (stone). He observed intumescence in zeolites when they were subjected to thermal treatment. Both natural and synthetic zeolites exist, the number known structures of the latter exceeding that of the former [31].

Though many different definitions have been proposed, for the purpose of this thesis, the following definition shall be adopted:

Zeolites are metastable crystalline aluminosilicate molecular sieves with ordered interconnected microporous channels.

Some materials have a zeolite structure, but have distinctly different compositions. Those substances are classified as zeotype materials, *e.g.* molecular sieve materials based on aluminium phosphate ($AlPO_4$). Other materials that can be found in this category are for example aluminophosphates ($AlPO_4$-n) or silicoaluminophosphates (SAPO-n) [4]. These are analogues in build to zeolites.

1.2.3 Structure of the zeolite framework

1.2.3.1 TO_4 units

The zeolite framework consists of SiO_4 and AlO_4^- tetrahedra connected through their oxygen atoms. These tetrahedra are commonly represented as TO_4 units and are also known as the primary building units (PBUs) of the zeolite.

Secondary building units (SBUs) consist of several TO_4 building blocks, arranging into a repeating structure throughout the framework. Zeolites posses an ordered, interconnected (microporous) channel system that provides stereo selectivity to a reaction, because the dimensions of the zeolite pores and channels are comparable to many small organic molecules [32]. The channel structure arises from the arrangement of SBUs. Channels can run through the material in one, two or three dimensions. Pore dimensions can be expressed as number of TO_4 units that form the pore opening [33-37]. An overview is given in Table 1.2-1.

Table 1.2-1: Dimensions of pores in zeolites.

Number of TO_4 units	Dimensions / [nm]
6	~0.25
8	~0.30 x 0.45
10	~0.45 x 0.60
12	~0.80

1.2.3.2 OH groups

In zeolites, the following OH groups can be found:

- Brønsted acid sites (Si-OH-Al groups, *vide* §1.3.3)
- Silanol groups on the external surface
- Hydroxyl groups on defect sites (so called silanol nests)
- Perturbed silanol groups (arise as a result of hydrogen-bonding interactions)

To illustrate the OH groups found in zeolite Y, the infrared spectrum of an ammonium form of zeolite-Y, activated *in vacuo*, can be seen in Figure 1.2-2. This spectrum shows the presence of OH-groups at 3744, 3640 and 3544 cm^{-1}, corresponding to terminal silanol groups, high frequency (HF) and low frequency (LF) Brønsted acid sites respectively, in agreement with earlier work done on these materials (*vide* Figure 1.2-1) [38, 39]. The HF bands correspond to protons located in the supercage, whereas the LF band corresponds to protons located in the sodalite cage of zeolite H-Y [40]. Silanol groups on the external surface can be seen at 3740 – 3745 cm^{-1}; silanol nests are seen between 3735 and 3715 cm^{-1} and perturbed silanol groups appear at around 3500 cm^{-1} [41]. Kustov, in a review on the prospects of infrared spectroscopy used as a characterisation tool, mentioned the band position for an Al-OH species at 3670 – 3720 cm^{-1} [42]. Kuehl *et al.* found a band at 3680 cm^{-1} on ZSM-5 that they ascribed to an aluminium hydroxyl [43].
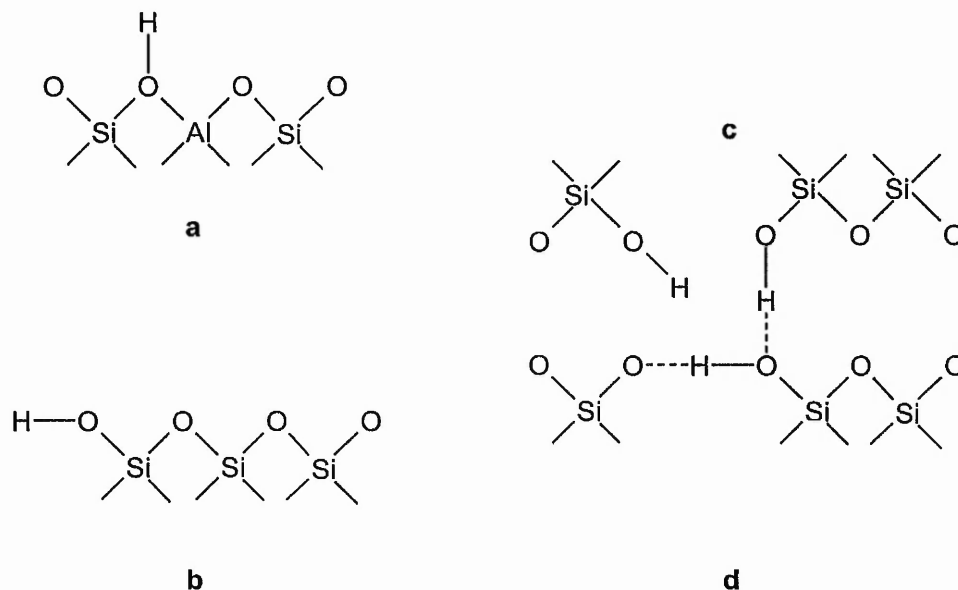
Figure 1.2-1: OH groups in zeolites. After Van Bekkum et al. [41]. Legend: a) Brønsted acid sites (3650 – 3550 cm^{-1}); b) Terminal silanol groups 3740 – 3745 cm^{-1}; c) Hydroxyl nests (3735 – 3715 cm^{-1}); d) Perturbed silanol groups (~3500 cm^{-1}).
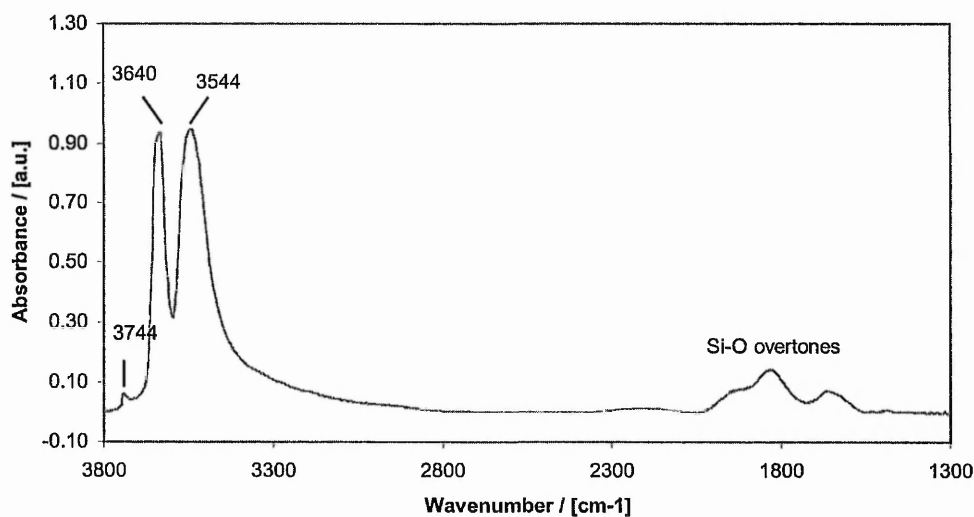
Figure 1.2-2: FTIR spectra of H-Y showing hydroxyl bands and zeolite Si-O overtones. The OH groups indicated are from higher to lower wavenumbers: terminal silanol groups, high-frequency OH groups and low-frequency OH groups. The spectrum is of a NH$_4$-Y sample, activated at 723 K (10 K min^{-1}), 4 h, vacuum. The spectrum is background subtracted.

1.2.3.3 The Faujasite framework

Zeolite X and zeolite Y are both examples of the structure type Faujasite (FAU), as defined by the International Zeolite Association [36]. Structurally, X and Y differ only in their Si/Al-ratio [44]:

$$1 < \left(\frac{Si}{Al} ratio \right)_{Zeolite-X} < 1.5 < \left(\frac{Si}{Al} ratio \right)_{Zeolite-Y} < 3.0 \qquad (1.1)$$

The Faujasite unit cell is made up of 192 silica and alumina tetrahedra, arranged into a way that forms α– and β cages. The latter (smaller of the two cages) is also known as the sodalite cage. The cage structures are shown in Figure 1.2-3.
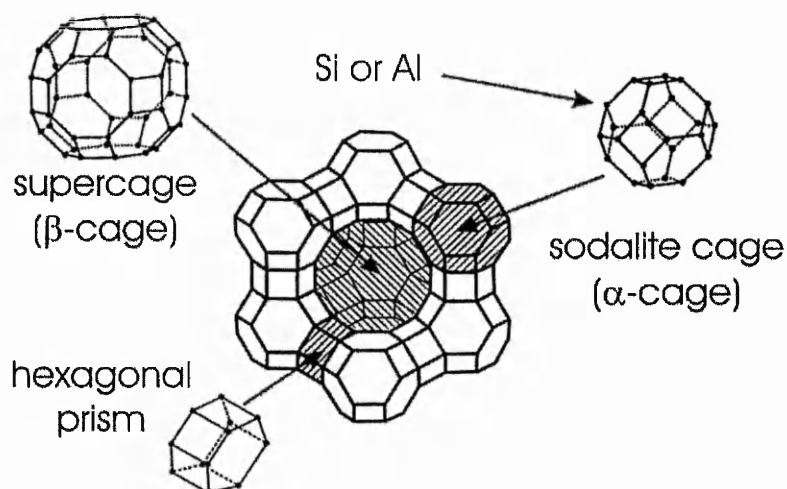
Figure 1.2-3: Simplified representation of the Faujasite framework, showing how the structure can be thought of as built up of supercages, sodalite cages and hexagonal prisms.

The sodalite cages are linked via hexagonal prisms and are stacked in a space filling structure (analogue to the diamond structure) [36, 37].
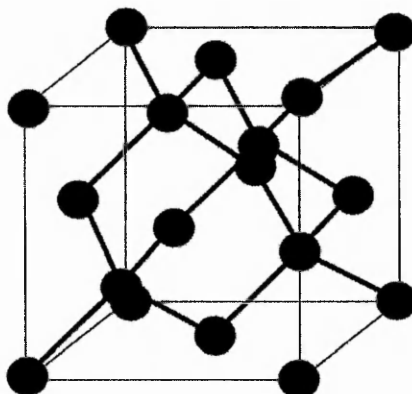
Figure 1.2-4: Schematic representation of the diamond structure (cubic unit cell). After Atkins [45].

The Faujasite cages can easily accommodate water molecules, and even hydrated ions. The maximum water content in Faujasite has been established at about four molecules of water per aluminium atom [37]. With this assumption, the mass percentage of water in Zeolite Y with for example an Si/Al-ratio of 2.36 can be estimated to be (*vide* §1.2.4):

$$\%H_2O\frac{m}{m} = 100\% \cdot \frac{M(zH_2O)}{M(Na_xAl_xSi_yO_{2(x+y)} \cdot zH_2O)} = \frac{4119}{16906} = 24.4\% \tag{1.2}$$

In equation (1.2), M is the relative molecular mass, expressed in grams per mole. Water molecules form a hydration mantle around the exchange cation. Heating the zeolite can remove most of the zeolitic crystal water [46, 47]. The water content of a Faujasite framework can be measured (*inter alia*) using thermo gravimetric analysis (T.G.A.).

1.2.3.4 The Beta framework

A schematic representation of the Beta structure can be seen in Figure 1.2-3.

Zeolite Beta consists of a mixture of three structural polytypes, commonly referred to as A, B and C [36, 37]. In zeolite Beta, a 12-ring interconnecting

channel system is found. The channels are connected through two four-rings and four five-rings. The channel system can be described as follows: two-dimensional interconnecting 12-ring channels running in the [100] direction (pore opening 6.6 x 6.7 Å), and one-dimensional 12-ring channels running in the [001] direction (pore opening 5.6 x 5.6Å).

There are 64 tetrahedra in the Beta unit cell, which are organised in a tetragonal arrangement [36, 37]. Crystalline samples of zeolite Beta have been reported with an Si/Al ratio of ~7.5 – 72 [48-50].
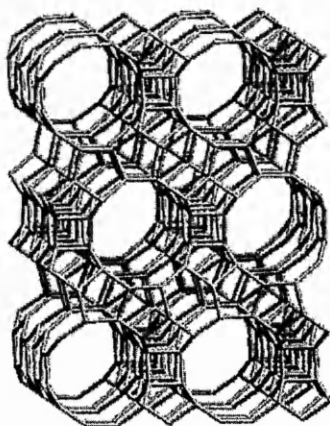
Figure 1.2-5 Zeolite Beta viewed along the [100] plane [36]

1.2.4 Notation

The zeolite framework can be represented by a chemical formula in many different ways and no uniformity can be discovered on this topic in literature. A simple notation is given here:

$$M_{n_i}^{q_i+}\left(AlO_2\right)_x\left(SiO_2\right)_y\cdot zH_2O \tag{1.3}$$
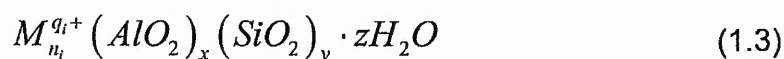
In formula (1.3), the total number of tetrahedra equals (x+y). A quantity often used is the Si/Al ratio, given as y/x in formula (1.3).

Because of surplus negative charge introduced by $[AlO_4]^-$ tetrahedra, charge compensating cations (e.g. Na^+, K^+, Pb^{2+}...) are needed, represented by M in (1.3), for which the following must apply:

$$\sum_i \frac{n_i}{q_i} = x \qquad (1.4)$$

A common notation for zeolites is provided by the IUPAC crystal chemical formula [36]. In this notation, for example a zeolite Y with Si/Al ratio of 2.31, is represented as follows:

$$\left| Na_{29}, Pb_{14.5} \right| \left[Al_{58} Si_{134} O_{384} \right] - \text{FAU}$$
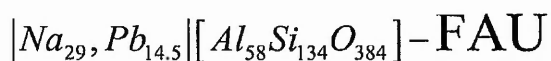
In this example the framework type is **FAU**. This framework type is independent of chemical composition. Guest species Na and Pb are denoted between vertical bars whereas the host framework is denoted between square brackets.

A different notation that can also often be found in literature is adopted for this work. In this notation, guest species are given together with their ion exchange percentage in brackets. This percentage is based on compensated charge introduced by the aluminium in the zeolite (vide §1.2.3). Thus, the zeolite shown above, would be written as Na(50)-Pb(50)-Y.

1.2.5 Ion exchange

1.2.5.1 General theory of zeolite ion exchange

An important property of zeolites is their ability to act as ion exchangers. As mentioned above, the presence of Al^{3+} in the zeolite warrants charge-compensating cations in the structure.

During the ion exchange procedure, a suspension (slurry) of the zeolite is in equilibrium with a solution of the cation to be introduced. This ion exchange equilibrium can be represented as follows [31, 51, 52]:

$$Z_B A^{Z_A} + Z_A \overline{B}^{Z_B} \rightleftharpoons Z_B \overline{A}^{Z_A} + Z_A B^{Z_B} \tag{1.5}$$
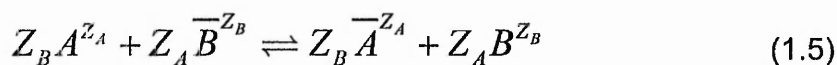
On the left hand side of equation (1.5), cation A (in solution) with charge Z_A, exchanges with cation $\overline{B}$, which has charge Z_B (the bar indicates that the species is part of the zeolite phase, and not of the solution).

An equilibrium isotherm can be constructed for an ion exchange process. In this isotherm, the concentration of framework cation species is plotted against the concentration of the same cation species in solution. Concentrations herein are expressed as mole fractions [31, 53-55].
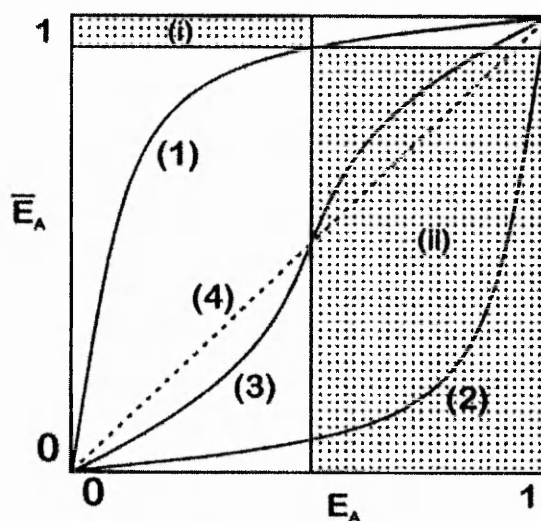
Figure 1.2-6: Ion exchange isotherms. Fraction of A in solution (indicated as E_A) plotted against fraction of A in the zeolite (indicated using a bar: $\overline{E}_A$). The lines given are: 1) $\alpha > 1$ (exchange is selective for B); 2) $\alpha < 1$ (exchange is selective for A); 3) α changes during the exchange; 4) $\alpha = 1$ (zeolite has no preference for either A or B). After Dyer [55].

From this representation (Figure 1.2-6), a selectivity factor can be deduced, which allows for estimation of the success of the exchange of cation B into the zeolite at the expense of cation A [55, 56]:

$$\alpha_A^B = \frac{area\ (ii)}{area\ (i)} \tag{1.6}$$

This selectivity factor is determined by the zeolite framework topology, exchange-ion size and shape, charge density in the zeolite channels and cages, exchange-ion valence, electrolyte composition and concentration in the aqueous phase [57, 58]. In very dilute solutions, hydrolysis and carbon dioxide adsorption can change the selectivity of the exchange [52, 57, 59].

Starting materials for ion exchange are often the Na^+ or NH_4^+ forms of the zeolite [31].

The ion exchange process can roughly be broken down into three steps: Nernst Layer [45] diffusion, particle diffusion and chemical reaction (*vide* Figure 1.2-7). Rate controlling steps for zeolitic ion exchange must undoubtedly be sought in diffusion steps, assuming that the exchange itself is rapid [56]. To derive a rate equation for the exchange process is beyond the scope of this work, however it can be said that such an equation is governed by the selectivity coefficient, particle size, film thickness and solution ionic concentration [56, 60].
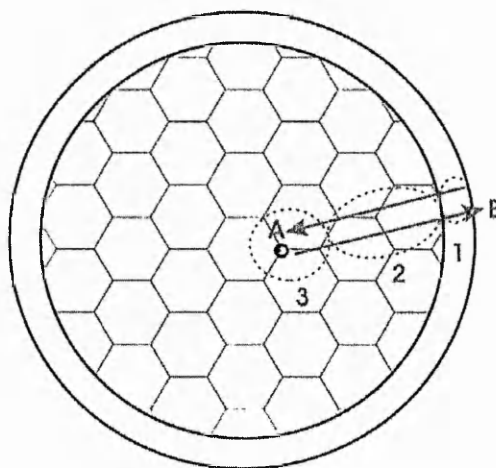
Figure 1.2-7: Ion exchange process in a zeolite particle. 1) Film diffusion (Nernst Layer [45]); 2) Particle diffusion; 3) Chemical reaction

In some cases, the ion exchange cannot proceed to the full extent. Some ion exchange sites in the zeolite framework are not accessible for certain guest cation species, because of sterical restrictions. The sodalite cages in Faujasite for example, are accessible through a window with an opening of 2.4 Å, which is in principle not sufficient for ions with a larger diameter.

In zeolites, hydrolysis may occur through hydronium exchange from water [52, 53, 59]. This process can be represented by the following equation:

$$2z_B H_2 O + \overline{B}^{z_B} \rightleftarrows z_B \overline{H_3 O^+} + B^{z_B} + z_B OH^- \tag{1.7}$$
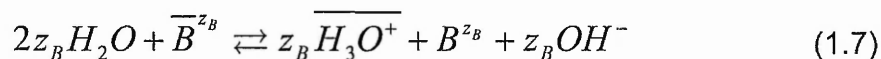
In equation (1.7), the bar indicates that the species is part of the zeolite phase and not of the solution. This hydrolysis leads to the formation of protons, which can remain as guest species in the zeolite. Thus, a low pH of the exchange solution can damage the zeolite structure; zeolite X is very sensitive to this effect [61]. From equation (1.7) it can be seen, that presence of OH⁻ in solution can drive this equilibrium to the left-hand side, according to the Le Chatelier-Van 't Hoff principle. However, increasing pH can lead to leaching of aluminium from the zeolite framework [59].

1.2.5.2 Ion exchange of alkali metals K and Cs into Faujasite

Ion exchange isotherms of the exchange of K^+ and Cs^+ into Na-X (at room temperature) are analogous to curve 3 in Figure 1.2-6 [34]. Selectivity reversal (thus) occurs. This can be understood as follows [34, 58, 62, 63]. Firstly, the sites located in the supercages undergo ion exchange (*vide* Figure 1.2-8). Coulombic interactions between the hydrated ion and the anionic site govern this exchange; therefore selectivity will be in order of decreasing hydrated ion radius: $Cs^+ > K^+ > Na^+$ (*vide* Table 1.2-2). Exchange of ions in the sodalite cages is governed by energy of dehydration, as the smaller sodalite cages cannot accommodate the complete hydration mantle of the ion. Thus, selectivity reverses: $Na^+ > K^+ > Cs^+$.
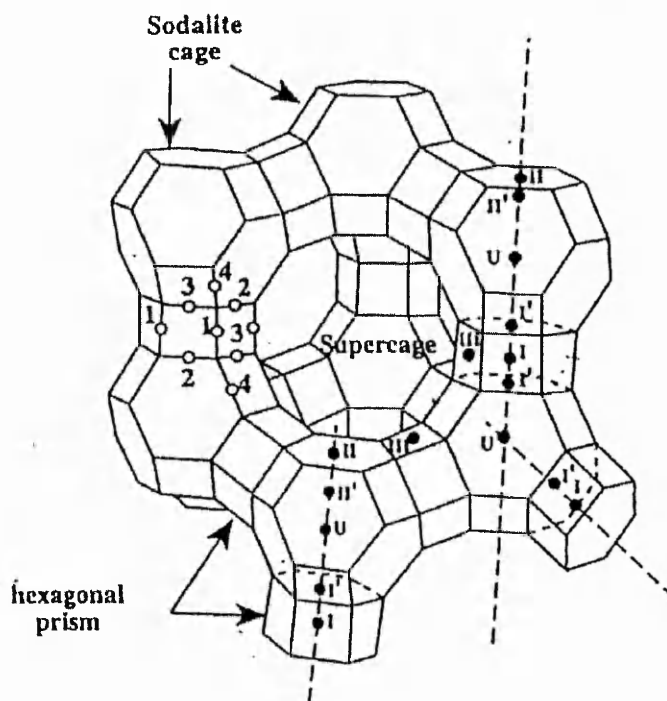
Figure 1.2-8: Ion exchange sites in Faujasite. Site I is located in the hexagonal prisms, site II and III in the supercages. Sites U and II' are located in the sodalite cages [36].

Table 1.2-2: Hydrated Ion radius [64] and Gibbs energy of formation ($\Delta_f G^0$) in aqueous solution [65] for selected alkali metals.

Cation	Hydrated ion radius	$\Delta_f G^0$ in aqueous solution
	[Å]	[kJ*mol^{-1}]
Na$^+$	3.58	-261.9
K$^+$	3.31	-283.3
Cs$^+$	3.29	-292.0

A high level of replacement of Na$^+$ in favour of e.g. Cs$^+$ or K$^+$ is a requirement for stronger basicity [66] (*vide* §1.3.2). Activation of the exchanged zeolite and subsequent re-hydration steps can achieve this. During activation, migration of alkali cations into the hexagonal prisms of Faujasite occurs (*vide* §1.2.7.3). Rehydration results in migration of Na$^+$ ions into the sodalite cages, thus becoming available for exchange. Repeated exchange-activation-rehydration-exchange recipes are thus recommended in order to obtain basic Faujasite [63, 67].

1.2.5.3 Ion exchange of lead (II) into zeolites

Zeolites have been shown to be successful in removal of lead (II) ions from wastewater effluent [14, 16, 18]. Studies of the introduction of lead (II) into mordenite (MOR) indicated lead (II) existed in the 2^+-valence state after exchange, and that the zeolite framework was intact after exchange [57]. Studies were also carried out on the ion exchange mechanisms and properties of lead (II) in Faujasites [15, 53, 68], however, to the best of our knowledge, no lead (II) ion exchange studies on zeolite beta have been published to date.

The equilibrium for the ion exchange of lead (II) into Faujasite can be represented as follows:

$$Pb^{2+}(aq) + 2Na^+_{FAU} \rightleftarrows 2Na^+(aq) + Pb^{2+}_{FAU} \qquad (1.8)$$
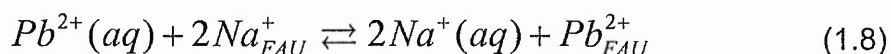
With selectivity coefficient α:

$$\alpha \frac{Pb^{2+}_{FAU}}{Pb^{2+}_{aq}} \qquad (1.9)$$

The exchange of lead (II) into Faujasite proceeds with considerable ease (*vide* Figure 1.2-9). Townsend and co-workers reported values of the selectivity factor α (*vide* equation (1.6)) that favoured the exchange of lead (II) into zeolite X. An apparent over-exchange was easily achieved [53]. This means, that more lead could be introduced into the zeolite than would be predicted on the basis of available charge (*vide infra*).
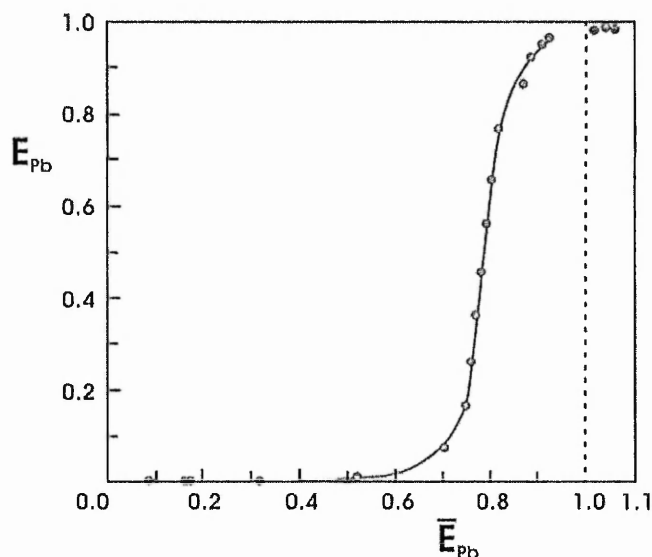
Figure 1.2-9: Ion exchange isotherm of lead (II)$^{2+}$ / Na-Y. After Townsend [53]. Plotted is the fraction of lead (II) in the zeolite (given by E-bar; plotted on the x-axis) versus fraction of lead (II) in solution (given by E; plotted on the y-axis). This example is analogous to line 2 in Figure 1.2-6.

The majority of exchangeable sites are located in the Faujasite α-cages (*vide* §1.2.3.3), that have a diameter of ~13 Å and are accessible through a 12 member ring opening that measures roughly 9 Å across. The sodalite cages however, measuring ~8 Å across are accessible through a 6-member ring that measures no more than 2.4 Å across [33, 34, 44, 47]. The ionic radius of the (non-hydrated) Pb^{2+} ion varies, depending on the coordination number, between 1,19 Å and 1,49 Å[65], which would be a critical size for passage into the smaller cavities of Faujasite. Ion exchange is sometimes performed at a higher temperature than room temperature, in order to (partly) remove the hydration mantle of exchange ions [33, 34], which facilitates access into the smaller zeolite cavities.

The over-exchange of lead in Faujasite found by researchers can be attributed to formation of lead (II) clusters in the zeolite cavities after the exchange has taken place [53]. Existence of $Pb_4(OH)_4^{4+}$ clusters inside sodalite cages has been put forward, with Pb^{2+} ions located at sites II and II' in the zeolite X framework [17, 69] (*vide* Figure 1.2-10).
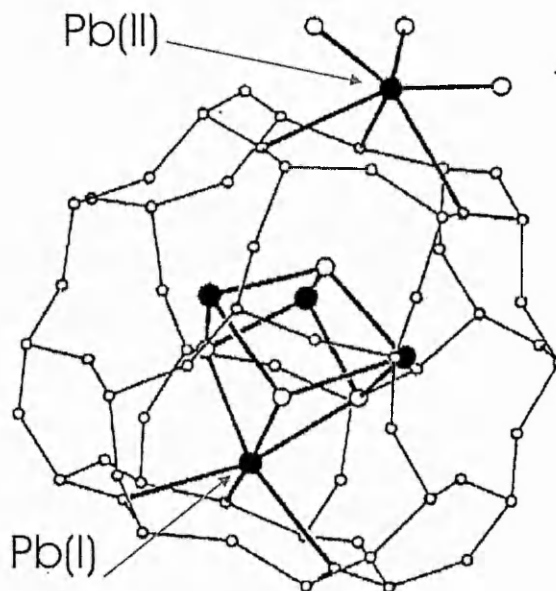
Figure 1.2-10: Sodalite cage of an X zeolite after introduction of Pb^{2+}. Smallest circles represent framework atoms (Si, Al and O). Intermediate size circles represent cluster oxygen atoms. Full circles represent lead (II) ions. Pb(I) is located at site I. Pb(II) is located at site II [17, 69].

1.2.6 Impregnation

Next to ion exchange, impregnation can be used to introduce material in a zeolite [70, 71]. In this, the zeolite is suspended in a solution of the exchange salt, with a much higher zeolite-to-liquid ratio than in the exchange process. The excess solution is subsequently evaporated off, followed by the drying of the zeolite. Indeed, a combination of the two techniques can be employed [66, 71-75].

1.2.7 Activation

1.2.7.1 Incentives for activation

With zeolites, pre-treatment (*i.e.* activation) of the catalyst is often necessary preceding any surface analysis or catalytic reaction. Aluminium rich zeolites, such as Faujasites, have a tendency to adsorb water (*vide* §1.2.3.3). This water can pose a problem in reactions or adsorption of probe molecules. Removal of

adsorbed water is usually achieved by thermal treatment. Removal of adsorbed water from divalent cation Faujasites for example requires temperatures of 673 – 773K or above [76]. A number of experimental parameters are important during activation. Amongst these are: the final temperature, heating rate and activation atmosphere.

Sometimes, oxygen is fed over the catalyst during activation. In that case, the term 'calcination' is used. Organic template molecules that can remain after synthesis in the zeolite crystal structure can for example be removed by calcination.

In basic catalysis involving zeolites, oxide species located in the zeolite cavities are in some cases attributed with activity in basic reactions [4, 66, 67, 77]. For instance, caesium oxide clusters in zeolite X are thought to be the catalytic sites responsible for proton abstraction in the dehydrogenation of isopropanol [66, 78, 79]. Formation of oxides from the precursor salts used during preparation of these catalysts requires high activation or calcination temperatures [80, 81]. As precursor salts, hydroxide or acetate salts can be used.

1.2.7.2 Thermal stability of zeolites

The thermal stability of zeolites is worth some consideration. Activation of ammonium exchanged zeolites such as NH_4-Beta and NH_4-Y at temperatures of roughly 773 K leads to formation of proton-form catalysts, which can be used in acid catalysis [82, 83]. Zeolitic protons weaken the Al-O bond during thermal treatment, leading to collapse of that part of the crystal structure. Framework destruction during thermal treatment is likely to be a more substantial problem in proton-form zeolites with a higher aluminium content, since higher aluminium content leads to a higher H^+ population of the framework.

From studies on thermal stability of zeolite X samples, Li and Rees concluded that temperature of structural collapse decreases as Si/Al ratio decreases [84]. Increasing H^+ content in the zeolite had the same effect, according to studies on activation of ammonium Faujasites [85-87]. Indeed, in zeolite sodium-

ammonium X, proton-mediated collapse can take place at moderate temperatures, such as 473 K [86].
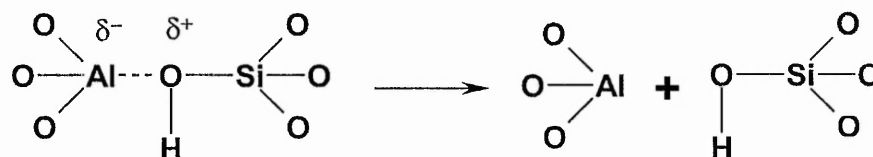
Figure 1.2-11: proton-mediated collapse of the zeolite framework. After Kühl and Schweizer [86].

Leaching out of aluminium from the zeolite framework can be achieved by water present in the zeolite during activation. This process is known as 'steaming' [61, 67, 83, 88]. The precise threshold of water content of the zeolite needed for the steaming process to occur, remains subject to debate [85]. Steaming can be used to obtain ultrastable zeolite Y (USY), which is a crystalline material with enhanced acidity.

Framework collapse can for example be investigated by differential thermal analysis (appearance of an exothermic peak in the thermogram is indicative for crystal collapse) [84], or with powder x-ray diffraction [61]. A linear relationship found experimentally relates number of Na^+ ions per unit cell to collapse temperature ($T_{collapse}$, in Kelvin) for La^{3+} and Ca^{2+} exchanged Faujasites:

$$T_{collapse} = 1301 - \left(2.16 \cdot \frac{Number\ of\ Na\ atoms}{unit\ cell} \right) \qquad (1.10)$$

Presence of heavy metal cations can further decrease the thermal stability of the zeolite framework. The solutions of these cations used in the ion exchange are often acidic, which can lead to hydrolysis of the Si-O-Al bonds and thus to poor thermal stability of the end product. Removal of water after ion exchange also changes the coordination of the heavy metals. This in turn can cause destabilisation of the framework. Removing of water through heating can lead to hydrolysis leading to hydronium ions, which can weaken the Si-O-Al bond as shown (*vide* Figure 1.2-11) [61]. Schmidt and Weidenthaler found that the ion exchange of Pb^{2+} into Faujasite X and Y lead to better thermal stability in the end-product than when for example Cu^{2+} or Fe^{2+} were used. Favourable acidity

of the lead-salts used and absence of complexation of Pb^{2+} with water in the hydrated zeolite are seen by Schmidt and Weidenthaler as the reasons for this [61].

1.2.7.3 Cation migration and framework ordering

Activation affects the ordering of the zeolite framework, changing among other things the unit cell parameter [85, 89]. This effect can be observed in *e.g.* changing line intensities and positions of reflections in powder x-ray diffractograms [85].

Cations located inside zeolite cavities do not have rigid, fixed positions in the zeolite structure. In fact, migration of cations, even at room temperature, has been shown to occur [84, 85, 90]. Motion of ions in the framework is possible through electrophillic interaction with Al-O-Si bonds [85].

Direct methods of observing cation migration are for example extended x-ray adsorption fine structure (EXAFS), with which the local structure around an atom can be studied. Long-range order can be examined with for example X-ray diffraction (XRD). Next to direct methods, indirect methods have been used as well. For example, Jacobs *et al.* have, through infrared analysis of adsorbed carbon dioxide, shown migration of bivalent cations from the supercages of zeolite X to the sodalite cages [25]. Cs^+ in Cs-Faujasites migrates into the hexagonal prisms at temperatures >673 K [63].

In Faujasites, monovalent ions tend to vacate site I (hexagonal prisms) in favour of divalent ions when temperature is raised [90].

1.2.8 Zeolite synthesis

Aluminosilicates such as zeolites can be synthesised under hydrothermal conditions through precipitation from aluminosilicate solutions in basic media. Synthesis proceeds roughly through the following steps [91-93]:

a) Batch preparation:

- Mixing of reaction sources
- Gel formation
- Aging of the gel (optional)

b) Nucleation

a) Crystallisation

b) Product recovery

Batch preparation takes place at room temperature, nucleation and crystallisation at elevated temperatures (typically 333 – 523 K) and sometimes at elevated pressures [38, 92]. Polymer (such as Teflon) or steel vessels are preferred, as species found in glass (*e.g.* Na and silica) can participate in the chemical formation of the zeolite framework [91]. The following species generally participate in zeolite synthesis:

Table 1.2-3: Species involved in synthesis of zeolites

Species	Function
SiO_2	Framework building units
AlO_2^-	Source of framework charge
OH^- / F^-	Mineralising agent
Alkali cation, template	Charge compensating cation, template species
Water	Solvent, guest molecule

The particle size of the silica source influences its solvability, which in turn affects the crystallisation process of the zeolite. Impurities in the silica source can also influence the crystallisation by acting as crystallisation nuclei [92]. Impurities also limit Si/Al ratios that can be achieved. The alumina source is commercially available in high purity and has a small particle size [92]. Adjustment of pH is required to prevent alkali salt being formed, which has a detrimental effect on gel formation [91]. Control of the pH is achieved through usage of OH^-, which also acts as a mineralising agent, i.e. a species that enhances solubility of a solute [92, 93]. Generally, zeolite synthesis is carried out in a pH that exceeds 10 [92].

The template molecule, around which the zeolite structure is formed, can be inorganic or organic, charged or neutral. Inorganic templates are often alkaline or ammonium ions. Recipes for synthesis have been well documented [91].

1.2.9 Usage

A partial listing of the industrial usage of zeolites includes:

a) Adsorbents
- Drying agents
- Gas purifiers
- Separators (*e.g.* of p-xylene from its isomers)

b) Catalysts
- In petroleum refining
- In synfuels production
- In production of petrochemicals

c) Detergents
- Phosphate substitutes

d) Miscellaneous
- Waste water treatment
- Soil improvement
- Animal feed supplements

In comparison with bulk materials, zeolites offer certain advantages. They possess a high surface area (or micropore volume). With zeolites it is possible to achieve a high surface area of the catalytically active element(s). Also advantageous is that zeolites possess ion exchange capability [38].

Limitations to the usage of zeolites are found in (thermal) instability and deactivation as a result of the tendency of the zeolite to strongly retain by-product depositions (a process known as 'coking' [94]).

1.3 Basicity

1.3.1 Concepts and definitions

A Brønsted base is a substance that is able to accept a proton in an acid-base reaction. Thus, a Brønsted acid-base reaction of acid HA with base B would appear as follows:

$$HA + B \rightleftarrows BH^+ + A^-$$ (1.11)

For this reaction, the corresponding mass action quotient K is given by:

$$K = \frac{[BH^+] \cdot [A^-]}{[HA] \cdot [B]}$$ (1.12)

The square brackets in equation (1.12) indicate that concentrations of the respective species are to be employed. In the case the acid HA in equation (1.11) is water, one can obtain the so called base dissociation constant (pK_B) for a compound:

$$pK_B = -\log\left(\frac{[BH^+] \cdot [OH^-]}{[B]}\right)$$ (1.13)

In literature, often acid dissociation constants (pK_A) are given. The acid and base dissociation constants are related to each other by the water dissociation constant (pK_W). At conditions of 298 K and atmospheric pressure, this dissociation constant satisfies:

$$pK_A + pK_B = pK_w = 14$$ (1.14)

The pK_A scale offers a numerical indicator for acid or base strength in aqueous solution.

A Lewis base is a substance that is able to donate an unshared electron pair in an acid-base reaction [45]. Thus, a Lewis acid-base reaction of acid A with base B would appear as follows:

$$A + :B \rightleftharpoons :A + B \qquad (1.15)$$

The Lewis base is a more general concept than the Brønsted one, as the Lewis definition includes the Brønsted definition. A proton acceptor of course, has an unshared pair of electrons with which it binds the proton.

Definition of basic strength of a solid catalyst is far from trivial [95, 96]. Assessment of basic strength is done using for example x-ray photoelectron spectroscopy (XPS) [11, 97-106], infrared monitoring of adsorbed probe molecules [24, 107, 108], TPD [24] and reaction data [95]. In the following, some considerations in the assessment of basicity will be presented.

1.3.2 Zeolite basicity

It is worth emphasising that Lewis basicity (i.e. the donation of an electron pair) is discussed for zeolite basicity. Brønsted basicity was defined as the ability to accept a proton (*vide* §1.3.1). As such, Brønsted basicity is already described by the Lewis theory, as a proton is accepted through donation of electrons. Presence of mobile OH⁻ groups as anionic species in zeolites does not occur, as this would require a positively charged framework, which is not found in zeolites [4].

Alkali metal oxides and alkaline earth oxides have to a large extent been the 'classic' basic catalysts [109-111]. However, with the advent of porous material chemistry, ways became available to increase concentration of catalytically active sites.

Essential to base catalysed reactions is sufficient 'proton abstraction ability' of a basic catalyst. Framework basicity (also termed intrinsic basicity) in zeolites is often ascribed to framework oxygen. This oxygen bears negative charge [4, 5, 101], and is thus thought to be able to abstract protons from target molecules.

Oxygen atoms belonging to the AlO_4 tetrahedra are suggested to be the strongest basic sites in a zeolite [4]. Bond angles and distances in the tetrahedra affect the oxygen partial charge. Furthermore, the nature and location of the charge compensating cations will influence framework oxygen charge [4, 5].

Basicity increases as Si/Al-ratio decreases. This relation has been observed experimentally [4]. Some further factors of zeolite acido-basicity are summarised by Table 1.3-1. These factors can be divided in structural and physicochemical features of the zeolite framework [4].

Table 1.3-1: Factors determining acido-basic character of the zeolite framework. These factors can be broken down into two categories: structural (left) and physicochemical (right).

Structural factor	Physicochemical factor
Bond angles	Electronegativity
Bond lengths	Polarising power of ions
Charge distribution	Ionicity of framework elements

Next to oxygen sites, basicity may also be generated in zeolites by incorporated species, such as oxide clusters, hydroxides and (supported) metals [4]. An example, which illustrates the influence of these species, is found in the isopropanol decomposition by Cs-FAU with excess caesium [4, 66, 71]. Here, the observed catalytic activity is attributed to caesium oxide species in the zeolite cavities.

1.3.3 Zeolite acidity

Brønsted acid sites (proton donating species) in zeolites are formed by OH groups on Si-O-Al bridges, leading to a species noted as Si(OH)Al. Evidence for the presence of such sites can be found in the infrared spectra of activated zeolites. Generally, these sites can be found in zeolites between roughly 3650 and 3550 cm^{-1} [41]. In Faujasites, two sharp OH-bands in the infrared spectrum of an activated sample can be seen (LF and HF bands, *vide* §1.2.3.2).

Lewis acid groups (electron accepting species) can be formed by the (guest) cations in the pores, or by defect sites created by dealumination. An example of the latter is AlO^+ [41].

1.3.4 Base catalysed reactions

Basic strength of a catalyst is related to its ability to abstract a proton from a target molecule [96]. This ability can be studied in catalytic reactions [4].

1.3.4.1 Isopropyl alcohol dehydrogenation and dehydration

The target molecule in this reaction is isopropyl alcohol (IPA). The dehydrogenation of IPA is base catalysed and yields acetone, whereas the dehydration is acid catalysed and results in propene. Product distribution analysis in the IPA reaction is widely used to assess the basic and acidic nature of catalytic sites (*vide* Table 1.3-2).

A minor product of the acidic products catalysis is isopropyl ether [20]. On the basic route, 4-methyl-2-pentanol and 3,3,5-trimethylcyclohexanol have been observed as minor products [110]. Further products in secondary reactions include mesityl oxide and mesitylene, when this reaction was carried out over hydrotalcites [110].

Several authors have discussed mechanisms of the isopropanol reactions dehydration and dehydrogenation [110, 112-120]. The mechanisms found are presented below:
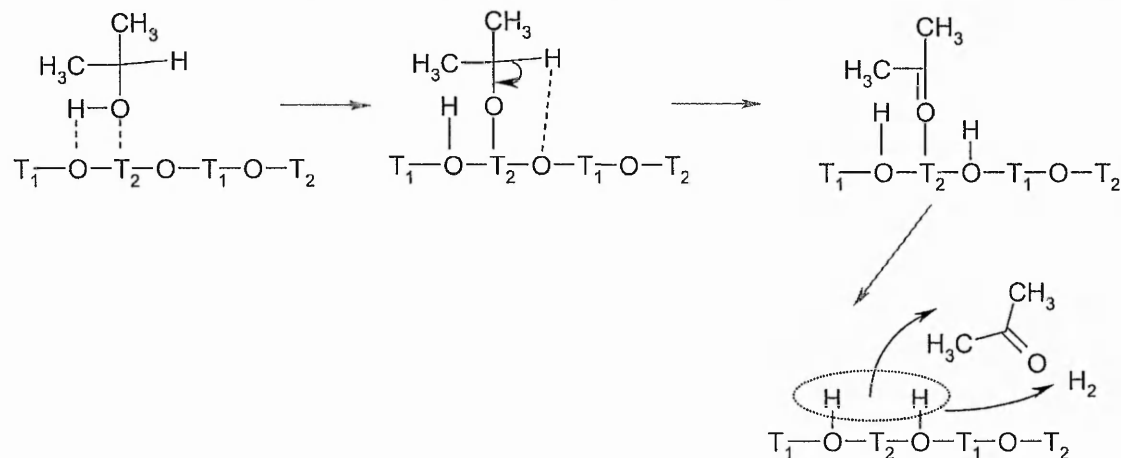
Figure 1.3-1: Dehydrogenation of isopropyl alcohol to acetone over a T-O-T framework via an alkoxide intermediate (Lewis acid-base mechanism). After references mentioned above (vide §1.3.4.1)
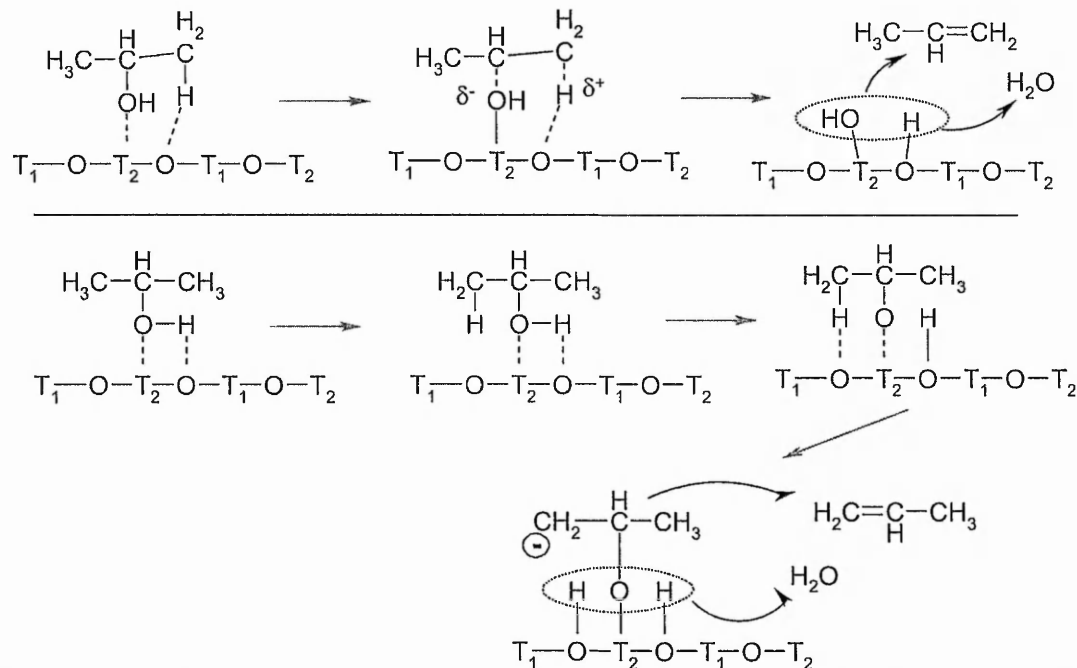
Figure 1.3-2: Dehydration of isopropyl alcohol over a T-O-T framework via two possible Lewis acid-base mechanisms: E_2 (top) and E_{1CB} (Bottom). After references mentioned above (vide §1.3.4.1)

Several authors have reacted IPA in order to identify acidic or basic nature of their catalysts. A selection of research published on isopropanol decomposition is given here (Table 1.3-2), to illustrate the various catalysts and reaction conditions involved.

Table 1.3-2: Various catalysts used by researchers for the isopropanol decomposition

Reference	Catalyst	Selectivity to acetone[a] /[%]	Reaction conditions[b]			Activation conditions[c]		
			T / [K]	Gas	IPA-concentr.	T / [K]	Gas	t / [h]
[121]	Zn oxides MgO Alumina	~100 0 0	483	He	2.2[d]	673	He	2
[122]	Cs-X CsOx/Cs-X	9 32<S<76	563	He	0.11	773	He	10
[75]	Na-X K-Na-X Cs-Na-X NaY K-Na-Y Cs-Na-Y	3 77 54 78 96 95	587	He	0.25	823	He	4
[123]	M-OMS-2[e]	>90	573	He	0.05	573	He	1
[124]	Dealuminated Faujasite-Y	0	343-403	He	0.04	703	He	3
[125]	TiO_2	100	448	O_2/He	0.01	673	air	2
[126]	ETS-10[f] K-X	78 62	623	Ar	0.06	673	Ar	n.a.
[127]	KNO_3/ZrO_2	30	673	N_2	n.a.	873	N_2	2
[20]	Al_2O_3 ZnO	0.053[g] 4.49, 35.5[g]	423 423 523	air	0.02	673	air	15
[110]	Mg/Al-HTLC	3	623	N_2	1	723	air	18
[128]	KOH/Na-Y MgO/Na-Y Na-Y	71 100 0	773 673 673			773 873 773		
[129]	SiO_2 Cs/SiO2	1.3 90.8	n.a.	N_2	n.a.	773	air	3

a) Selectivity to acetone, expressed as %(mol/mol)

b) Reaction circumstances are characterised here (from left to right) by reaction temperature, reaction atmosphere and concentration of isopropanol (ratio of moles isopropanol to moles carrier gas)

c) Activation is characterised here (from left to right) by final activation temperature, activation atmosphere and activation time

d) Given as a molar stream; no total flow rate and/or space velocity given

e) Metal cation doped manganese oxide molecular sieves

f) Engelhard titanosilicates: zeolite like materials

g) Expressed as ratio of reaction rates of dehydrogenation between catalyst and MgO. In other words: MgO dehydrogenation activity is set as 1

1.3.4.2 Other reactions

A number of base catalysed reactions exist [3-5, 96], of which a couple examples are given here.

Double bond isomerisation, initiated by proton abstraction, is a widely used indication reaction to characterise basicity. An example is the isomerisation of 1-butene to 2-butene [5, 70, 77, 130, 131]. This reaction proceeds at low temperatures, e.g. 223 K for 1-butene isomerisation over MgO. As the reaction can be acid catalysed as well, cis-trans ratios serve as a diagnostic tool [5]. The cis allyl anion that is formed after proton abstraction is more stable than the trans form, thus, cis to trans ratio is bigger than unity for a basic catalyst.

Dehydrogenation and dehydration reactions are often reactions of choice to characterise catalysts. Olefins and ethers are formed on acidic sites (dehydration), whereas aldehydes and ketones can be formed on basic sites (dehydrogenation). An example, which illustrates the general case, can be found in §1.3.4.1.

Aldol-type condensations and additions have been performed over basic catalysts [3, 12, 132-139]. Proton abstraction from a ketone leads to formation of a carbenium anion, which then reacts with a second ketone molecule. The aldol addition of acetone to diacetone alcohol is for example catalysed by $Ba(OH)_2$ [3]. Bifunctionality can be used in aldol condensations. The basic product of diacetone alcohol can dehydrate over acidic sites to give mesityl oxide [5, 12].

1.3.5 Assessing zeolite basicity

Characterisation of basic sites can be performed directly, by acid-base interactions with probe molecules or by catalytic reactions. Disadvantage of usage of probe molecules (and indeed usage of catalytic reactions) is found in the accessibility of basic sites. Constraints resulting from probe molecule size can limit for example access to sodalite cages in Faujasite. Furthermore,

migration of cations in the zeolite framework may be a consequence of cation - probe molecule interaction (*vide* §1.2.7.3).

1.3.5.1 Catalytic reactions

Assessing basic strength from reaction data or probe molecule adsorption data is not without hazards; pK_A values of substances strongly depend on the medium they are in, and indeed, their aggregation state.

Further information on catalytic reactions used can be found in §1.3.4.

1.3.5.2 Adsorption of carbon dioxide

Adsorption of gas phase carbon dioxide has been used to investigate basic sites on oxides and zeolites by many researchers [24-26, 122, 140-143]. On metal oxides, CO_2 can adsorb on basic surface hydroxyls, via the following mechanism:
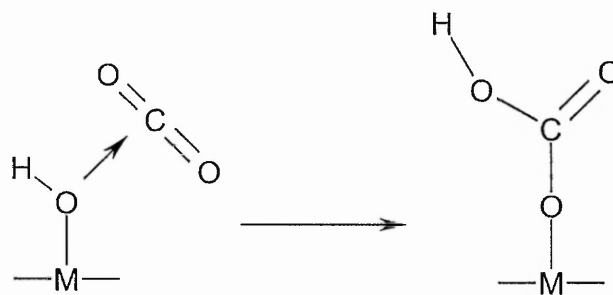
Figure 1.3-3: CO_2 adsorption on basic surface hydroxyls [24]. M represents a metal.

Type I   Type II   Type III
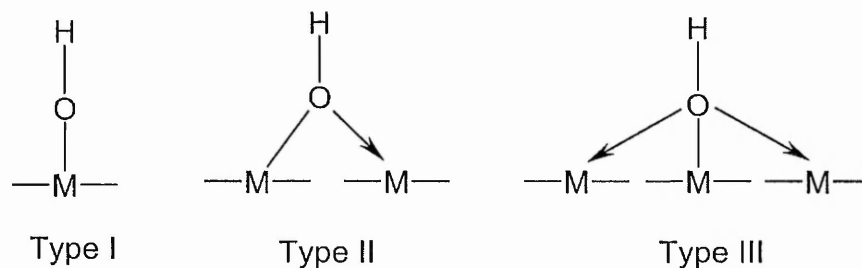
Figure 1.3-4: Three types of surface hydroxyls [24]. M represents a metal.

In the infrared region, the process in Figure 1.3-3 would lead to a reduction in intensity of the surface hydroxyl bands at ~3741 cm^{-1} (type I) or ~3668 cm^{-1} (type II) [24]. Further, an OH band appears at ~3610 cm^{-1} and at 1230 cm^{-1}, indicating formation of $HOCO_2^-$ species.

Next to adsorption on OH groups, CO_2 can also adsorb on cations. Jacobs *et al.* have published in the 1970s on IR studies of adsorbed CO_2 on Zeolites X and Y [25, 26]. On Ca-Na-Y, bands at 2367, 2349 and 1385 cm^{-1} (weakly adsorbed CO_2) increase with Ca^{2+} content. They observe over zeolite Y that: "the asymmetric stretching vibration of CO_2 on a high exchanged alkaline earth Y zeolite was cation dependent". A band at ~2360 cm^{-1} is indicative of cation-dipole interactions [24]. This ν_3 band shifts to higher wavenumbers with decreasing cation size [25], and to higher frequencies with increasing polarising strength of the cation [24]. Species of weakly adsorbed CO_2 (adsorbed through ion-dipole interaction) can be represented as follows:

$$Me^{x^+} \text{---} O^{\delta^-} = C = O^{\delta^+} \tag{1.16}$$

Adsorption leads to asymmetry in the adsorbed CO_2 molecule, resulting in an additional band (ν_2) at ~1385 cm^{-1}.

Jacobs found for the system he studied, Ca-Na-Y, that cation content at exchange levels lower than ~46% could not be detected by CO_2 adsorption, which is explained by the location of these cations in site I (hexagonal prisms), where the positive charge of the cation is screened, and no interaction with CO_2 takes place [25]. Thus, he used relative intensities of Na^+-CO_2 and M^{x+}-CO_2 as a measure of metal content in the supercage.

Upon adsorption, CO_2, with aid of zeolite framework oxygen, converts into carbonate species, which are infrared active [25, 26, 142]. Generally, adsorbed carbonate species are unidentate, bidentate or bridged, in order of decreasing binding strength to the surface on which they are adsorbed [111]. These species are illustrated in Figure 1.3-5.
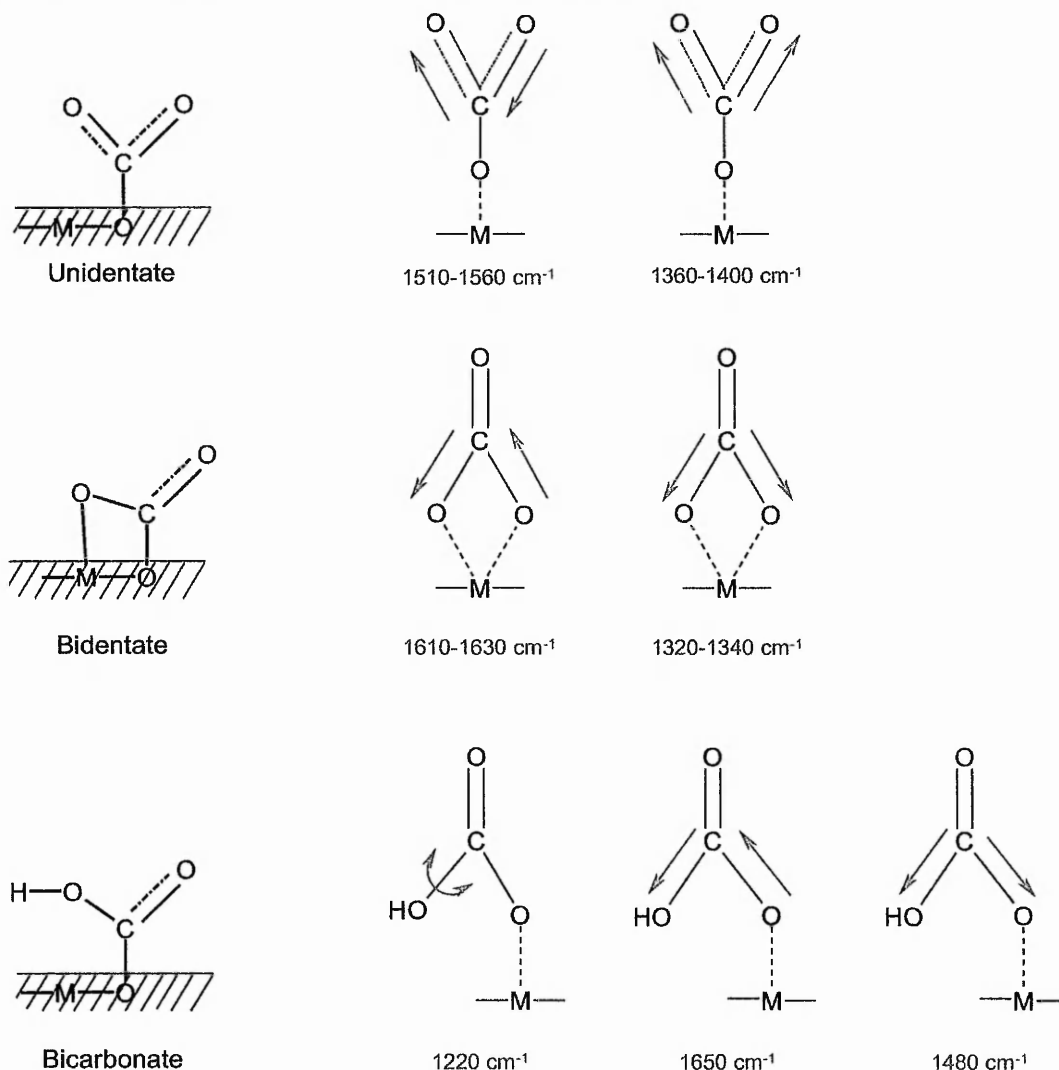
Figure 1.3-5: Carbonate species on Mg-Al based oxides [111]. Wavenumbers of infrared vibrations is given underneath each species. Symmetry of the vibration is indicated by usage of arrows.

Apart from usage of infrared, methods such as calorimetry have been used to assess binding of CO_2 to a solid's surface [24]. As stronger basic sites are able to bind the acidic CO_2 more strongly, it seems a valid approach to use CO_2 adsorption to investigate basic character of a catalyst.

1.3.5.3 Adsorption of ammonia

Traditionally, ammonia has been used to asses zeolite acidity, both qualitative and quantitative [24, 142].[144]. Ammonia is a strong Lewis base, reported to interact with acidic sites in zeolites [42, 145, 146]. Ammonia can adsorb in different modes:
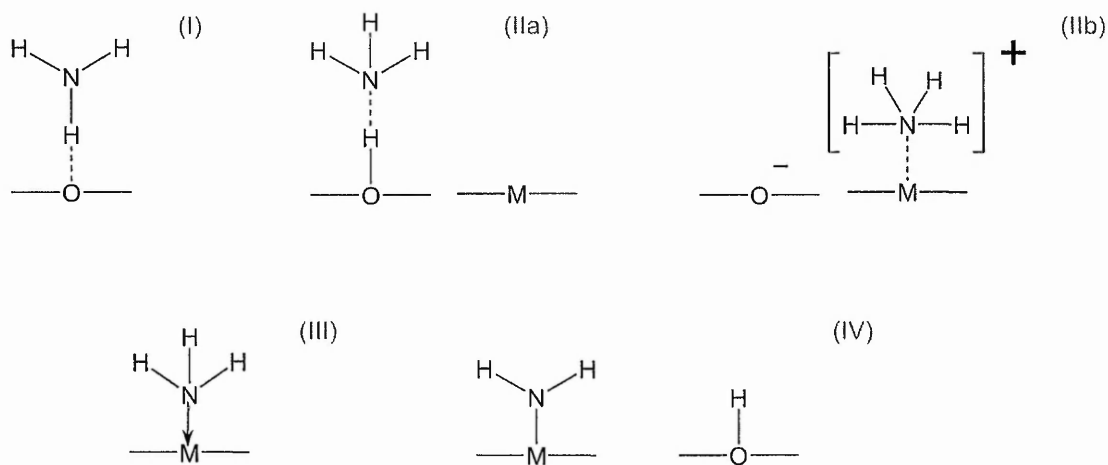
Figure 1.3-6: Different adsorption modes of ammonia on a solid oxide surface. After Lavalley [24].

Ammonia disproportionation can take place on acid-base pairs. Species I in Figure 1.3-6 is indicative for a basic site, whereas species IV can be found on amphoteric sites. Thus, ammonia adsorption and may not represent a sole characterisation of the basic oxygen atoms [24]. Species IV is characterised by an absorption band at 1550 cm^{-1} (δNH_2) in the infrared spectrum.

Adsorption on (acidic) surface hydroxyls is represented by species II. A diminishing of surface hydroxyls can be observed in the infrared, accompanying this adsorption [144, 147]. Adsorption on Lewis acid sites is seen in species III.

Because the kinetic diameter of ammonia (1.65 Å [41]) permits, in principle, penetration of the sodalite cages, it is a suitable probe to investigate acid sites in zeolites X and Y.

Kanizarev and Borisova performed ammonia-TPD experiments on zeolite X and Y samples with varying Si/Al ratios [148]. They adsorbed ammonia, in a gas stream of helium, at atmospheric pressure, and at elevated temperature (423 – 573 K). They identified two peaks during thermal desorption, one at low desorption temperature ("LTP peak"), and one at high desorption temperature ("HTP peak"). The LTP peak was always seen; the HTP peak was seen only on zeolite Y, not on zeolite X.
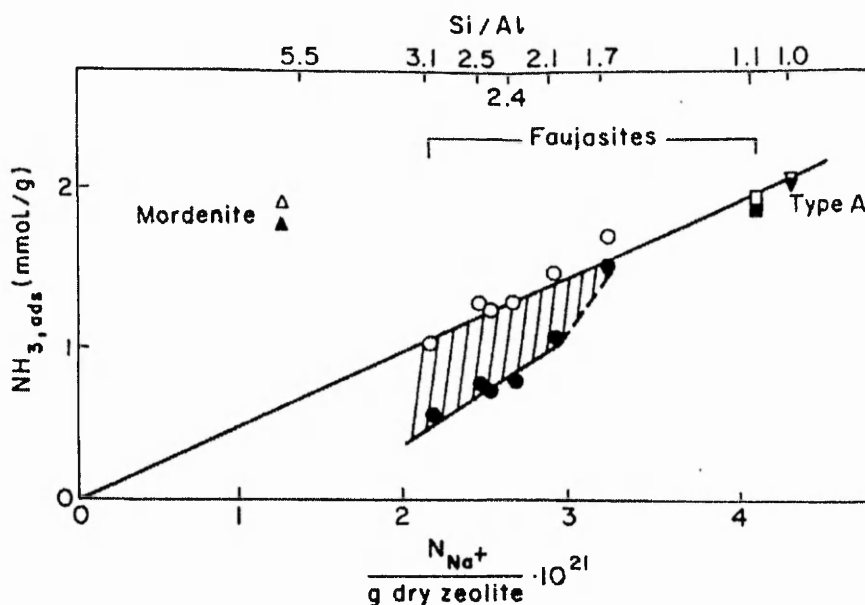
Figure 1.3-7: Ammonia adsorbed on Faujasites, mordenite and zeolite A, from Kanizarev and Borisova [148]. A mixture of ammonia and helium was passed over the samples. Open data points: adsorption at 573 K (0.5 h); rapid cooling of sample to 423 K; further adsorption (0.5 h); isothermal desorption in pure He; subsequent thermal desorption. Closed data points: as open data points, but no adsorption step at 573 K.

From their experiments Kanizarev and Borisova concluded that:

- Accessibility of sodalite cages to ammonia is diffusion controlled and dependant on Si/Al ratio. Increasing the silica content results in shrinking of sodalite cages, because the Si-O distance is shorter than the Al-O distance

- The main adsorption sites for ammonia in Na-Faujasites are the Na^+ cations

- Sodalite cages in zeolite X are more accessible to ammonia than those in zeolite Y, as no HTP peak was found on zeolite X samples

- Dehydration of the zeolite facilitates access of ammonia to sodalite cages

- Increasing the adsorption temperature increases both the vibrational amplitude of the sodalite cage and the kinetic energy of ammonia, thus facilitating admission of ammonia to the sodalite cages

- Even small amounts of polyvalent exchange-cations in the zeolite accelerate penetration of ammonia into the sodalite cages

1.3.5.4 Adsorption of nitromethane

From adsorption studies Nesterenko *et al.* interpreted that nitromethane chemisorbs on basic and amphoteric sites at room temperature [29]. It forms an aci-anion on basic sites, which is not found on acidic sites [29, 149]. An aci-anion is the conjugate anion base remaining after an α-hydrogen has been abstracted from a substance. Deprotonation of NM in basic solutions leads to formation of aci-anion-NM [150]. Thermal treatment of adsorbed nitromethane results in formation of isocyanic acid (473 − 673 K) on both basic and acidic sites. A schematic of the adsorption and (subsequent) thermal desorption can be seen in Figure 1.3-8.

Figure 1.3-8: Adsorption pathway of nitromethane, after Yamaguchi [150]. Isocyanic acid has a pK$_A$ of 3.46.

Isocyanate can be hydrolysed by water (desorbed from the adsorbate's surface) to form ammonia and carbon dioxide on γ-alumina [150]:

$$NCO^- + 2H_2O \rightleftarrows NH_3 + CO_2 + OH^- \tag{1.17}$$

Alternatively, hydrolysis can proceed directly from adsorbed carbamic acid on ZSM-5 [151]:
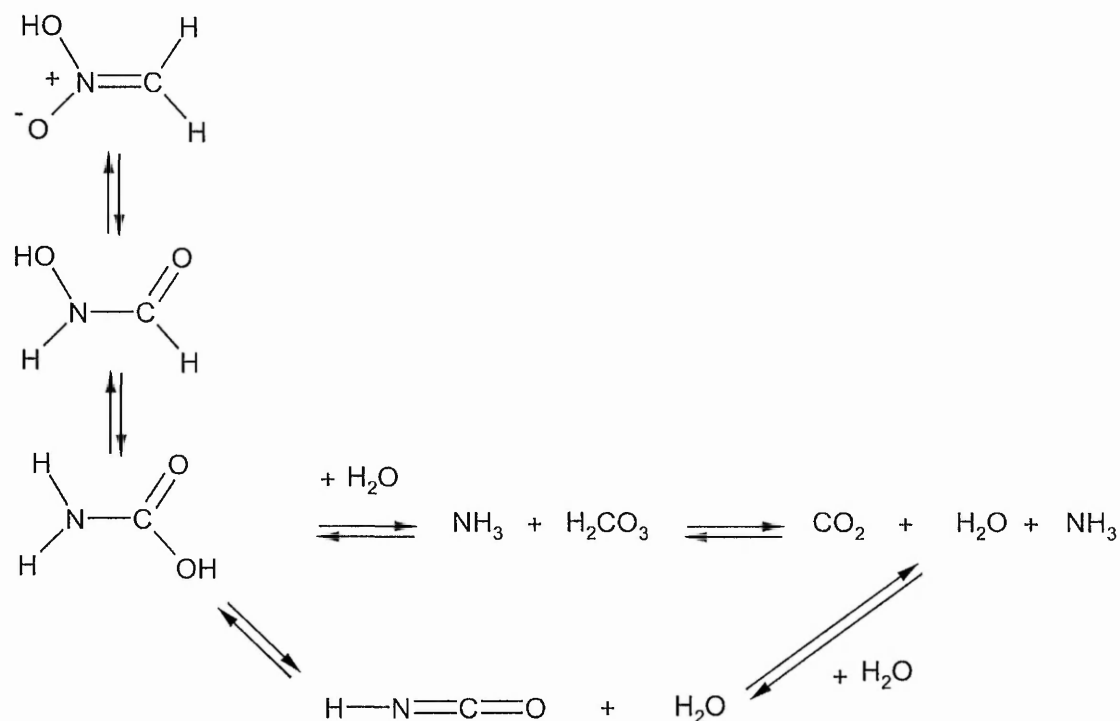
Figure 1.3-9: Reactions of adsorbed nitromethane on ZSM-5 after Lombardo [151]. Reactions carried out between 473 – 773 K.

Some NMR evidence is available for formation of methazonate (a dimer of a-NM) on the surface of basic solids [152]. A prerequisite for formation of this compound is the combination of strong basicity and weak Lewis acidity. The authors state that aci-anion-nitromethane (aa-NM) is stabilised by Lewis acid sites.

Adsorbed isocyanate species are infrared active [153, 154]. Peak positions in the infrared region can be used as a measure for basicity. The covalently bound NCO is interpreted as evidence for acidic sites, whereas the ionic NCO⁻ is viewed as evidence for basic sites [29] (see Figure 1.3-10). The frequency of these adsorbed isocyanate species apparently shifts to higher wavenumbers with increasing acidity [29].
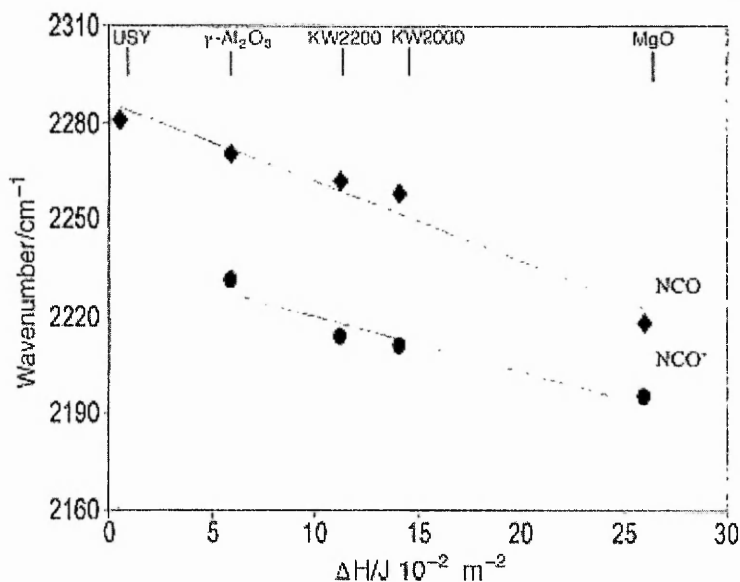
Figure 1.3-10: Correlation between the IR frequencies of the adsorbed isocyanate species and the heats of carbon dioxide adsorption on various solids. USY is ultrastable Y. KW2200 and KW2000 are Mg-Al mixed oxides.

1.3.5.5 Direct methods

Framework basic strength in zeolites is often ascribed to the amount of negative charge on the framework oxygen atoms [4, 5, 101]. Various researchers have attempted assessing the basicity of zeolite framework oxygen. One approach is to be found in the electronegativity equalisation method (EEM) [4, 101, 155, 156]. Sanderson electronegativities [157] can be used to assess framework basicity. The calculation of intermediate electronegativity rests, in Sanderson's words on the hypothesis that "if two or more initially different atoms combine chemically, they become adjusted to an equal intermediate electronegativity in the compound" [157].

Thus, framework electronegativity of a zeolite can be taken as the geometric mean of all atoms, which constitute this framework. Once framework electronegativity is obtained, it can be used to calculate partial charge on an atom type. It should be noted however, that this method averages all different sites of one atom type to one value. Notable distinctions between different oxygen sites in for example Faujasites [101] are ignored in this approach.

Sanderson's method is to be summarised in a couple of formulae [157]:

$$S_z = \left(\prod_i (S_i)^{\nu_i} \right)^{\frac{1}{\sum_i \nu_i}} \qquad (1.18)$$

Where S_z is the zeolite framework electronegativity and S_i is the electronegativity of atom i with stoichiometric coefficient ν_i.

$$\delta_j = \frac{S_z - S_j}{1.57\sqrt{S_j}} \qquad (1.19)$$

Where δ_j is the partial charge on atom j, which has electronegativity S_j. A constant of 1.57 is used in equation (1.19), which relates the electronegativity scale to the acquisition of one unit of charge. In other words, the acquisition of one unit of charge equals 1.57 times the square root of the electronegativity [157]. The magnitude of this constant depends on the electronegativity scale used.

Core level binding energies contain chemical information. Shifts in binding energy are a direct result from electrostatic screening of core electrons. Equally, the chemical environment of an atom influences binding energy levels of its core electrons [158]. X-ray photoelectron spectroscopy (XPS) provides information about the oxygen binding energy. Core level shifts of framework oxygen could in principle be related to partial charge of framework oxygen, which in turn could then be used as a measure for basicity.

Experimentally, increased basicity of framework oxygen was related to decreased O 1s binding energy in studies of alkali exchanged zeolite samples with low Si/Al ratio, such as zeolite X, Y and mordenite [11, 97]. It is worth here to point out that all factors determining XPS binding energy (E_b) have not been fully established yet.

Several influences on the binding energy of the O 1s line in zeolites have been identified using XPS experimentation. An increase in Si/Al ratio is correlated with an upfield binding energy shift of the O 1s line, regardless of crystal

structure [98, 158, 159]. A similar effect can be seen for the Si 2p, Al 2p and Na 2s lines [98, 160].

Furthermore, a decrease in electronegativity of the zeolitic counter-cation is accompanied by a downfield binding energy shift for the O 1s line [98].

One formula summarises the effects mentioned above [98, 158]:

$$E_{b,i} = kq_i + \sum_j \frac{q_j}{r_{ij}} + E_{b,ref} \qquad (1.20)$$

In equation (1.20), $E_{b,i}$ is the binding energy of atom i. The first term on the right hand side, kq_i is the charge (q) of atom i, multiplied by a constant (k). The second term on the right hand side is often named Madelung potential. This is a summation of the charge on surrounding atoms (q_j) divided by their distance to the central atom i (r_{ij}). The third term is a reference term ($E_{b,ref}$). It is related to Fermi levels.

It was reasoned, that with changing aluminium content and/or changing cation, Madelung potential changes, or, charge density around atoms changes [98]. Detailed discussions of core-level energies however, are beyond the purpose of this work.

1.3.5.6 Other methods

Some other methods are mentioned below, in addition to the ones commented on above (*vide* §1.3.5.1- 1.3.5.5)

Titration with an acidic molecule yields the acidic strength of a solid catalyst. Hammett indicators can be used to this end [3, 5, 161]. The principle of the titration is the acid-base reaction of indicator HIn with the solid under investigation.

$$HIn + B \rightleftarrows BH^+ + In^- \qquad (1.21)$$
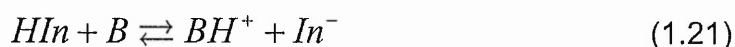
Concentrations of the indicator and its conjugated base In⁻ are measured. The H_ function is defined as follows:

$$H_- = pK_{A,HIn} + \log\frac{\left[In^-\right]}{\left[HIn\right]} \qquad (1.22)$$

Although this method provides an easy scale on which to rank basicity of various solids, it is carried out in the liquid phase, which carrier diffusion limitations, which will be especially problematic in zeolites [5]. Next to this, solvation may be important in the liquid phase, and lead to results that are not reflected in the gas phase.

Adsorbed pyrrole can be monitored by both infrared and XPS. XPS "sees" the shifts of the binding energy of the nitrogen atoms as a result of adsorption, whereas FTIR is used to study shifts of the N-H stretching vibration [4, 5].

Dissociation of hydrogen on solid surfaces can be monitored by TPD. H_2 dissociates in H^+ and H^-, which adsorb on surface oxide and cation respectively. Surface hydroxyls formed are active in the infrared region [5]. Interpretation is not an easy task however, as H_2 desorption on MgO for example yields 7 peaks [5].

1.4 References

1.   Brait, A., K. Seshan, and J.A. Lercher, *Applied Catalysis A - General* **169**, 299-313, (1998).

2.   Tanabe, K. and W.F. Holderich, *Applied Catalysis A - General* **181**, 399-434, (1999).

3.   Hattori, H., *Heterogeneous Catalysis and Fine Chemicals III* **78**, 35-49, (1993).

4.   Barthomeuf, D., *Catalysis Reviews-Science and Engineering* **38**, 521-612, (1996).

5.   Hattori, H., *Chemical Reviews* **95**, 537-558, (1995).

6.   Yashima, T., H. Suzuki, and N. Hara, *Journal of Catalysis* **33**, 486-492, (1974).

7.   Meyer, U., H. Gorzawski, and W.F. Holderich, *Catalysis letters* **59**, 201-206, (1999).

8.   Weiss, A.H., et al., *ACS Symposium Series* **437**, 243-253, (1990).

9.   Davidova, N., P. Kovacheva, and A.H. Weiss, *Catalysis Today* **13**, 625-626, (1992).

10.   Igelesia, E., et al., *Catalysis Today* **38**, 339-360, (1997).

11.   Okamoto, Y. and T. Kubota, *Microporous and Mesoporous Materials* **48**, 301-307, (2001).

12.   Veloso, C.O., J.L.F. Monteiro, and E.F. Sousaaguiar, *Studies in Surface Science and Catalysis* **84**, 1913-1920, (1994).

13.   Gentry, S.J. and R. Rudham, *Journal of the Chemical Society, Faraday Transactions I* **70**, 1685-1692, (1974).

14.   Ahmed, S., S. Chughtai, and M.A. Keane, *Separation and purification technology* **13**, 57-64, (1998).

15.   Biskup, B. and B. Subotic, *Physical Chemistry Chemical Physics* **2**, 4728-4733, (2000).

16.   Echevarria, M.S., et al., *Ecletica quimica* **22**, 15-22, (1997).

17.   Nardin, G., L. Randaccio, and E. Zangrando, *Zeolites* **15**, 684-688, (1995).

18.   Maliou, E., M. Malamis, and P.O. Sakellarides, *Water science and technology* **25**, 133-138, (1992).

19.   Kovacheva, P., N. Davidova, and A.H. Weiss, *Collection of Czechoslovak Chemical Communications* **57**, 2548-2552, (1992).

20.   Gervasini, A. and A. Auroux, *Journal of Catalysis* **131**, 190-198, (1991).

21.   Dong, J.L., J.H. Zhu, and Q.H. Xu, *Applied Catalysis A - General* **112**, 105-115, (1994).

22.   Batis, N.H. and A. Ghorbel, *Journal de chimie physique et de physico-chimie biologique* **94**, 77-92, (1997).

23.   Calsavara, V., et al., *Brazilian Journal of Chemical Engineering* **17**, 91-98, (2000).

24.   Lavalley, J.C., *Catalysis today* **27**, 377-401, (1996).

25.   Jacobs, P.A., F.H. Van Cauwelaert, and E.F. Vansant, *Journal of the Chemical Society, Faraday Transactions I* **69**, 2130-2139, (1973).

26.   Jacobs, P.A., et al., *Journal of the Chemical Society, Faraday Transactions I* **69**, 1056-1068, (1973).

27.   Satyanarayana, C.V.V. and D.K. Chakrabarty, *Indian journal of chemistry section a-inorganic bio-inorganic physical theoretical & analytical chemistry* **30**, 422-427, (1991).

28.   Guisnet, M., P. Ayrault, and J. Datka, *Microporous and Mesoporous Materials* **20**, 283-291, (1998).

29.   Nesterenko, N., et al., *New Journal of Chemistry* **23**, 665-666, (1999).

30.   Madonna, J.A., (1975).

31.   Dyer, A., *An introduction to zeolite molecular sieves* (1st ed.), John Wiley & Sons Inc., Bath, 1988.

32.   Ernst, S., *Angewandte Chemie-International Edition in English* **35**, 63-64, (1996).

33.   Sherry, H.S., *Journal of colloid and interface science* **28**, 288-292, (1968).

34.   Sherry, H.S., *Journal of physical chemistry* **70**, 1158-1168, (1966).

35.   Sherry, H.S., *Journal of physical chemistry* **71**, 1457-1465, (1967).

36.   International Zeolite Association, http://www.iza-structure.org/databases/,

37.   Szostak, R., *Handbook of molecular sieves* (1st ed.), New York, 1992.

38.   Breck, D.W., *Zeolite molecular sieves : structure, chemistry, and use* (1st ed.), Wiley-Interscience, London, 1974.

39.   Hunger, B., et al., *Journal of the chemical society-faraday transactions* **92**, 499-504, (1996).

40.   Jacobs, W.P.J.H., *Spectroscopic studies of the proton-ammonia interaction in zeolite Y*, in *PhD thesis, Schuit institute of Catalysis*. 1993, Technische Universiteit Eindhoven: Eindhoven.

41.   van Bekkum, H., et al., *Introduction to Zeolite Science and Practice* (2nd ed.), 2001.

42.   Kustov, L.M., *Topics in catalysis* **4**, 131-144, (1997).

43.   Woolery, G.L., et al., *Zeolites* **19**, 288-296, (1997).

44.   Jaramillo, E. and S.M. Auerbach, *Journal of Physical Chemistry B* **103**, 9589-9594, (1999).

45.   Atkins, P.W., *Physical Chemistry* (6th ed.), Oxford, 2001.

46.   Higgins, F.M., N.H. de Leeuw, and S.C. Parker, *Journal of materials chemistry* **12**, 124-131, (2002).

47.   Yang, S.Y. and A. Navrotsky, *Microporous and Mesoporous Materials* **37**, 175-186, (2000).

48.   Lohse, U., et al., *Journal of the Chemical Society-Faraday Transactions* **92**, 159-165, (1996).

49.   Carvalho, M. and D. Cardoso, *Synthesis of zeolite Beta with low template content*, in *Progress in Zeolite and Microporous Materials, Pts a-C*. 1997. p. 349-356.

50.   Camblor, M.A., et al., *Synthesis of nanocrystalline zeolite Beta in the absence of alkali metal cations*, in *Progress in Zeolite and Microporous Materials, Pts a-C*. 1997. p. 341-348.

51.   Gaines, G.L. and H.C. Thomas, *Journal of Chemical Physics* **21**, 714-718, (1953).

52.   Harjula, R., et al., *Journal of the Chemical Society-Faraday Transactions* **89**, 971-976, (1993).

53.   O'Connor, J.F. and R.P. Townsend, *Zeolites* **5**, 158-164, (1985).

54.   Harjula, R., et al., *Journal of the Chemical Society-Faraday Transactions* **88**, 1591-1597, (1992).

55.   Dyer, A., H. Enamy, and R.P. Townsend, *Separation Science and Technology* **16**, 173-183, (1981).

56.   Grimshaw, R.W. and C.E. Harland, *Ion-exchange: introduction to theory and practice* (1st ed.), London, 1975.

57.   Yuan, G., et al., *Journal of environmental science and health part a-Toxic/hazardous substances & environmental engineering* **34**, 625-648, (1999).

58.   Kuronen, M., et al., *Physical Chemistry Chemical Physics* **2**, 2655-2659, (2000).

59.   Harjula, R., A. Dyer, and R.P. Townsend, *Journal of the Chemical Society-Faraday Transactions* **89**, 977-981, (1993).

60.   Ertl, G., H. Knozinger, and J. Weitkamp, *Handbook of Heterogeneous catalysis* (1st ed.), Weinheim, 1997.

61.   Schmidt, W. and C. Weidenthaler, *Proceedings of the International Congress on Applied Mineralogy, 6th, Goettingen, Germany*, 241-244, (2000).

62.   Yagi, F., et al., *Microporous materials* **9**, 229-235, (1997).

63.   Koller, H., et al., *Microporous Materials* **5**, 219-232, (1995).

64.   Nightingale, E.R., Jr., *J. Phys. Chem.* **63**, 1381-1387, (1959).

65.   Lide, D.R., *Handbook of chemistry and physics* (80th ed.), Boca Raton, 1999.

66.   Hathaway, P.E. and M.E. Davis, *Journal of Catalysis* **116**, 279-284, (1989).

67.   Yagi, F., et al., *Acid-base catalysis II* **90**, 349-354, (1994).

68.   Ju, W.S., et al., *Journal of Synchrotron Radiation* **8**, 608-609, (2001).

69.   Geremia, S., G. Nardin, and L. Randaccio, *Acta Chimica Slovenica* **43**, 357-363, (1996).

70.   Bordawekar, S.V. and R.J. Davis, *Journal of Catalysis* **189**, 79-90, (2000).

71.   Lasperas, M., et al., *Microporous materials* **7**, 61-72, (1996).

72.   Meyer, U. and W.F. Hoelderich, *Journal of molecular catalysis a-chemical* **142**, 213-222, (1999).

73.   Kanada, A., et al., *Physical Chemistry Chemical Physics* **1**, 373-381, (1999).

74.   Sueto, S., et al., *Journal of the chemical society-faraday transactions* **93**, 659-664, (1997).

75.   Hathaway, P.E. and M.E. Davis, *Journal of Catalysis* **116**, 263-278, (1989).

76.   Olson, D.H., *Journal of Physical Chemistry* **72**, 1400-1401, (1968).

77.   Tsuji, H., F. Yagi, and H. Hattori, *Chemistry Letters*, 1881-1884, (1991).

78.   Schwarz, H.B., et al., *Applied Catalysis A - General* **130**, 227-241, (1995).

79.   Concepcion-Heydorn, P., et al., *Journal of Molecular Catalysis A - Chemical* **162**, 227-246, (2000).

80.   Mimura, H., M. Shibata, and K. Akiba, *Journal of Nuclear Science and Technology* **27**, 167-173, (1990).

81.   Lasperas, M., et al., *Studies in Surface Science and Catalysis* **97**, 319-326, (1995).

82.   Kotrel, S., M.P. Rosynek, and J.H. Lunsford, *Journal of Catalysis* **182**, 278-281, (1999).

83.   Kung, H.H., et al., *Topics in Catalysis* **10**, 59-64, (2000).

84.   Li, C.Y. and L.V.C. Rees, *Reactive Polymers, Ion Exchangers, Sorbents* **7**, 89-99, (1988).

85.   Ambs, W.J. and W.H. Flank, *Journal of Catalysis* **14**, 118-125, (1969).

86.   Kuehl, G.H. and A.E. Schweizer, *Journal of Catalysis* **38**, 469-76, (1975).

87.   Shiralkar, V.P. and S.B. Kulkarni, *Journal of Thermal Analysis* **25**, 399-407, (1982).

88.   Ray, G.J., B.L. Meyers, and C.L. Marshall, *Zeolites* **7**, 307-10, (1987).

89.   Kuman, V.D., B.P. Prasad, and V.V. Rao, *Indian Journal of Chemical Technology* **3**, 95-100, (1996).

90.   Dyer, A., R.B. Gettins, and J.G. Brown, *Journal of Inorganic and Nuclear Chemistry* **32**, 2389-94, (1970).

91.   Robson, H. and K.P. Lillerud, *Verified synthesis of zeolitic materials* (2nd ed.), Elsevier, Amsterdam, 2001.

92.   Oudshoorn, O.L., *Zeolitic coatings applied in structured catalyst packings (PhD thesis)*Delft, 1998.

93.   Elliot, S., *The chemistry and physics of solids* (1st ed.), Chichester, 1997.

94.   Joly, J.F., et al., *Catalysis Today* **9**, 31-38, (1991).

95.   Tanabe, K., et al., *Studies in Surface Science and Catalysis* **51**, (1989).

96.   Spivey, J.J., *Catalysis* (1st ed.), Royal Society of Chemistry, Cambridge, 2000.

97.   Vayssilov, G.N. and N. Rosch, *Journal of Catalysis* **186**, 423-432, (1999).

98.   Okamoto, Y., et al., *Journal of Catalysis* **112**, 427-436, (1988).

99.   Pijpers, A.P. and R.J. Meier, *Chemical Society Reviews* **28**, 233-238, (1999).

100.   Choi, S.Y., Y.S. Park, and K.B. Yoon, *Studies in Surface Science and Catalysis* **105**, 671-678, (1997).

101.   Heidler, R., et al., *Journal of Physical Chemistry* **100**, 19728-19734, (1996).

102.   Heidler, R., et al., *Microporous Materials* **12**, 1-11, (1997).

103.   Huang, M., A. Adnot, and S. Kaliaguine, *Journal of Catalysis* **137**, 322-332, (1992).

104.   Huang, M., A. Adnot, and S. Kaliaguine, *Journal of the American Chemical Society* **114**, 10005-10010, (1992).

105.   Huang, M.M., S. Kaliaguine, and A. Auroux, *Studies in Surface Science and Catalysis* **97**, 311-318, (1995).

106.   Liu, J., et al., *Zeolites* **19**, 197-199, (1997).

107.   Forster, H., et al., *Physical Chemistry Chemical Physics* **1**, 593-603, (1999).

108.   Huang, M.M. and S. Kaliaguine, *Journal of the Chemical Society-Faraday Transactions* **88**, 751-758, (1992).

109.   Handa, H., et al., *Catalysis letters* **59**, 195-200, (1999).

110.   Corma, A., V. Fornes, and F. Rey, *Journal of Catalysis* **148**, 205-212, (1994).

111.   Di Cosimo, J.I., et al., *Journal of Catalysis* **178**, 499-510, (1998).

112.   Hussein, G.A.M., et al., *Journal of the Chemical Society-Faraday Transactions I* **85**, 1723-1742, (1989).

113.   Zaki, M.I. and N. Sheppard, *Journal of Catalysis* **80**, 114-122, (1983).

114.   Cunningham, J., et al., *Faraday Discussions*, 283-302, (1981).

115.   Noller, H. and G. Ritter, *Journal of the Chemical Society-Faraday Transactions I* **80**, 275-283, (1984).

116.   Deo, A.V., T.T. Chuang, and I.G. Dalla Lana, *Journal of physical chemistry* **75**, 234 - 239, (1971).

117.   Hertl, W. and A.M. Cuencia, *Journal of physical chemistry* **77**, 1120 - 1126, (1973).

118.   Weitkamp, J., M. Hunger, and U. Rymsa, *Microporous and Mesoporous Materials* **48**, 255-270, (2001).

119.   Cunningham, J., et al., *Journal of Catalysis* **102**, 160-171, (1986).

120. Di Cosimo, J.I., et al., *Journal of Catalysis* **190**, 261-275, (2000).

121. Lahousse, C., et al., *Journal of Molecular Catalysis* **87**, 329-332, (1994).

122. Doskocil, E.J. and R.J. Davis, *Journal of Catalysis* **188**, 353-364, (1999).

123. Chen, X., et al., *Journal of Catalysis* **197**, 292-302, (2001).

124. Triantafillidis, C.S. and N.P. Evmiridis, *Industrial & engineering chemistry research* **39**, 3233-3240, (2000).

125. Rekoske, J.E. and M.A. Barteau, *Journal of Catalysis* **165**, 57-72, (1997).

126. Philippou, A., J. Rocha, and M.W. Anderson, *Catalysis Letters* **57**, 151-153, (1999).

127. Wang, Y., et al., *Materials Letters* **46**, 198-204, (2000).

128. Zhu, J.H., et al., *Catalysis Today* **51**, 103-111, (1999).

129. Bal, R., et al., *Journal of Catalysis* **204**, 358-363, (2001).

130. Kim, J.C., et al., *Microporous Materials* **2**, 413-423, (1994).

131. Wang, Y., et al., *Microporous and Mesoporous Materials* **26**, 175-184, (1998).

132. Choudary, B.M., et al., *Tetrahedron Letters* **39**, 3555-3558, (1998).

133. Dumitriu, E., et al., *Microporous and Mesoporous Materials* **43**, 341-359, (2001).

134. Kantam, M.L., et al., *Chemical Communications*, 1033-1034, (1998).

135. Rao, K.K., et al., *Journal of Catalysis* **173**, 115-121, (1998).

136. Philippou, A. and M.W. Anderson, *Journal of Catalysis* **189**, 395-400, (2000).

137. Rode, E.J., et al., *Abstracts of Papers of the American Chemical Society* **198**, 7-CATL, (1989).

138. Rode, E.J., et al., *Catalysis Letters* **9**, 103-114, (1991).

139. Wierzchowski, P.T. and L.W. Zatorski, *Catalysis Letters* **9**, 411-414, (1991).

140. Davis, R.J., E.J. Doskocil, and S. Bordawekar, *Catalysis Today* **62**, 241-247, (2000).

141. Garrone, E., et al., *Proceedings of the International Zeolite Conference, 12th, Baltimore, July 5-10, 1998* **4**, 2705-2710, (1999).

142. Martra, G., et al., *Research on chemical intermediates* **25**, 77-93, (1999).

143. Philipp, R. and K. Fujimoto, *Journal of Physical Chemistry* **96**, 9035-9038, (1992).

144.   Hunger, B. and J. Datka, *Journal of thermal analysis and calorimetry* **53**, 217-225, (1998).

145.   Teunissen, E.H., F.B. Van Duijneveldt, and R.A. Van Santen, *Journal of Physical Chemistry* **96**, 366-71, (1992).

146.   Teunissen, E.H., et al., *Journal of Physical Chemistry* **97**, 203-10, (1993).

147.   Basini, L., U. Cornaro, and A. Aragno, *Langmuir* **8**, 2172-2177, (1992).

148.   Kanazirev, V. and N. Borisova, *Zeolites* **2**, 23-8, (1982).

149.   Kheir, A.A. and J.F. Haw, *Journal of the American Chemical Society* **116**, 817-818, (1994).

150.   Yamaguchi, M., *Journal of the Chemical Society-Faraday Transactions* **93**, 3581-3586, (1997).

151.   Lombardo, E.A., et al., *Journal of Catalysis* **173**, 440-449, (1998).

152.   Lima, E., et al., *Studies in Surface Science and Catalysis* **135**, 3662-3669, (2001).

153.   Silverstein, R.M. and F.X. Webster, *Spectrometric identification of organic compounds* (6th ed.), New York, 1998.

154.   van der Maas, J.H., *Basic infrared Spectroscopy* (2nd ed.), London, 1972.

155.   Vangenechten, K.A. and W.J. Mortier, *Zeolites* **8**, 273-283, (1988).

156.   Vangenechten, K., W. Mortier, and P. Geerlings, *Journal of the Chemical Society-Chemical Communications*, 1278-1279, (1986).

157.   Sanderson, R.T., *Chemical periodicity* (1st ed.), London, 1960.

158.   Stoecker, M., *Microporous Materials* **6**, 235-257, (1996).

159.   Jirka, I., *Zeolites* **17**, 310-313, (1996).

160.   Barr, T.L., *Applied Surface Science* **15**, 1-35, (1983).

161.   Bartnicka, H., I. Bojanowska, and M.K. Kalinowski, *Australian Journal of Chemistry* **46**, 31-36, (1993).

2   Experimental

2.1 Introduction

This chapter describes the experimental methods that have been used to modify zeolites as well as to analyse and to characterise them. The techniques and methods that have been applied to study their behaviour as adsorbents and catalysts are also discussed. In each case the physical and/or chemical principles underlying each method are given, followed by a description of the instrumentation used and the way in which the technique has been applied.

2.2 Heterophase ion exchange

2.2.1 Principle

Heterophase ion exchange is used to introduce cations into the zeolite cavities. The procedure, though executed with different nuances, essentially consists of suspending powdered zeolite in a solvent (usually water, but also other solvents can be used, *e.g.* methanol [1, 2]) together with an amount of the exchange salt.

The suspension is stirred or agitated for a certain time, after which it is filtered. The procedure can be repeated several times. Nuances in the *modus operandi* of this technique are slurry temperature, exchange salt(s) concentration(s), total exchange time, pH of the suspension, number of exchange repetitions and stirring velocity. All of these factors can be optimised to arrive at a homogeneous distribution of the exchange ion on the parent material [3, 4].

After the final exchange, it can be opted to wash the resulting zeolite, either in distilled water or a diluted salt solution [5, 6]. The washed product is dried either in ambient conditions, or at slightly elevated temperatures e.g. 353 K [7].

A degree of ion exchange can be expressed as a percentile, based on aluminium content of the zeolite. Thus, the amount of moles of cation is multiplied by its charge, and subsequently divided by the amount of moles of aluminium [8-11].

2.2.2 Instrumentation

Temperature during ion exchange was maintained using an IKA-Labortechnik heater-stirrer (model RCT basic), which was equipped with an IKA ETS-D4 temperature control unit. The stirring speed was kept constant throughout the exchange, at a setting of five.

For separation of solution and solid phase after the exchange, either a centrifuge (Manufacturer: Wifug; model: 500E) or a Büchner filtration setup was used. The vacuum in the filtration set-up was achieved by usage of a water jet pump.

2.2.3 Application

The starting materials ('parent zeolites' or 'carriers') were commercially available zeolites. Table 2.2-1 summarises the parent zeolites used.

Table 2.2-1: Parent zeolites used in heterophase ion exchange. Si/Al ratios are taken from manufacturers specification.

Zeolite	Supplier	Code	Si/Al ratio
NH_4-ZSM-5	Zeolyst International	CBV 3024E	15.0
Na-A	Union Carbide	13X	1.0
Na-Y	Zeolyst International	CBV-100	2.55
Na-X	Süd Chemie	-	1.5
NH_4-Beta	Catal International Ltd.	CT-121	12.5
Na-Y	Aldrich	33,444-8	2.36
NH_4-Y	Aldrich	33,441-3	2.36
NH_4-Y	Zeolyst International	CBV-300	2.55

Typically, 3-6 grams of carrier were suspended with the exchange salt in 250-500 ml distilled water. The slurry was stirred for 24 hours, either at room

temperature, or at 343 K. The resulting catalysts were dried overnight at ambient conditions and stored in glass sample bottles. The conditions employed for individual ion exchanges can be found in chapter 3 (*vide* §3.2.3).

2.3 Thermo-gravimetric analysis

2.3.1 Principle

Thermo-gravimetric analysis (T.G.A. [12-14]) can be used to determine the loss of mass from a solid sample as it is heated. Heating of zeolite samples causes crystal water to evaporate. Thus, the mass of the powdered sample decreases as temperature increases.

2.3.2 Instrumentation

For this analysis a custom made (in house built) rig was used. A sample of ~10 mg was weighed on a microbalance, which was enclosed in a furnace.

2.3.3 Application

The sample was outgassed at room temperature by flowing dry nitrogen (BOC, H_2O < 1 ppmv) over it. The sample was subsequently heated to ~1100 K, at a heating rate of ~5 K min^{-1}. Water content was established as the percentile difference between the initial (not outgassed) mass and the final mass of the sample, at 1100 K. The number of water molecules could then be calculated per formula unit (*vide* §1.2.5).

2.4 Atomic spectroscopy

2.4.1 Principle

Spectroscopy is based on the interaction with electromagnetic radiation with matter. Absorption spectroscopy usually consists of measurement of the radiation transmitted through a sample as a function of the radiant energy, whereas in emission spectroscopy the frequencies present in radiation emitted by the analyte itself are measured [15, 16].

2.4.1.1 Interaction of electromagnetic radiation with matter

Interaction can take place in the following ways: transmission, dispersion, refraction, reflection, scattering, polarisation, absorption and emission through the photoelectric effect. In the particle description of electromagnetic radiation, a photon is considered to have a discrete energy (E), which is related to its frequency (ν) or wavelength (λ) by the following equation [15]:

$$E = \frac{h \cdot c}{\lambda} = h \cdot \nu \qquad (2.1)$$

Where h is Planck's constant ($6.63 \cdot 10^{-34}$ J s) and c is the speed of light in vacuum ($3.0 \cdot 10^{8}$ m s^{-1}).

An overview of the spectroscopic techniques used for this work is given in Table 2.4-1.

Table 2.4-1: Interaction of electromagnetic radiation with matter. The spectroscopic methods applied in this work are listed in the first column. The radiation causes a quantum transition in the analyte material, which is listed in the second column. Wavelengths of the radiation used given in the third column are arbitrary [16-19].

Type of spectroscopy	Type of quantum transition	λ range / [nm]
X-ray absorption (XAS)	Inner electron	0.01 – 10
X-ray diffraction (XRD)	n.a.	0.01 – 10
Atomic absorption (AA)	Bonding electrons	180 – 780
Atomic emission (AE)	Bonding electrons	180 – 780
Infrared absorption (IR)	Rotation / vibration of molecules	0.78 – 300

The absorption of radiation by matter can be depicted in a simplified manner as follows:
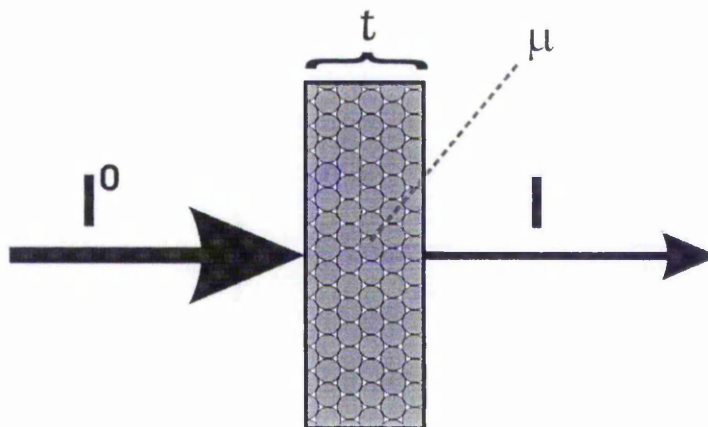
Figure 2.4-1: Absorption of EM radiation. Incident beam of intensity I^0 interacts with a body of matter having an absorption coefficient μ and thickness t, resulting in a reduction of the intensity to I.

The macroscopic quantification of the absorption process in Figure 2.4-1 is described in the Lambert-Beer law [16, 19]:

$$I = I^0 e^{-\mu \cdot t} \tag{2.2}$$

For an explanation of the symbols in equation (2.2) *vide* Figure 2.4-1. The thickness t is also known as the optical path length.

A quantity called absorbance can be represented in a dimensionless way. Absorbance is related to transmission [16]:

$$A = -\log T = -\log \frac{I}{I^0} \tag{2.3}$$

In equation (2.3), the absorbance is defined as A, whereas the transmission is defined as T. Absorbance is also known as extinction or optical density [16].

2.4.1.2 Atomic absorption spectroscopy

Atomic absorption spectroscopy (abbreviated to AA) is based on the absorption of electromagnetic radiation (in the ultraviolet, visible or near-infrared region) by atoms or elementary ions. Absorption causes [16] transitions in an atom of the outermost electrons from the ground state to an excited state (*vide* Table 2.4-1). The absorption lines tend to be narrow and well defined when the analyte is in the gaseous atomic state [15, 16]. Lambert-Beer's law is used for quantitative analyses (*vide* §2.4.1).

2.4.1.3 Atomic emission spectroscopy

One type of atomic emission spectroscopy (abbreviated to AE) is known as flame photometry. It is for example often used for analysis of Na, K, Li and Ca in biological samples [16]. Thermal excitation is the governing principle in atomic emission spectroscopy, in contrast to atomic absorption spectroscopy where electromagnetic excitation is used [16]. Lambert-Beer's law is used for quantitative analyses (vide §2.4.1).

2.4.1.4 Inductively coupled plasma spectroscopy

An atomic emission spectroscopy technique that uses an inductively coupled plasma (ICP) source can be used for quantification of constituent elements in a sample [20-22]. A plasma can be initiated from a flow of argon by a spark from a so called Tesla coil, which is a high-voltage air-core resonant transformer [16].

An induction coil powered by a radio-frequency generator then induces a changing magnetic field, which interacts with the argon ions that arise as a result of the spark. This interaction causes the charged particles to move in an annular way. The resistance of the particles to this trajectory leads to ohmic heating. By employing a plasma source the excitation temperature achieved is much higher than for flame sources, which results lower inter-element interference [16]. This in turn allows the measurement of multiple elements using a single set of excitation conditions, whereas flame sources require that for each element the excitation conditions have to be changed (e.g. fuel and oxidant used). A further advantage of a plasma source is greater reproducibility of the atomisation conditions, which leads to a better precision in the measurement [16]. A disadvantage of the usage of inductively coupled plasma spectroscopy is the high operational and instrumental costs associated with this technique.

2.4.1.5 Zeolite matrix dissolution methods

Where the analytical method of interest requires the sample to be presented as a solution, it is firstly necessary to dissolve the zeolite. A few dissolution techniques are available [20, 21].

The method used for this work is the dissolution of a sample in a mixture of acids at room temperature. Crucial is the presence of hydrofluoric acid in the acid mixture, since it can dissolve silica. After dissolution the solvent is evaporated off, followed by re-dissolving of the residue in diluted nitric acid. It is worth pointing out that it is not possible to analyse silicon with this method. During the evaporation step, silicon may escape from the sample, through formation of volatile (silicon-fluoride) compounds [21].

An alternative method is the cold digestion of zeolites [21], at room temperature in an acid mixture. The solvent is not evaporated. After dissolution the solution is analysed directly using atomic spectroscopy. An important advantage is the retaining of the elements that form volatiles with fluoride. Since the analyte solution will contain traces of hydrofluoric acid, instrument compatibility is

required since hydrofluoric acid corrodes glass parts, which excluded the use of this method for this work.

Dissolution in a mixture of molten salts is a third possibility for zeolites. In this technique, a mixture of lithium tetraborate and lithium carbonate is used [20]. The sample is mixed in with the salts and is subsequently heated until the mixture melts. The hot mixture is then quenched and dissolved in a nitric acid solution.

2.4.2 Instrumentation

The general build of optical instruments can be found in Figure 2.4-2 [16].
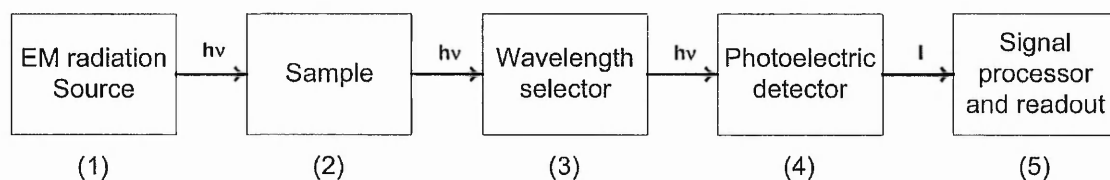
Figure 2.4-2: Schematic build-up of optical instruments. Electromagnetic (EM) radiation originates from a source (1). Photons are indicated by 'hv'. The generated electromagnetic radiation passes through the sample (2). A specific wavelength is analysed using a wavelength selector (3). The radiation is converted into electric current (hv ➔ I) in the detector (4). Finally, the signal is processed and can be read (5) [16]

A stable source for radiant energy generation is needed (1), for which a so-called hollow cathode lamp can be used [16]. For atomic emission spectroscopy the radiation source is omitted, as the sample, which is thermally excited by means of a flame, acts as the radiation source itself. In atomic absorption spectroscopy often a flame is used to atomise the sample. Common fuels are acetylene or hydrogen and general oxidants are air or nitrous oxide. Choice of the type of fuel and oxidant (and indeed their ratio) is element dependant. For ICP, a plasma from argon, created by an induction coil, is the source.

The radiation impinges on the sample (2). The purpose of the wavelength selector (3) is to filter the radiation and to allow only those frequencies suited for the measurement to pass. Narrow bands of radiation enhance the sensitivity of absorbance measurements. These devices can be *e.g.* prisms or gratings.

The radiation is detected by means of a photo-electric detector (4), which converts the radiant energy to a usable (electrical) signal. Examples are photomultipliers or silicon diodes. The reading of a measurement is then achieved by means of a recording device (5), which allows the signal to be displayed.

2.4.3 Application

Zeolite samples were dissolved in a mixture of concentrated acids: 5 ml nitric acid, 1 ml hydrochloric acid and 1 ml hydrofluoric acid. This mixture allowed for dissolution of the elements of the zeolite framework [20, 21]. For instrumental and safety reasons, the acid mixture was subsequently evaporated off in a fume hood, and the residue re-dissolved in 1 ml nitric acid. This solution was washed into a volumetric flask containing demineralised water. A calibration series consisting of 5 points was made up of the element under investigation. The extinctions for Pb and Na were measured at 217.0 nm and 589.0 nm respectively on a Perkin Elmer AAS 3110 spectrometer.

Atomic emission spectroscopy was used for analysis of Na and K in zeolite samples. The dissolution process was identical to the procedure described above. For emission spectroscopy measurements a calibration series was made analogues to the series used for the atomic absorption measurements. A Scientific and Medical Products Ltd. flame photometer model 410 was used.

2.5 Powder X-ray diffraction

2.5.1 Principle

The general principle of x-ray diffraction is based on the scattering of x-rays by a crystalline solid. A prerequisite for constructive interference is a crystalline nature of the solid sample, as is demonstrated in Figure 2.5-1.
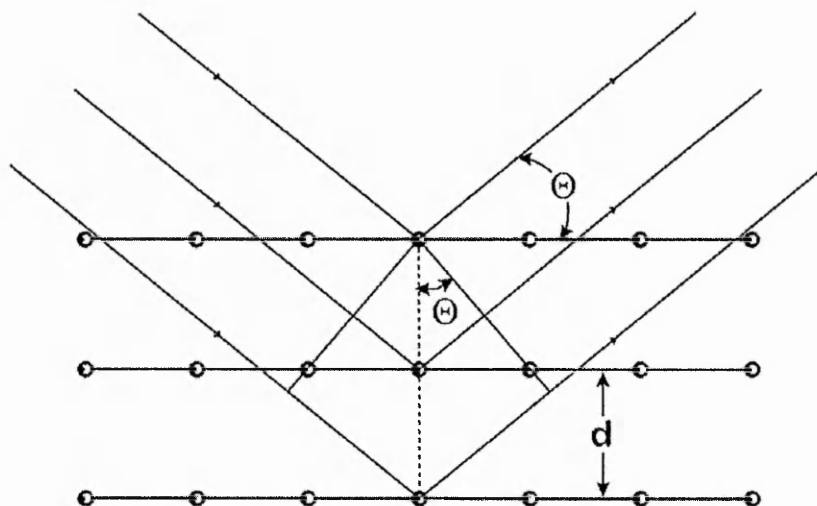
Figure 2.5-1: X-ray diffraction by a crystalline solid demonstrating angle of incidence θ and distance d between lattice plains. After Lipson and Steeple [18]

From Figure 2.5-1 Bragg's law for constructive interference can be deduced [16]:

$$n \cdot \lambda = 2 \cdot d \cdot \sin(\theta) \qquad (2.4)$$

In the powder diffraction experiments done for this work, we are only concerned with diffraction, and neglect absorption phenomena. Because lattice structures are determined by chemical composition, XRD can be used as an identification tool for crystalline phases. From the XRD pattern structural information can also be deduced using both the Bragg equation and knowledge about the shape and dimensions of the unit cell. A more elaborate treatise on this topic can be found elsewhere and is beyond the scope of this work [17, 18, 23, 24]. Simulated and indexed powder XRD patterns of zeolites are readily available through the International Zeolite association [23], the JCPDS database [25] and the Chemical Database Service from Daresbury Laboratory [26].

Peak broadening in x-ray diffractograms is a source of information concerning the apparent dimension of the crystallite in the direction perpendicular to the reflecting plane, as described in the Scherrer equation [18, 19]:

$$< L > = \frac{K \cdot \lambda}{\beta \cdot \cos \theta} \qquad (2.5)$$

Apart form broadening due to apparent crystallite size, instrumental broadening and structural faults are causes of peak broadening in the powder XRD pattern. Amorphous phases in the solid appear as a broad background feature. Too small particles cannot be detected by XRD [19].

2.5.2 Instrumentation

Powder diffraction patterns were recorded on a Hiltonbrooks Ltd. modified Philips 1050 x-ray diffractometer. The sample holder consisted of an aluminium plate with a right-angled cutout. The diffractometer was equipped with a Philips goniometer, which allowed for detector and sample holder rotation. Radiation used was that of the Cu Kα line (at 1,5406 Å), provided by an AEG x-ray tube. A scintillation detector (using a NaI crystal) from Hilger Analytical was used.

Data from the diffractometer were fed into a computer using an interface. Data was processed using a software package called Traces (v. 3.0) from Hiltonbrooks Ltd. The data files, consisting of detector counts versus Bragg angle were stored in a comma delimited text file, which could be read into various graphical processing packages for further analysis. For this, the Grams/32 software package (version 5.10) was used [27].

2.5.3 Application

Measurements were performed on powdered samples. Before measurement, samples were ground using a pestle and mortar. The sample was pressed manually into the sample holder, creating a smooth layer.

Patterns were recorded of both untreated ('as is') and activated samples. The activation procedure consisted of heating the samples in an atmosphere of helium.

Experimentally obtained patterns were compared with reference patterns in order to identify possible lead phases and/or loss of crystallinity/symmetry.

Reference patterns for several lead oxides were obtained using the databases mentioned in §2.5.1 [23, 25, 26].

2.6 X-ray photoelectron spectroscopy

2.6.1 Principle

X-ray induced photoelectron spectroscopy (XPS) was formerly known as ESCA (electron spectroscopy for chemical analysis). It is based on the absorption of an x-ray photon by an atom, which will result in ejection of a core electron (*vide* Figure 2.6-1). This electron was bound with binding energy E_b. A prerequisite for this process is that the x-ray photon energy ($h\nu$) is above a certain threshold. The ejected electron carries kinetic energy (E_k) with it, and if the x-ray photon energy is known, the binding energy of this electron can be probed. The photoelectron kinetic energy must satisfy eq. (2.6) [16, 19, 28, 29].

$$E_k = h \cdot \nu - E_b - \varphi \tag{2.6}$$

In association with photoelectrons, x-ray induced secondary electron emission can also occur. In this process, an electron from a higher level fills the core hole left by the original photoelectron. Simultaneously, a further electron is ejected, which is called the Auger electron. Both processes are illustrated in Figure 2.6-1.

photoelectron

KL_1L_3 Auger electron

E_K

E_k

vacuum level

Fermi level

ϕ

energy levels

$2p_{3/2}$ (L_3)

$2p_{1/2}$ (L_2)

E_b

$2s$ (L_1)

$h\nu$

$1s$ (K)

photo emission
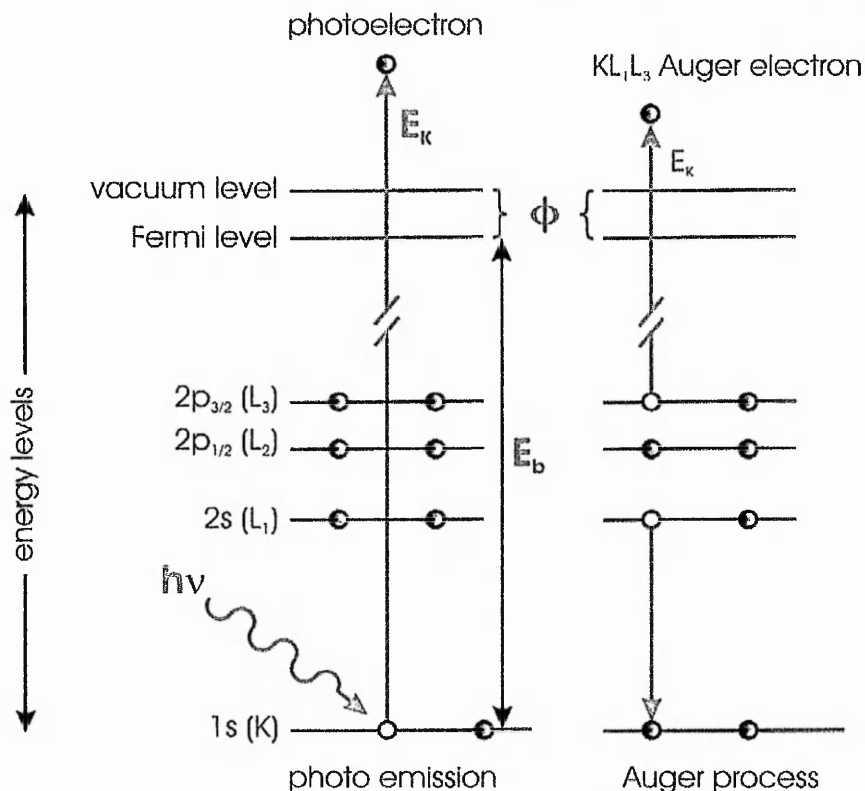
Auger process

Figure 2.6-1: Schematic of XPS (left) and Auger (right) processes. In the XPS process an x-ray photon is absorbed and a core electron ejected. In the Auger process a core hole is filled, followed by ejection of an Auger electron. After Niemantsverdriet [19], Skoog [16] and Stöcker [28].

It is worth remembering that XPS is a surface sensitive technique, as it is limited by the inelastic mean free paths of elements under study (typically 1 – 2 nm). XPS provides information mainly on elemental composition, elemental oxidation states and bond ionicities [28].

2.6.2 Instrumentation

A Vacuum Generators ESCA3 spectrometer was used. The base pressure of the analyser was maintained at $<10^{-6}$ mbar during measurements. A magnesium anode was used (1253.6 eV photon energy), together with an aluminium window. The X-ray source was operated at 20 mA with an accelerating voltage of 11 keV.

The apparatus was equipped with a pre-chamber for sample treatment purposes.

2.6.3 Application

Powdered samples were taken (as is) after ion exchange and mounted on a copper sample holder, using double-adhesive tape. Samples were evacuated in a pre-chamber at room temperature, after which they were analysed.

All samples were referenced to the C 1s line (285.0 eV) belonging to adventitious carbon, as is common practice [19, 28]. Choice of reference is not without ambiguity. Differential charging between the zeolite matrix and the adventitious carbon may lead to a wrongful 'correction' of binding energies of other elements under study. Thus, often the Si 2p peak is used as an internal reference [29, 30].

Data was analysed using a software package, Spectra v6 (made by R.Unwin). This program allowed for determination of peak position, peak width (FWHM [16]) and peak integration.

The atomic ratio between atomic species A and B in the surface region of the sample can be calculated with the aid of the normalised counts and so called relative sensitivity factors. These sensitivity factors are empirically determined and tabulated in literature [31]. CasaXPS Software [32] was used to perform these calculations.

2.7 Extended X-ray absorption fine structure

2.7.1 Principle

EXAFS is an acronym that stands for extended x-ray absorption fine structure. This technique is used to obtain information about the local structure around an atom type in the sample. This information consists of type and number of neighbouring atoms and their distance to the central atom.

Absorption of x-ray radiation by the sample is described by the Lambert-Beer law (equation (2.2) in §2.4.1.1). The absorption coefficient μ is energy dependent. When the energy of an incident x-ray beam is above a certain threshold, a core electron is ejected. This is called the absorption edge, indicated by E_0 on the energy scale. The ejected electron can be considered as a wave that is scattered by neighbouring atoms. The interference between the outgoing electron waves and the back-scattered waves causes the absorption coefficient to fluctuate above the absorption edge. Constructive interference yields a peak maximum, whereas destructive interference results in a peak minimum. An example of an x-ray absorption spectrum is given in Figure 2.7-1. The edge and ~50 eV above it is referred to as XANES (x-ray absorption near edge structure). This region is used for fingerprinting purposes.
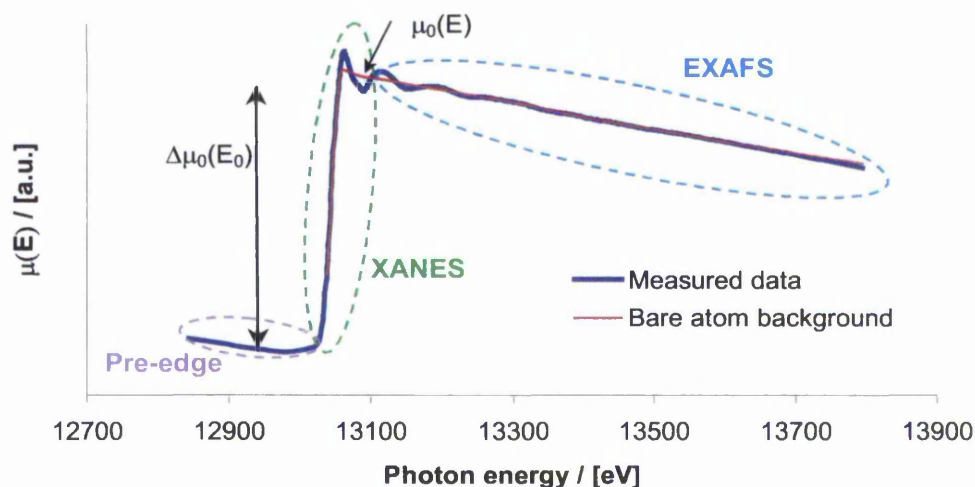
Figure 2.7-1: Example of an x-ray absorption spectrum, showing the arbitrarily defined regions for the pre-edge, the XANES and the EXAFS. The measured data is indicated by a thick line. Shown here is the lead L_{III}-edge of a lead(IV) oxide sample. Indicated are the edge step ($\Delta\mu_0(E_0)$) and, by a thin line, the bare atom background ($\mu_0(E)$). For an explanation of these symbols *vide infra*.

The oscillations above the edge seen in Figure 2.7-1 are commonly displayed as χ, defined as:

$$\chi = \frac{\mu(E) - \mu_0(E)}{\Delta\mu_0(E_0)} \tag{2.7}$$

Where $\mu_0(E)$ is the absorption coefficient is the smooth varying portion of $\mu(E)$ above the edge. This $\mu_0(E)$ is equal to the absorption coefficient of the free atom. Current theory cannot reliably give $\mu_0(E)$, which is the main reason why the XANES are treated as a fingerprint region ($\mu_0(E)$ changes rapidly around the edge). The χ function is normalised to the absorption step, indicated as $\Delta\mu_0(E_0)$.

To display the oscillations, the wave vector (also referred to as "k") is defined [19]:

$$k = \sqrt{\frac{2m_e}{\hbar^2} \cdot \left(E - E_0\right)} \qquad (2.8)$$

Where m_e is the mass of an electron, $\hbar$ is Planck's constant, E is the photon energy and E_0 is the energy of the absorption edge. This wave vector is found in the EXAFS equation, which describes χ as a function of k [19]:

$$\chi(k) = S_0^2 \sum_j \left(N_j \frac{f_j(k)}{kR_j^2} \sin\left\{2kR_j + 2\delta_1 + \varphi_j(k)\right\} e^{\frac{-2R_j}{\lambda(k)}} e^{-2\sigma_j^2 k^2} \right) \qquad (2.9)$$

Essentially, equation (2.9) states that EXAFS is a sum of individual sine waves corresponding to individual coordination shell contributions. In equation (2.9) S_0 is an amplitude reduction factor. The valence electron rearrange as a result of a hole left after excitation. These multi-electron interactions are collected into S_0. They contribute to the edge jump, but not to the EXAFS. N_j is the number of scattering atoms of type j, R_j is the distance to the central atom j. The photoelectron undergoes a phase shift at the central atom, which is seen as δ_1 in equation (2.9). The backscattering factor is given as $f_j(k)$ in equation (2.9). This factor describes the scattering performance of the jth neighbouring atom. Its dependence on energy is characteristic for the scattering atom. The phase shift that the photoelectron undergoes when it bounces off the scattering atom is seen as φ in equation (2.9). The static and thermal disorder in the solid is given by the term $e^{-2\sigma_j^2 k^2}$. In this term, the parameter σ_j^2 is known as the Debye-Waller factor. It accounts for static and dynamic disorder in a solid. Static disorder arises because atoms of the same coordination shell can have slightly different distances to the central atom. Dynamic order is a result of lattice vibrations in

the solid, and is thus temperature dependant. Finally, the electron mean free path length is seen as λ in equation (2.9). A few assumptions were made to devise equation (2.9):

- The ejected electron is a K-shell
- Only single scattering events are considered
- The scattering amplitude at atom j is independent of the distance to the this atom
- Distances are distributed harmonically

In equation (2.9), three structural parameters appear, which are Rj, Nj, and σ_j^2. In order to assess these from the measured EXAFS, the measured signal needs to be Fourier transformed at first [19]:

$$\theta_n(r) = \frac{1}{\sqrt{2\pi}} \int\limits_{k_{\min}}^{k_{\max}} k^n \lambda(k) e^{2ikr} dk \qquad (2.10)$$

In equation (2.10), a correction needs to be made to the amplitude (because of element-specific backscattering amplitude) and to the distance (because of phase shifts). This correction leads to equation (2.11) [19]:

$$\theta_n(r) = \frac{1}{\sqrt{2\pi}} \int\limits_{k_{\min}}^{k_{\max}} k^n \chi(k) \frac{e^{-i\varphi(k)}}{f_j(k)} e^{2ikr} dk \qquad (2.11)$$

Phases and backscattering amplitudes can be obtained from reference compounds, such as oxides, whose crystallographic structure is known in great detail.

2.7.2 Instrumentation

A simplified representation of the EXAFS experimental setup is given in Figure 2.7-2. Usually EXAFS experiments are conducted using synchrotron radiation. Although this is not an absolute requirement, scan collecting times are greatly reduced using synchrotron radiation, as it is far more intense than radiation used in for example tabletop EXAFS machines. The synchrotron radiation is focussed using a plane mirror. Next, it is passed through a monochromator

crystal. This crystal can be used to select the required energy to discard harmonic contamination (according to the Bragg law, *vide* equation (2.4)).
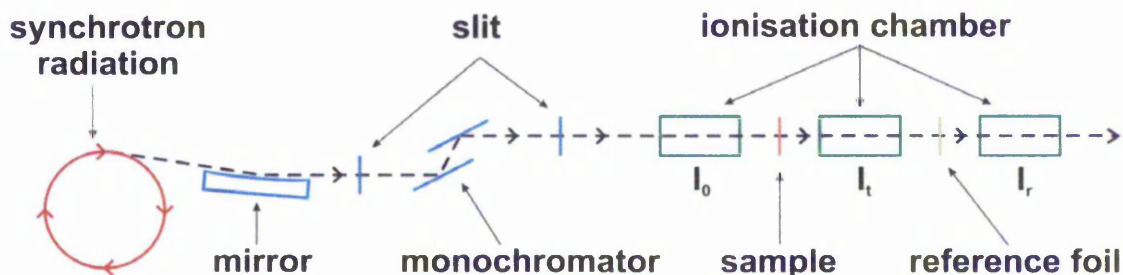
Figure 2.7-2: EXAFS experimental setup.

The ionisation chambers drawn are filled with low pressures of a gas such as argon. The pressure used depends on the energy of the beam passing through the chambers, and hence on the element measured. The gas ionises by the incident energetic radiation. The current in these ionisation chambers is measured using Keithley amplifiers, which convert current to voltage. This voltage is subsequently converted to frequency using a V/f converter. The pulses from this V/f converter are a measure for the intensity of the incident radiation. The absorption coefficient is then equal to (*vide* Figure 2.7-2):

$$\mu = \ln\left(\frac{I_0}{I_t}\right) \tag{2.12}$$

2.7.3 Application

The EXAFS spectra were recorded mode at beamline 9.3 at the SRS Daresbury Laboratory [33]. This beamline was equipped with double crystal harmonic rejecting Si[220] monochromator. Vertical collimation or focussing was achieved with a Pd coated 1 m long plane mirror. For the standard materials (lead(II) and lead(IV) oxide), a mixture of the respective oxide with boron nitride was used, and the spectra were recorded in transmission mode. The zeolite was pressed into a self-supporting wafer and measured in transmission mode.

The obtained spectra were summed and calibrated for E_0 (arbitrarily chosen edge-energy) using EXCALIB software. This software can also be used to eliminate glitches from the data. The calibrated dataset was then background subtracted and Fourier transformed using EXSPLINE software. Phaseshifts and muffin-tin potentials were calculated using EXCURV98. The parameters obtained from this calculation were used to fit the experimental data to a structural model of the local structure around the central element (lead), again using EXCURV98. All software is available at the Synchrotron Radiation Source laboratory in Daresbury [33]. Further descriptions of the software used can be found there as well.

2.8 Reactor studies

2.8.1 Principle

Catalytic performance can be assessed using reactor studies. Conversion and selectivity to a desired product are useful parameters.

A simplified reaction equation applicable to the reaction under study for this work might look like the following:

$$A \rightarrow products \tag{2.13}$$

When describing the kinetics of this reaction, and assuming a first order reaction, the Arrhenius equation can be applied to find experimental rate constants and activation energies [24, 34]:

$$k = A \cdot e^{\frac{-E_A}{R \cdot T}} \tag{2.14}$$

It should be remembered, that this equation is employed with experimental data, and is only applicable over a finite temperature range [34]. In order to minimize influence of heat effects as a result from the progressing reaction, the Arrhenius equation is applied at low conversions (typically below 30%) [34].

2.8.2 Instrumentation

A quartz reactor tube was used, placed in a tubular furnace (manufacturer: Carbolite, model: MTF 12/25/400). This furnace was equipped with a Eurotherm 91e controller, which allowed setting of temperatures and ramp rates.

Isopropanol was obtained from Aldrich Chemical Ltd (catalogue number 27,847-5; purity 99.5%; water content smaller than 0.003%).

Gas flows were regulated using Brooks 8250 mass flow controllers. Helium (BOC gases; 99.996%) was used for most activations, however the rig was equipped with an oxygen line to use an alternative activations procedure. He was dried by a drying column from Phase Separations Ltd. (model Puritube SS F2-M2S), as is shown in a schematic of the reactor set-up (Figure 2.8-1). Isopropanol was injected by means of a syringe pump (Razel Scientific Instruments Inc. A-99 Infusion/Syringe Pump).
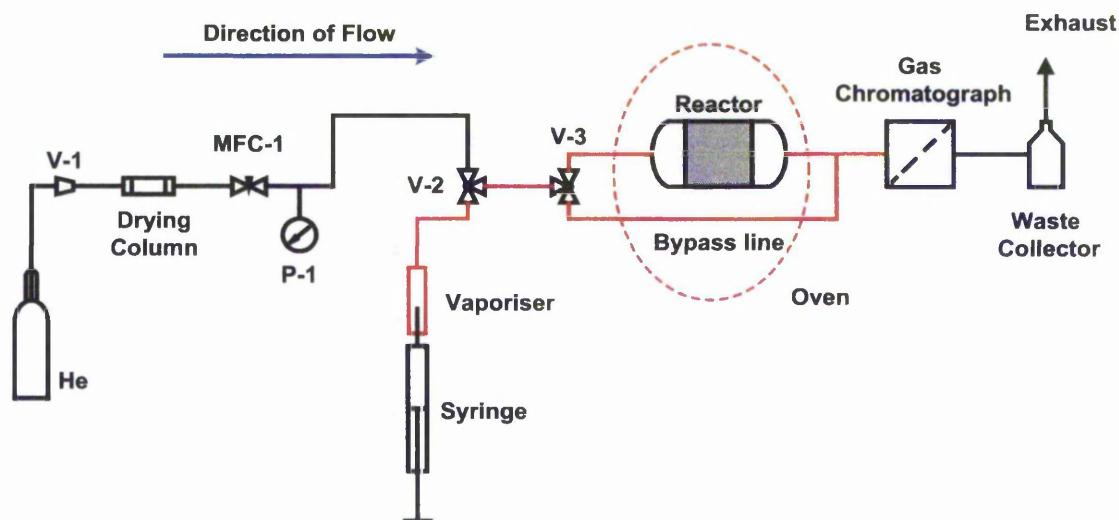
Figure 2.8-1: Reactor setup used for isopropanol decomposition. Red lines indicated heated areas. Valves are numbered V-1 through V-3. P-1 is a pressure indicator. MFC-1 is a mass flow controller.

Samples of the reacted gas were fed into a ATI GC610 gas chromatograph equipped with a 4 m Porapak T column (80-100 mesh, i.d.=2 mm) for analysis. This GC was fitted with a flame ionisation detector (FID). FID data was fed to an interface, which was connected to a personal computer. This way, data could

be captured using data treatment software supplied by the manufacturer of the GC. The CG was calibrated by determining retention times for propene (1% propene in He from Air Products Ltd.), acetone (Fisher, >99.8%; catalogue no. A/0600/25) and isopropanol (Aldrich; 99.5%; catalogue no. 27,847-5), in order to identify products. Quantification of product distribution, and calculation of conversion and selectivity is shown in §2.8.3.

2.8.3 Application

Catalyst samples were pressed into pellets, which were subsequently sieved to select a particle diameter between 250 and 425 μm. About 125 mg of these catalyst grains were introduced into a 50 cm long quartz reactor tube (i.d.= 4 m). They were kept in place by using quartz wool plugs, to give a catalyst bed of ~2 cm length.

Catalyst samples were activated in helium prior to reaction. During activation, the helium flow was maintained so that the gas hourly space velocity (GHSV) was roughly $4.0 \cdot 10^4$ h^{-1}. To study activation for zeolite X, several final activation temperatures were used. The activation procedures are summarised in Table 2.8-1. After activation, the reactor temperature was lowered to the initial reaction temperature, and the reaction was started by introduction of isopropanol.

Table 2.8-1: Activation procedures used for zeolite catalysts in reactor studies

Zeolite	Activation temperature	Ramp rate	Activation atmosphere	GHSV[b]	Activation time
	[K]	[K*min^{-1}]		[h^{-1}]	[h]
Beta	723	5	He	$4.0 \cdot 10^3$	8
Y	723	20	He	$4.0 \cdot 10^3$	8
X	773, 973, 1123[a]	10	He	$4.0 \cdot 10^3$	4

a) For studies of the effect of activation, the activation temperature was varied.
b) Gas hourly space velocity, defined as the flow rate of the carrier gas used, divided by the volume of the catalyst bed.

To convert measured peak areas to moles, a FID correction factor (F_x) was used:

$$F_i = \frac{1}{14 \times ECNC_i} \qquad (2.15)$$

This factor for product "i" is based on the calculation of the effective number of carbons of that product ($ECNC_i$). From the corrected peak areas found in the GC traces, conversion and selectivity were calculated:

$$\xi_R = \frac{\varphi_{n_{R,0}} - \varphi_{n_{R,1}}}{\varphi_{n_{R,0}}} \equiv \frac{\dfrac{N_{FID,R,1}}{F_R}}{\displaystyle\sum_j \left(\frac{N_{FID,P_j,1}}{F_{P_j}} \right) + \frac{N_{FID,R,1}}{F_R}} \qquad (2.16)$$

Where ξ_R is the conversion of reactant R, with corresponding FID response factor F_R. This is equal to the molar flow of reactant R prior to reaction ($\varphi_{nR,0}$) minus the molar flow of reactant post reaction ($\varphi_{nR,l}$), divided by the molar flow of reactant prior to reaction. The conversion corresponds to the corrected counts of reactant post reaction ($N_{FID,R,1}/F_R$) divided by sum of the corrected counts of products ($N_{FID,Pj,1}/F_{Pj}$) plus the corrected counts of the reactant post reaction.

Selectivity towards product i was defined as:

$$S_i = \frac{\varphi_{n,P_i}}{\displaystyle\sum_j \varphi_{n,P_j}} \equiv \frac{\dfrac{N_{FID,P_i}}{F_{P_i}}}{\displaystyle\sum_j \left(\frac{N_{FID,P_j}}{F_{P_j}} \right)} \qquad (2.17)$$

Where S_i is the selectivity towards product i. This selectivity is equal to the molar flow of product i ($\varphi_{n,Pi}$) divided by the sum of the molar flows of all products (Σ_{nPj}). This corresponds to the corrected counts for product i ($N_{FID,Pi}/F_{Pi}$) divided by the sum of the corrected counts of all products ($\Sigma(N_{FID,Pj})/F_{Pj}$).

2.9 Fourier transform infrared spectroscopy

2.9.1 Principle

Absorption of an infrared (IR) photon can promote a molecule simultaneously to an excited vibrational and rotational state. The energy range for vibrational transitions in solids lies in the IR range of the electromagnetic spectrum. For solids, a commonly used model to describe the phenomena observed in infrared spectrometry is that of a harmonic oscillator. In this model, the photon energy is absorbed by a molecule and converted to vibrational energy. The frequency (ν) of an infrared absorption band of bonded atoms A and B is dependent on the reduced mass of the atoms, and of the force constant of the bond, which is best described by a derivation of Hooke's law [35-37] (equation (2.18)). The force constant is a measure of bond strength.

$$\nu = \frac{1}{2 \cdot \pi} \cdot \sqrt{\frac{f}{\left(m_A \cdot m_B\right)\Big/\left(m_A + m_B\right)}} \qquad (2.18)$$

$$f = \left(\frac{d^2 V}{dq^2}\right)_{q \to 0} \qquad (2.19)$$

Absorption in the infrared region can only take place if an oscillating dipole moment is present in the absorber. The oscillating dipole couples with the electric component of EM radiation. The intensity of an infrared band satisfies the Lambert-Beer law (*vide* §2.4.1.1).

Two types of molecular vibrations exist: stretching and bending, where stretching is movement in the direction of the bond axis, whereas bending is accompanied by a change in bond angle. A fundamental vibration does not result in a change in the centre of gravity of the molecule.

Centrosymmetric vibrations are not active in the infrared region, as there is no net change in dipole as a result of the molecular vibration around the centre of symmetry. As most functional groups are not centrosymmetric, infrared spectrometry is a useful tool for their study. An example of such a vibration is the fundamental symmetrical stretching vibration in the CO_2 molecule, which is infrared inactive.

Interpretation of infrared spectra is an empirical matter, as vibrational frequencies cannot be calculated with good accuracy. Functional groups tend to have absorption lines in a narrow region of the spectra, characteristic for that functional group. This is understood by assuming that the vibrations of a functional group are relatively independent of those of the rest of the molecule [35]. Assignment of wavenumbers of functional groups is readily available from literature [35-37]. Difficulties arise when absorption of IR radiation by different functional groups are in the same region, *e.g.* -CN and -NCO.

2.9.2 Instrumentation

For the infrared measurements an ATI RS1 Fourier transform spectrometer equipped with an *in-situ* stainless steel cell with calcium fluoride windows was used. A schematic of the IR set-up can be seen in Figure 2.9-1. This set-up allows for dosage of adsorbates (*vide* Table 2.9-1). The cell allows for heat treatment and evacuation, making it suitable for *in-situ* experiments.
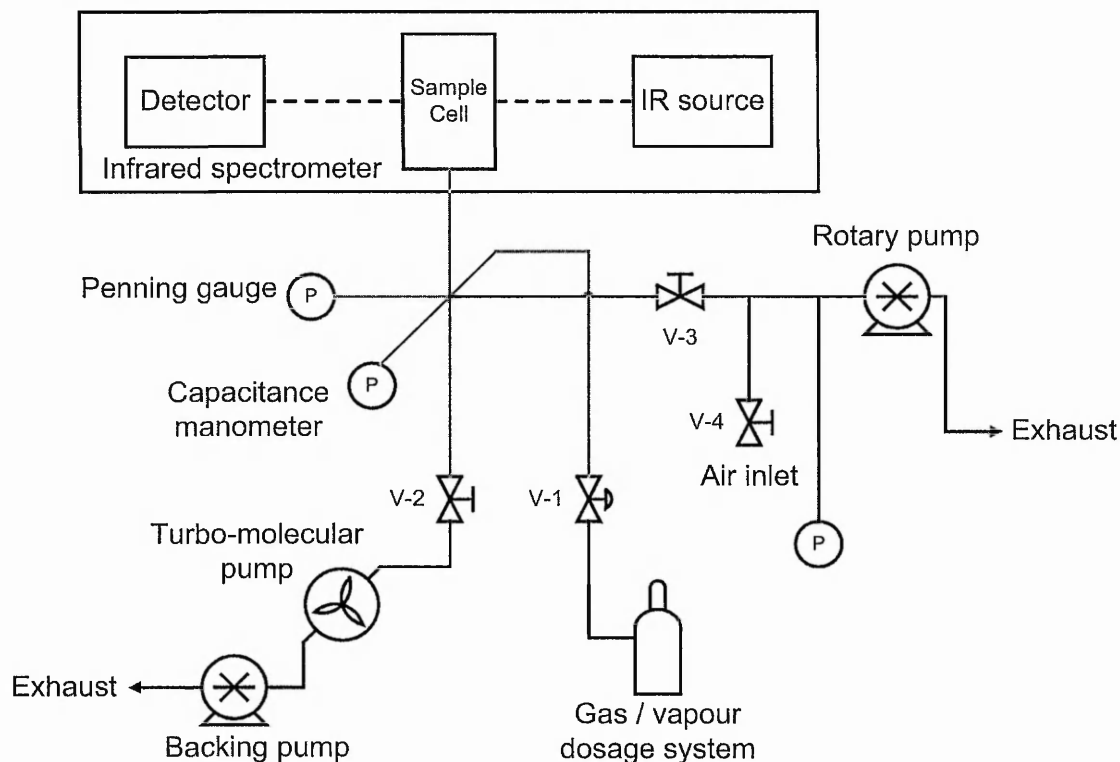
Figure 2.9-1: Flow diagram of the infrared apparatus used for this work. The apparatus consists of a dosage and pumping system Gas is dosed via a small bottle. When a vapour was to be dosed, a bulb containing the respective liquid was attached instead of the gas bottle. Lines depicted red are heated.

Table 2.9-1: Vapour and gas phase adsorbates used.

Adsorbate	Manufacturer	Purity
Carbon dioxide	Argo	99%
Ammonia	Argo	99%
Nitromethane	Aldrich	99%

The spectrometer is of a multiplex design. Multiplex instruments allow for transport of many sets of information through a single channel [16]. To this end, the infrared spectrometer is equipped with a Michelson interferometer [16, 36]. The interferometer is shown schematically in Figure 2.9-2. The movable mirror causes constructive and destructive interference. The difference in path length between the beams reflected of the movable mirror and of the fixed mirror is called retardation. When retardation is plotted against the output power from the detector, as a function of time, an interferogram is produced. The power output versus time, can now be Fourier transformed to give a power output versus frequency, thus producing a recognisable infrared plot.
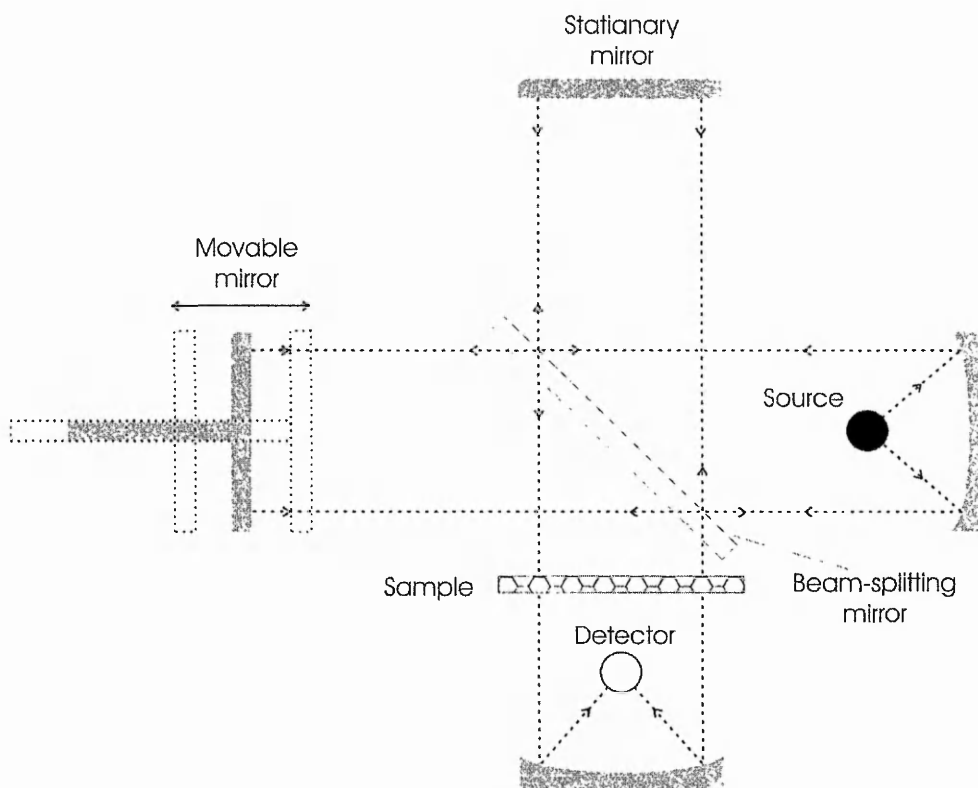
Figure 2.9-2: Optical pathway in a spectrometer equipped with a Michelson interferometer. After Skoog and Leary [16]

There are some advantages of using spectrometer equipped with a Michelson interferometer [16]:

1) Fewer optical elements (*e.g.* no slits). This leads to a greater intensity of radiation reaching the detector. Thus, the signal-to-noise ratio is better than with a conventional (dispersive) design. This is called Jacquinot's advantage

2) Small acquisition times. All wavelengths making up the spectrum are recorded simultaneously, thus reducing the acquisition time. This in turn allows for signal averaging, which leads to a reduction of the signal-to-noise ratio. This is called Fellgett's advantage.

3) Better wavelength accuracy. The interferometer is calibrated with a laser, which uses a known, monochromatic wavelength. The calibration is thus highly accurate, leading to increased accuracy in wavelength measurement. This is called Connes' advantage.

The *in-situ* cell used for measurements is drawn schematically in Figure 2.9-3. Samples are pressed into self-supporting wafers. Provisions are made to insert a K-type thermocouple into the copper sample holder close to the sample wafer, in order to monitor temperature nearest the sample.
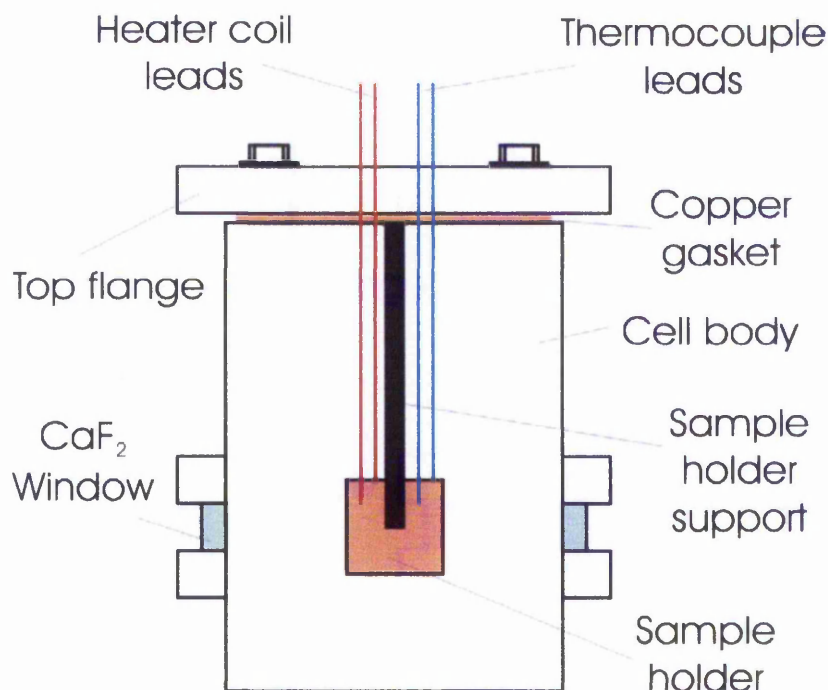
Figure 2.9-3: Cross section of the custom made infrared cell used for this work (schematic). The sample holder is made of copper, to ensure good thermal conductivity between the sample holder and the thermocouple. The thermocouple is placed as closely as possible to the sample wafer.

2.9.3 Application

Samples were pressed into self-supporting wafers, and introduced into the sample holder. The cell was pumped down to a vacuum of 10^{-6} mbar or better, after which activation was initiated. Samples were activated from room temperature to their final activation temperature, and kept at that temperature for the activation time, in order to remove adsorbed species (such as water) from the zeolite. After activation, the cell was cooled down, followed by adsorption of gas or vapour of adsorbate species. Adsorption was conducted at different pressures. For low pressures ($10^{-4} - 10^{-3}$ mbar) adsorption was done dynamically, i.e. with both the turbo-molecular pump and the dosing valve opened (valve V-1 and V-2 in Figure 2.9-1 respectively).

After adsorption, the sample cell was evacuated for 0.5 h to a pressure of 10^{-6} mbar or better, after which further desorption was conducted by raising temperature whilst evacuating.

Data were fed into a PC, after which they could be treated. Firstly, a background correction was made using a spectrum of an empty cell. Normalisation of spectra for varying wafer thickness was performed through dividing by the area of the zeolite Si-O lattice overtone bands (~1753 – 2095 cm^{-1}). A spectrum of a clean, activated catalyst was subtracted from all spectra taken during adsorption / desorption experiments, in order to highlight the differences arisen as a result of the experiment.

2.10 References

1.   Sayed, S.A., *Zeolites* **17**, 361-364, (1996).

2.   Stockenhuber, M., M.J. Hudson, and R.W. Joyner, *Journal of Physical Chemistry B* **104**, 3370-3374, (2000).

3.   Ertl, G., H. Knozinger, and J. Weitkamp, *Handbook of Heterogeneous catalysis* (1st ed.), Weinheim, 1997.

4.   Grimshaw, R.W. and C.E. Harland, *Ion-exchange: introduction to theory and practice* (1st ed.), London, 1975.

5.   Hathaway, P.E. and M.E. Davis, *Journal of Catalysis* **116**, 263-278, (1989).

6.   Hathaway, P.E. and M.E. Davis, *Journal of Catalysis* **116**, 279-284, (1989).

7.   Yang, S.Y. and A. Navrotsky, *Microporous and Mesoporous Materials* **37**, 175-186, (2000).

8.   Sherry, H.S., *Journal of colloid and interface science* **28**, 288-292, (1968).

9.   Wallau, M. and U. Schuchardt, *Journal of the brazilian chemical society* **6**, 393-403, (1995).

10.   Hattori, H., *Chemical Reviews* **95**, 537-558, (1995).

11.   Dyer, A., H. Enamy, and R.P. Townsend, *Separation Science and Technology* **16**, 173-183, (1981).

12.   Ganemi, B., et al., *Microporous and Mesoporous Materials* **38**, 287-300, (2000).

13.   Quincoces, C.E., et al., *Industrial & engineering chemistry research* **38**, 4236-4240, (1999).

14.   Zholobenko, V., A. Garforth, and J. Dwyer, *Thermochimica acta* **294**, 39-44, (1997).

15.   Softley, T.P., *Atomic spectra* (2nd ed.), Oxford University Press, Oxford, 2002.

16.   Skoog, D.A. and J.J. Leary, *Principles of instrumental analysis* (4th ed.), Fort Worth, 1992.

17.   Elliot, S., *The chemistry and physics of solids* (1st ed.), Chichester, 1997.

18.   Lipson, H. and H. Steeple, *Interpretation of x-ray powder diffraction patterns* (1st ed.), London, 1970.

19.   Niemantsverdriet, J.W., *Spectroscopy in catalysis* (2nd ed.), Weinheim, 2000.

20.   Mackey, J.R. and W.J. Murphy, *Zeolites* **5**, 233-239, (1985).

21.   Peru, D.A. and R.J. Collins, *Fresenius Journal of Analytical Chemistry* **346**, 909-913, (1993).

22.   Koller, H., et al., *Microporous Materials* **5**, 219-232, (1995).

23.   International Zeolite Association, http://www.iza-structure.org/databases/,

24.   Atkins, P.W., *Physical Chemistry* (6th ed.), Oxford, 2001.

25.   International Centre for Diffraction Data, http://www.icdd.com, (1996).

26.   http://cds.dl.ac.uk,

27.   Galactic, T., *Grams/32*, v. 5.10

28.   Stoecker, M., *Microporous Materials* **6**, 235-257, (1996).

29.   Gruenert, W., et al., *Journal of Physical Chemistry* **98**, 10920-9, (1994).

30.   Remy, M.J., et al., *Journal of Physical Chemistry* **96**, 2614-17, (1992).

31.   Briggs, D. and M.P. Seah, *Practical surface analysis by Auger and X-ray photoelectron spectroscopy* (2nd ed.), London, 1983.

32.   Fairley, N., *CasaXPS*, v. 2.2.37c (2003).

33.   http://www.srs.ac.uk/srs/,

34.   Pilling, M.J. and P.W. Seakins, *Reaction kinetics* (3rd ed.), New York, 1999.

35.   Nakamoto, K., *Infrared and Raman spectra of inorganic and coordination compounds* (4th ed.), New York, 1986.

36.   Silverstein, R.M. and F.X. Webster, *Spectrometric identification of organic compounds* (6th ed.), New York, 1998.

37.   van der Maas, J.H., *Basic infrared Spectroscopy* (2nd ed.), London, 1972.

3   Results

3.1 Introduction

The aims of this work centre on the assessment of basicity in zeolites. It is recognised that an absolute scale in this assessment is difficult if not impossible to find. The method of assessment will no doubt influence the outcome of the experiments, and it is of particular importance to draw appropriate conclusions from the observed results. For example, if reactions are undertaken, it must be established with a fair degree of certainty that the reaction is indeed base catalysed, or that a different reaction mechanism could be applicable. Likewise, when basicity is assessed through adsorption of probe molecules, it is vital to ask the question of whether sites are indeed accessible to the probe molecule. Indeed, it is necessary to establish whether adsorption of the probe molecule on other than the investigated basic sites in the zeolite is taking place.

In this chapter catalytic behaviour of the ion-exchanged zeolites prepared for this work will be compared to observations made in adsorption experiments. To do so, firstly the elemental make-up of the catalysts need to be studied in order to relate any changes in catalytic activity and / or adsorption behaviour to alterations in the zeolite composition. Further, thermal stability is a requirement for any structural description of a zeolite to hold. Destruction of the porous channel system of a zeolite as a result of thermal treatment is a real possibility with some of the zeolites under study [1].

Next, catalytic behaviour in the isopropyl alcohol (IPA) decomposition is examined for several (ion exchanged) zeolites. As this reaction is widely accepted as a probe reaction for basicity and acidity in zeolites (*vide* §1.3.4.1), reactor studies serve a clear purpose.

It will be established whether it is possible to relate catalytic activity found in the IPA decomposition to adsorption of the probe molecules carbon dioxide, ammonia and nitromethane. These probe molecules have been used in the scientific community to assess basicity of catalysts.

At the end of the presentation of results it is assessed whether the distinction between 'acidic' and 'basic' catalysts is clear and unambiguous, based on the experimental results. Also, it is examined which of the chosen methods is best applicable to serve as a diagnostic tool for basicity, and indeed whether multiple diagnostic methods (rather than a single one) are required.

3.2 Structural analysis of zeolite samples

3.2.1 Abstract

Ion exchange is a procedure for introduction of cations into the zeolite cavities. Ion exchanged zeolites have been shown to be active in catalytic reactions that require basicity. Cations that have conventionally been used to this end are (*inter alia*) potassium and caesium. A novel approach is introduction of Pb^{2+} into the zeolite with the aim of increasing zeolite basicity.

Atomic adsorption and atomic emission results indicate ion exchange of potassium, caesium and lead using acetate salts is indeed feasible for zeolites X, Y and Beta. X-ray photoelectron spectroscopy studies indicate slight dealumination occurred when lead was introduced into zeolite X via ion exchange. Inductively coupled plasma (ICP) results have shown that the bulk Si/Al ratio remains unchanged.

X-ray diffraction studies show that in general, the zeolites remained highly crystalline after the ion exchange procedure. X-ray absorption studies (EXAFS) have shown that the lead is present in the 2^+ oxidation state after ion exchange in zeolite Na-Y.

3.2.2 Background

Often, synthetic zeolites are available commercially in their sodium or ammonium form. As will be shown in this work, and indeed is known from literature, activity for base catalysed reaction products is increased when either cation is replaced by a different cation such as potassium or caesium [2-5]. Indeed, some evidence seems to point to an increase in basicity when lead is introduced into Na-X zeolite [6-8].

Zeolites X, Y and Beta have been ion exchanged in aqueous solutions with various cations such as potassium, caesium and lead. A theoretical account of ion exchange of potassium, caesium and lead into zeolites can be found in § 1.2.5.

In this chapter, it will be examined whether the ion exchange procedure does indeed yield the incorporation of cations into the zeolite cavities. Atomic absorption and emission spectroscopy performed on solutions of the elements that constitute the zeolite samples is a widely accepted method for determination of cation content of the zeolite. X-ray photoelectron spectroscopy (XPS) is a useful technique to investigate the surface layer of ion-exchanged zeolites [9, 10]. Thermo-gravimetric analysis will be used as a method for estimation of water content of the zeolite samples.

Also, it will be investigated whether incorporation of cations leads to the zeolite crystal structure remaining intact. This will be done via x-ray powder diffraction (XRD) studies. X-ray diffraction is used to study the long-range order of (crystalline) materials. Properties of reflections in the x-ray powder diffractogram, such as peak area or peak width, can be used to assess changes in unit cell parameters [11-14].

The coordination environment of lead in zeolite Na-Y will be investigated using x-ray absorption spectroscopy (XAS). This method can be used to assess local environment around a central atom [15, 16]. Extended x-ray absorption fine

structure (EXAFS) is a technique used to study the short-range order of materials.

3.2.3 Bulk composition of zeolite samples

The bulk composition was determined using atomic absorption and emission spectrometry. Results comprise of weight percentages of metals under investigation. Further, thermo-gravimetric analysis yields a mass loss as a result of heating the sample. This mass loss can be expressed as a percentage. It is assumed here, that most of the mass loss is due to loss of water.

The general formula of a zeolite (*vide* §1.2.4) is shown again here.

$$(M_i)_{v_i} (AlO_2)_x (SiO_2)_y \cdot zH_2O \tag{3.1}$$
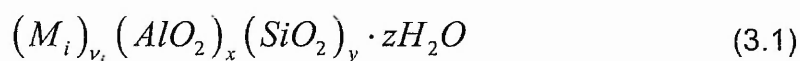
Where M_i represents charge-compensating cations.

In formula (3.1), coefficients v_i, x, y and z are unknown and are of interest. Coefficients v_i can be calculated from atomic spectroscopy results. Coefficients x and y follow from the manufacturers specification of both the zeolite's Si/Al ratio and the number of tetrahedra per unit cell (T) (*vide* equation (3.2)). Thermo-gravimetric results were used to calculate coefficient z.

$$\frac{Si}{Al} ratio = \frac{y}{x} \quad \wedge \quad y + x = T \tag{3.2}$$

From formula (3.1), an exchange level can be calculated, expressed as an atomic percentage. This relates the amount of positive charge (q_i) introduced by a cation species M_i to the amount of available negative charge stemming from the $[AlO_4]^-$ tetrahedra present in the zeolite structure:

$$\left(\text{ion exchange}\%\right)_{M_i} = \frac{v_i \times q_i}{x} \times 100\% \tag{3.3}$$

Where ion exchange % (sometimes written as i.e.%) is the atomic exchange level.

3.2.3.1 Atomic spectroscopy results

Atomic spectroscopy was done on Na-X and Na-Y zeolites exchanged with potassium or lead and NH_4-Beta zeolites exchanged with lead. For K-Na-X and K-Na-Y zeolites atomic emission spectroscopy was used, whereas for Pb-Na-Y, Pb-Na-X and Pb-H-Beta samples atomic absorption spectroscopy was employed. In Table 3.2-1 – Table 3.2-5 the ion exchange conditions as well as the resulting zeolite are listed. In the first column of each table the sample designation is given. This designation includes numbers in brackets, which indicate the ion exchange level, as discussed in §3.2.3 (*i.e.* %, equation (3.3), *vide supra*). The second and the third column indicate the concentration of the exchange solution used and whether or not a rinsing procedure after the final ion exchange step was carried out. In the next two columns weight percentages of the metals as determined by atomic spectroscopy are given. The numbers in brackets indicate the number of determinations that gave the (averaged) result listed. Next, the water content is given as a weight percentage. Thermo-gravimetric analysis (TGA) was used to determine this level. For a more detailed discussion of thermo-gravimetric results *vide* §3.2.3.2. The last column lists the unit cell description for the zeolite. This type of description is often found in literature, and should serve as an indication of the composition of the zeolite [17, 18].

As an example for how these tables should be read, the last entry in Table 3.2-3 is discussed. It lists data for K(87)-Y. The ion exchange level for this zeolite was calculated to be 87%. It was exchanged three times using a 0.09 molar potassium acetate solution, and rinsed twice after the final exchange using a 0.02 molar KOH solution. Two determinations by atomic absorption spectroscopy found 11.0 weight percent potassium and 0.0 weight percent sodium. Thermo-gravimetric analysis found 20.4 weight percent water in the final ion-exchanged product. The unit cell composition for the K(87)-Y sample was calculated to be $K_{46.9} Al_{54.1}Si_{137.9}O_{384} \cdot 189H_2O$.

Table 3.2-1: K-Na-X samples. Parent material was Na-X with an Si/Al ratio of 1.5 and 192 tetrahedra per unit cell. All exchanges carried out at 343 K, in 250 ml water. For a description of this table *vide supra*.

Sample	Exchange solution	Wash	wt% K	wt% Na	wt% H$_2$O	Unit cell
Na-X[a]	-	-	0.0 (0)	9.9 (0)	25.9	Na$_{76.8}$Al$_{76.8}$Si$_{115.2}$O$_{384}$·257H$_2$O
K(27)-Na(67)-X	1 x 0.03 M KAc	-	4.6 (2)	6.7 (2)	23.0	K$_{21.1}$Na$_{51.6}$Al$_{76.8}$Si$_{115.2}$O$_{384}$·242H$_2$O
K(100)-X	2 x 0.03 M KAc	-	16.4 (2)	0.0 (2)	21.1	K$_{76.9}$Al$_{76.8}$Si$_{115.2}$O$_{384}$·214H$_2$O

a) Values for mass percentages calculated from supplier's specifications

Table 3.2-2: Pb-Na-X samples. Parent material was Na-X with an Si/Al ratio of 1.5 and 192 tetrahedra per unit cell. All exchanges carried out at 343 K, in 250 ml water. For a description of this table *vide supra*.

Sample	Exchange solution	Wash	wt% Pb	wt% Na	wt% H$_2$O	Unit cell
Na-X[a]	-	-	0 (0)	9.9 (0)	25.9	Na$_{76.8}$Al$_{76.8}$Si$_{115.2}$O$_{384}$·257H$_2$O
Pb(9)-Na(96)-X[b]	1 x 0.01 M Pb(Ac)$_2$	-	3.8 (4)	9.4 (2)	23.0	Pb$_{3.3}$Na$_{73.4}$Al$_{76.8}$Si$_{115.2}$O$_{384}$·229H$_2$O
Pb(34)-Na(76)-X	1 x 0.02 M Pb(Ac)$_2$	-	13.8 (2)	4.5 (2)	17.5	Pb$_{13.2}$Na$_{58.0}$Al$_{76.8}$Si$_{115.2}$O$_{384}$·240H$_2$O
Pb(43)-Na(61)-X[c]	1 x 0.03 M Pb(Ac)$_2$	-	16.9 (4)	5.4 (2)	20.3	Pb$_{16.3}$Na$_{46.8}$Al$_{76.8}$Si$_{115.2}$O$_{384}$·225H$_2$O
Pb(63)-Na(27)-X	1 x 0.05 M Pb(Ac)$_2$	-	24.1 (2)	2.2 (2)	25.2	Pb$_{24.3}$Na$_{20.4}$Al$_{76.8}$Si$_{115.2}$O$_{384}$·215H$_2$O
Pb(131)-Na(0)-X	2 x 0.06 M Pb(Ac)$_2$	-	41.5 (4)	0.0 (2)	12.7	Pb$_{50.2}$Al$_{76.8}$Si$_{115.2}$O$_{384}$·177H$_2$O

a) Values for mass percentages calculated from supplier's specifications
b) For this zeolite sodium was determined in the exchange solution after the exchange, corresponding to 7.1% loss of sodium from the parent material.
c) For this zeolite sodium was determined in the exchange solution after the exchange, corresponding to 45.7% loss of sodium from the parent material.

Table 3.2-3: K-Na-Y samples. Parent material was Na-Y with an Si/Al ratio of 2.55 and 192 tetrahedra per unit cell. All exchanges carried out at 343 K, in 250 ml water. For a description of this table *vide supra*.

Sample	Exchange solution	Wash	wt% K	wt% Na	wt% H$_2$O	Unit cell
Na-Y[a]	-	-	-	7.4 (0)	24.0	Na$_{54.1}$Al$_{54.1}$Si$_{137.9}$O$_{384}$·223H$_2$O
K(69)-Na(15)-Y	2 x 0.09 M KAc	-	8.8 (2)	1.1 (2)	21.5	K$_{37.4}$Na$_{8.1}$ Si$_{139.9}$O$_{384}$·199H$_2$O
K(70)-Y	3 x 0.09 M KAc	2 x H$_2$O	9.0 (2)	0.0 (2)	21.5	K$_{37.8}$ Al$_{54.1}$Si$_{139.9}$O$_{384}$·197H$_2$O
K(72)-Y	3 x 0.09 M KOH	2 x H$_2$O	9.2 (2)	0.0 (2)	21.5	K$_{39.1}$ Al$_{54.1}$Si$_{139.9}$O$_{384}$·197H$_2$O
K(78)-Na(1)-Y	3 x 0.09 M KAc	2 x H$_2$O	10.3 (2)	0.1 (2)	21.7	K$_{44.7}$ Al$_{54.1}$Na$_{0.5}$ Si$_{139.9}$O$_{384}$·204H$_2$O
K(87)-Y	3 x 0.09 M KAc	2 x 0.02 M KOH	11.0 (2)	0.0 (2)	20.4	K$_{46.9}$ Al$_{54.1}$Si$_{137.9}$O$_{384}$·189H$_2$O

a) Values for mass percentages calculated from supplier's specifications

Table 3.2-4: Pb-Na-Y samples. Parent material was Na-Y with an Si/Al ratio of 2.36 and 192 tetrahedra per unit cell. All exchanges carried out at 343 K, in 250 ml water. For a description of this table *vide supra*.

Sample	Exchange solution	Wash	wt% Pb	wt% Na	wt% H2O	Unit cell
Na-Y[a]	-	-	-	7.7 (0)	25.1	Na$_{57.1}$Al$_{57.1}$Si$_{134.9}$O$_{384}$·238H$_2$O
Pb(306)-Na(7)-Y	3 x 0.04 M Pb(Ac)$_2$	-	4.6 (2)	6.7 (2)	16.5	Pb$_{174.8}$Na$_{3.9}$Si$_{134.9}$O$_{384}$·202H$_2$O

a) Values for mass percentages calculated from supplier's specifications

Table 3.2-5: Pb-H-Beta samples. Parent material was NH$_4$-Beta with an Si/Al ratio of 12.5 and 64 tetrahedra per unit cell. The exchange of Pb(85)-H(15)-Beta was carried out at 298 K; the exchange of Pb(219)-H(15)-Beta at 343 K. Exchanges carried out in 500 ml water. For a description of this table *vide supra*.

Sample	Exchange solution	Wash	m% Pb	m% NH$_4$[b]	m% H$_2$O	Unit cell
NH$_4$-Beta[a]	-	-	-	1.8 (0)	15.6	H$_{4.7}$Al$_{4.7}$Si$_{115.2}$O$_{384}$·39H$_2$O
Pb(85)-H(15)-Beta[d]	3 x 0.005 M Pb(Ac)$_2$	2 x H$_2$O	8.5 (2)	0.3 (0)	13.4	Pb$_{2.0}$H$_{0.7}$ Al$_{4.7}$Si$_{115.2}$O$_{384}$·36H$_2$O
Pb(219)-H(0)-Beta	3 x 0.01 M Pb(Ac)$_2$	2 x H$_2$O	19.1 (4)	0.0 (0)	12.6	Pb$_{5.2}$ Al$_{4.7}$Si$_{115.2}$O$_{384}$·39H$_2$O

a) Values for mass percentages calculated from supplier's specifications
b) Hydrogen exchange level calculated

3.2.3.2 Thermo-gravimetric analysis results

Water content for the zeolites used has been calculated from thermo-gravimetric analysis (TGA) experiments (*vide infra*). The water content expressed as a percentage has been calculated from the relative mass difference between samples at room temperature, and at their final activation temperature of ~900 K.

The profiles obtained from these experiments have been differentiated with respect to time using a Savitski-Golay algorithm [19] yielding dTGA curves. These curves for Pb-Na-X samples can be seen in Figure 3.2-1. Clearly, after 773 K no further mass loss occurs. Notably, curve f in Figure 3.2-1 showed a further peak at ~625 K next to the main peak at ~373 K, indicating that mass loss occurred in two stages for this sample.
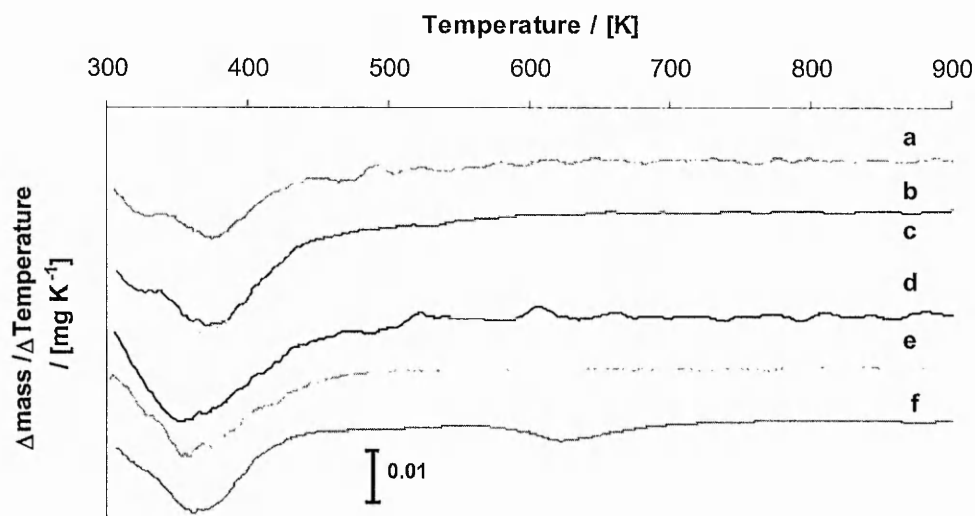
Figure 3.2-1: Differential TGA curves of Pb-Na-X zeolite samples. Samples were activated with a ramp rate of ~5 K min^{-1}, under dry nitrogen atmosphere. Legend: a) Na-X (parent zeolite); b) Pb(9)-Na(96)-X; c) Pb(34)-Na(76)-X; d) Pb(43)-Na(76)-X; e) Pb(63)-Na(27)-X; f) Pb(131)-X. Lines are artificially separated for clarity.

If the lead loading of Pb-Na-X samples, expressed as a wt% lead, is plotted against mass loss determined by thermo-gravimetric analysis, a linear relation was found (*vide* Figure 3.2-2). This linear relation is mainly governed by the exchange of sodium for lead. This can be seen as follows. When we consider

the exchange equilibrium, on a charge basis, for every two sodium ions leaving the zeolite, one ion of lead is introduced:

$$Pb^{2+}(aq) + 2Na^+_{FAU} \rightleftarrows 2Na^+(aq) + Pb^{2+}_{FAU} \qquad (3.4)$$
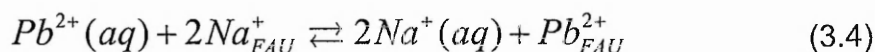
The change in volume associated with such a single exchange can be readily calculated to be ~2.45 nm^3, using the ion radii of Na$^+$ (0.095 Å) and Pb^{2+} (0.132 Å) [20]. When assuming that this change in volume occurs fully at the expense of zeolitic water, and assuming that the density of water equals to 1 g cm^{-3}, this water loss amounts to 2.45·10^{-24} g (the equivalent of 1.36·10^{-25} moles or 0.08 molecules of water). At the same time, the mass difference between two sodium ions and one lead ion equals 2.68·10^{-22} g (the equivalent of 1.29·10^{-24} moles of lead). Thus, the mass difference between two atoms of sodium and one atom of lead is roughly two orders of magnitude larger than the mass change resulting from the displacement of water.

The mass loss during heating of the sample can also be calculated as a percentage of the original mass of water in the zeolite. The results of this calculation are plotted in the graph of the thermo-gravimetric analysis experiments (*vide* Figure 3.2-2).
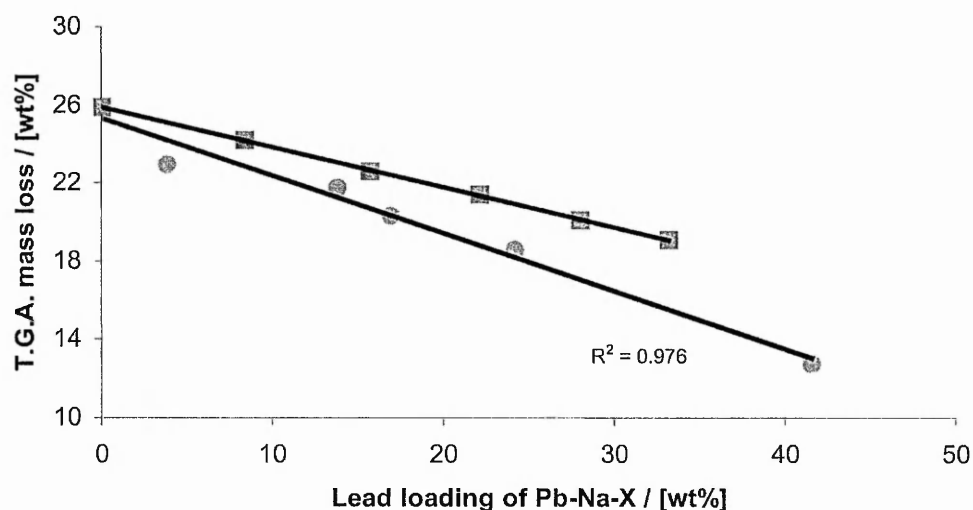
Figure 3.2-2: Lead loading of Pb-Na-X samples versus the mass loss measured by thermo-gravimetric analysis. Legend: ▣) Calculated mass percentage of water in Pb-Na-X on an assumption of an exchange stoichiometry of 2Na$^+$ for 1Pb^{2+}; ◉) Actual mass loss as measured by T.G.A. for Pb-Na-X

If however, the assumption is made, that lead is present in the form of $[Pb_4(OH)_4]^{4+}$ clusters, which has been suggested by other researchers [21-24] the exchange equation based on charge should then be $1Na^+$ for $1Pb^{2+}$, instead of $2Na^+$ for $1Pb^{2+}$. Thus, the mass change for a single exchange would then be larger, and the theoretical linear curve for mass loss would be steeper. Of course, the volume of the $Pb_4(OH)_4^{4+}$ cluster needs to be taken into account when calculating the extent of water displacement, which however is beyond the scope of this work.

Furthermore, mass loss can be expected from the decomposition of the species deposited in the zeolite cavities (either $Pb_4(OH)_4^{4+}$ or lead(II) acetate trihydrate) to Pb^0, PbO, CO and H_2O, which takes place from around 348 K [20, 25]. It is however, not possible to assess the extent of mass loss as a result of such decomposition based on the observed TGA data alone.

3.2.3.3 Inductively coupled plasma spectroscopy results

A bulk ratio of for example exchange metals to aluminium can be helpful. Inductively coupled plasma spectrometry (ICP) can be a useful tool to this end. Samples were analysed by inductively coupled plasma spectrometry, using the services of Viridian Partnership (*vide* appendix A). Results were received in the form of weight percentages of elements analysed, which can then be divided by the respective relative molecular masses of said elements in order to obtain atomic ratios. After correction for ion charge, metal content can be expressed as a percentile of the aluminium content. The results of these calculations can be seen in Table 3.2-6.

Table 3.2-6: Metal content of selected zeolite samples. Content corrected for ionic charge of the exchange cation and expressed as a percentile of aluminium.

Sample	Na-content[a]	Exch. metal content[a]	Si/Al-ratio[b]
	[% i.e.]	[% i.e.]	[-]
Na-Y	103.2 (-)	n.a.	2.97 (2.55)
Na-Y (washed)	95.2 (-)	n.a.	2.53 (2.55)
Pb-Na-Y	12.5 (7)	138.8 (306)	2.84 (2.55)
K-Na-Y	6.9 (0)	61.3 (87)	3.52 (2.55)
Na-X	102.9 (-)	n.a.	1.35 (1.5)
Na-X (washed)	94.3 (-)	n.a.	1.17 (1.5)
Cs-Na-X	75.2 (-)	21.6 (-)	1.36 (1.5)
Pb-Na-X	69.8 (76)	32.6 (34)	1.34 (1.5)

a) Numbers in brackets indicate corresponding AA experimental results (§3.2.3.1).
b) Numbers in brackets indicate corresponding specifications from the manufacturer of the zeolite

3.2.4 Surface composition of ion exchanged zeolites

From x-ray photoelectron spectroscopy (XPS) surface properties can be deduced. It can be interesting to establish whether the surface composition of a zeolite, which is the part of the catalyst exposed to reactants, deviates from the bulk composition. Ion exchange is a potential candidate to cause changes in the surface region. As an example of photoelectron spectroscopy measurements, a survey plot of Pb(43)-Na(61)-X is shown (vide Figure 3.2-3). The sample was activated in helium at 773 K (*ex-situ*) prior to XPS measurement.
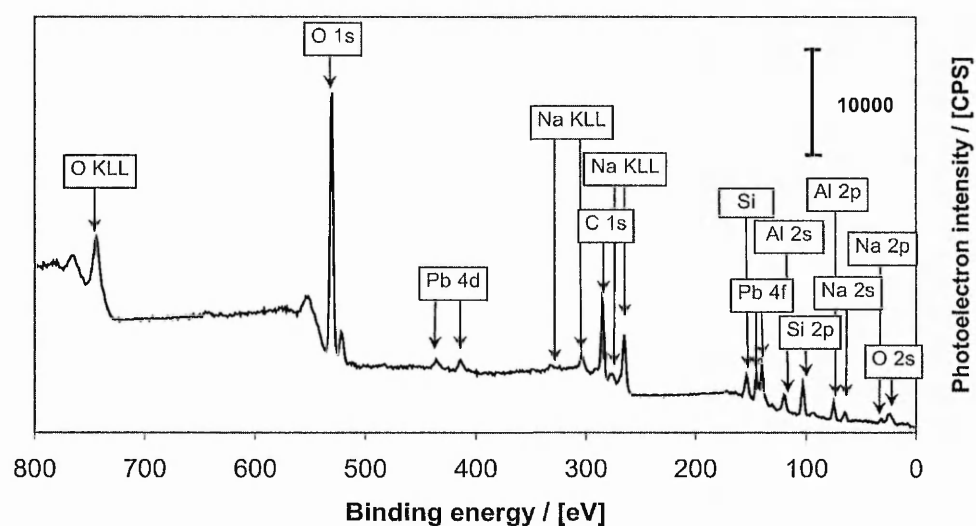
Figure 3.2-3: X-ray photoelectron spectrum of Pb(43)-Na(61)-X, activated (*ex-situ*) in helium at 773 K for 4h. The labelling of the peaks is according to literature [26].

The entries in the table shown next were calculated by using the measured counts divided by the corresponding relative sensitivity factors. These factors are tabulated empirical values incorporated [26]. Single measurements are presented in Table 3.2-7.

Table 3.2-7: Si/Al-ratios and exchange ion content of selected zeolite samples determined using XPS. Content expressed as an ion exchange percentage (i.e.%).

Sample	Si/Al-ratio	Na content[c]	Exchange metal content[c]
Na-X[a]	1.24	113	0
Pb(9)-Na(96)-X[a]	1.27	98	4
Pb(34)-Na(76)-X[a]	1.33	62	8
Pb(43)-Na(61)-X[a]	1.35	78	14
Pb(63)-Na(27)-X[a]	1.53	47	34
K(27)-Na(67)-X[b]	1.31	92	30
Cs(22)-Na(75)-X[b]	0.49	35	5

a)   Numbers in brackets indicate corresponding atomic absorption values (*vide* §3.2.3.1).
b)   Numbers in brackets calculated from ICP spectroscopy results (vide §3.2.3.3).
c)   Lines used: Na 2s, Pb $4f_{5/2}$, K $2p_{3/2}$ and Cs $3d_{5/2}$.

For Pb-Na-X zeolites, a slight dealumination was observed in the surface layer with increasing lead loading. The surface lead loadings were significantly lower than those obtained for the bulk. For the Cs-Na-X sample, an apparent surface enrichment of aluminium was seen.

3.2.5 Framework oxygen partial charge

With the aid of equations (1.18) and (1.19), Sanderson's tabulated electronegativities [27] and the bulk composition of zeolites found by AA (*vide* §3.2.3.1), the partial charge on framework oxygen atoms can be calculated. The results of this calculation can be seen in Figure 3.2-4. The introduction of lead into zeolite Na-X leads to a decrease of partial (negative) charge on the framework oxygen.
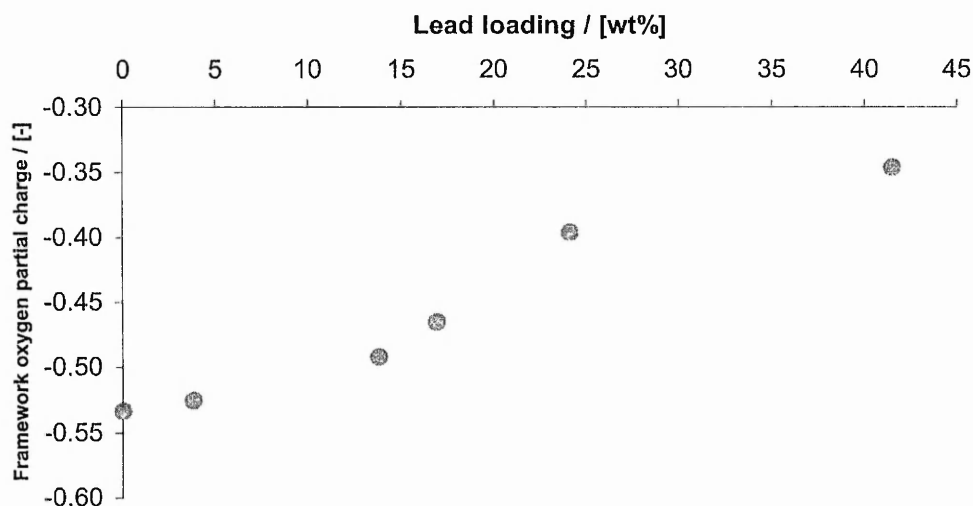
Figure 3.2-4: Calculated partial charge of the oxygen atom as a function of lead loading for Pb-Na-X samples. Calculations are based on the electronegativity equalisation principle, as described by Sanderson [27].

A decrease in O 1s binding energy with increasing lead loading was observed for lead loadings under ~25 wt% (*vide* Figure 3.2-5). When lead loading was increased further, a sharp increase of the O 1s binding energy was seen. It can be speculated that this effect is due to deposition of a lead compound in the zeolite cavities, which resulted in a higher average binding energy for the O 1s line. Remarkably, the binding energies measured for lead exchanged zeolite X samples were all considerably higher than those observed for two standards, lead(II) and lead(IV) oxide (*vide* Figure 3.2-5).

Generally, line widths for the O 1s line were between 2.6 and 3.3 eV. The O 1s line was not further deconvoluted, as there was no information on the possibility of different (Pb,O) species existing in the zeolite cavities. No trends were observed between line widths of the measured lines and lead loading.
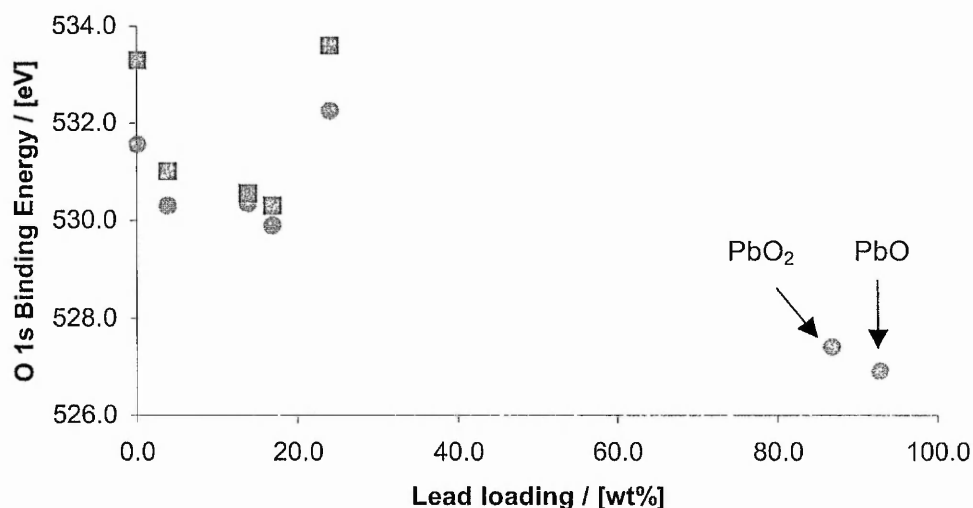
Figure 3.2-5: O1s binding energy measured by XPS versus lead loading in weight percentage. Lead weight percentages for the oxides used are calculated. Legend: ▦) Corrected to the measured binding energy of the Si 2p line at 103.3 eV[28]. ◉) Corrected to the measured binding energy of the C 1s line at 284.5 eV[28]

When the Pb 4f line was observed, again no trend with lead loading could be seen (*vide* Figure 3.2-6). Binding energies measured for the zeolite samples were higher than those measured for the lead oxide standards.
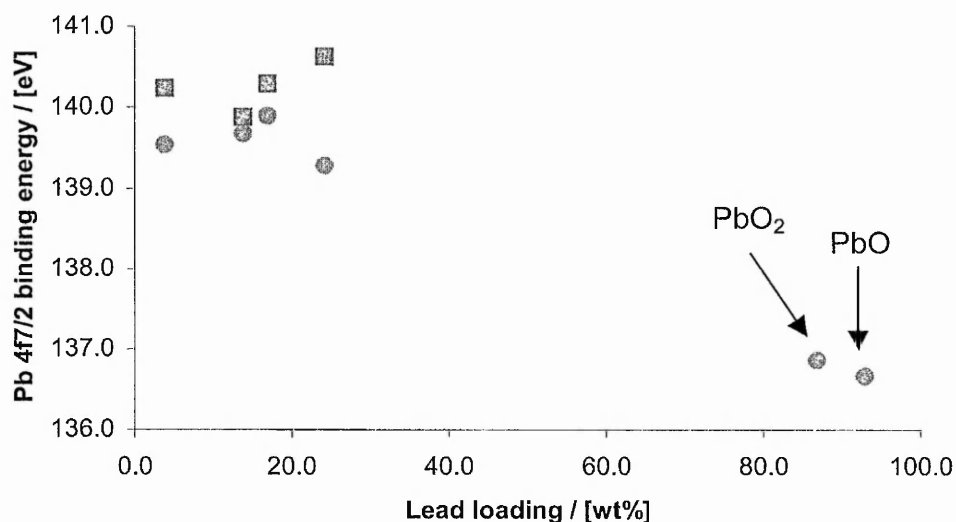
Figure 3.2-6: Pb 4f7/2 binding energy measured by XPS versus lead loading in weight percentage. Lead weight percentages for the oxides used are calculated. Legend: ▦) Corrected to the measured binding energy of the Si 2p line at 103.3 eV [28]. ◉) Corrected to the measured binding energy of the C 1s line at 284.5 eV [28].

3.2.6 X-ray diffraction studies on ion exchanged zeolites

X-ray diffraction (XRD) patterns of "as is" zeolites are given in this chapter. For the elemental composition of the samples presented here, vide § 3.2.3.1. Unless mentioned otherwise, all measurement conditions were as follows: 3-50 degrees 2θ-range, 0.03 degrees 2θ-step; 5 seconds per step. In order to examine which phases were present in the sample a study was made of the Miller indices [29], commonly denoted in the format [h k l] (*e.g.* [1 1 1]). Sources for literature x-ray diffraction patterns were either:

- A database of zeolite structures published by the International Zeolite Association [18, 30]
- The JCPDS database [31]
- The Chemical Database Service [32]

For the parent zeolites, Na-X and Na-Y, all reflections found in the x-ray diffraction patterns were matched to patterns found in literature (Na-X [33], Na-Y [34] and simulated Na-X and Na-Y [18]). From this it was concluded that no extra phases could be "seen" by x-ray diffraction studies.

3.2.6.1 Na-X zeolite exchanged with potassium acetate

The exchange of sodium for potassium led only to small changes in the observed x-ray diffraction pattern. After ion exchange, crystalline materials remained. The x-ray diffraction patterns for three K-Na-X samples measured for this work can be seen in Figure 3.2-7.
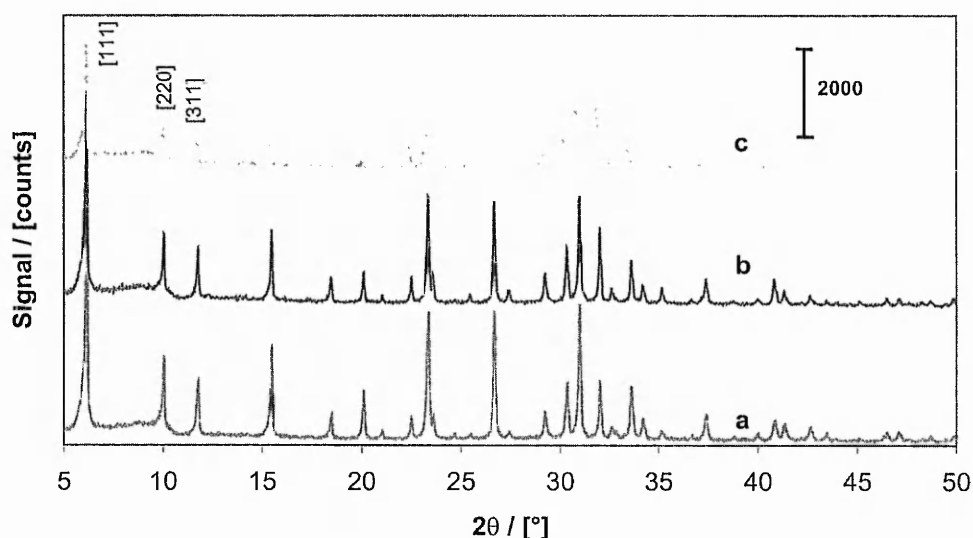
Figure 3.2-7: Powder x-ray diffraction patterns of K-Na-X zeolites. Samples were exchanged with KAc, were not washed after exchange, and measured "as is". Legend: a) Na-X (parent material); b) K(27)-Na(63)-X; c) K(100) –X. The first three peaks are indexed.

In order to establish whether any extra phases occurred in the measured K-Na-X samples, the first 25° 2θ are presented in more detail (*vide* Figure 3.2-8). A study of all reflections in the diffractograms K-Na-X samples prepared revealed that apart from the zeolite phase, no extra phases were detected by x-ray diffraction, as all peaks matched to patterns of either the parent Na-X or a K(98)-Na(2)-X [32, 35].
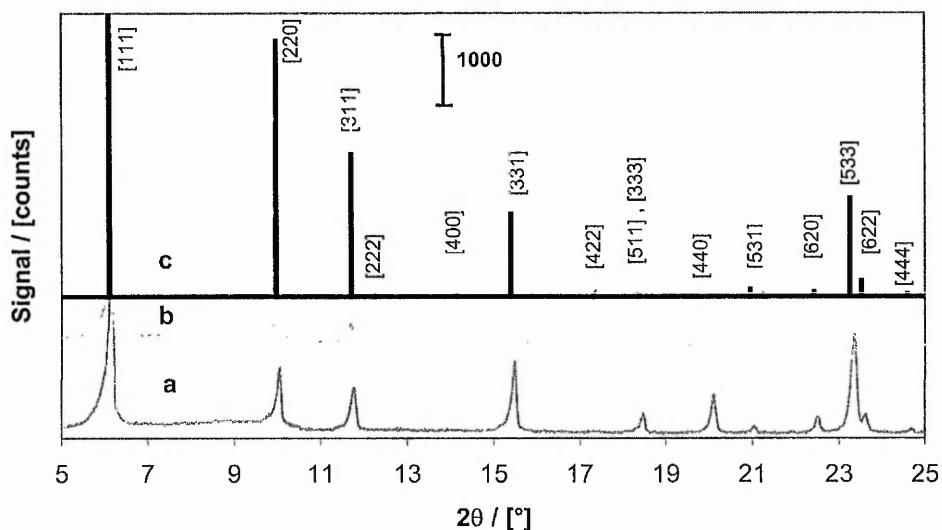
Figure 3.2-8: Closer examination of K-Na-X zeolites and comparison to literature data. Legend: a) Na-X; b) K(100)-X; c) K(98)-Na(2)-X. Traces a and b were data measured for this work. Trace c after Zhu *et al.* [32, 35]. Reflections were indexed based on pattern c. Intensities of peaks in trace c are relative to the [111] reflection. All reflections found in the samples prepared for this work were part of the zeolitic phase and no extra phases were discovered.

3.2.6.2 Na-X zeolite exchanged with lead(II) acetate

Ion exchange of lead for sodium in zeolite X, led to changes in intensity ratios of various reflections (*vide* Figure 3.2-9).
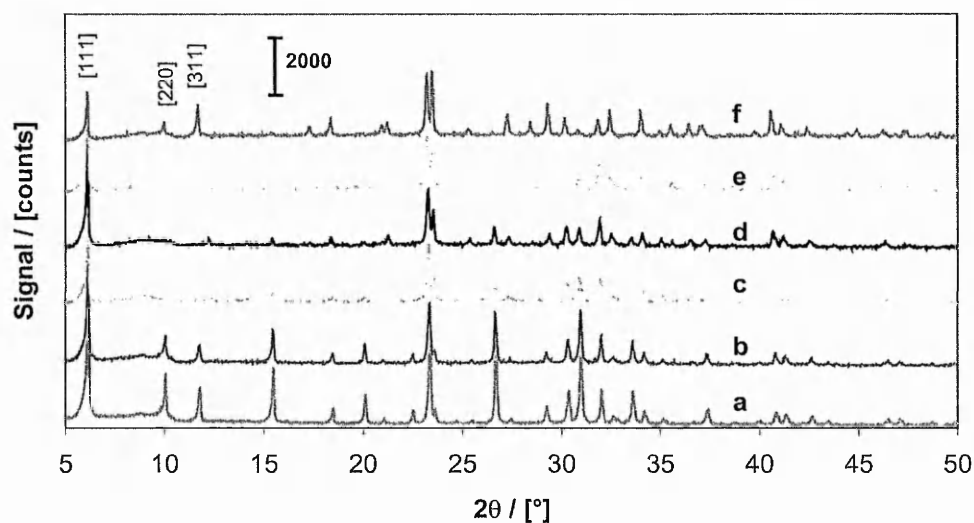
Figure 3.2-9: Powder x-ray diffraction patterns for Pb-Na-X zeolites. Legend: a) Na-X; b) Pb(9)-Na(96)-X; c) Pb(34)-Na(76)-X; d) Pb(43)-Na(61)-X; e) Pb(63)-Na(27)-X; f) Pb(131)-Na(0)-X.

In order to establish the presence of extra phases in the ion-exchanged samples, two x-ray diffraction patterns of samples made for this work are compared to data found in literature. This comparison can be seen in Figure 3.2-10.
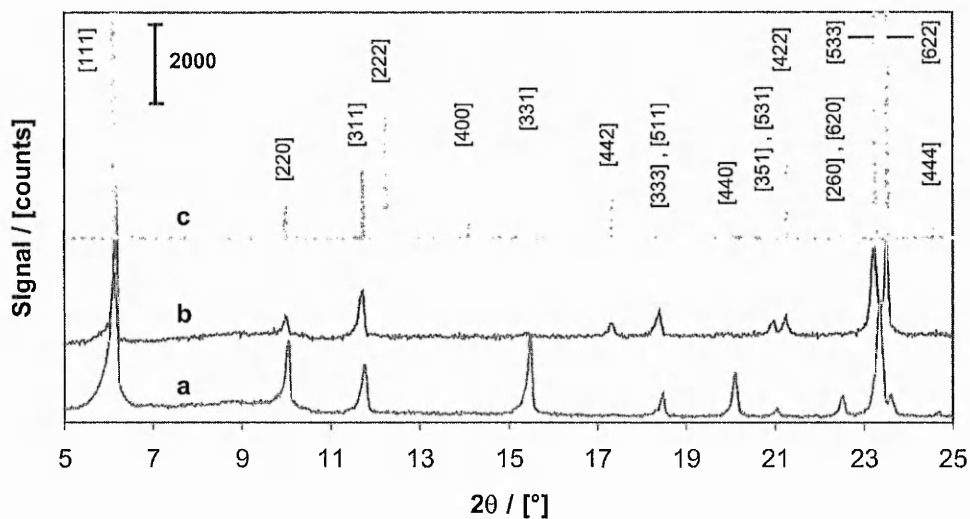
Figure 3.2-10: Powder x-ray diffraction data for Pb-Na-X zeolites. Legend: a) Na-X (parent material); b) Pb(131)-Na(0)-X; c) Pb(100)-Na(0)-X. Traces a and b were measured of "as is" samples. Trace c taken from a study by Nardin *et al.* [32, 36]. Peak intensities for trace c are relative to the [111] reflection.

The indexes seen in Figure 3.2-10 are listed in Table 3.2-8. The example given is indicative for the x-ray diffraction patterns of Pb-Na-X zeolites prepared for this work.

Table 3.2-8: Reflections of measured x-ray diffraction patterns compared to patterns found in literature. The h,k,l indices are given in the first column. The position of the reflection is given (2θ column) as well as the relative intensity for patterns found in literature. For the samples measured for this work it is indicated whether or not the reflection was found. *Vide* also Figure 3.2-10.

h k l	Na(100)-X[a]		Pb(100)-Na(0)-X[b]		Na-X[c]	Pb(131)-Na(0)-X[c]
	2θ	relative intensity	2θ	relative intensity	reflection found	
1 1 1	6.09	1000	6.10	1000	√	√
2 2 0	9.96	147	9.98	7	√	√
3 1 1	11.68	68	11.70	15	√	√
2 2 2	12.20	0	12.23	29		
4 0 0	14.10	3	14.13	15		
3 3 1	15.37	153	15.40	18	√	
4 2 2	17.29	1	17.32	10		√
5 1 1	18.35	10	18.38	1	√	√
3 3 3	18.35	1	18.38	1	√	√
4 4 0	19.99	20	20.03	2	√	
3 5 1	20.92	0	20.96	1	√	√
5 3 1	20.92	1	20.96	1	√	√
4 4 2	21.22	2	21.26	17		√
2 6 0	22.38	0	22.42	3	√	
6 2 0	22.38	1	22.42	3	√	
5 3 3	23.21	98	23.26	85	√	√
6 2 2	23.49	2	23.53	106	√	√
4 4 4	24.55	0	24.59	6	√	

a) After Zhu *et al.* [32, 33]
b) After Nardin *et al.* [32, 36]
c) Samples made and measured for this work

From Table 3.2-8 and Figure 3.2-10 it is evident that for the samples prepared for this work, the number of reflections seen in the x-ray diffraction patterns decreased when sodium was substituted for lead in zeolite X.

Some indications of the existence of an additional phase appearing in the XRD pattern of Na-X ion exchanged with lead were found in literature. Kovacheva *et al.* [7] identified metallic lead and lead(II)oxide in a Na-X zeolite which they had ion exchanged with lead(II)nitrate, and subsequently dried at 393 K. Thus, a search in two databases (JCPDS [31] and CDS [32]) was undertaken in order exclude any phases that might be present in the Pb-Na-X samples. No lead salt could be matched to any of the observed patterns of "as-is" samples. Further, it was seen that the positions of reflections found in the Pb(131)-Na(0)-X sample (*vide* Figure 3.2-10) matched either to the measured pattern of the parent Na-X,

or to the reflections found in the work of Nardin *et al.* on Pb(106)-Na(0)-X [32, 36]. It is therefore concluded that the Pb(131)-Na-X sample is a mixture of Pb-X and Na-X, and that no extra phases are "seen" by x-ray diffraction in the as-is samples of Pb-Na-X.

Figure 3.2-11 shows the [1 1 1] reflection of prepared Pb-Na-X samples in more detail. It can be seen that increasing the lead loading produced no clear movement in its position.
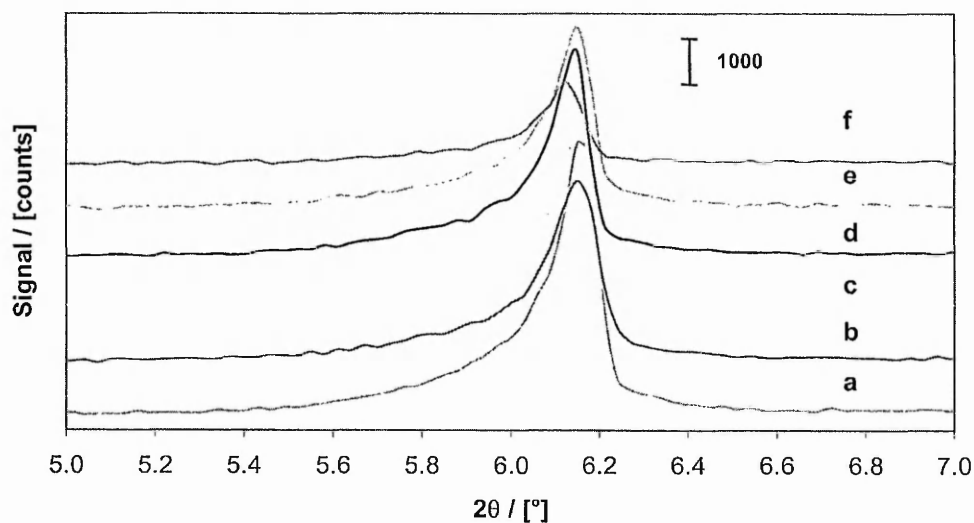
Figure 3.2-11: Powder x-ray diffraction patterns for Pb-Na-X zeolites, showing the [111] reflection (indicated on Na-X). Legend: a) Na-X; b) Pb(9)-Na(96)-X; c) Pb(34)-Na(76)-X; d) Pb(43)-Na(61)-X; e) Pb(63)-Na(27)-X; f) Pb(131)-Na(0)-X

However, a shift to lower degrees 2θ can be observed when the [533] and the [622] reflections are considered (*vide* Figure 3.2-12). The maximum shifts were 0.13 degrees 2θ and 0.10 degrees 2θ respectively. In the simulated patterns for hydrated and dehydrated Na-X, a similar shift to lower degrees 2θ can be found. This shift amounts to ~0.08 degrees 2θ [18, 30].

In the powder pattern of the parent material (Na-X), which was recorded five times, peak position of the [533] reflection was 37.37 degrees 2θ with a standard deviation of 0.04 degrees 2θ. This shift is interpreted in the light of changes in hydration state of the zeolite and instrumental factors. The shift to lower degrees 2θ for the [533] and [622] lines observed in Figure 3.2-12 for Pb-Na-X samples clearly increased with increasing Pb loading. The maximum shift amounts to ~0.13 degrees 2θ and is thus considered a significant shift.
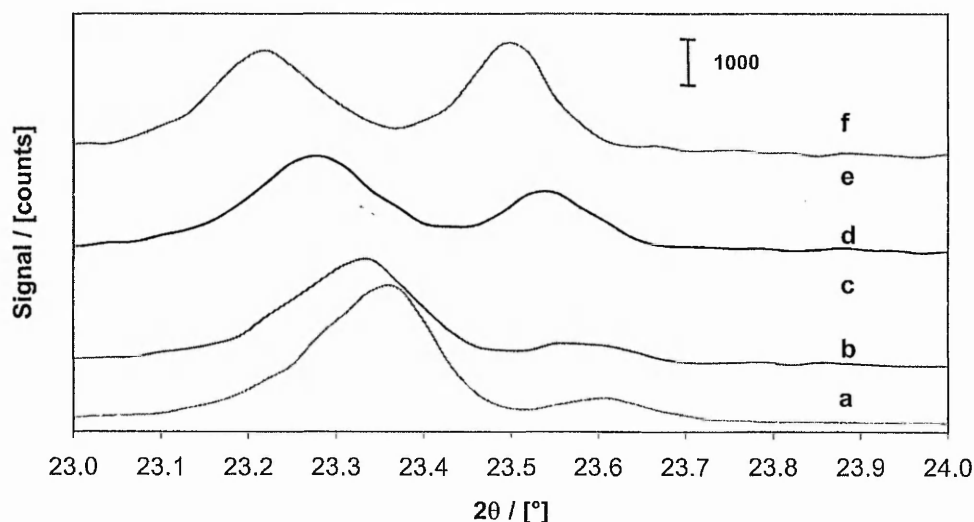
Figure 3.2-12: Powder x-ray diffraction patterns for Pb-Na-X zeolites, showing the [533] and [622] reflections (indicated on Na-X). Legend: a) Na-X; b) Pb(9)-Na(96)-X; c) Pb(34)-Na(76)-X; d) Pb(43)-Na(61)-X; e) Pb(63)-Na(27)-X; f) Pb(131)-Na(0)-X

The peak parameters full width at half maximum (FWHM) and peak area for the [111] reflection are plotted versus Pb loading in Figure 3.2-13. There seems to be a trend when the data are fitted with a straight line.
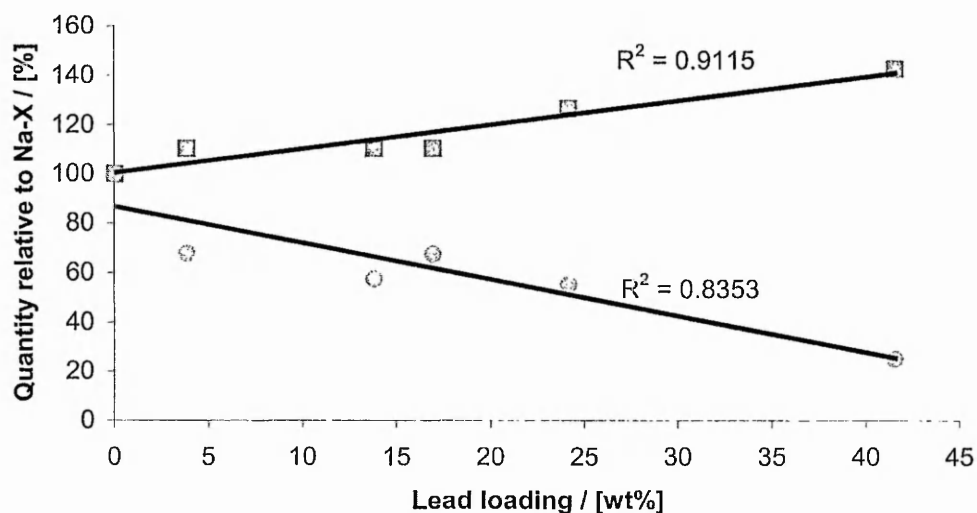
Figure 3.2-13: Comparison of peak properties of the [111] reflection. All data points represent peak properties using K_α stripped traces. The quantities are expressed as a percentage of the [111] reflection of the parent Na-X zeolite. The Na-X data point (found at zero weight percent lead loading) is an average of five measurements; the rest are single measurements. Legend: ▩) Peak width of the [111] reflection. ○) Peak area of the [111] reflection.

3.2.6.3 Na-Y zeolite exchanged with potassium acetate

X-ray diffraction patterns of ion exchanged Na-Y zeolite can be seen in Figure 3.2-14. Ion exchange conditions for these zeolites can be found in §3.2.3.1. Although these samples have been ion exchanged in different ways, no substantial difference is observed in the diffraction patterns. Some changes in peak intensity and a shift in peak position was observed on K(91)-Y (curve f in Figure 3.2-14). This sample was exchanged twice with potassium acetate, and not washed after the exchange.
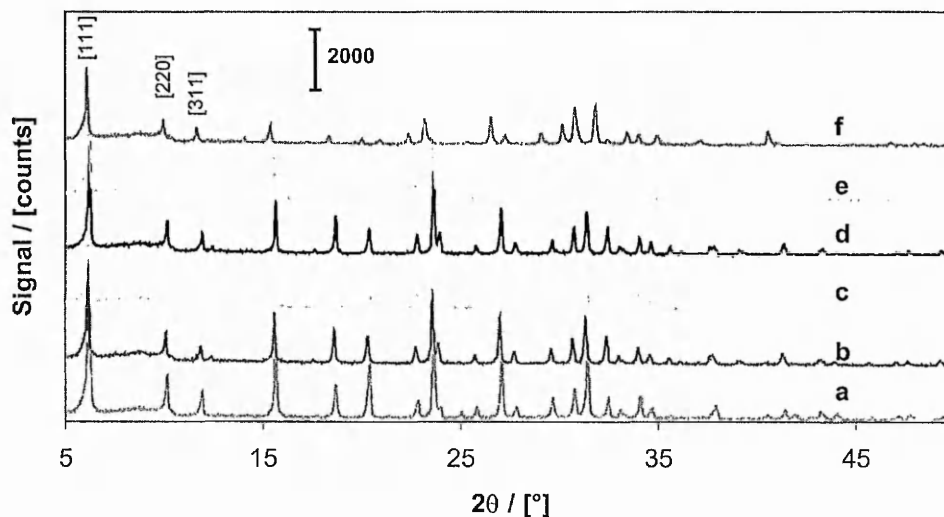
Figure 3.2-14: Powder x-ray diffraction patterns for K-Na-Y zeolites. Legend: a) Na-Y (parent zeolite); b) K(72)-Y (exchanged with potassium hydroxide and washed with water); c) K(70)-Y (exchanged with potassium acetate and washed with water); d) K(87)-Y (exchanged with potassium acetate and washed with potassium hydroxide); e) K(69)-Na(15)-X (exchanged once with potassium acetate, not washed); f) K(91)-Y (exchanged twice with potassium acetate, not washed)

In Figure 3.2-15, the region $5 - 25°$ 2θ of Figure 3.2-14 is examined in more detail. When the measured data of samples prepared for this work were compared to data from a study of a K(100)-Y zeolite by Eulenberger *et al.* [34], it was seen that all reflections measured for the prepared K-Na-Y samples matched either to the pattern for the parent Na-Y or to the K(100)-Y sample found in literature. Thus, no extra (potassium) phases were observed in prepared samples. A clear shift was observed to lower degrees two theta for the pattern of K(91)-Y. The reasons for this might include changes in the unit cell size, but instrumental factors cannot be ruled out. It is beyond the scope of this work to determine accurate unit cell sizes.
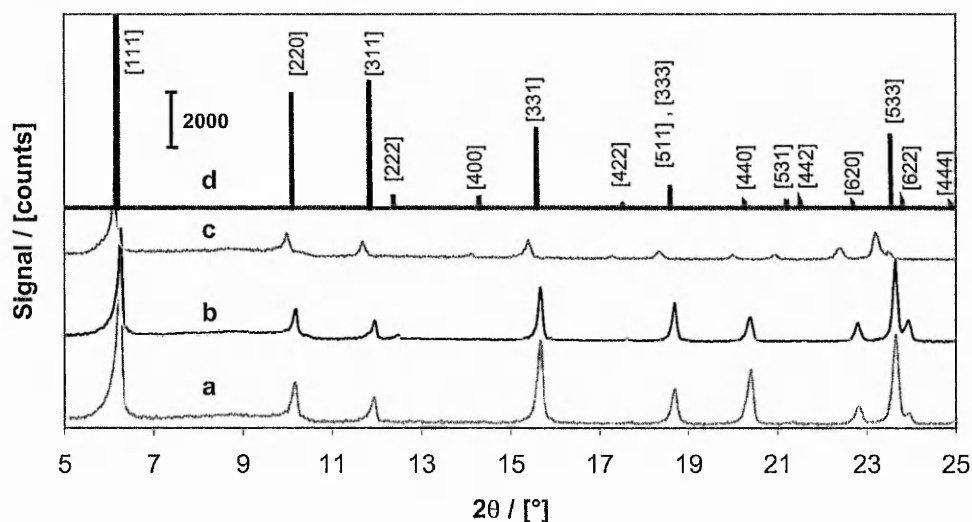
Figure 3.2-15: Powder x-ray diffraction data for K-Na-Y zeolites. Legend: a) Na-Y (parent material); b) K(87) -Y; c) K(91) –Y; d) K(100)-Y. Traces a, b and c were measured of "as is" samples. Trace d taken from a study on ion exchanged Y zeolites by Eulenberger *et al.* [32, 34]. Peak intensities for trace d on a relative scale, the [111] reflection being equal to 1000.

3.2.6.4 Na-Y zeolite exchanged with lead(II) acetate

X-ray diffraction patterns of lead ion exchanged Na-Y zeolite can be seen in Figure 3.2-16. Ion exchange conditions can be seen in §3.2.3.1.

As was the case for the lead ion-exchanged Na-X samples, a drop in intensity could be observed in the XRD patterns of Na-Y when lead acetate was introduced. The Miller indices of the major reflections have been assigned in accordance with a simulated pattern of a Na-Y material of similar Si/Al-ratio (curve a). The simulated pattern shown as curve a) in Figure 3.2-16 is of (Ca,Na)-Y zeolite [18, 30]. No additional Pb-phases in the zeolite samples could be matched to lead phases in the JCPDS database.
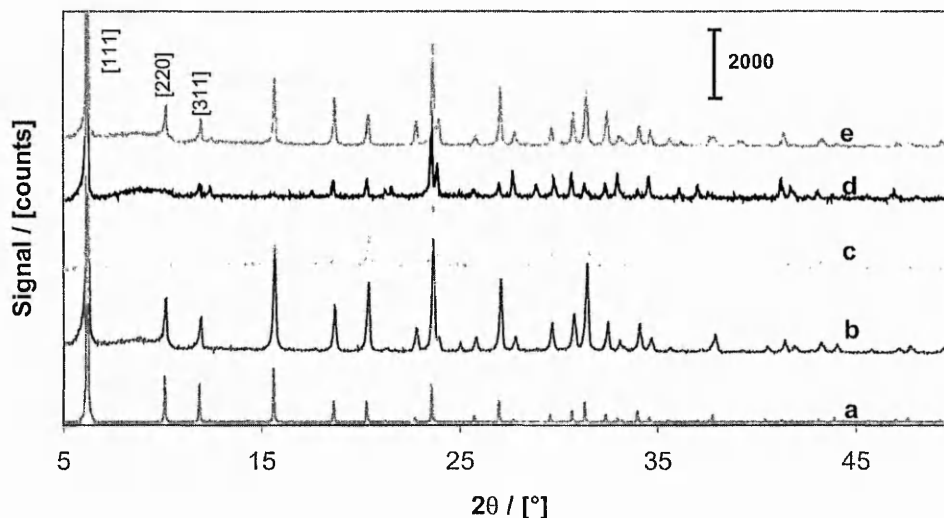
Figure 3.2-16: Powder x-ray diffraction patterns for Pb-Na-Y zeolites. Measurement conditions curve b: 3-50 degrees 2θ-range, 0.02 degrees 2θ-step; 8 seconds per step (displayed is the measured intensity, multiplied by 5/8 in order to fit it on the same scale as the other traces). Legend: a) Simulated (Na,Ca)-Y [18]; b) Na-Y (parent zeolite); c) Pb(~50)-Na(~50)Y (exchanged once with lead(II) acetate, not washed); d) Pb(~100)-Y (exchanged twice with lead(II) acetate, not washed); e) Pb(306)-Na(7)Y (exchanged thrice with lead(II) acetate, not washed)

In Figure 3.2-17 a close-up of the region 5 – 25° 2θ can be seen. It is evident from this figure that all reflections seen in Pb(306)-Na(7)-Y (curve b) are present in either the parent zeolite or in a Na-Y sample from Eulenberger et al. [32, 34]. It is thus concluded that no extra phases occurred in the lead-exchanged Y zeolites prepared for this work.
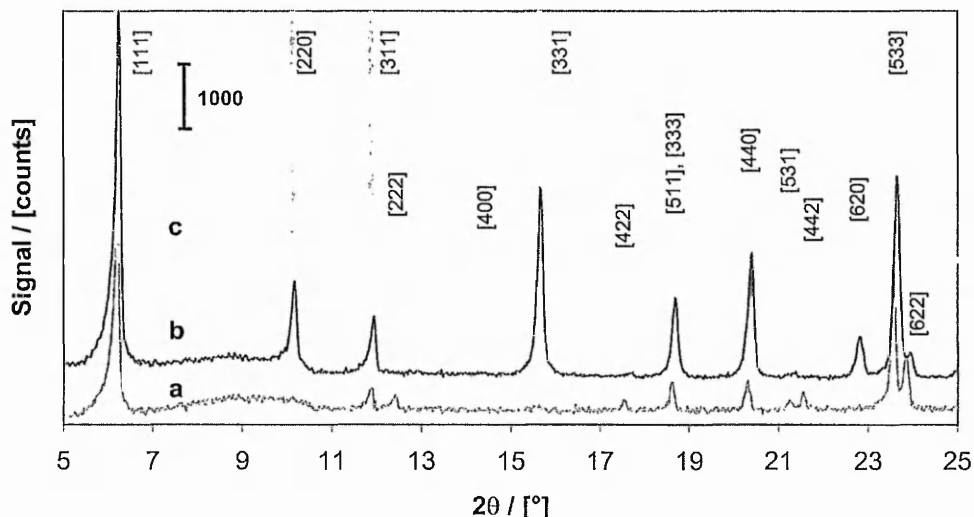
Figure 3.2-17: Powder x-ray diffraction patterns for Pb-Na-Y zeolites, compared with the parent material and a pattern found in literature. This figure shows two traces from Figure 3.2-17 plus an additional trace from the CDS database [32]. Legend: a) Pb(~100)-Y; b) Na-Y (parent zeolite); c) Na-Y, after Eulenberger *et al.* [32, 34].

3.2.6.5 NH$_4$-Beta zeolite exchanged with lead(II) acetate

X-ray diffraction patterns for zeolite beta appear to indicate less long-range ordering than is the case in zeolite X, as reflections are generally broad and noisy. The ion exchange of NH$_4$-Beta with lead(II) acetate resulted in a decrease of the signal intensity in the XRD patterns. Absorption phenomena as well as a decrease in long-range ordering (*i.e.* a loss of crystallinity) might be considered reasons for this phenomenon. Zeolite beta is a mixture of three different polytypes (*vide* §1.2.3.4). This causes overlap of reflections [30], and makes the diffractogram seem to resemble a partly amorphous material. The measured patterns of the zeolite beta samples were noisier than simulated patterns in the International Zeolite Association's database (not shown). These simulated patterns are based on a single type of zeolite beta, rather than on a mixture of three polytypes.
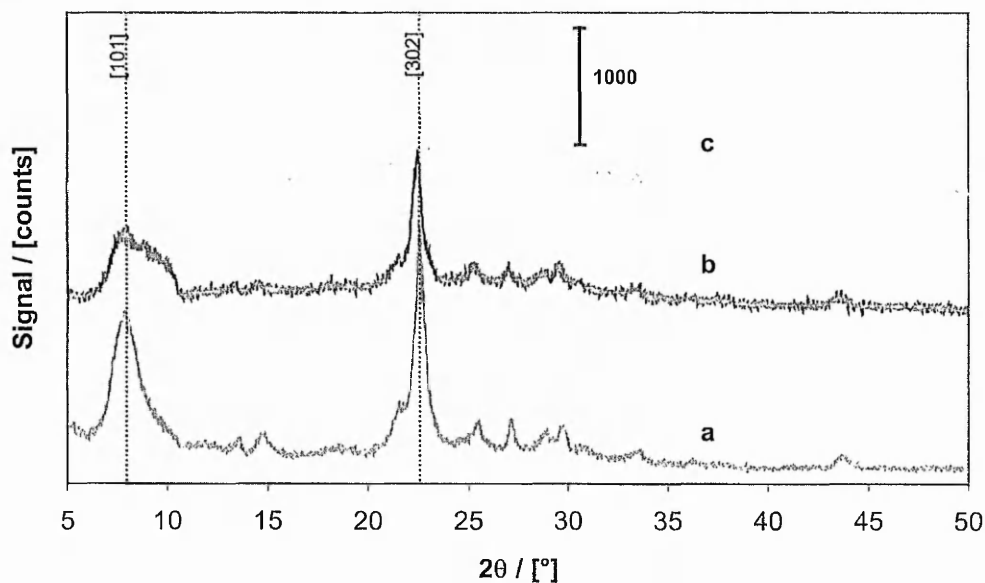
Figure 3.2-18: Powder x-ray diffraction patterns for Pb-NH4-Beta zeolites. Legend: a) NH4-Beta (parent material); b) Pb(85)-NH4(15)-Beta; c) Pb(219)-Beta.

3.2.7 X-ray absorption spectroscopy studies of Pb-Na-Y

The Fourier transformations of x-ray absorption spectra of lead(IV)oxide and lead(II,IV) oxide are shown in Figure 3.2-19. The spectrum of and Pb(306)-Na(7)-Y is shown in Figure 3.2-20. The EXAFS spectra were modelled using EXCURV'98, which is available at Daresbury Laboratories [37]. Numerical data of the models is given in Table 3.2-9. The fit index is an indication of goodness-of-fit. A lower fit index corresponds to a better agreement between experimental data and the model.

Table 3.2-9: Model parameters of EXAFS data shown in Figure 3.2-19 and Figure 3.2-20

Sample	Fit index	n^a [-]	N^b [-]	Atom type	r^c [Å]	σ^d [-]
Pb_3O_4	22.28	1	6.0	O	2.158	0.007
		2	2.0	Pb	3.373	0.011
		3	4.0	O	3.395	0.012
		4	8.0	Pb	3.892	0.017
PbO_2	22.28	1	6.0	O	2.191	0.016
		2	2.0	Pb	3.309	0.018
		3	3.0	Pb	3.652	0.017
Pb(306)-Na(7)-Y	33.20	1	2.0	O	2.266	0.017
		2	2.0	O	2.418	0.012
		3	2.0	Pb	3.699	0.009
		4	4.0	Si	4.006	0.011

a) Number of the shell that was fitted
b) Number of atoms in the shell
c) Distance to central atom in Ångstrøm
d) Debye-Waller factor

The values for the lead-oxygen distances and coordination of lead given in Table 3.2-9 were found to correspond to crystallographic data for the oxide standards measured. From neutron diffraction studies on $Pb_{12.2}Na_{2.7}D_{34.1}Si_{137}Al_{55}O_{384}$ (Pb-Na-Y), Sun and Seff found a Pb-O distance of 2.852 Å, which is larger than found in this study. For this apparent discrepancy, the following needs to be considered. Diffraction data will give distances between lattice planes, irrespective of the atom type present in the lattice plane. By contrast, extended x-ray absorption fine structure (EXAFS) studies provide information about the average local environment of an atom type, regardless of the distance between lattice plains. Thus, the different physical phenomena probed by absorption and diffraction studies can explain discrepancies found between distances observed by means of diffraction studies and by means of EXAFS studies. Furthermore, in a study on lead containing soil, Manceau *et al.* suggested that static disorder and thermal vibrations complicated precise determination of crystallographic distances in lead compounds [38]. Some literature (Pb – O) distances in lead compounds are summarised in Table 3.2-10. The lead – oxygen distance found in the first shell for the Pb(306)-Na(7)-Y sample measured clearly deviates from distances found for lead compounds with a 4^+ oxidation state. The distance found (about 2.3 Å) is therefore seen as indicative of a 2^+ oxidation state for the lead in the zeolite.

Table 3.2-10: Distances in Ångstrom to the central lead atom for lead-faujasites found in literature. All distances are deduced from diffraction data. Numbers in brackets indicate number of atoms coordinated to the central lead atom

Sample	Pb-O			Pb-Pb	Pb-Si[a]	Ref.
Pb-Na-X	2.437(3)	2.769(3)	3.076(3)	3.859(3)	3.555(7)	[21]
Pb-Na-Y[b]	2.852(3)	3.274(3)	4.471(6)	2.991(1)	3.649(6)	[39]
α-PbO	2.307(4)	4.300(4)	4.588(4)	3.662(2)	-	[40]
β-PbO$_2$	2.140(2)	2.176(4)	3.765(4)	3.385(2)	-	[41]
Pb$_3$O$_4$	2.131(2)	2.206(4)	3.913(4)	3.282(2)	-	[42]
Pb(Ac)$_2$	2.24(1)	2.62(4)	2.86(3)	-	-	[43]
PbSiO$_3$	2.27(2)	2.52(1.6)	2.95(2)	-	-	[38]

a) As diffraction methods are not able to distinguish between silicon and aluminium, this bond is arbitrarily referred to here as Pb-Si.
b) Neutron diffraction technique used to determine the crystallographic distances
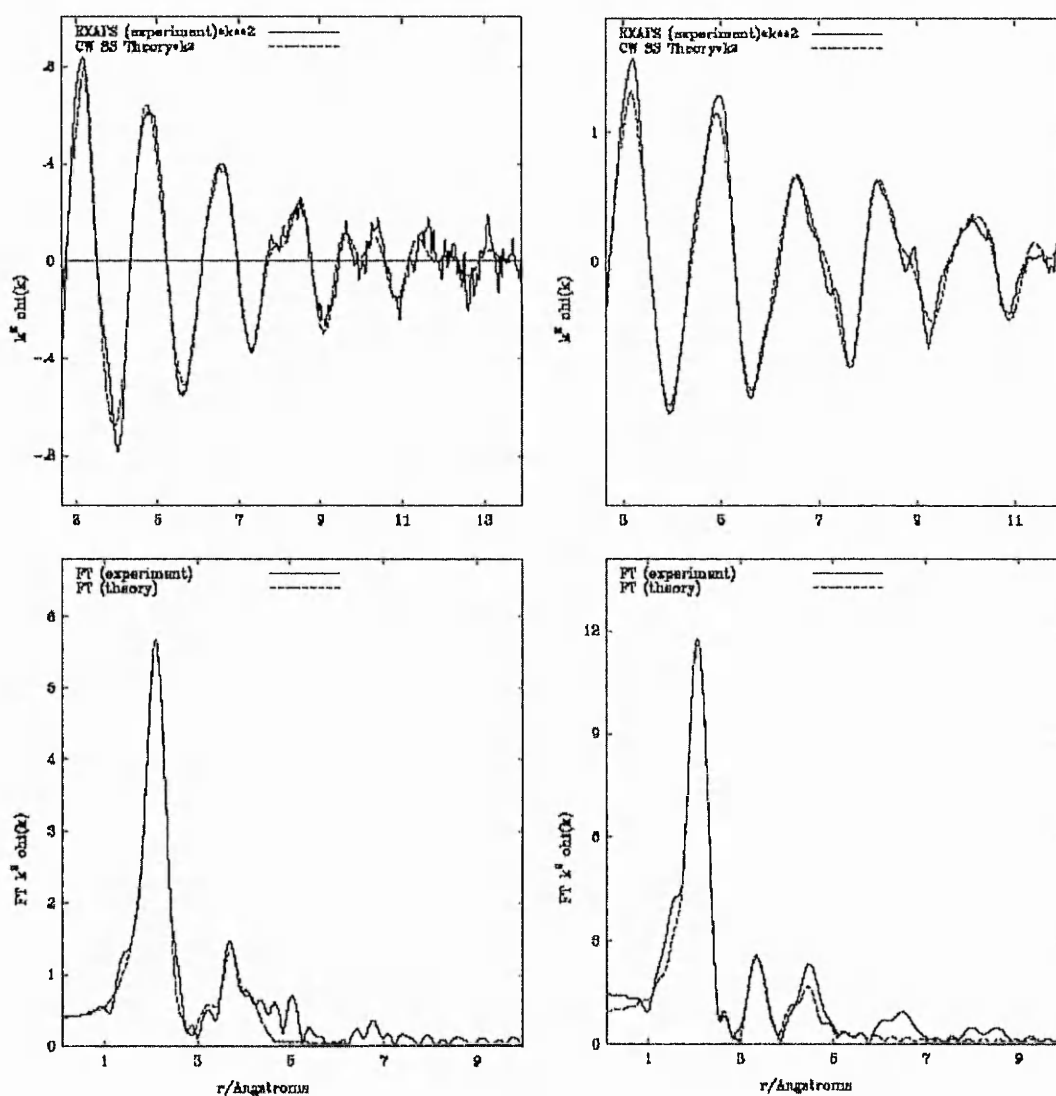
Figure 3.2-19: EXAFS spectra of PbO$_2$ (left) and Pb$_3$O$_4$ right. Top graphs show EXAFS plotted in k^2 space, bottom graphs show the Fourier transform of the EXAFS, also in k^2 space. Dotted lines represent the model that was fitted to the data (solid lines).
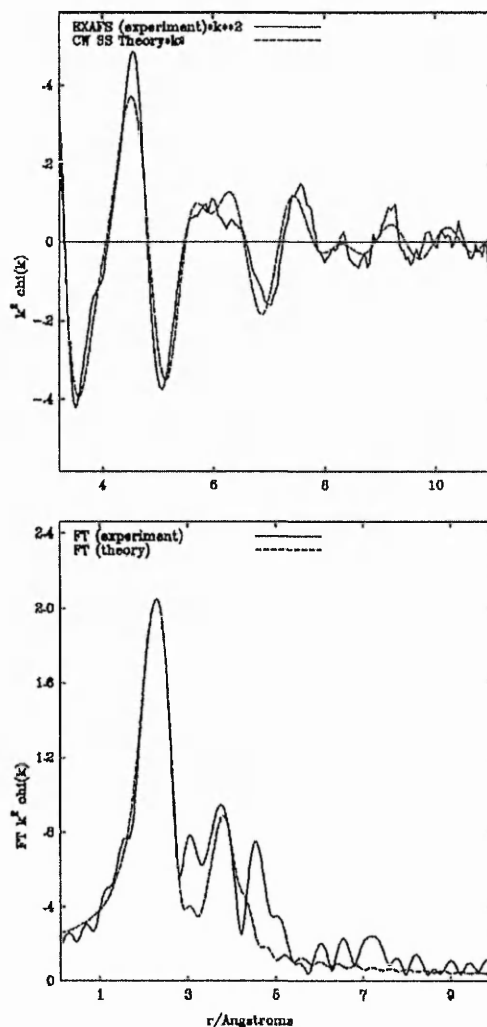
Figure 3.2-20: EXAFS spectra of Pb(306)-Na(7)-Y. Top graphs show EXAFS plotted in k^2 space, bottom graphs show the Fourier transform of the EXAFS, also in k^2 space. Dotted lines represent the model that was fitted to the data (solid lines).

3.2.8 Discussion and conclusion

From the AA, ICP, TGA, XPS and XRD data it is concluded that it is indeed feasible to incorporate potassium or lead in the zeolite samples used. For potassium, sufficient literature data are available to suggest ion exchange is successful in depositing potassium in zeolite cavities [44]; no particular problems were expected *a priori* with this ion exchange. The Pb^{2+} ion is considerably larger however, which might lead to problems with respect to Pb^{2+} entering the sodalite cages. No evidence was found here to suggest such high levels of ion exchange were not attainable with the ion exchange of X, Y and

Beta zeolites with lead(II) acetate. This was found to be in agreement with literature published on this subject [36, 45, 46].

The fact that mass loss observed by TGA in zeolite Pb-Na-X is more than it would be for a theoretical exchange of $1Pb^{2+}$ for $2Na^+$ (Figure 3.2-2) can, without further data not be sufficiently explained. However, a reason might be suggested here. With respect to the lead(II)-water stoichiometry, literature data indicates three water molecules coordinate to Pb^{2+} in zeolite X where lead is reported to exist in a cubic-like $Pb_4(OH)_4^{4+}$ form (*vide* §1.2.5.3) [36]. Effectively, this leads to a 1:1 ratio of water molecules to Pb^{2+} ions. In contrast, in Na-X, the water to Na^+ ratio was reported as being 2:1 [47]. Thus, the amount of water decreases more with increasing Pb^{2+} content than it would under the assumption that only the difference in volume between (Pb^{2+} and $2Na^+$) would be expelled. Linear fits for mass loss versus cation loading in thermograms (as presented in Figure 3.2-2) were not drawn up for other zeolites than Pb-Na-X, as not enough data points were available to achieve a statistically relevant relation between exchange-cation loading and mass loss determined by TGA.

Levels of ion exchange, calculated from atomic absorption results seem to indicate that high exchange levels (>80 exchange %) are easily attainable for all lead exchanged zeolites. It is however, with the data presently available impossible to pass judgement on the location of the lead in the zeolite. It needs to be remembered, that the experimental techniques mentioned above yield information on the bulk composition of the zeolite. In order to determine the local structure around lead in Pb-Na-Y, x-ray absorption spectra were recorded and absorption fine structure spectra were modelled. The bond distances found are indicative for a 2^+ oxidation state of lead in the measured Pb-Na-Y sample. Further x-ray absorption studies would be required to draw a model picture of the local lead environment in zeolites.

Some evidence for a small surface dealumination following ion exchange was found by x-ray photoelectron spectroscopy for Pb-Na-X samples. X-ray photoelectron spectroscopy was used to measure surface properties of the exchanged zeolites. The usage of XPS as a tool to assess basicity via

measurement of the O 1s binding energy is not without ambiguity for these lead exchanged zeolite samples:

- Sample charging effects could have caused a shift in the apparent O 1s binding energy
- The size of a possible shift in O 1s binding energy was within the systematical error of the XPS measurement of binding energy
- Presence of oxygen containing lead compounds in the zeolite cavities could have caused a shift in the measured O 1s binding energy

After the ion exchange crystalline materials were obtained (except for lead-exchanged beta zeolites) as was evident from x-ray diffraction patterns. It is beyond the scope of this work to give a full line profile analysis for the observed powder diffraction patterns. A few possible causes for changes in the x-ray diffraction peak properties such as width and position can be listed [11, 48, 49]:

a) Pb^{2+} is a large ion, and is a good scatterer as well as a good absorber of x-rays. Depending on its location in the zeolite framework, it may affect the reflection pattern significantly

b) Introduction of Pb^{2+} as guest species in the zeolite cavities might lead to a decrease in particle size, which in turn leads to peak broadening

c) Lattice distortion as a result of Pb^{2+} introduction could lead to alterations in peak width and position

d) Structural faults, which could occur as a result of Pb^{2+} introduction, could lead to peak broadening

e) Slight loss of crystallinity of the zeolite framework could lead to changes in apparent particle size, which causes peak broadening

Without more structural information from other sources, it is not possible to draw any firm conclusions regarding the observed peak broadening. It is however, likely, that the introduction of a bulky ion such as Pb^{2+} would induce a lattice distortion effect, leading to peak shifts and broadening.

For all "as is" ion-exchanged faujasite samples, no reflections are observed that can be solely attributed to any phase other than a zeolitic one. Peaks could be

matched against simulated patterns of either hydrated or dehydrated faujasite, against the parent zeolite or against data found in literature. There were no reflections in the XRD patterns that could be matched against any pattern for *e.g.* lead salts found in the JCPDS database [31]. Thus, as far as x-ray diffraction is concerned no lead salt phases in the Pb-Na-X samples exist. Concentration of such an extra-zeolitic phase is either too low to be picked up by means of x-ray diffraction, or the particle size is such that this phase was invisible to XRD. Likewise, no evidence was found for additional salt phases in zeolite Beta samples. Here, comparison against simulated patterns is not a very helpful technique, as real samples differ too much from simulated patterns. Shifts of reflections to lower degrees 2θ as observed for two reflections in the XRD patterns of Pb-Na-X (*vide* Figure 3.2-12), are interpreted in light of changes in hydration state of the zeolite, or of changes in unit cell size.

3.3 Activation of ion exchanged zeolites

3.3.1 Abstract

Activation of zeolite catalysts is a prelude to further experimentation (such as adsorption experiments or catalytic reactions). Activation is required to remove water present in zeolite cavities and promote migration of cations.

In this chapter, effects of heat treatment on the zeolite crystal structure were examined. X-ray diffraction studies indicate heating of zeolites to 973 K and above leads to the emergence of an addition Pb^0 phase for some of the zeolite samples.

3.3.2 Background

Heat treatment of catalysts may have some implications for the crystal structure of the zeolite. As has been pointed out in section one of this work (*vide* §1.2.7), high activation temperatures are required for water removal from the zeolite

cavities. Water could adsorb on basic sites, and thus render them inaccessible to isopropyl alcohol, the reactant used in this work. Thus, prior to catalytic experiments and adsorption experiments, all zeolite samples were activated at elevated temperatures (typically 773 K) in an inert atmosphere. Furthermore, cation migration occurs at higher temperatures, which is for example a necessary step in the preparation of very basic potassium zeolite [5].

On the other hand, low temperatures are required to keep the crystal structure of zeolites with a low Si/Al-ratio (such as zeolites X and Y) intact [1, 21, 50]. As stability issues seem to arise with the activation of Pb-zeolite X [1], it seems valid that the structure of zeolite Pb-Na-X exposed to thermal treatment should be investigated. There is a clear trade-off between high and low temperatures during activation, and a balance will need to be struck.

The structural stability can be assessed with the use of x-ray diffractograms [51]. Thermo-gravimetric analysis and Fourier transform infrared spectra of activation experiments will be used to support evidence from x-ray diffraction experiments.

3.3.3 Activation of Pb-Na-X in helium

When a Pb-Na-X sample of moderate lead loading (34 exchange percent or 13.8 wt%) is activated in flowing helium, at activation temperatures of 973 and 1123 K, two reflections (at 31.35 and 36.33 degrees 2θ) appeared in the x-ray diffraction patterns. These were not present in either the parent Na-X (*vide* Figure 3.3-1) or in any pattern of Pb-Na-X or Na-X found in literature [18, 30, 33, 36]. They do, however match the [111] reflection at 31.31 degrees 2θ and the [200] reflection at 36.27 degrees 2θ of the diffraction pattern of metallic lead (JCPDS pattern number 04-686 [31]).
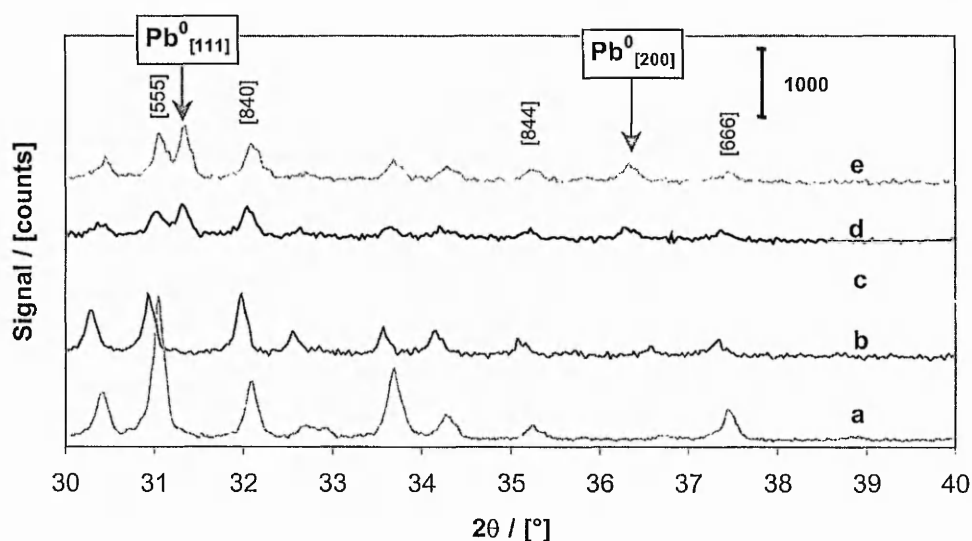
Figure 3.3-1: Powder x-ray diffraction patterns of activated Pb(34)-Na(76)-X. All activations were performed in a flowing helium atmosphere. The Pb^0 reflections are indicated using arrows. Legend: a) Na-X (parent material), activated 793 K; b) Pb(34)-Na(76)-X, as is; c) Pb(34)-Na(76)-X, activated 793 K; d) Pb(34)-Na(76)-X, activated 973 K; e) Pb(34)-Na(76)-X, activated 1123 K. The indexed reflections apply to trace e.

When Pb-Na-X samples of different lead loading were subjected to an activation regime of 773 K in flowing helium, the same Pb^0 reflections that arose after activation of Pb(34)-Na(76)-X at 973 K or above (*vide* Figure 3.3-1), can be seen to appear in the diffraction patterns of Pb-Na-X with a lead loading of 63 and 131 exchange percent lead (24 and 42 wt% lead respectively; *vide* curves d and e in Figure 3.3-2).
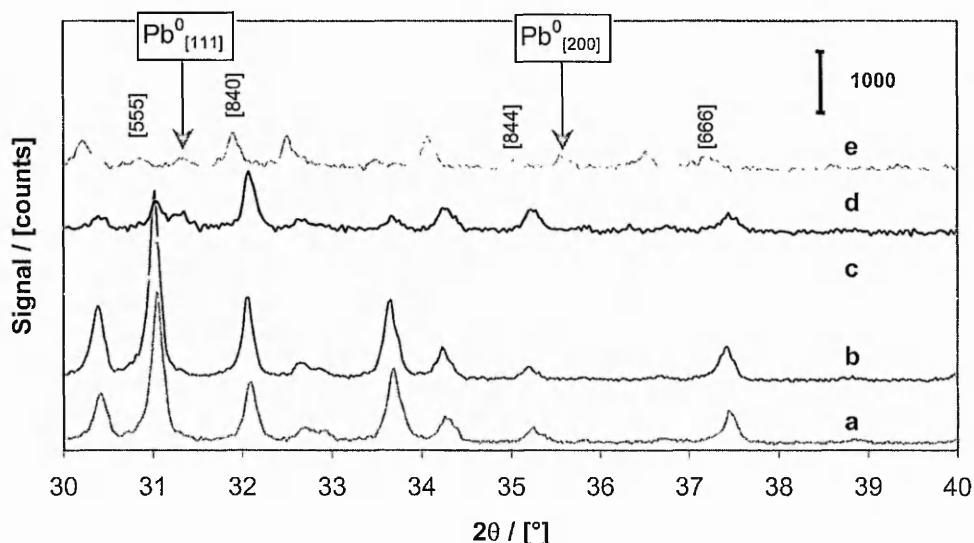
Figure 3.3-2: Powder x-ray diffraction patterns for activated Pb-Na-X zeolites. All samples were activated at 773 K for 2 hours in a flowing helium atmosphere. Legend: a) Na-X (parent material); b) Pb(9)-Na(96)-X, as is; c) Pb(34)-Na(76)-X; d) Pb(63)-Na(27)-X; c) Pb(131)-X. The indexed reflections apply to trace e. Note that a slight shift has occurred with trace e as compared to the other traces; probably for instrumental reasons.

Prior to the isopropanol dehydrogenation reaction, Pb-Na-X samples were activated in flowing helium, as is described in §3.4. After activations of the Pb(131)-Na-X sample at 973 K or above, a discoloration with a metallic sheen was noticed on the inside of the quartz reactor tube used for the activation. After the reactor tube was removed from the helium atmosphere, this shining colour turned dull over time.

3.3.4 Activation of Pb-Na-X samples in vacuum

In Figure 3.3-3 Fourier transform infrared spectra can be seen of the activation of Pb(9)-Na(96)-X (Pb loading: 3.8 wt%). At the start of activation, water was present as was evident from the deformation vibration at 1648 cm^{-1}, and the broad feature around 3700 – 2500 cm^{-1}. Increasing temperature caused adsorbed water to vacate the zeolite. At around 673 K most water has been removed. The bands at 1482 and 1431 cm^{-1} may be attributed to adsorbed carbon dioxide. It is clear, that most of this was desorbed when the temperature reached 773 K. The peak at 3688 cm^{-1} can be assigned to terminal OH groups; these are removed between 473 K and 573 K.
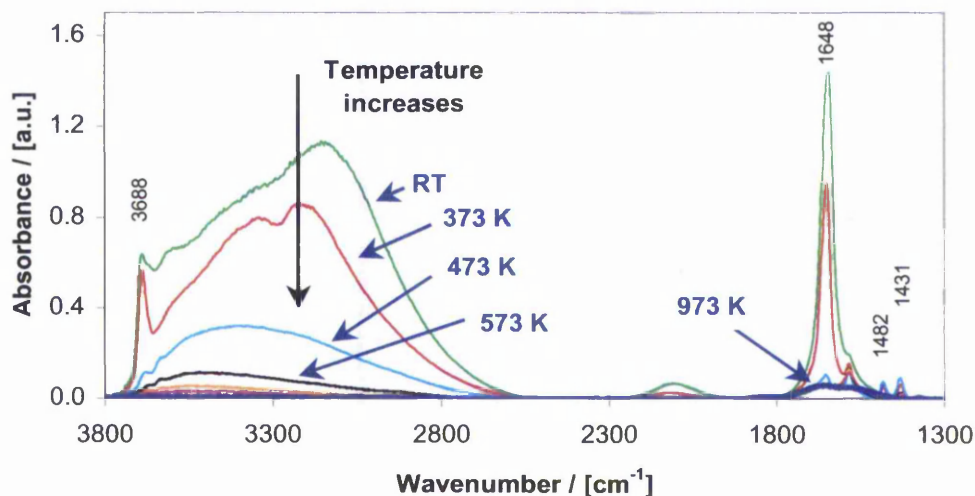
Figure 3.3-3: FTIR spectra of the activation of Pb(9)-Na(96)-X. Activation conditions: ramp rate = 10 k min^{-1}; final activation temperature = 973 K; pressure in the IR cell < 10^{-6} mbar. Spectra displayed at RT and then at 373 – 973 K in 100 K intervals. The end of the experiment (973 K) is indicated with a thick line. The peaks indicated belong to hydroxyl groups (3688 cm^{-1}), water (1648 cm^{-1}) and carbonates (1482 and 1431 cm^{-1}).

By contrast, when the lead loading was 42 rather than 3.8wt%, activation to 973 K resulted in the disappearance of intensity in the infrared spectrum measured (*vide* Figure 3.3-4). This effect was found in two separate measurements of this sample, and was not observed for any other Pb-loaded zeolite X sample. It was also not observed for zeolites exchanged with other metals used in the work. It can be speculated that metallic lead was released from the sample and deposited on the windows of the infrared spectrometer, which are much colder than the sample itself during activation. In several studies researchers described the absorption of infrared light by thin metal films [52-56]. The absorption of infrared light by a metal film is not necessarily linear over the wavelength range. When the transmission of the metal film approaches zero, the absorption approaches infinity. This is in fact the effect observed in the wavenumber region 3800 – 3150 cm^{-1} during the activation of Pb(131)-Na(0)-X (spectrum at 973 K). It was found that mechanical cleaning removed this layer, and transmission was once again possible.
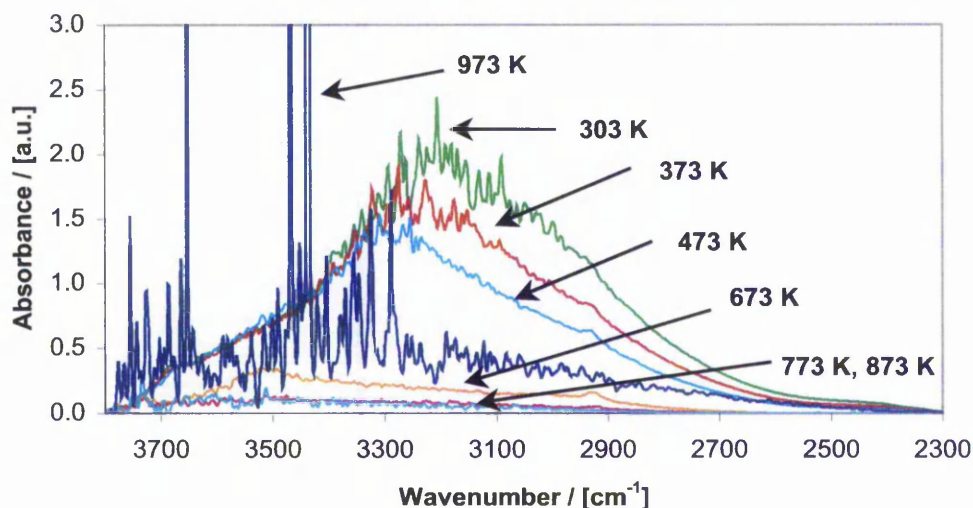
Figure 3.3-4: FTIR spectra of the activation of Pb(131)-X. Activation conditions: ramp rate = 10 k min^{-1}; final activation temperature = 973 K; pressure in the IR cell < 10^{-6} mbar. The "peaks" at 3653, 3467 and 3435 cm^{-1} in the curve corresponding to 973 K were seen to go towards infinity. For clarity the spectrum is shown on the same scale as the spectra at other temperatures.

3.3.5 Discussion and conclusion

It is clear from XRD, FTIR and TGA (*vide* 3.2.3.2) data that for a Pb-Na-X sample with lead loading of 42wt% structural changes occur as a result of thermal treatment.

The additional reflections found in powder patterns of activated Pb-Na-X could not be matched up to any lead compound or indeed to alumina phases in the JCPDS database [31]. The match with metallic lead was however, striking. It is thus concluded that some metallic lead is present after activation of Pb-Na-X samples in an inert atmosphere. Kovacheva et al., who studied the application of Pb-Na-X in the coupling of methane, also observed the emergence of lead phases during the activation of Pb-Na-X. The activation temperature for their samples was 1123 K [6-8]. Further evidence was provided by the observations of the activation in vacuum of an X zeolite with a high lead content. Here, the loss of intensity in the infrared region is seen as indicative for the emergence of metallic lead.

When the parent Na-X was activated in helium, no additional reflections were found in thee XRD pattern (maximum activation temperature 973 K) beyond the Na-X reflections present at room temperature or in the simulated Na-X patterns.

Thus, in light of XRD, TGA, FTIR and literature evidence it is concluded that metallic lead can be formed in Pb-Na-X zeolites during thermal treatment in an inert atmosphere (helium or vacuum). Although this is clearly demonstrated to occur at high temperatures (973 K) and with high lead loading ($\geq$ 24 wt%), formation of metallic lead might occur in samples with low lead loading, or indeed at lower activation temperatures. It was simply not visible to any of the investigative techniques XRD, FTIR and TGA.

3.4 Zeolite basicity: isopropanol dehydrogenation

3.4.1 Abstract

In section 1 of this work, the usage of the isopropyl alcohol decomposition in the assessment of basicity of zeolite catalysts has been discussed. From literature it is put forward that acetone is formed over basic sites (dehydrogenation), whereas propene is formed over acidic sites (dehydration).

Form isopropanol reactions on K-Na-X zeolites, it became clear that increasing loading of potassium led to an increase in selectivity towards acetone, as well as a decrease in conversion.

From experiments using Pb-Na-X catalysts, it became clear that a low loading of lead, namely 3.8wt% led to the highest yield of acetone, at a temperature of 523 K. Increasing the lead loading further proved to decrease the yield of acetone. An activation temperature of 973 K led to a smaller selectivity to acetone compared with an activation temperature of 773 K. From space velocity experiments it was concluded that acetone was a primary product, whereas propene can be both a primary and a secondary product. Deactivation of the catalyst during the reaction was observed for one Pb-Na-X sample.

On K-Na-Y samples, which had roughly similar potassium loadings, the highest selectivity's to acetone were achieved with a catalyst preparation that involved ion exchanging with potassium acetate and subsequent washing with potassium hydroxide.

Over Pb-Na-Y and Pb-H-Beta samples it was impossible to achieve any significant selectivity to acetone.

3.4.2 Background

As has been illustrated in a previous chapter (*vide* §1.3.4.1), the dehydrogenation of isopropyl alcohol (IPA) to give acetone is a reaction used often to assess basicity of a solid [2]. Product distribution in the IPA reaction could thus be taken as a measure of basicity of a catalyst.

The main focus of this chapter will be on Pb-Na-X zeolites. Reactions were done with various types of zeolites, however, as will be shown, the principal candidates for basicity studies are X zeolites. Because potassium and caesium exchanged zeolites involving isopropanol dehydrogenation and its relation with basicity have been studied by many other authors [57-63], such materials were prepared and studied as reference materials here.

Attempts will be made to investigate various variables that could be of influence on catalytic performance. Were possible equal reaction conditions were maintained, to allow for better comparison of results.

In all reaction data shown, propene and acetone were the products. The reader is reminded, that acetone is considered to be the product formed over basic sites, whereas propene is formed over acid sites [63].

Some minor products were formed at higher temperatures (723 and 773 K), but their amounts were of no significance, with selectivity's to these products remaining far below one percent. Thus, these products are not displayed in the

graphs below, and are not taken into account in the discussion of results. Unless mentioned otherwise, the reaction conditions in Table 3.4-1 were used.

Table 3.4-1: Standard reaction conditions for the dehydrogenation / dehydration reactions presented in this chapter. Deviation from these conditions is mentioned in captions with figures.

Variable	Value	Unit
Activation temperature	773	K
Ramp rate during activation	10	$K\ min^{-1}$
Activation duration	2	h
Gas flow during activation	177	$ml\ He\ min^{-1}$
Gas Hourly Space Velocity (GHSV)	$40 \cdot 10^4$	h^{-1}
Particle size	250 – 425	μm
Molar ratio of He to IPA	4	-

3.4.3 Catalytic behaviour of K-Na-X samples

In Figure 3.4-1, the product distribution in the IPA decomposition catalysed by Na-X, by K-Na-X and by a fully exchanged K-X material can be seen. The figure reports conversion / molar% and selectivity to acetone /molar%.

For Na-X a drop in IPA conversion was found to occur at 673 K. Some acetone was produced over this catalyst; however, yield did not surpass five molar percent (*vide* Figure 3.4-1). In the case of potassium-exchanged zeolite samples, increased potassium loading led to an increase in selectivity towards acetone. The increase in potassium loading was accompanied by a decrease in conversion, over the temperature range measured.
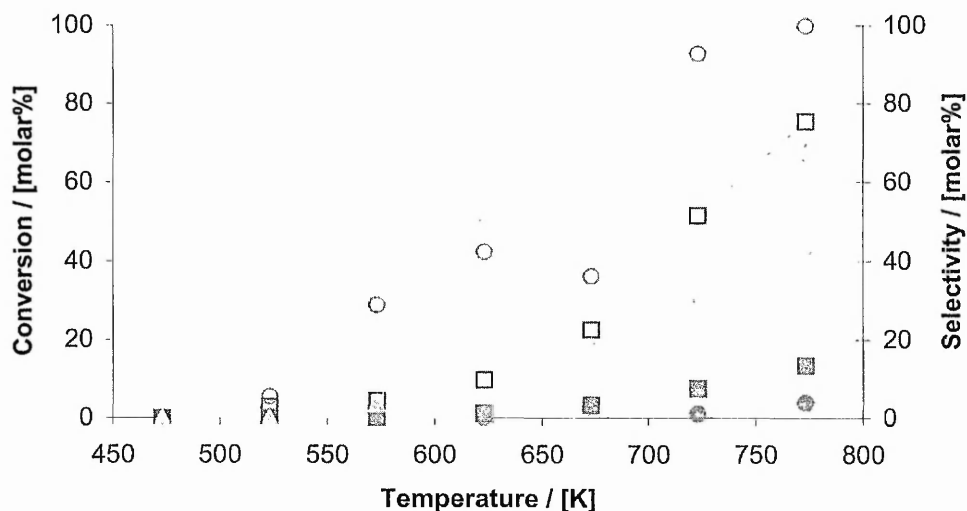
Figure 3.4-1: Isopropyl alcohol decomposition over K-Na-X zeolites showing conversion (open data points) and selectivity to acetone (solid data points). Legend: ⊖ / ⬤) Na-X (parent zeolite); ⊟ / ▧) K(27)-Na(67)-Y;   / ▲ K(100)-Y.

3.4.4 Catalytic behaviour of Pb-Na-X samples

3.4.4.1 Conversion and selectivity to acetone

When IPA was reacted over Pb-Na-X zeolites in the temperature range 473 – 773 K, acetone was one of the products. At the highest temperatures, 723 and 773 some minor by-products were detected, however, their amounts were very small indeed (selectivity <1 molar%). In Figure 3.4-2, the product distribution in the IPA decomposition catalysed by Na-X and by Pb-Na-X samples of varying lead content can be seen. The figure reports conversion / molar%.
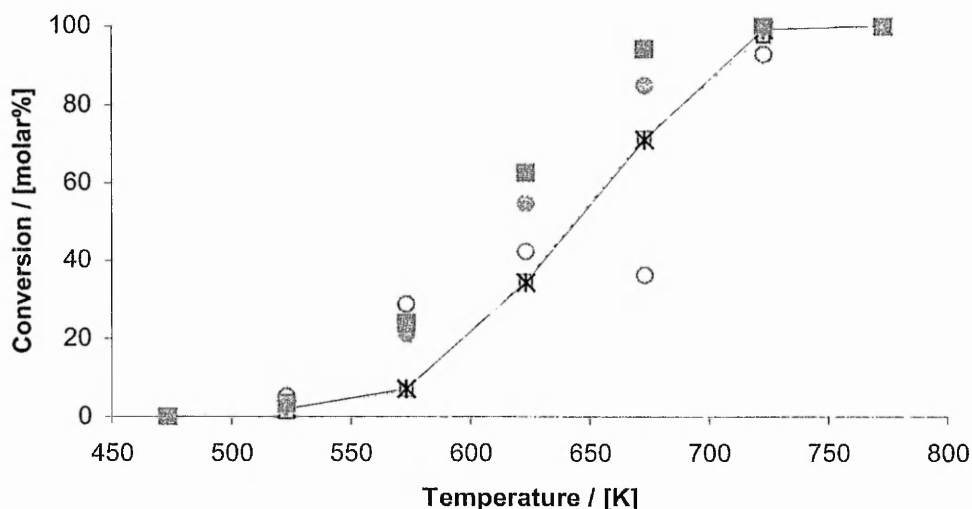
Figure 3.4-2: Isopropyl alcohol decomposition over Pb-Na-X zeolites showing conversion versus reactor temperature. Legend: ⊖) Na-X (parent zeolite); ⊟) Pb(9)-Na(96)-X;   ) Pb(34)-Na(76)-X; ✳) Pb(43)-Na(61)-X; ◉) Pb(63)-Na(27)-X; ▩)Pb(131)-Na-X

In Figure 3.4-3, selectivity for acetone /molar% is reported. This selectivity reached between 60 and 80 molar percent for some samples, and was achieved at a temperature of 523 K. When the reaction temperature was increased further, the selectivity to acetone dropped down to around 20 molar percent.
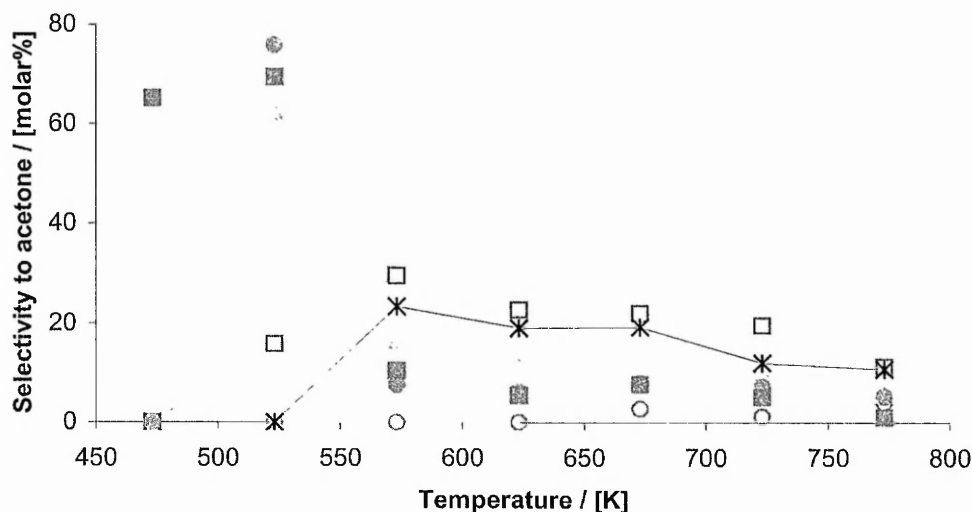
Figure 3.4-3: Isopropyl alcohol decomposition over Pb-Na-X zeolites showing selectivity to acetone / molar% versus reactor temperature. Legend: ⊖) Na-X (parent zeolite); ⊟) Pb(9)-Na(96)-X;   ) Pb(34)-Na(76)-X; ✳) Pb(43)-Na(61)-X; ◉) Pb(63)-Na(27)-X; ▩)Pb(131)-Na-X

3.4.4.2 Effect of activation temperature

In order to investigate the influence of activation temperature in relation to lead loading the Pb-Na-X catalysts were activated at 973 K. The conversion and the selectivity to acetone are plotted in Figure 3.4-4 and Figure 3.4-5. These figures should be compared to Figure 3.4-2 and Figure 3.4-3, which showed catalysts activated at 773 K (*vide* §3.4.4.1).
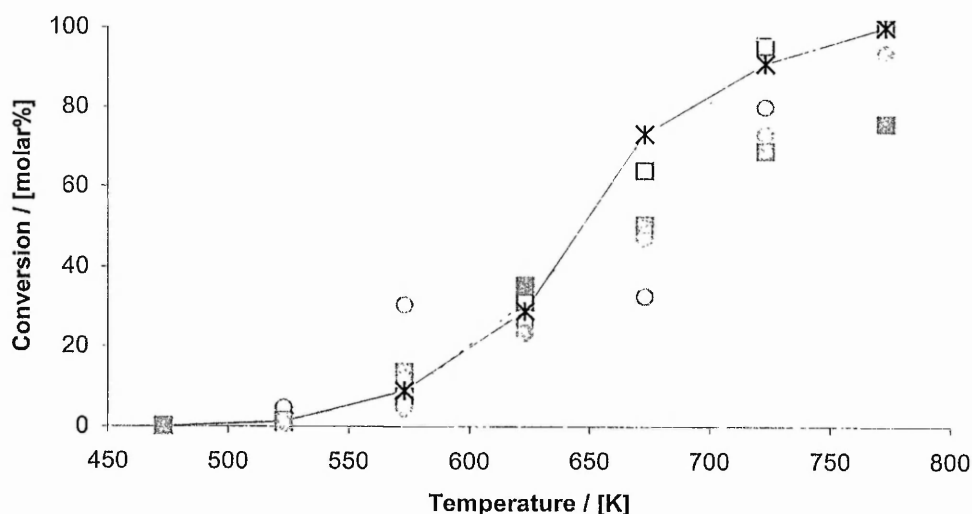
Figure 3.4-4: Isopropyl alcohol decomposition over Pb-Na-X zeolites showing conversion as a function of temperature for X zeolites with different lead loading. Activation temperature = 973 K. Legend: ○) Na-X (parent zeolite); ⊟) Pb(9)-Na(96)-X;   ) Pb(34)-Na(76)-X; ✳) Pb(43)-Na(61)-X; ◎) Pb(63)-Na(27)-X; ▨)Pb(131)-Na-X

From Figure 3.4-4 it is clear that the 973 K-activated catalysts with a lead loading of circa 17wt% or more show a decreased conversion when compared to the 773 K-activated catalysts.
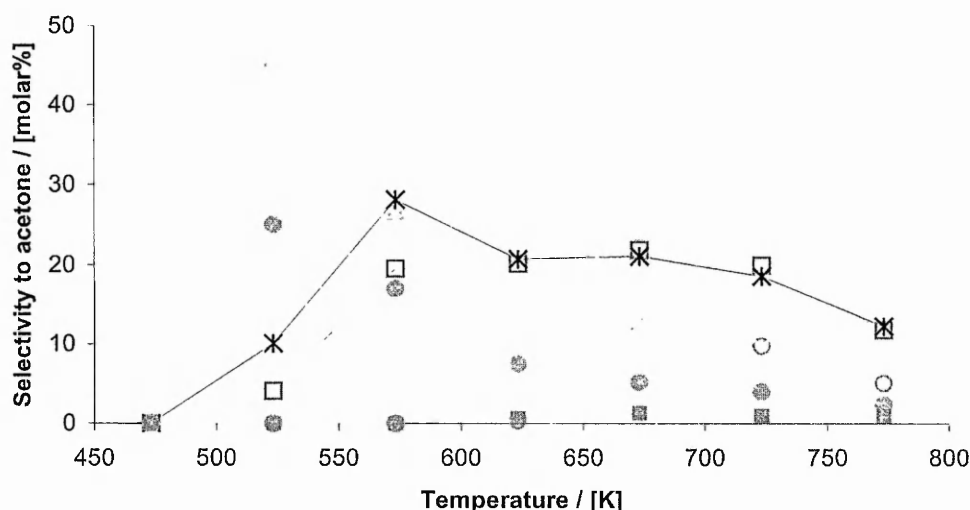
Figure 3.4-5: Isopropyl alcohol decomposition over Pb-Na-X zeolites showing selectivity to acetone as a function of temperature for X zeolites with different lead loading. Activation temperature = 973 K. Legend: ○) Na-X (parent zeolite); ⊟) Pb(9)-Na(96)-X;) Pb(34)-Na(76)-X; ✳) Pb(43)-Na(61)-X; ◉) Pb(63)-Na(27)-X; ▨)Pb(131)-Na-X

The selectivity to acetone profile for Pb-Na-X zeolites after activation at 973 K can be seen in Figure 3.4-5. Some distinct differences can be noted between the 773 K-activated and the 973 K-activated catalysts. Again the catalysts with high lead loading (≥ 17wt%) show a lower selectivity to acetone when compared to the 773 K-activated catalysts. The selectivity for the other catalysts seems to be enhanced slightly when the activation temperature is raised from 773 to 973 K. Remarkably, selectivity to acetone is also found for the parent Na-X, at the three highest reaction temperatures (673, 723 and 773 K).

In order to compare the two activation temperatures in a different way, yield of acetone is plotted. This yield is calculated by multiplying the conversion (in molar percent) by the selectivity (calculated as a fraction of unity). The result can be seen in Figure 3.4-6 and Figure 3.4-7.
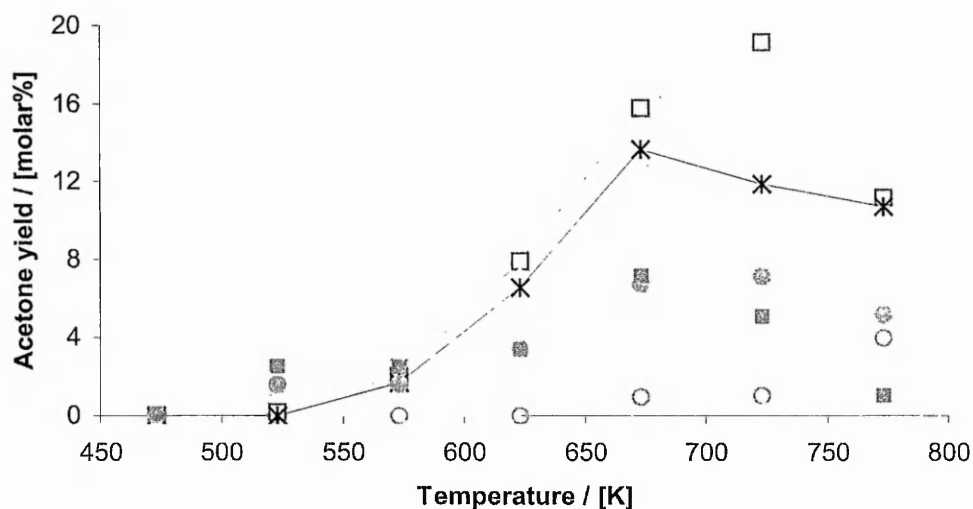
Figure 3.4-6: Isopropyl alcohol decomposition over Pb-Na-X zeolites showing acetone yield as a function of temperature for X zeolites with different lead loading. Activation temperature = 773 K. Legend: ⊖) Na-X (parent zeolite); ⊟) Pb(9)-Na(96)-X;   ) Pb(34)-Na(76)-X; ✷) Pb(43)-Na(61)-X; ◉) Pb(63)-Na(27)-X; ▩)Pb(131)-Na-X

The acetone yield using Pb-Na-X zeolites activated at 773 K reaches a maximum at 673 – 723 K. At these temperatures selectivity is not so significant, however, conversions are rather high, which explains the general shape of the curves in Figure 3.4-6. In terms of yield, the best catalyst has a loading of 3.8wt% lead. The maximum yield is reached at 723 K.
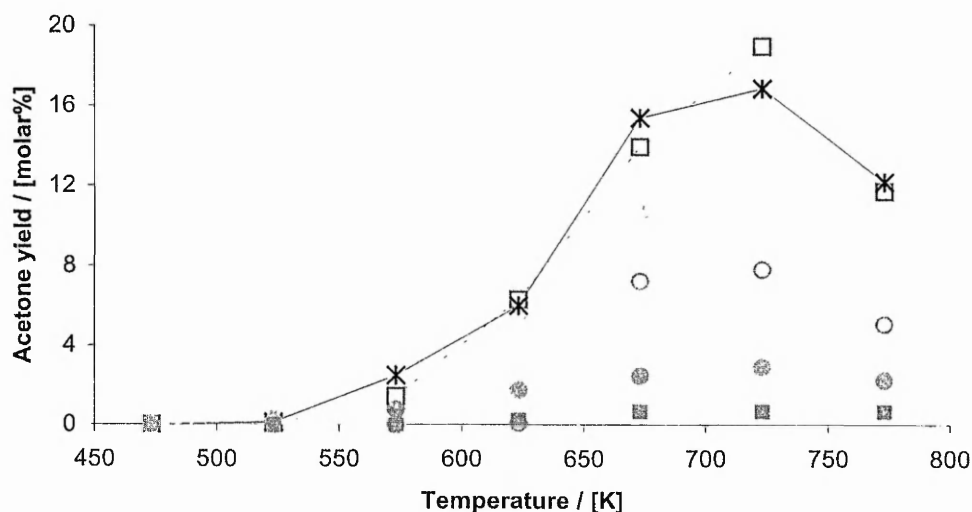
Figure 3.4-7: Isopropyl alcohol decomposition over Pb-Na-X zeolites showing acetone yield as a function of temperature for X zeolites with different lead loading. Activation temperature = 973 K. Legend: ○) Na-X (parent zeolite); ▱) Pb(9)-Na(96)-X;   ) Pb(34)-Na(76)-X; ✳) Pb(43)-Na(61)-X; ◉) Pb(63)-Na(27)-X; ▦)Pb(131)-Na-X

When the acetone yield is plotted for 973 K-activated catalysts, Figure 3.4-7 results. The temperature at which maximum yield is reached is 723 K for all catalysts tested. For catalysts with a low lead loading (≤ 16.9wt%) the yield either improves or stays roughly the same when the activation temperature is raised from 773 to 973 K. Clearly, activation at 973 K had a detrimental effect on the acetone yield for the two catalysts with the highest lead loading (Pb(63)-Na(27)-X and Pb(131)-Na(0)-X, with a lead loading of 24.1 and 42.5wt% respectively).

To further investigate the effect of activation temperature, a zeolite X sample containing 13.8wt% lead (Pb(34)-Na(76)-X) was activated at different temperatures. The conversion and selectivity can be seen in Figure 3.4-8 and Figure 3.4-9.
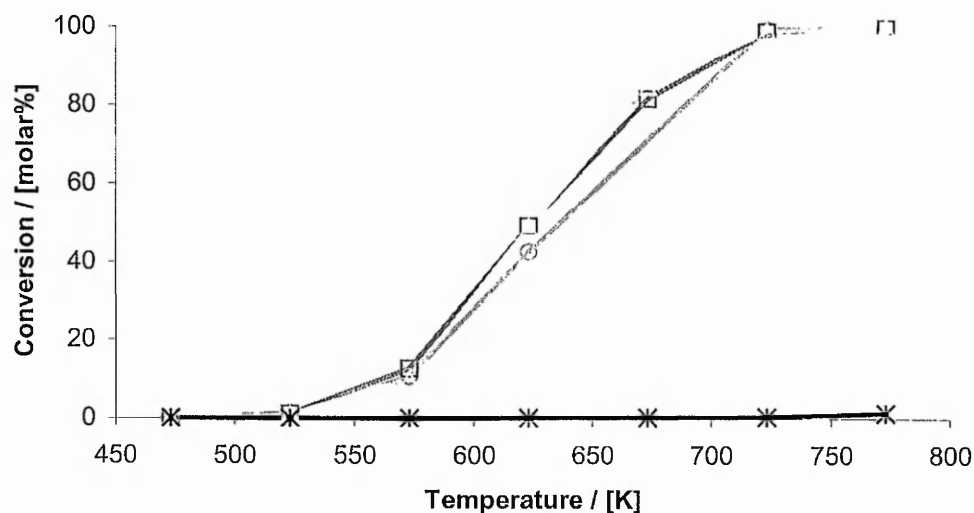
Figure 3.4-8: Isopropyl alcohol decomposition over Pb(34)-Na(76)-X showing influence of activation temperature on conversion. Legend: ⋯) Activated at 673 K; ⊟) Activated at 773 K;   ) Activated at 973 K; ✳) Activated at 1123 K

A small variation could be seen in the conversion profiles of the IPA dehydrogenation for catalysts activated at 673, 773 and 973 K (*vide* Figure 3.4-8). The highest activation temperature, 1123 K, results in a virtually inactive catalyst. When the selectivity to acetone was considered (*vide* Figure 3.4-9), raising the activation temperature from 773 to 973 only seemed to affect selectivity at a reaction temperature of 523 K. Again, activating at 1123 K resulted in an inactive catalyst, which meant the selectivity to acetone was negligible.
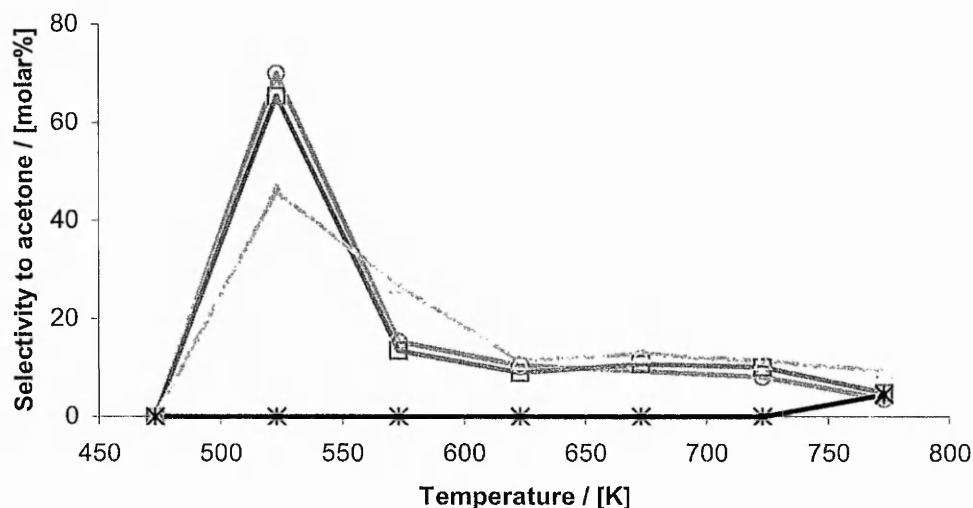
Figure 3.4-9: Isopropyl alcohol decomposition over Pb(34)-Na(76)-X showing influence of activation temperature on selectivity to acetone. Legend: ⊕) Activated at 673 K; ⊟) Activated at 773 K;) Activated at 973 K; ✳) Activated at 1123 K

When Figure 3.4-8 (conversion) and Figure 3.4-9 (selectivity to acetone) are collected into Figure 3.4-10 (acetone yield), it becomes apparent that activating at 973 K results in higher acetone yield when compared to catalysts activated at lower temperatures, at reaction temperatures of 523 K or above.
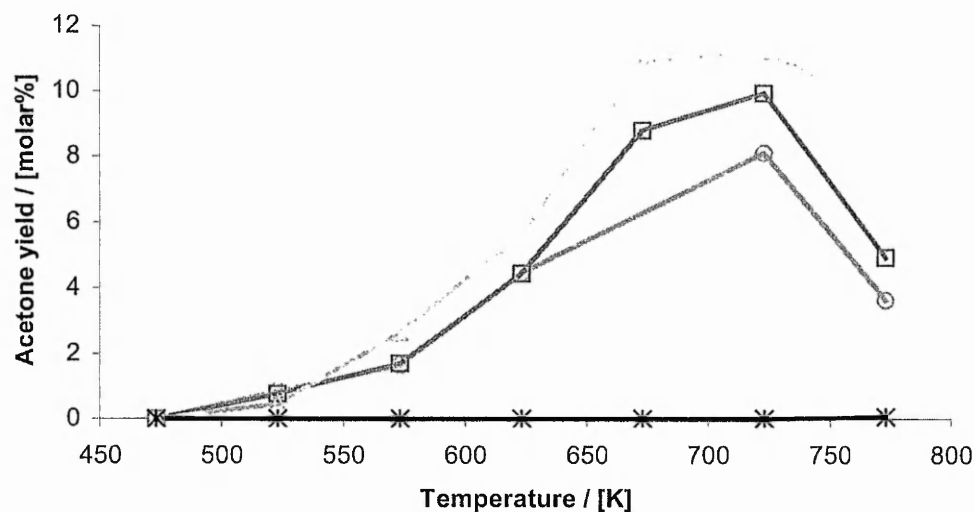
Figure 3.4-10: Isopropyl alcohol decomposition over Pb(34)-Na(76)-X showing influence of activation temperature on the acetone yield. Legend: ⊕) Activated at 673 K; ⊟) Activated at 773 K;) Activated at 973 K; ✳) Activated at 1123 K

3.4.4.3 Effect of space velocity

The gas hourly space velocity (GHSV) was varied during the reaction of isopropanol over Pb(34)-Na(76)-X (*vide* Figure 3.4-11), at a constant temperature of 523 K. This experiment was performed at a low temperature (and hence low conversion) for the following reason. When conversion is high (at high reaction temperatures), build-up of by-products in the zeolite cavities and pores might occur, which would lead to deactivation of the catalyst (*vide* 3.4.4.4). Thus, in order not to pollute the reaction data with possible deactivation effects, conversion was kept at low levels.
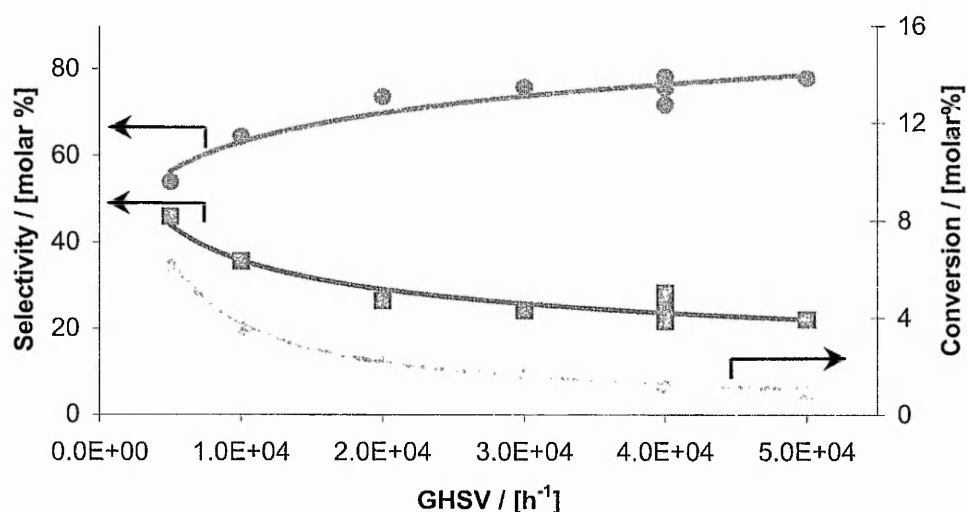
Figure 3.4-11: Effect of space velocity on conversion and selectivity in the isopropyl alcohol decomposition over Pb(34)-Na(76)-X (13.8 wt% lead). Reaction temperature was 523 K. Lines were drawn only to highlight trends in the data. Legend: ⚫) Selectivity to acetone; ▣) Selectivity to propene; ▲) Conversion

Space velocity increase favours selectivity towards primary products, and decreases the selectivity towards secondary products. Thus, it can be seen from Figure 3.4-11 that acetone could indeed be a primary product in the IPA decomposition. When space velocity was increased, the selectivity towards propene decreased. Thus propene could be a secondary product. The curves in Figure 3.4-11 could be seen to go towards a horizontal line with increasing space velocity. This is indicative that propene could be formed via a direct way as well, *i.e.* as a primary product. From Figure 3.4-11 a schematic

representation of IPA decomposition over Pb(34)-Na(76)-X can be drawn which includes the rate constants (k):
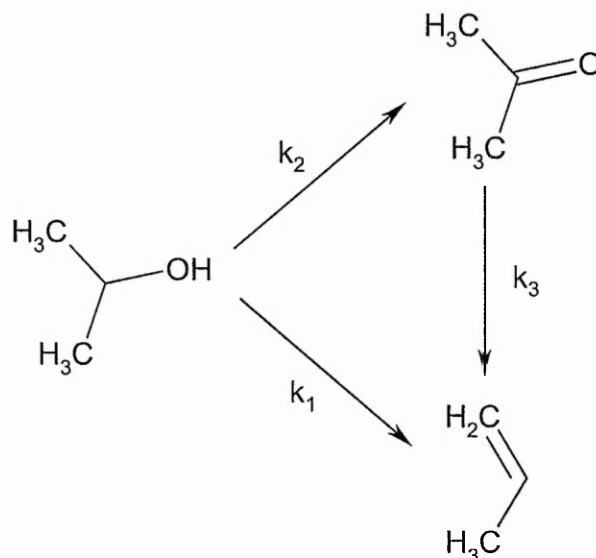
Figure 3.4-12: Schematic of the reaction pathway of isopropyl alcohol over Pb(34)-Na(76)-X.

In this representation, rate constants are represented by k_i. Although quantitative conclusions about rate constants are not possible, under these conditions, the following is apparent: $k_2 > k_1$. The ratio of $k_1 : k_2$ can be estimated to be ~3.5, based on selectivity's at the highest space velocity measured. Some acetone was converted into propene, albeit that this side reaction proceeded slowly.

3.4.4.4 Deactivation

After one reactor run, Pb(34)-Na(76)-X was kept at 423 K overnight. The run was repeated the next day, with the exception of the highest temperature (773 K). Figure 3.4-13 shows that acetone yield decreased from the first run to the second, whilst conversion seems not to have changed noticeably. Each data point corresponds to about 45 minutes on-stream.
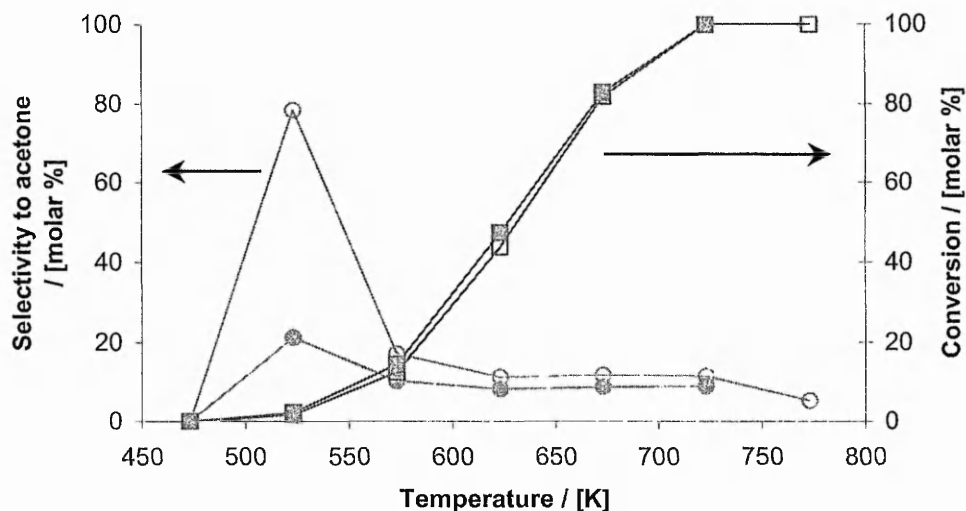
Figure 3.4-13: Two successive runs of the isopropyl alcohol decomposition on Pb(34)-Na(76)-X. The open data points indicate the first run; the solid points indicate the second run. Activation (only for 1st run): 2 h at 773 K in flowing helium. The lines are drawn to highlight trends in the data. Legend: ⊟ / ▨) Conversion; ⊕ / ◉) Selectivity to acetone

3.4.5 Catalytic behaviour of K-Na-Y samples

3.4.5.1 Conversion and selectivity to acetone

Zeolite Y samples were ion exchanged in different ways, in order to explore influence of the preparation of the zeolite on catalytic behaviour in the IPA decomposition reaction. Conversion profiles for the IPA decomposition are shown in Figure 3.4-14. Selectivity profiles are shown in Figure 3.4-15. For the sake of convenience, ion exchange conditions used in the preparation of these samples (*vide* Table 3.2-3) are given again here.

Table 3.4-2: Excerpt from Table 3.2-3 (vide §3.2.3.1). All exchanges were carried out at 343 K, in 250 ml water.

Sample[a]	Exchange solution	Wash
K(69)-Na(15)-Y	2 x 0.09 M KAc	-
K(70)-Na(0)-Y	3 x 0.09 M KAc	2 x H_2O
K(72)-Na(0)-Y	3 x 0.09 M KOH	2 x H_2O
K(78)-Na(1)-Y	3 x 0.09 M KAc	2 x H_2O
K(87)-Na(0)-Y	3 x 0.09 M KAc	2 x 0.02 M KOH

a) Numbers in brackets indicate ion exchange level (exchange %)

The conversion in the IPA reaction over K-Na-Y catalysts can be seen in Figure 3.4-14. As the ion exchange levels of these catalysts are roughly equal, the only difference between them is the preparation procedure. Clearly, highest conversions were achieved with the parent zeolite and a sample that was exchanged with acetate and washed twice after the exchange (sample K(70)-Na(0)-Y, vide Table 3.4-2).
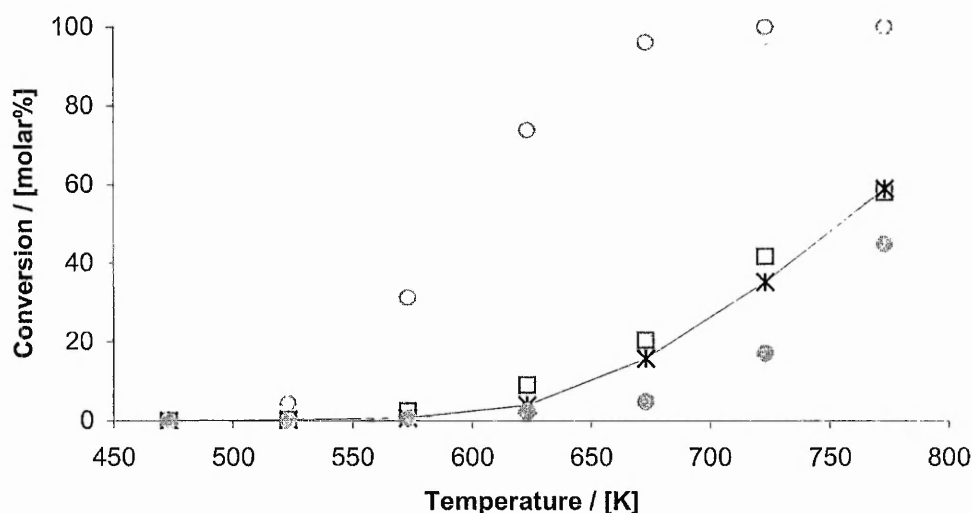
Figure 3.4-14: Isopropyl alcohol decomposition over K-Na-Y zeolites showing conversion versus temperature. Legend: ⊖) Na-Y (parent zeolite); ⊟) K(72)-Na(0)-Y;   ) K(70)-Na(0)-Y; ✳) K(87)-Na(0)-Y; ◉) K(69)-Na(15)-Y

By contrast, over the samples with highest conversions (vide Figure 3.4-14), no acetone was formed. A small amount of acetone was formed on K(72)-Na(0)-Y, which was a sample exchanged twice using a potassium hydroxide solution and was washed twice after the exchange (vide Table 3.4-2). The best selectivity to acetone was achieved over a catalyst that was exchanged using potassium acetate, and washed in dilute potassium hydroxide solution. At low temperatures acetone was not produced over any of these samples. A steep rise to high selectivity to acetone with respect to temperature was observed for K(87)-Y and K(69)-Na(15)-Y. Selectivity reached a maximum on K(87)-Y at 673 K, and increased no further with increasing temperature.

Apparently, washing K-Na-Y zeolite has a detrimental effect on selectivity to acetone, compared to either leaving the material unwashed, or washing with potassium hydroxide.
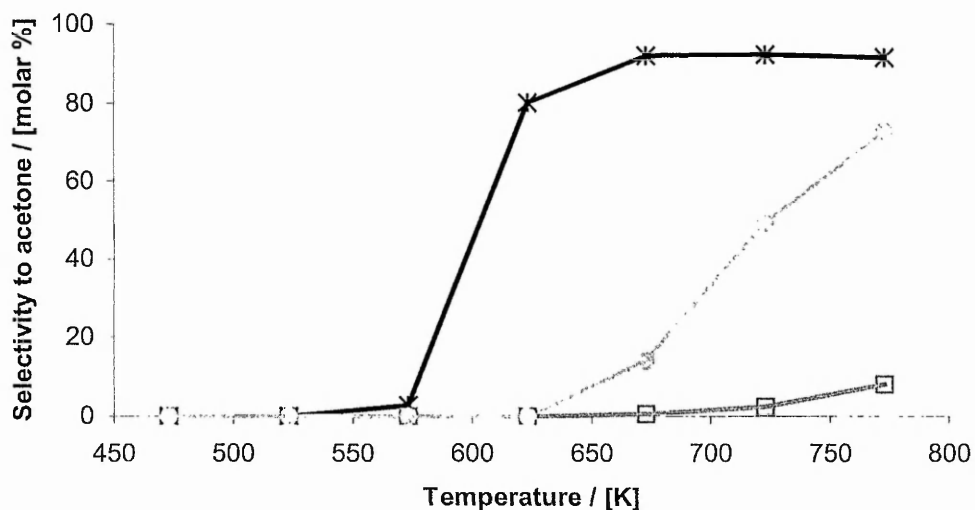
Figure 3.4-15: Isopropyl alcohol decomposition over K-Na-Y zeolites showing selectivity to acetone as a function of temperature. Legend: ⊟) K(72)-Na(0)-Y; ✳) K(87)-Na(0)-Y; ○) K(69)-Na(15)-Y. Two samples that were tested showed no detectable selectivity to acetone: Na-Y and K(70)-Na(0)-Y

3.4.5.2 Deactivation

In order to examine the deactivation of K-Na-Y samples during the isopropyl alcohol reaction, the reaction was monitored over a longer period of time, at a constant reactor temperature (*vide* Figure 3.4-16 and Figure 3.4-17).
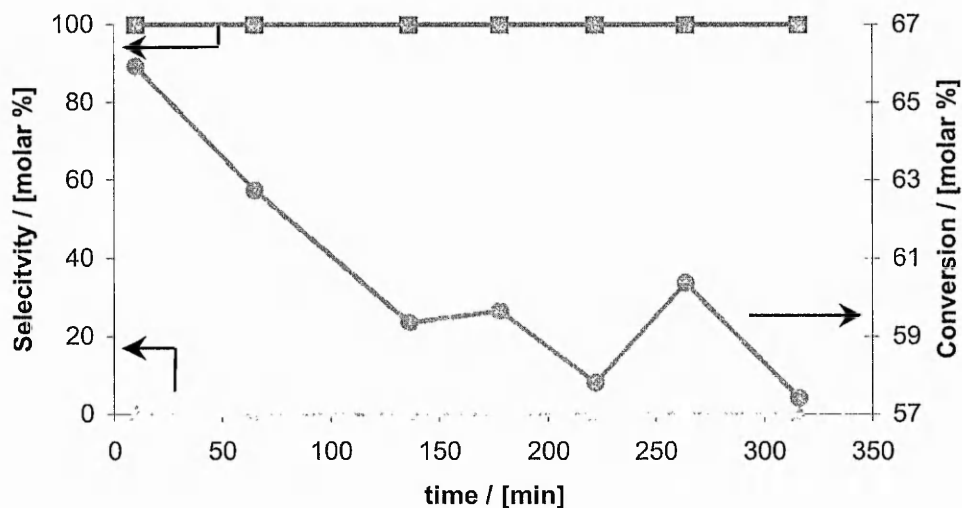
Figure 3.4-16: Reaction of isopropyl alcohol over K(70)-Y, showing conversion and selectivity as a function of time-on-stream. The reaction temperature was 623 K. Legend: ⊚) Conversion; ▦) Selectivity to propene; ⚛) Selectivity to acetone

As can be seen, some deactivation was observed over the K-Na-Y catalysts. Whereas the product distribution remained unchanged for K(70)-Y over the time interval measured (Figure 3.4-16), on K(87)-Y a clear trend was seen with increasing reaction time in favour of selectivity to propene (Figure 3.4-17).
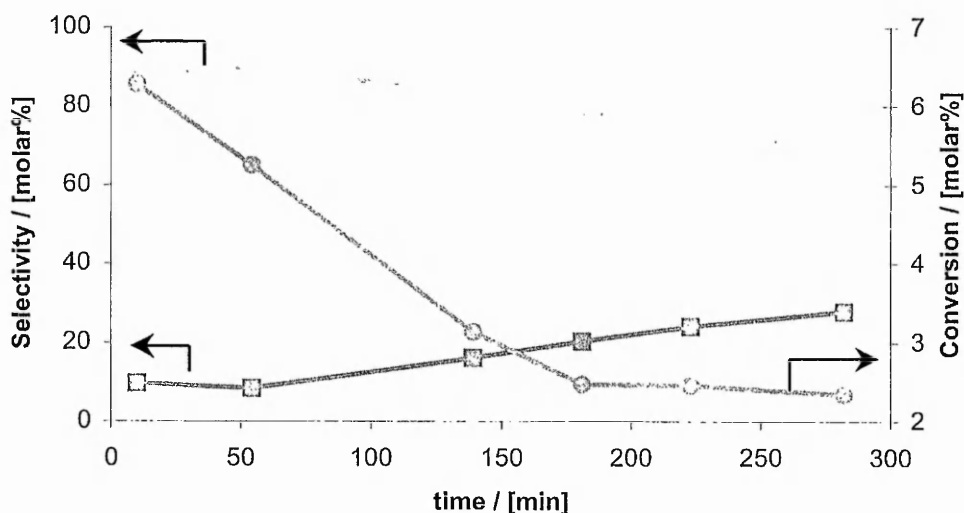
Figure 3.4-17: Reaction of isopropyl alcohol over K(87)-Y, showing conversion and selectivity as a function of time-on-stream. The reaction temperature was 623 K. Legend: ◯) Conversion; ▣) Selectivity to propene; ◬) Selectivity to acetone

3.4.5.3 Effect of activation temperature

K-Na-Y samples were activated at 773 K and 973 K and subsequently studied in the IPA reaction. The activation temperature had no significant effect on acetone yields for Na-Y, K(70)-Na(0)-Y, K(87)-Na(0)-Y, and K(69)-Na(15)-Y. The effect of activation temperature on acetone conversion and selectivity for K(72)-Y can be seen in Figure 3.4-18. This sample had been exchanged with potassium hydroxide, and was not washed after the exchange. Conversion increased, whilst selectivity to acetone decreased when a higher activation temperature was used.
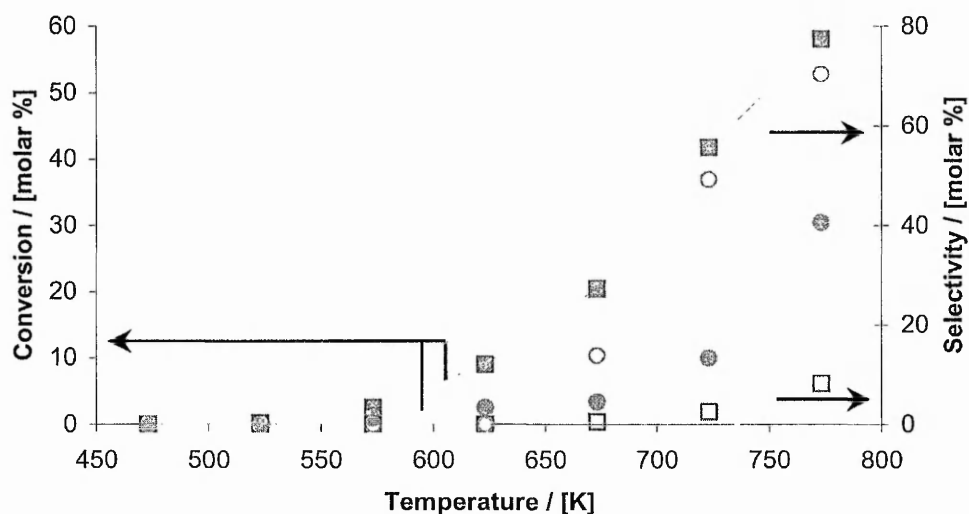
Figure 3.4-18: Isopropyl alcohol decomposition over K(72)-Y showing conversion (solid points) and selectivity to acetone (open points) as a function of reactor temperature. Legend: $\ominus$/$\oplus$) Activation temperature = 773 K; $\boxminus$/$\blacksquare$) Activation temperature = 973 K

3.4.6 Catalytic behaviour of Pb-Na-Y samples

Two Pb-Na-Y samples were prepared using ion exchange with lead(II) acetate. The samples were not washed after the exchange. The quantities of lead were calculated to give 50 and 100 exchange percent in the end product; lead contents were not determined by atomic adsorption for these samples. They will be referred to as Pb(~50)-Na(~50)-Y and Pb(~100)-Y. The catalysts were activated in flowing helium for 4 h at 773 K. It became clear that selectivity to acetone over these samples was negligible. Reaction data can be seen in Figure 3.4-19 and Figure 3.4-20, which show conversion and selectivity respectively.
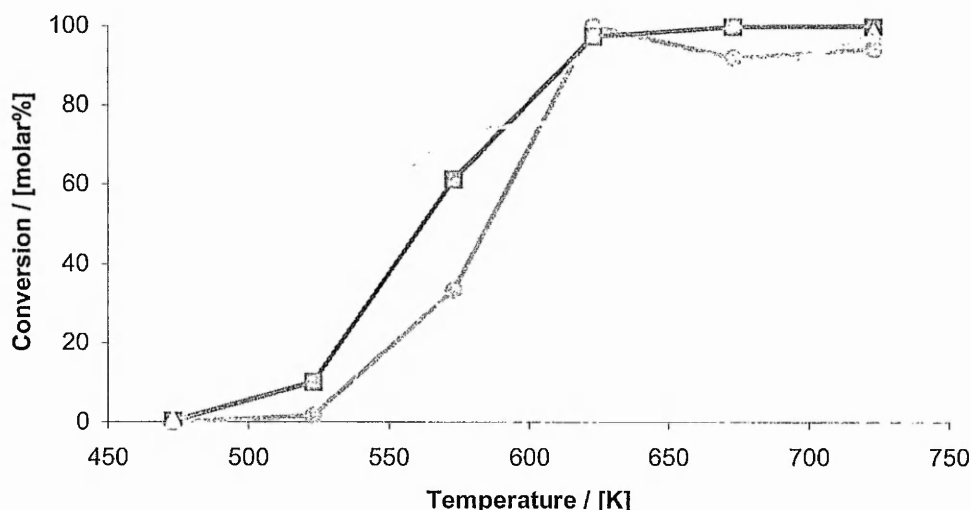
Figure 3.4-19: Isopropyl alcohol decomposition over Pb-Na-X zeolites showing conversion as a function of reactor temperature. Legend: ◌) Na-Y (parent zeolite); ▣) Pb(~50)-Na(~50)-Y; Pb(~100)-Y.

As can be seen from Figure 3.4-19, the conversion pattern of lead-exchanged Y zeolites deviates somewhat from the parent Na-Y. Both exchanged zeolites show higher conversion at lower temperatures when compared to Na-Y. The selectivity to acetone can be seen in Figure 3.4-20. Very little acetone is produced. Pb(~50)-Na(~50)-Y displays better selectivity to acetone at 523 K, whereas Pb(~100)-Y shows better selectivity above 623 K.
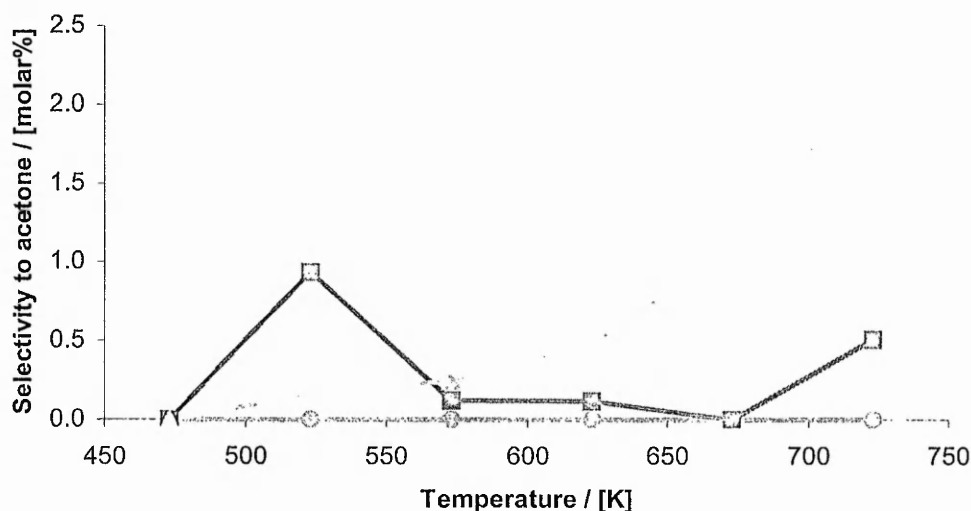
Figure 3.4-20: Isopropyl alcohol decomposition over Pb-Na-X zeolites showing selectivity to acetone as a function of reactor temperature. Legend: ◌) Na-Y (parent zeolite); ▢) Pb(~50)-Na(~50)-Y; ▸ Pb(~100)-Y.

3.4.7 Catalytic behaviour of Pb-H-Beta samples

Zeolite Beta samples were activated at 723 K for 8h in flowing helium, and reacted with IPA. In Figure 3.4-21 and Figure 3.4-22, conversion and selectivity to acetone are shown, respectively.
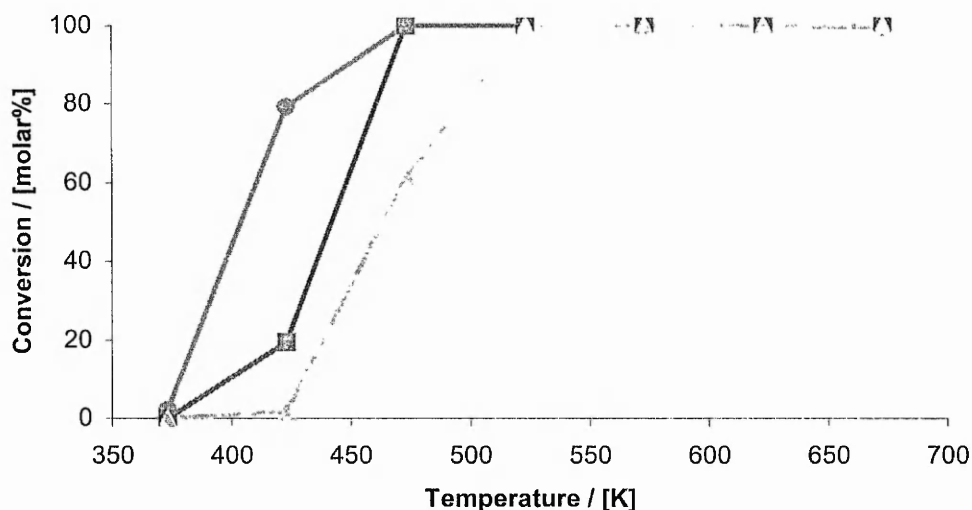
Figure 3.4-21: Isopropyl alcohol decomposition over Pb-H-Beta zeolites showing conversion as a function of temperature. Legend: ⊚) H-Beta (parent zeolite); ▣) Pb(85)-H(15)-Beta; ⊿ Pb(219)-Beta.

As is apparent from Figure 3.4-21 H-Beta converts more isopropyl alcohol at lower temperatures (< 473 K). At temperatures above 523 K all catalysts convert all of the isopropanol reacted.

As is clear from Figure 3.4-22, hardly any acetone is produced. These beta catalysts therefore display acidic behaviour in the IPA reaction.
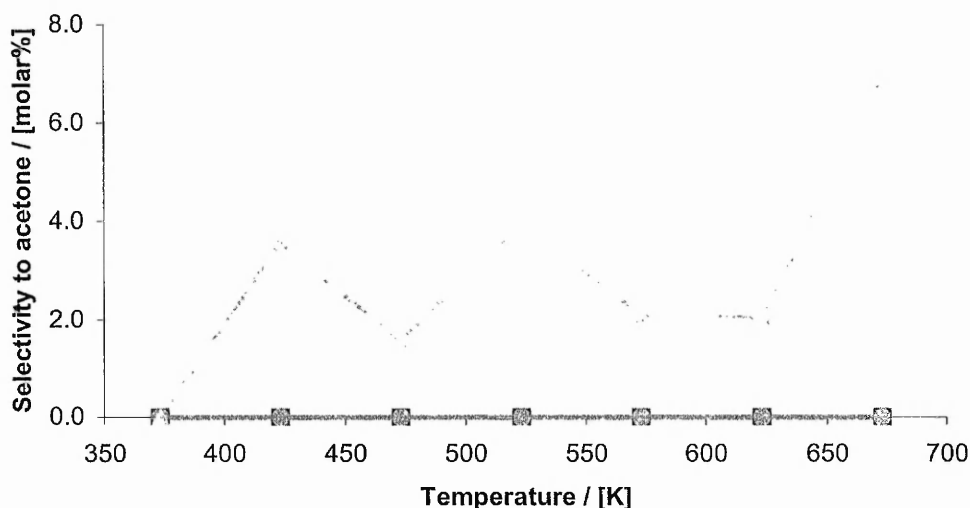
Figure 3.4-22: Isopropyl alcohol decomposition over Pb-H-Beta zeolites showing selectivity to acetone as a function of temperature. Legend: ◉) H-Beta (parent zeolite); ▥) Pb(85)-H(15)-Beta; ▲ Pb(219)-Beta.

3.4.8 Discussion and conclusions

It was possible to produce acetone over some of the ion-exchanged zeolites prepared for this work. This is indicative for the presence of basic sites if the interpretation found commonly in literature is correct, namely that acetone production in the IPA reaction can indeed be viewed as evidence for basic sites in a zeolite [2, 60, 62].

For traditional basic zeolites, such as K-Na-Y, dehydrogenation activity to give acetone has been reported previously [2, 61]. With K-Na-Y samples it was shown here, that washing with water after the ion exchange procedure has a negative influence on the catalysts' ability to yield acetone. Possibly, water washing caused acidic protons to remain in the zeolite cavities. After activation these protons were active in the IPA reaction, leading to dehydration of IPA.

For lead-containing faujasites, less information is available concerning activity in base catalysed reactions. Some evidence for activity in the oxidative conversion

of methane is available, which can be considered to be base catalysed [7]. However, this reaction is often thought to occur by a radical mechanism [64, 65]. To solely rely on the oxidative coupling of methane as evidence for zeolite basicity [6-8] seems not tenable. It should further be noted that catalysts used in the oxidative coupling of methane [7] were activated at 1123 K, whilst the reaction was carried out at 973 K. Evidence in literature exists that decomposition of the parent material, Na-X, starts from about 1123 K [66]. Evidence is also available that introduction of lead is not beneficial to the stability of X zeolite at higher temperatures. Decomposition of lead(II) species was reported to start from 973 K onward, culminating in the existence of metallic lead [1]. From this work it is also clear that increasing amounts of lead in an X zeolite led to existence of a Pb^0 phase after activation at 973 K or above (*vide* §3.3.3).

The IPA reaction however, provides better quality evidence that some basic sites are present in Pb-Na-X. A trend of increased selectivity towards acetone with decreasing lead loading was observed, which is a trend also noted in oxidative conversion of methane experiments [8]. A reason for this might be the following: as lead loading increases, so does the occupancy of the zeolite cages. Accessibility of basic sites to the reactant is then the limiting factor any reaction to occur. The acidic reaction was nevertheless seen to proceed, which might indicate that the material deposited in the zeolite cages (possibly clusters of lead hydroxide) was either active in the dehydration of isopropyl alcohol to give propene, or inactive altogether.

For the lead exchanged zeolite X samples, the best acetone yield was seen at 723 K with a catalyst loaded with ~4wt% lead. Activation at 973 K instead of 773 K led to an unchanged or improved catalyst when the lead loading was low – intermediate (≤ 17wt%), whereas when lead loading was high (≥ 24wt%) raising the activation temperature was detrimental for catalysis. It might be argued that at lower activation temperatures some water or carbon dioxide remains adsorbed on the basic sites catalyst, resulting is poorer ability for isopropyl alcohol to adsorb and subsequently react. With the high-loaded catalysts it is likely that the thermal stability of the zeolite is decreased, leading to poorer results for catalysis.

The mechanism of isopropyl alcohol dehydrogenation is not without ambiguity though [67]. It has been argued, that a redox mechanism lies at the foundation of acetone formation. Evidence used in that work [67] was the inability to form acetone in the IPA reaction over magnesium oxide, whereas zinc oxide did act as a dehydrogenation catalyst in the IPA reaction. However, this reaction was performed at a low temperature (483 K) only, which does not provide a sound basis on which to discount a base catalysed mechanism in the IPA reaction. Ample evidence on various basic oxides points in a direction of a base catalysed mechanism [68, 69].

Concluding, it can be stated that the dehydrogenation of isopropyl alcohol, seen to proceed over Pb-Na-X, K-Na-X and K-Na-Y samples, is a strong indication, but not exclusive evidence for the presence of basic sites. Further evidence must follow from other experiments, such as adsorption of probe molecules.

3.5 Zeolite basicity: carbon dioxide adsorption

3.5.1 Abstract

Other researchers have employed carbon dioxide adsorption to investigate basicity of solids. Carbonate formation upon adsorption is seen as the main indication for the presence of basic sites. In order of decreasing basic site strength, the following carbonate species were identified in literature: unidentate, bidentate and bridged. Carbon dioxide was also adsorbed on zeolite X and Y catalysts used in this work. Some spectra of carbon dioxide adsorption on Na-X were different to the ones found in literature, although no uniformity exists. Experimental conditions, such as activation temperature and presence of water are thought to be the cause of this variation.

Normalising infrared spectra to wafer thickness of the samples used is needed in order to quantify adsorption studies. Problems arose with normalisation

however with lead exchanged X zeolites, as an additional peak was found on top of the Si-O overtones, which are normally used for this purpose.

Carbon dioxide adsorption on zeolites led to features in the infrared spectrum between 3800 and 1300 cm^{-1}. Band positions were assigned according to data available from literature. Upon adsorption, small peaks arose in the 3800 – 3000 cm^{-1} region on Pb-Na-X which were ascribed to surface hydroxyl species. It was speculated that these hydroxyl peaks appeared as a results of the formation of carbonate species on the same sites where residual water was adsorbed. Thus, carbon dioxide replaced the water, which subsequently re-adsorbed elsewhere on the zeolite. Weakly adsorbed carbon dioxide was found around 2350 cm^{-1}. Several peaks were found in the carbonate region (1800 – 1300 cm^{-1}).

The amount of carbon dioxide adsorbed decreased with increasing lead loading.

Thermal desorption experiments of carbon dioxide shows that the bulk of the carbonate species disappeared from Pb-Na-X samples below 600 K, although some carbonate species on lead exchanged X zeolites remained adsorbed at higher temperatures. Generally, the bulk of adsorbed carbon dioxide species desorbs at lower temperatures with increasing lead content of Pb-Na-X samples.

On a K-Na-X and a Cs-Na-X sample a similar pattern could be seen as was observed on Pb-Na-X samples. On K-Na-Y samples, no adsorption features could be distinguished in the carbonate region on adsorption of carbon dioxide.

The presence of surface adsorbed water during carbon dioxide adsorption experiments on Pb-Na-X samples cannot be excluded. This was concluded from differences between experiments with X zeolites activated at 973 K and at 773 K. Adsorbed water did not impede carbonate formation on Pb-Na-X.

3.5.2 Background

In chapter 1 of this work, the usage of carbon dioxide adsorption for assessment of basicity in zeolite catalysts has been discussed. Classification of adsorbed species with respect to basic strength can be found in the literature [2, 70, 71] and was discussed in §1.3.5. A commonly held view is that carbon dioxide on basic solids is found as adsorbed carbonates. Thus, the presence of carbonates was seen as indicative of basic sites. Further, carbonate desorption temperatures were used as a measure for assessment of basicity [2, 70, 72]. A higher desorption temperature was thought to correspond to a stronger basic site. Results of desorption experiments have lead to the classification of basic sites. Basicity decreases in the following order: unidentate > bidentate > bridged [70].

In a review of probe molecule adsorption, Lavalley concluded that the integral intensity of the carbonate region of (normalised) FTIR spectra could be used as a measure for basicity of a solid [70]. In a study of carbon dioxide adsorption on various supported caesium oxide catalysts, Sivasanker used the integral intensity of the entire carbonate region, which he took from $1200 - 1700$ cm^{-1}, as a measure for basicity [72]. In a study by Jentoft *et al.* on carbon dioxide adsorbed onto caesium exchanged zeolite X and Y samples [62], the authors quoted a kinetic diameter for carbon dioxide of 3.3 Å, whereas the diameter of a six-ring opening of a sodalite cage measures only 2.2 Å [17]. Thus, they concluded that carbon dioxide cannot enter the sodalite cage, and interactions with cations could only have taken place within the supercages of the zeolite.

Jacobs, who investigated carbon dioxide adsorbed on Ca-Na-X samples by infrared spectroscopy, observed an asymmetric stretch band (identified as ν_3) at 2360 cm^{-1} [73, 74]. This band could be associated with cation dipole interactions [70]. A satellite peak at ~2290 cm^{-1} was observed together with this ν_3 peak. Martra *et al.* who have adsorbed carbon dioxide on Na-X and Ba-X, concluded from their studies that the satellite peak belongs to the ν_3 band of $^{13}CO_2$ [75]. Jentoft *et al.* found the carbon dioxide ν_3 vibration at 2354 cm^{-1} for Na-Y and 2343 cm^{-1} for Cs-Y [62]. In a Cs-Na-X sample (~50 exchange %),

they found a band at 2342 cm^{-1}, which was also found by Jacobs on a similar sample [74]. For a rubidium exchanged Na-X zeolite (66 exchange % Rb$^+$) Jacobs found a band at 2347 cm^{-1} [74]. Martra observed a band at 2360 cm^{-1} on a Ba-Na-X zeolite (53 exchange % Ba^{2+}) [75], whereas Jacobs found a band at 2365 cm^{-1} for a Ca-Na-X zeolite (37 exchange % Ca^{2+}) [74]. According to Jacobs, increasing cation size leads to a shift of the ν_3 band at 2354 cm^{-1} to lower wavenumbers [73]. On the other hand, Martra *et al.* observed a shift of the ν_3 band to higher wavenumbers as they exchanged Na$^+$ in favour of Ba^{2+} in Na-X, which they attribute to an increase in strength of the positive field around the cation adsorption sites [75].

In the carbonate region, many examples exist of peak identification of adsorbed carbon dioxide species on *e.g.* Na-X and on metal oxides [59, 62, 70, 71, 73-75]. In a study on carbon dioxide adsorbed on X zeolites, Jacobs proposed structures for two band-pairs: one at 1705 and 1365 cm^{-1}, assigned to a bidentate carbonate, and one at 1470 and 1425 cm^{-1}, assigned to a carboxylate structure adsorbed on Na$^+$ [74]. Jentoft *et al.* identified a carbonate species on Cs-Na-X that exhibited bands at 1650 and 1385 cm^{-1} [62]. Interestingly, Martra *et al.* did not comment on the appearance of the bands observed at ~1650 cm^{-1} during carbon dioxide adsorption studies of X and Y zeolites, however, a weak band was visible at ~1650 cm^{-1} on their spectrum of carbon dioxide adsorbed on Na-X. They found no bands in the 1610 – 1630 region [75]. Some literature found on the FTIR monitored adsorption of carbon dioxide on Na-X is summarised in Table 3.5-1.

Table 3.5-1: Literature data for carbon dioxide adsorption on Na-X zeolites. Bands in the carbonate region of the infrared spectrum of adsorbed carbon dioxide.

Ref	Activation[a]	CO_2 ads.[b]	Carbonate peaks
[59]	773 K; (4 K min^{-1}); 10 h, He	373 K; He:CO_2 = 1:1, 1 atm	1710, 1657, 1620, 1591, 1565, 1484, 1430, 1365
[75]	623 K; (1 K min^{-1}); 1 h, vacuum	RT; CO_2; 1.33 10^3 - 2.66 10^3 Pa	1710, (1650), 1485, 1430, 1360
[76]	648 K; (n.g.); 5 h, He	RT; 14 ppm CO_2 in He; 1 atm total pressure	~1710, 1687, 1621, 1560, ~1480, ~1430, 1360
		RT; 3.73% CO_2 in He; 1 atm total pressure	1687, 1644, 1362
		RT; 658 ppm H_2O, 149 ppm CO_2 in He; 1atm total pressure	~1687, 1638, 1359
[77]	873 K; (n.g.); n.g., vac	RT; CO_2; 0.5 mbar	1712, 1365
[74]	673 K; (3 K min^{-1}); 2 h, vac	285 K; CO_2; 0 – 132 mbar	1700, 1485, 1425, 1365

a) Recorded as: final temperature (heating rate), time at final temperature, atmosphere. "N.G." denotes "not given"

b) Recorded as: adsorption temperature; adsorption gas composition; adsorption pressure

3.5.3 Normalisation of infrared spectra

A word on normalisation of adsorption spectra is perhaps appropriate at this point. Comparison of FTIR spectra of different zeolite samples is possible in a quantitative manner if these spectra are normalised to the amount of sample irradiated by the infrared beam [78]. As with any absorption technique, the relation between transmitted intensity and sample thickness is given by the Lambert-Beer law [79] (*vide* §2.4.1.1). Since all infrared absorption features are attenuated to the same law, normalisation to sample thickness can be done by taking peak areas of structure related bands. Commonly, three bands in the region of 1560 – 2074 cm^{-1} are used to this end. These correspond to Si-O overtone vibrations [78].

The situation for the lead exchanged samples used in this work is complicated by the absorption of infrared light by the acetate precursor in the same region as the Si-O overtones. In Figure 3.5-1, four "snapshots" of the activation *in vacuo* of two zeolite samples can be seen: before activation, at 473 K, 773 K and 973 K. The peaks in the spectra of the zeolites in Figure 3.5-1 at 1641 and 1651 cm^{-1} can be attributed to adsorbed water. When the sample was heated, these decreased. The peak at 1670 cm^{-1} (in the case of Na-X) remained

constant in size, even though temperature was raised to 773 K, whereas the peak at 1586 cm-1 decreased slightly until 773 K. Thus, the peak at 1670 cm^{-1} might be attributed to a zeolite Si-O overtone vibration, whereas the peak at 1586 cm^{-1} probably belongs to adsorbed water. For the lead containing sample, it would appear that the water band at 1586 cm^{-1} and the overtone band at 1670 cm^{-1} seem to have shifted towards each other. This further complicates analysis of the overtone bands.

In principle, lead(II) acetate should start to melt and subsequently decompose from 553 K [20]. The band at 1564 cm^{-1} in the spectrum of Pb(63)-Na(27)-X (Figure 3.5-1–I) might be attributed as belonging to lead(II) acetate. Next to this band, adsorbed carbon dioxide was present. Bands at 1710, 1478 and 1424 could be attributed to carbonate species (*vide* §3.5.4). These disappear completely only at 973 K. When samples were activated in vacuum, carbonate bands disappeared as well after 120 minutes at 773 K (spectra not shown). It was assumed that no bands associated with lead(II) acetate remained at this temperature.

The approach used for normalisation was based on the integration of the overtone region (between ~1460 and ~1800 cm^{-1}) of the infrared spectra, obtained at 773 K during activation of the sample. To this end, graphical processing software [80] was used. The area obtained was taken as a measure for wafer thickness.
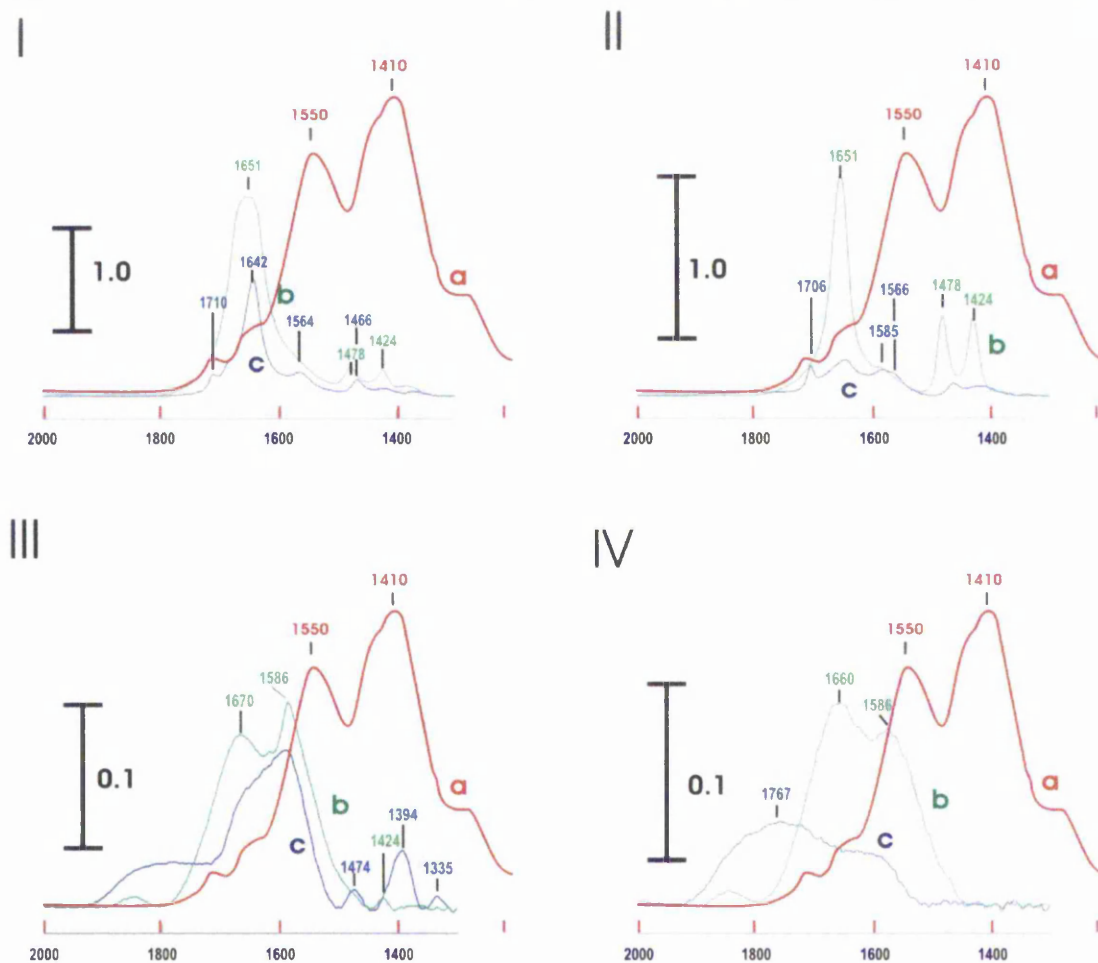
Figure 3.5-1: Activation of zeolite X samples in vacuum, showing the extended Si-O overtone region: before activation (I), then at 473 K (II), at 773 K (III) and at 973 K (IV). Legend: a) $Pb(Ac)_4$ [81]; b) Na-X (parent zeolite); c) Pb(63)-Na(27)-X (24.1wt% Pb). The vertical in each spectrum represents the absorption scale / [a.u.]. Verticals apply only to the zeolite spectra. The horizontal scale represents wavenumbers / cm^{-1}.

In the following, each catalyst was given the following treatment (in the order listed) unless otherwise noted:

1) Activation at 773 K (10 K min⁻¹) for 2 h in vacuum.
2) Ammonia adsorption at 423 K subsequently at:
    a) 10^{-3} mbar, 45 min
    b) 10^{-2} mbar, 30 min
    c) 10^{-1} mbar, 30 min
    d) 10^0 mbar, 30 min
3) Evacuation of the cell: 15 minutes on a rotary pump followed by 15 minutes on a turbo-molecular pump.

3.5.4 Adsorption of carbon dioxide on Pb-Na-X zeolites

Adsorption experiments on Pb-Na-X samples showed that carbon dioxide adsorbed on cations (*vide* Figure 3.5-2), on OH groups (*vide* Figure 3.5-8 and Figure 3.5-13 – Figure 3.5-14) and as (pseudo-)carbonates (Figure 3.5-4 – Figure 3.5-7 and Figure 3.5-9 – Figure 3.5-12), giving rise to different features in the infrared spectrum.

The peak observed at ~2354 cm^{-1} on X zeolites can be identified as carbon dioxide adsorbed on Na^+ cations. Following the reasoning by authors mentioned above (*vide* §3.5.2), the peak observed at ~2345 cm^{-1} would be associated with carbon dioxide adsorbed on Pb^{2+}.
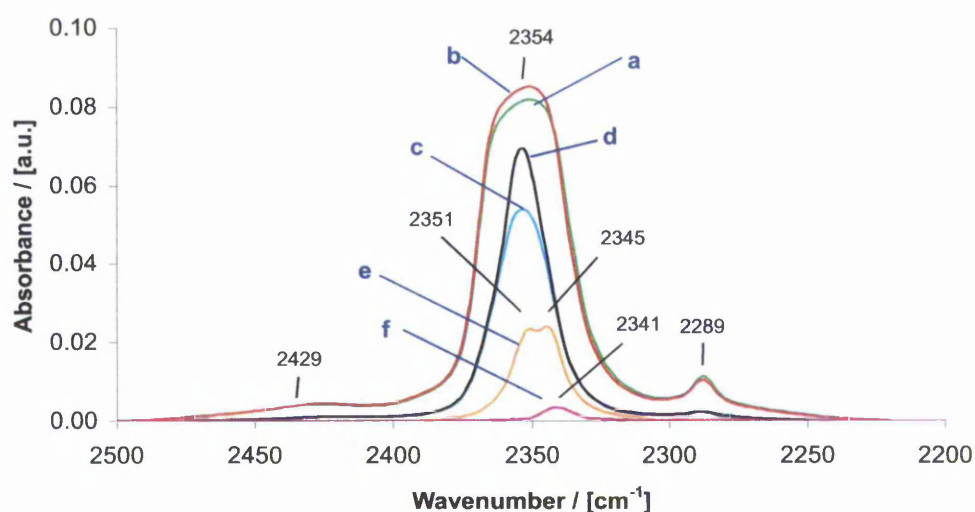
Figure 3.5-2: Normalised FTIR spectra of the adsorption of CO_2 at 1 mbar, showing the peaks associated with linearly adsorbed CO_2. All spectra shown are difference spectra with respect to the activated catalyst. Legend: a) Na-X (parent zeolite); b) Pb(9)-Na(96)-X; c) Pb(34)-Na(76)-X; d) Pb(43)-Na(61)-X; e) Pb(63)-Na(27)-X; f) Pb(131)-X

Adsorption of carbon dioxide on lead containing zeolites gave rise to peaks in the carbonate region as well. From normalised infrared spectra of adsorbed carbon dioxide (*vide* Figure 3.5-4 and Figure 3.5-5) it appears that the amount of adsorbed carbon dioxide decreased with increasing lead loading. When lead loading increased beyond 3.8 wt%, the spectrum changed quite dramatically. Most of the carbonate bands seemed to disappear, whilst a band at 1575 cm^{-1}

appeared, as well as a band at 1316 cm^{-1}. For the sample with the highest lead loading (42wt%), no normalisation could be achieved, because overtone peaks could not clearly be distinguished from other absorptions in that region. Possibly, decomposition of all of the lead(II) acetate was not completed at 773 K. Very little carbon dioxide adsorbed on this sample. It is left out in Figure 3.5-5.

The band assignment used in this work is pictured in Figure 3.5-3.
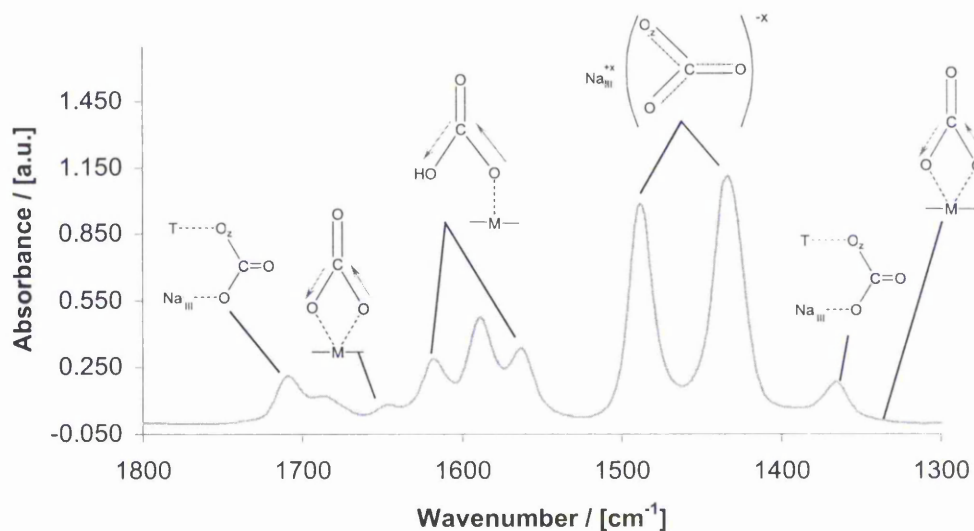
Figure 3.5-3: FTIR spectrum (not normalised) of the carbonate region, showing adsorbed carbon dioxide on Na-X after evacuation of the cell. The depicted spectrum shows the difference with respect to the activated ("clean") catalyst. Identification followed the work of Jacobs [73, 74] who adsorbed carbon dioxide on Na-X and of Di Cosimo *et al.*, who adsorbed carbon dioxide on magnesium oxide [71].
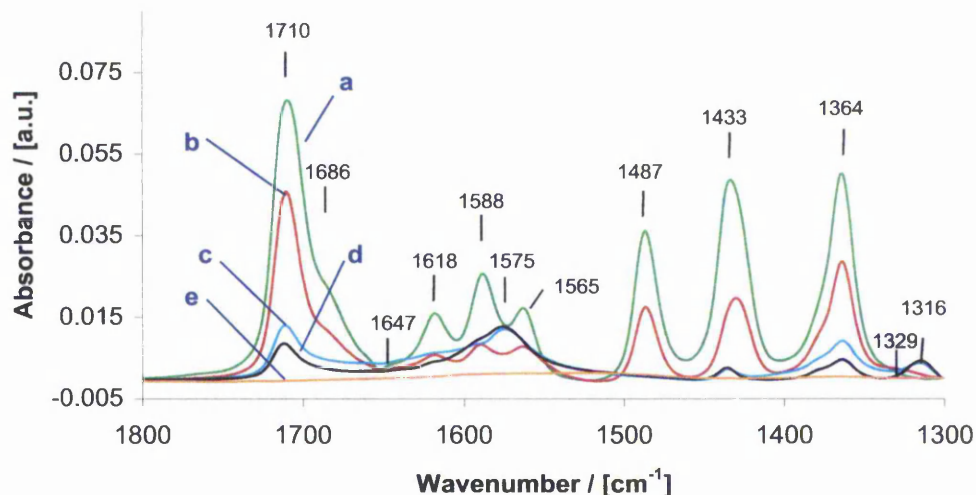
Figure 3.5-4: Normalised FTIR spectra of the carbonate region, showing adsorbed carbon dioxide at 1 mbar total pressure. All spectra shown are difference spectra with respect to the activated catalyst. Legend: a) Na-X (parent zeolite); b) Pb(9)-Na(96)-X; c) Pb(34)-Na(76)-X; d) Pb(43)-Na(61)-X; e) Pb(63)-Na(27)-X
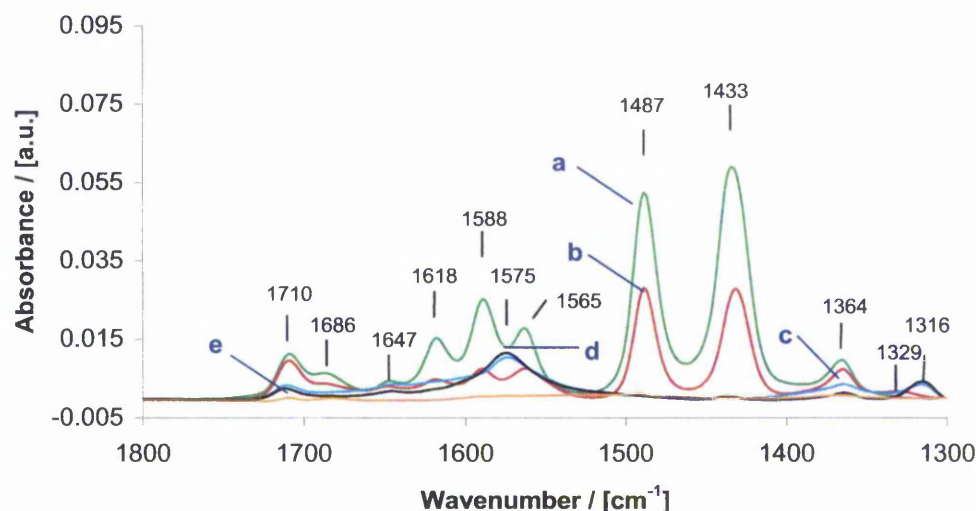
Figure 3.5-5: Normalised FTIR spectra of the carbonate region, showing results after evacuation of the cell. All spectra shown are difference spectra with respect to the activated catalyst. Legend: a) Na-X (parent zeolite); b) Pb(9)-Na(96)-X; c) Pb(34)-Na(76)-X; d) Pb(43)-Na(61)-X; e) Pb(63)-Na(27)-X

When the normalised peak area of the carbonate region (1300 – 1750 cm^{-1}) are plotted as a function of Pb loading, the following graph is produced:
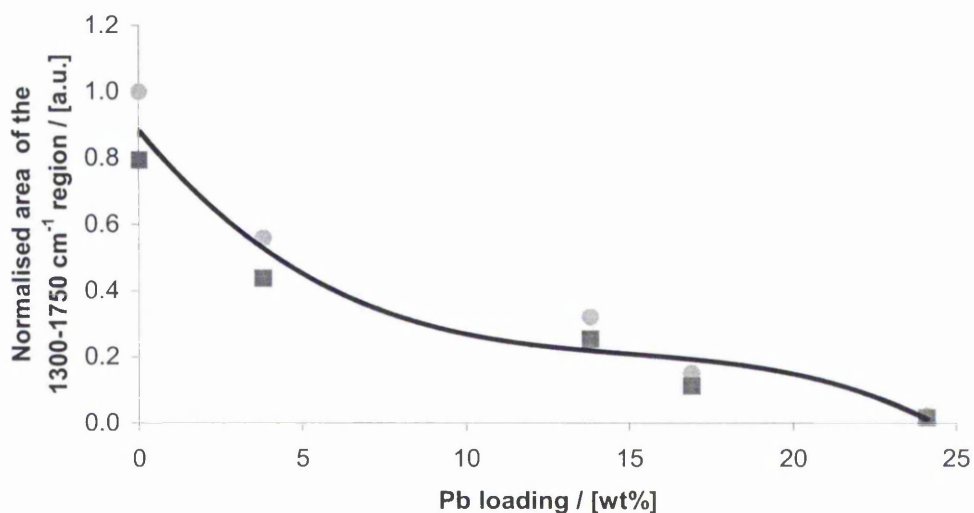
Figure 3.5-6: Normalised integral intensity of the carbonate region (1750 – 1300 cm⁻¹) in FTIR spectra of adsorbed carbon dioxide versus lead loading. Legend: ●) Carbon dioxide pressure in the cell of 1 mbar; ■) After evacuation of the sample cell for 30 min (residual pressure ~10⁻⁶ mbar). The line is drawn only to highlight a trend in the data.

Not all of the adsorbed carbonate species could be removed by evacuation of the cell alone. Samples were heated in order to remove chemisorbed species. The total intensity in the carbonate region (arbitrarily chosen here as 1300 – 1750 cm⁻¹) versus temperature can be seen in Figure 3.5-7. From this graph, it becomes clear that the desorption temperature (taken as the point in the desorption thermogram where no further change occurs) decreases as lead loading increases.
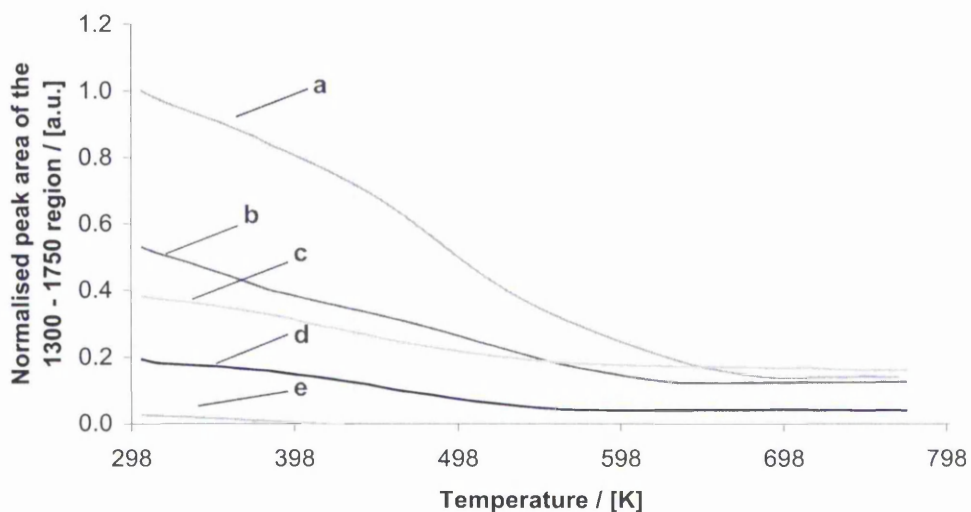
Figure 3.5-7: Normalised total peak area in the carbonate region (1300-1750 cm^{-1}) versus temperature during thermal desorption. Legend: a) Na-X (parent zeolite); b) Pb(9)-Na(96)-X;) Pb(34)-Na(76)-X; d) Pb(43)-Na(61)-X; e) Pb(63)-Na(27)-X

Desorption behaviour of individual bands belonging to various carbonate species can be compared as well. Bands belonging to the same species can be expected to show the same behaviour as temperature is raised. Thus, band-pairs belonging to the same species were identified on Na-X and Pb(9)-Na(96)-X: one at 1710 and 1366 cm^{-1}, one at 1487 and 1432 cm^{-1} and a final one at 1617 and 1564 cm^{-1}. From a lead weight percentage of 13.8 and higher, different species were observed. The bands are summarised in Table 3.5-2.

Table 3.5-2: Desorption temperatures of bands having a similar desorption behaviour versus temperature. A point was chosen were no change in peak area could be observed as temperature increased. No clear identification of desorption species was possible on Pb(63)-Na(27)-X (Pb loading 24 wt%) due to the low amount of adsorbed carbon dioxide.

Sample	wt% Pb	Bands (Desorption temperature / [K])					
Na-X	0	1710/1364 (519)	1686 (416)	1650 (571)	1617/1564 (497)	1487/1432 (676)	
Pb(9)-Na(96)-X	3.8	1710/1364 (517)	1686 (516)	1650 (573)	1617/1564 (561)	1487/1432 (765)	
Pb(34)-Na(76)-X	13.8	1710/1364 (436)	1650 (576)	1575 (>773)	1510 (>773)	1436 (>773)	1316 (462)
Pb(43)-Na(61)-X	16.9	1710/1364 (533)	1650 (540)	1575 (>773)	1436 (>773)	1316 (534)	

a) Taken as the temperature, after which no change occurred in the integral intensity of the respective band.

Activation of lead loaded Na-X zeolites at a higher temperature (973 K rather than 773 K) was investigated in combination with carbon dioxide adsorption as well. Activation of Na-X at 773 K led to the disappearance of a sharp band at ~1650 cm^{-1}, a band which is associated with water adsorbed on Na-X [76]. Upon cooling down of the cell, a smaller band once again appeared at this wave number (spectra not shown). When the activation temperature was carried out at 973 K and subsequently cooled down to room temperature, no significant increase of a band at ~1650 cm^{-1} was seen. During carbon dioxide adsorption, which followed activation, in contrast to the four peaks observed in the 3700 – 3000 cm^{-1} with Pb(9)-Na(96)-X activated at 773 K, this catalyst showed only peaks at 3712 and 3637 cm^{-1} and no features at 3524 and 3424 cm^{-1} when activated at 973 K. At the same time, the effect of carbon dioxide adsorption on the broad feature at 3400 – 3000 cm^{-1} seemed less pronounced on the catalyst activated at 973 K compared to that of the catalyst activated at 773 K (*vide*

Figure 3.5-8 - Figure 3.5-12). Further, on Pb(9)-Na(96)-X (lead loading 3.8 wt%), with increasing temperature the significance of bands at around 1560 and 1329 cm^{-1} increased, whilst bands at 1588, 1618 and 1647 cm^{-1} were reduced. The same differences for high (973 K) and low (773 K) temperature activated catalysts were observed for the parent Na-X zeolite (spectra not shown). When lead loading was increased beyond 3.8 wt%, activation at 973 K did not yield any changes in the 3600 – 3000 cm^{-1} region that could be distinguished from background noise. In the carbonate region, less pronounced differences between a sample activated at 973 K and at 773 K were observed for catalysts with a higher lead loading (>3.8 wt%) (spectra not shown).
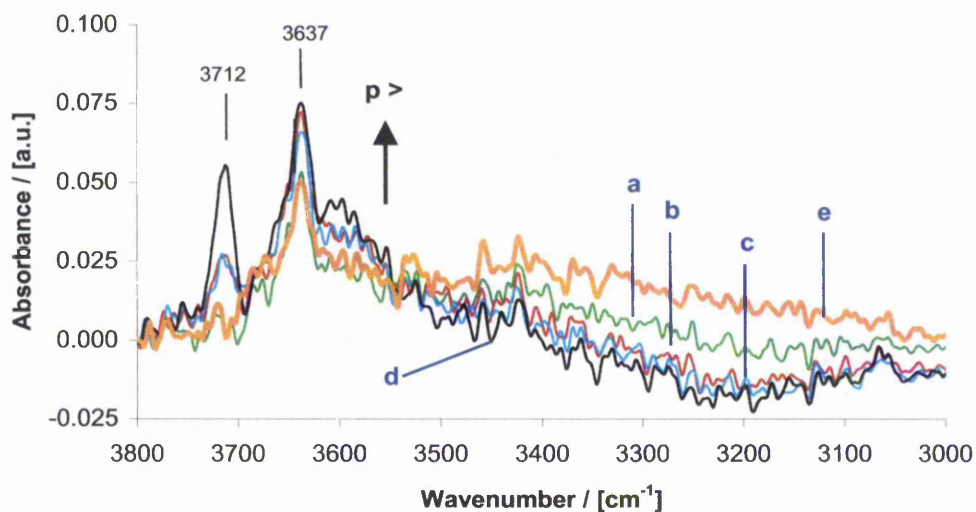
Figure 3.5-8: FTIR spectra of carbon dioxide adsorbed at different pressures on Pb(9)-Na(96)-X (activated at 973 K). All spectra shown are difference spectra with respect to the activated catalyst. Carbon dioxide pressure increased as shown by the arrow. Legend: a) 10^{-3} mbar; b) 10^{-2} mbar; c) 10^{-1} mbar; d) 10^{0} mbar; e) (thick line) evacuated cell.
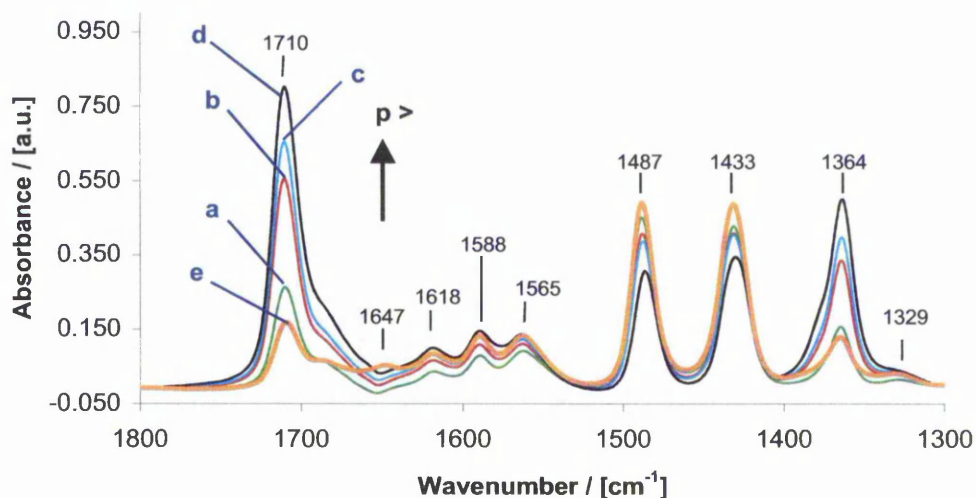
Figure 3.5-9: FTIR spectra of carbon dioxide adsorbed at different pressures on Pb(9)-Na(96)-X (activated at 773 K). All spectra shown are difference spectra with respect to the activated catalyst. Carbon dioxide pressure increased as shown by the arrow. Legend: a) 10^{-3} mbar; b) 10^{-2} mbar; c) 10^{-1} mbar; d) 10^{0} mbar; e) (thick line) evacuated cell.
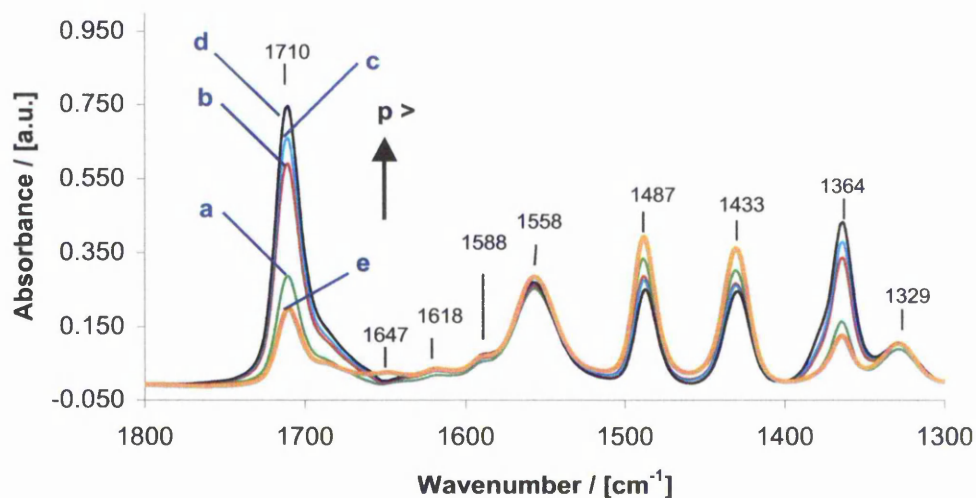
Figure 3.5-10: FTIR spectra of carbon dioxide adsorbed at different pressures on Pb(9)-Na(96)-X (activated at 973 K). All spectra shown are difference spectra with respect to the activated catalyst. Carbon dioxide pressure increased as shown by the arrow. Legend: a) 10^{-3} mbar; b) 10^{-2} mbar; c) 10^{-1} mbar; d) 10^{0} mbar; e) (thick line) evacuated cell.
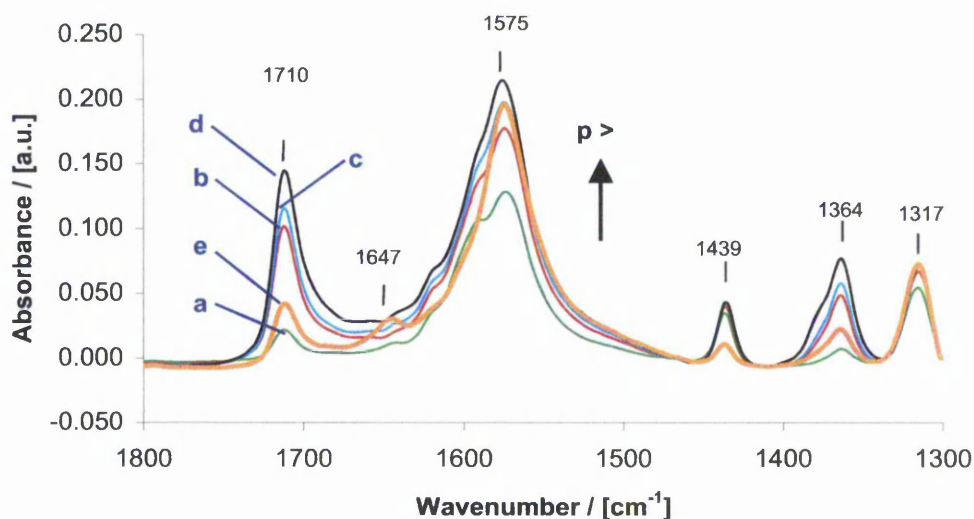
Figure 3.5-11: FTIR spectra of carbon dioxide adsorbed at different pressures on Pb(43)-Na(61)-X (activated at 773 K). All spectra shown are difference spectra with respect to the activated catalyst. Carbon dioxide pressure increased as shown by the arrow. Legend: a) 10^{-3} mbar; b) 10^{-2} mbar; c) 10^{-1} mbar; d) 10^{0} mbar; e) (thick line) evacuated cell.
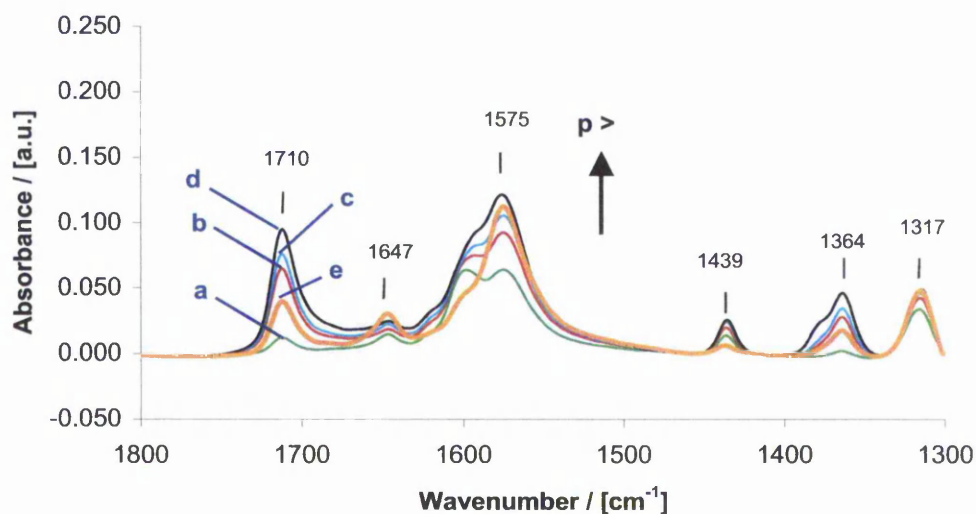
Figure 3.5-12: FTIR spectra of carbon dioxide adsorbed at different pressures on Pb(43)-Na(61)-X (activated at 973 K). All spectra shown are difference spectra with respect to the activated catalyst. Carbon dioxide pressure increased as shown by the arrow. Legend: a) 10^{-3} mbar; b) 10^{-2} mbar; c) 10^{-1} mbar; d) 10^{0} mbar; e) (thick line) evacuated cell.

In normalised spectra of adsorbed carbon dioxide on X zeolites, several features could be seen in the OH region. Adsorbing carbon dioxide led to the disappearance of peaks at 3690 and 3645 cm^{-1} that were seen after activation of Na-X in helium, and to a reduction of a broad feature between 3400 and 3000 cm^{-1}. Peaks further appeared at 3712 cm^{-1}, with a shoulder at 3733 cm^{-1}, 3637

cm^{-1} (shoulder at 3657 cm-1), 3595, 3524 and 3424 cm^{-1} (*vide* Figure 3.5-13 and Figure 3.5-14). Evacuation of the cell lead to the disappearance of all but four peaks: at 3693, 3640 (shoulder at 3665 cm^{-1}), 3524 and 3424 cm^{-1} (*vide* Figure 3.5-13). Increasing the amount of lead in zeolite Na-X led to a decrease of peak areas in the OH stretch region (*vide* Figure 3.5-14).
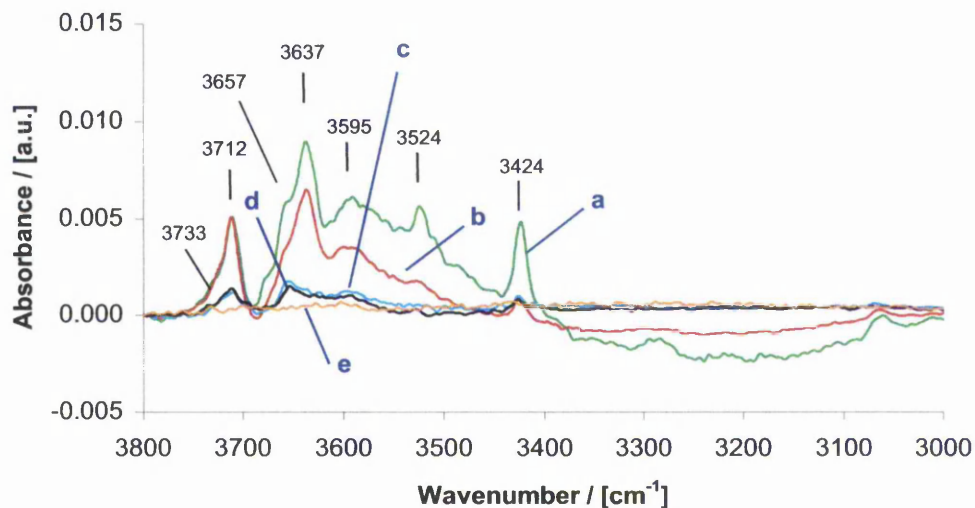
Figure 3.5-13: FTIR spectra of the adsorption of CO_2 at 1 mbar, showing peaks in the OH-region. All spectra shown are difference spectra with respect to the activated catalyst. Legend: a) Na-X (parent zeolite); b) Pb(9)-Na(96)-X; c) Pb(34)-Na(76)-X; d) Pb(43)-Na(61)-X; e) Pb(63)-Na(27)-X
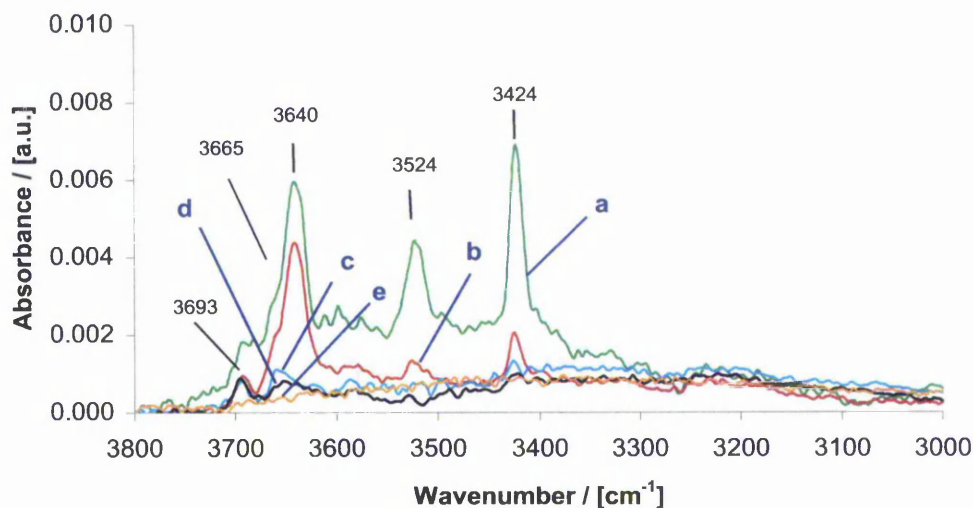
Figure 3.5-14: FTIR spectra of the adsorption of CO_2 after evacuation of the cell, showing peaks in the OH-region. All spectra shown are difference spectra with respect to the activated catalyst. Legend: a) Na-X (parent zeolite); b) Pb(9)-Na(96)-X; c) Pb(34)-Na(76)-X; d) Pb(43)-Na(61)-X; e) Pb(63)-Na(27)-X

3.5.5 Carbon dioxide adsorption on K-Na-X and Cs-Na-X

When carbon dioxide was adsorbed on K-Na-X and Cs-Na-X zeolites, bands could be seen in the ν_3 carbon dioxide region and the carbonate region. The spectra are given in Figure 3.5-15 – Figure 3.5-18). The ν_3 band of carbon dioxide was found at 2349 cm^{-1} for K-Na-X, and at 2344 cm^{-1} for Cs-Na-X. The $^{13}CO_2$ contributions at roughly 2282 cm^{-1} [73, 74] shifted to lower wavenumbers compared to Na-X; thus following the trend observed in the ν_3 band of $^{12}CO_2$.

In the carbonate region, several species could be observed. Though fairly similar to the spectrum recorded for carbon dioxide adsorbed on Na-X, a few key differences can be seen. Notably, contributions at 1487 and 1433 cm^{-1} were of far less significance on the K and Cs exchanged samples compared to the parent Na-X zeolite. It appears the peak seen at 1710 cm^{-1} on Na-X has shifted to ~1695 cm^{-1} on K-Na-X and to 1693 cm^{-1} on Cs-Na-X. This observation is in agreement with data from Garrone *et al.* who have adsorbed carbon dioxide on Cs-Na-X. They however, do not believe unambiguous conclusions regarding an increased basicity of a Cs-Na-X relative to Na-X can be deduced from this shift in band position [77].

Analysis of the desorption spectra was rather complicated for these samples. Overlapping peaks and peak shifts during desorption made distinction of separate peaks difficult. Thus, only rough estimates of desorption temperatures can be extracted from the desorption curves as drawn in Figure 3.5-16. In the next four figures, a thick line indicates the end point of an experiment.
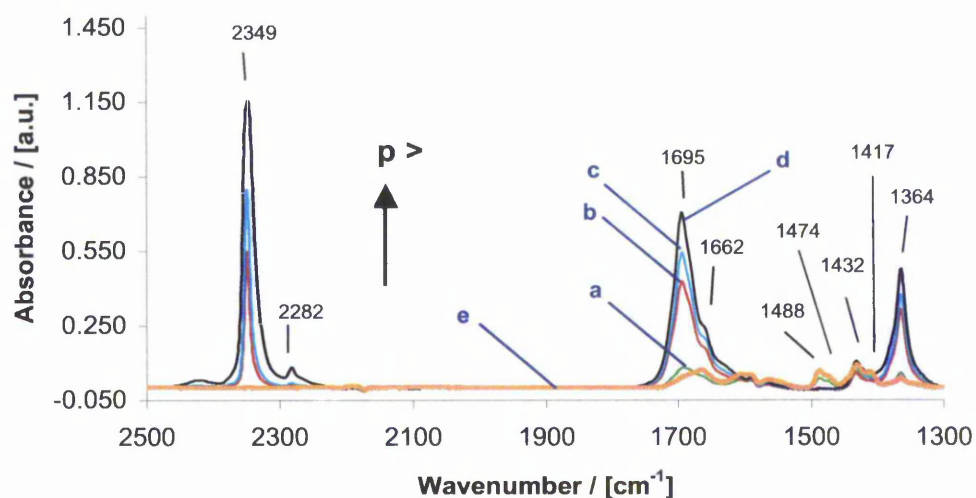
Figure 3.5-15: FTIR spectra of carbon dioxide adsorbed on K(27)-Na(67)-X, at different pressures. All spectra shown are difference spectra with respect to the activated catalyst. Carbon dioxide pressure increased as shown by the arrow. Legend: a) 10^{-3} mbar; b) 10^{-2} mbar; c) 10^{-1} mbar; d) 10^{0} mbar; e) (thick line) evacuated cell.
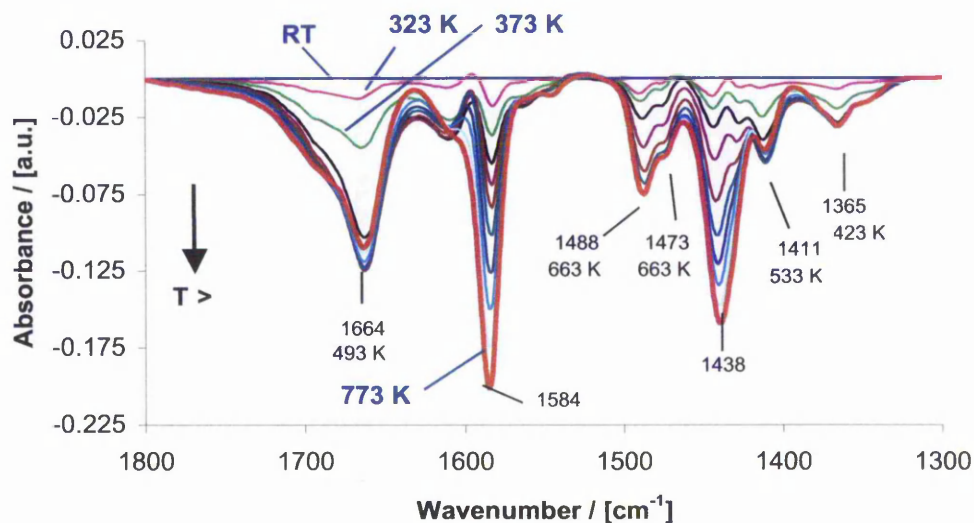
Figure 3.5-16: FTIR spectra of carbon dioxide desorption from K(27)-Na(67)-X, at 50 K increments. All spectra shown are difference spectra with respect to the last spectrum of the adsorption experiment. Temperatures shown are those where no further decrease was noted in the peak height. Temperature increased as shown by the arrow. Thick line indicates endpoint of the experiment (773 K).
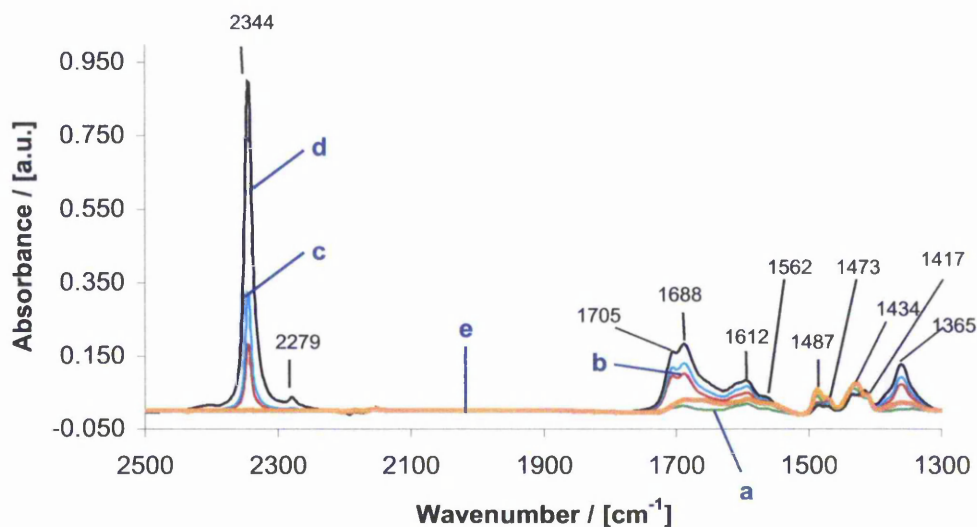
Figure 3.5-17: FTIR spectra of carbon dioxide adsorbed on Cs(22)-Na(75)-X, at different pressures. All spectra shown are difference spectra with respect to the activated catalyst. Carbon dioxide pressure increased as shown by the arrow. Legend: a) 10^{-3} mbar; b) 10^{-2} mbar; c) 10^{-1} mbar; d) 10^{0} mbar; e) (thick line) evacuated cell.
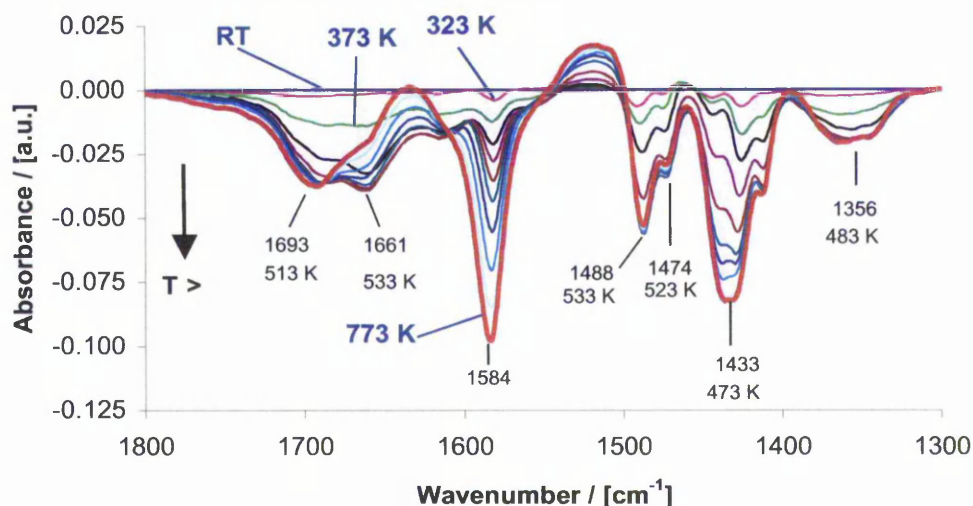
Figure 3.5-18: FTIR spectra of carbon dioxide desorption from Cs(22)-Na(75)-X, at 50 K increments. All spectra shown are difference spectra with respect to the last spectrum of the adsorption experiment. Temperatures shown are those where no further decrease was noted in the peak height. Temperature increased as shown by the arrow. Thick line indicates endpoint of the experiment (773 K).

3.5.6 Carbon dioxide adsorption on other zeolite samples

On zeolite Y samples, no significant peaks could be seen in the carbonate region (spectra not shown). Martra *et al.* are of the opinion that the lower Si/Al-ratio of Y zeolites compared to X zeolites, explains this absence of carbonate features in the infrared spectrum of adsorbed carbon dioxide. They state that the negative charge on the framework oxygen atoms is simply too low for them to act as a nucleophilic agent towards carbon dioxide [75]. A NH_4-ZSM-5 sample was subjected to the same adsorption regime as the X-zeolites, and, as expected, no absorption bands were seen in the carbonate region (spectra not shown).

3.5.7 Discussion and conclusion

Many researchers have used carbon dioxide in order to draw conclusions about basicity in their zeolites. In this work, clear differences existed between a parent Na-X zeolite and a lead exchanged zeolite with for example ~14 wt% lead.

After activation of the samples at 773 K in the evacuated infrared cell, possibly some water remained adsorbed on the zeolite. It could be speculated that carbon dioxide adsorption led to the removal of water molecules from certain adsorption sites. On these sites, carbon dioxide then adsorbed as carbonate species. The desorbed water re-adsorbed elsewhere in the zeolite, giving rise to features in the OH region.

The amount of carbon dioxide adsorbed decreased with increasing lead loading. The desorption of carbonates (taken as total peak area between 1300 and 1750 cm^{-1}) occurred at lower temperatures with lead exchanged samples compared to the parent Na-X. From the isopropyl alcohol (IPA) dehydrogenation experiments (*vide* §3.4), it was seen that introduction of lead increased the selectivity to acetone relative to the parent Na-X at a low lead loading (3.8 wt%), following a drop in selectivity for acetone at higher loadings. In contrast, from Na-X to Pb(9)-Na(96)-X the amount of carbon dioxide decreases. Higher lead loadings correspond to a further decrease of the amount of adsorbed carbon dioxide. A few explanations for the apparent disagreement with catalytic data are considered.

Firstly, it needs to be remembered that carbon dioxide cannot enter the sodalite cages; therefore it cannot be used to directly assess the basic sites in those cages.

Next, Doskocil and Davis point out that carbon dioxide adsorbs in different adsorption modes. This makes unambiguous linking of carbon dioxide desorption temperature to basicity of the zeolite impossible [59].

Thirdly, it was observed that some carbonate bands on Pb-Na-X samples disappeared only at very high temperatures, thus indicating a stronger interaction of those carbonate species with the substrate.

Finally, Doskocil and Mankidy compared microcalorimetry studies of carbon dioxide adsorbed on Na-X zeolites with reactivity to acetone in the isopropyl alcohol (IPA) dehydrogenation [82]. When they reacted IPA over Na-X containing occluded NaO_x species (3 NaO_x per unit cell), they found a low

carbon dioxide uptake, and yet they found the highest reactivity to acetone in their IPA dehydrogenation experiment.

With regard to the v_3 band of carbon dioxide, an alternative assignment for this peak was suggested by Jentoft *et al.* who quoted a band position of 2350 cm^{-1} for the asymmetric stretch of carbon dioxide on alumina [62]. Thus, it could be suggested that the bands at around 2350 cm^{-1} observed on X zeolites in this work (vide Figure 3.5-2) belong to carbon dioxide adsorbed on alumina. This would then be indicative of a severe dealumination process. The exchange of Na-X with lead (II) would have lead to substantial amounts of alumina being deposited in the supercages of the zeolite. However, no further evidence (from XRD for example) was observed to substantiate this hypothesis of severe dealumination, and subsequently it is rejected. Furthermore, for the sample with highest lead content (~42wt%), no contribution of a band at 2350 cm^{-1} can be distinguished, suggesting that sodium in the supercages has been replaced fully by lead, without alumina being deposited there simultaneously. Also, Rege and Yang have adsorbed carbon dioxide on γ-alumina, and they found a peak at 3605 cm^{-1}, which they assigned to the OH stretching vibration of a hydroxyl group on which a bidentate carbon dioxide species was adsorbed. Around this wavenumber, no adsorptions can be seen in the spectra of X zeolites in this work, which further supports that no alumina is present in the supercages of the zeolite.

A shift to higher wavenumbers in the v_3 band of carbon dioxide corresponds to an increase in strength of the positive field around the cation on which carbon dioxide is adsorbed, according to Martra *et al.* [75]. Taking this fact as a starting point, a higher positive field would draw away electrons from the zeolite framework oxygen atoms, leaving them less able to abstract a proton from a target molecule, and thus less basic. Indeed, this is what Martra et al observed for a Ba-Na-X sample [75]. For the lead exchanged samples used in this work, a decrease in wavenumbers for the v_3 band of adsorbed carbon dioxide band was observed. Thus, it can be speculated that the strength of the positive field around the guest-cation decreases from Na$^+$ to Pb^{2+}, which in turn would allow more negative charge to be situated on the zeolite framework oxygen.

With respect to the carbonate region, it seems that the peak assignments for the bidentate structure (bands at ~1710 and ~1360 cm^{-1}) and the carboxylate structure (bands at ~1485 and ~1430 cm^{-1}) adsorbed on Na-X are agreed upon with a fair degree of certainty in literature, but beyond those, identification is not so unambiguous. From the summary of reported peak positions in the carbonate region of carbon dioxide adsorbed on Na-X (Table 3.5-2), it becomes clear that carbon dioxide adsorption is very sensitive to minute changes in the circumstances of the experiment. Perhaps even small structural differences, such as an excess of Na$^+$ in the supercages that might remain on an unwashed Na-X, are the cause of the differences observed in what should be identical adsorption experiments. Pre-treatment of the catalyst has also been seen to be of paramount importance. Different activation temperatures for a low-loaded Pb-Na-X sample (3.8wt% Pb^{2+}) showed clear differences in the carbonate region, which was also observed on the parent zeolite. It might be speculated that the higher temperature led to migration of Na$^+$ cations away from the supercages and into the sodalite cages, thus reducing the number of bidentate Na$^+$ adsorption sites.

Rege and Yang observed a peak at 1644 cm^{-1} when they flowed 0.06 volume percent carbon dioxide in helium over Na-X, at room temperature. When they used a lower flow ratio of carbon dioxide to helium (14 ppmv carbon dioxide), their spectrum of the carbonate region appeared fairly similar to the carbonate spectrum for Na-X found in this work. Further, they adsorbed water on Na-X, and found a peak at 1650 cm^{-1}, as well as a sharp band in the 3960 – 3970 cm^{-1} region (at 87 ppmv water). They assigned peaks in the 1645 – 1660 region to the H-O-H bending vibration of water [76]. Bands in the hydroxyl region could clearly be seen in spectra of carbon dioxide adsorption on Pb-Na-X samples activated at 773 K. Their number and significance decreased when activation temperature was raised. Observations in the hydroxyl region both of the activation of these samples, and of carbon dioxide adsorption, suggest the difference observed in the hydroxyl region could be caused by water not being fully desorbed at 773 K, whereas the desorption is more complete when the catalyst is activated at 973 K. Jacobs suggests hydrolysis might explain bands he observed at 3685 and 3595 cm^{-1} on Ca-Na-X samples, which he activated at 673 K for 12 h [74]. With carbon dioxide adsorption on Ca-Na-Y samples, he

argued that residual adsorbed water had no influence on the adsorption mechanism for carbon dioxide [73]. He also stated that, "at high temperatures the presence of carbon dioxide molecules hinders the removal of the water molecules". Rather than removal, hydrolysis occurs, leaving hydroxyl bands at 3650, 3685 and 3590 cm^{-1} on Ca-Na-Y [73].

3.6 Zeolite acidity: ammonia adsorption

3.6.1 Abstract

In zeolite research, adsorption of ammonia is an often-used tool to assess the acidity of catalysts. Ammonia can act both as a Brønsted base, when it forms NH_4^+, and as a Lewis base, when it interacts through electron pair donation. Ammonia interaction with both Brønsted and Lewis acid sites has been reported on zeolite samples in literature. Bridging Al-OH-Si hydroxyl groups form Brønsted acid sites (proton donor species) in zeolites. Lewis acid sites (electron accepting species) are formed by cations. Both TPD and FTIR techniques can be used to investigate interaction of ammonia with solids.

Peak identification of adsorbed ammonia on solid samples is complicated in infrared experiments by the overlap of gas-phase (or weakly bound) ammonia with peaks of ammonia chemisorbed on Brønsted and Lewis acid sites. Thus, adsorption was carried out at elevated temperature (423 K) in order to avoid the presence of weakly bound ammonia. Ammonia interacting with Brønsted sites was identified by a band at ~1440 cm^{-1} and ammonia interacting with Lewis acid sites by a band at ~1655 cm^{-1}.

On Y samples, the most marked difference was seen between a proton form of the zeolite and an alkali-form. Far greater amounts were adsorbed on H-Y than on alkali-Y, indicating the acidity was reduced for alkali-Y samples relative to H-Y. Desorption curves were difficult to analyse, as amounts of ammonia adsorbed on alkali-Y samples was small, and consequently, noisy spectra resulted.

On K-Na-X samples, a peak found at ~1655 cm^{-1} was seen when ammonia was adsorbed on K(27)-Na(67)-X, which was absent when ammonia was adsorbed on K(100)-X. Thus, when sodium was replaced by potassium, the number of Lewis acid sites of the zeolite was decreased. For the same reason as mention with alkali-Y samples, infrared spectra of adsorbed ammonia were rather noisy.

3.6.2 Background

Interaction of ammonia with acid sites on solid surfaces was briefly described in §1.3.5.3. Some fundamental frequencies of ammonia in the infrared region have been tabulated by Tsyganenko et al. [83]. A selection of these frequencies is shown here.

Table 3.6-1: Selected fundamental frequencies for IR bands of ammonia. After Tsyganenko et al. [83].

Structure	Stretching modes		Deformation modes	
	ν_{as}	ν_s	δ_{as}	δ_s
NH$_3$ gas	3344	3336	1628	950
NH$_4{}^+$	3145	3040[a]	1680[a]	1400
NH$_2{}^-$	3420-3235	3360-3180	1580 - - 1505	

a) IR inactive mode

Ammonia can adsorb on both Lewis and Brønsted acid sites, as described in §1.3.5.3. In the case of zeolites used for this work these are (guest) metal cations and bridging hydroxyl groups, respectively. Tsyganenko et al. have adsorbed ammonia on silica and alumina. The results of these investigations are repeated here [83].

Table 3.6-2: Selected frequencies for IR bands of ammonia adsorbed on silica and alumina. After Tsyganenko *et al.* [83].

Solid	Structure	Stretching modes		Deformation modes	
		ν_{as}	ν_s	δ_{as}	δ_s
SiO$_2$	OH····NH$_3$	3400	3320		
	–NH$_2$	3526	3446	1555	
Al$_2$O$_3$	OH····NH$_3$ H$_2$NH····O	3360	3310		
	←NH$_2$H····O	3400, 3360	3180	1620	1280-1240
	←NH$_3$		3270	1620	1280-1240
	–NH$_2$			1560	
	–NH$_2$			1510	
	NH$_4^+$			1460	

Gilles *et al.* have adsorbed ammonia on a Na-Y zeolite [84]. They observed peaks in the hydroxyl region of infrared spectrum at 3398, 3369, 3317 and 3267 cm^{-1}, as well as shoulders at 3464 and 3197 cm^{-1}. Further, they found two peaks at 1652 and 1643 cm^{-1}, and a shoulder at 1510 cm^{-1}. W. Jacobs, in a PhD-thesis on proton-ammonia interaction in zeolite Y, found a band at 1430 cm^{-1} for ammonia adsorbed on H-Y, which he ascribed to N-H deformation mode of ammonium ions [85]. Zhang *et al.* deconvoluted a broad feature at ~1640 cm^{-1} in the spectra of ammonia adsorbed on H-β and H-ZSM-12 samples. From this, they deduced that Brønsted acid sites were indicated by a peak at 1454 cm^{-1} and Lewis acid sites by a peak at 1625 cm^{-1} [86].

Table 3.6-3: Reported infrared band positions by Gilles *et al.* [84] of ammonia adsorbed on Faujasites.

Peak / [cm^{-1}]		Identification
Na-Y	Na-X	
3464		amine group
3398		ν_3 asymmetric N-H stretching vibration
3384	3368	ν_3 asymmetric N-H stretching vibration
3317	3312	ν_1 symmetric N-H stretching vibration
3263		ν_4 H-N-H bending vibration
	1652	ν_4 H-N-H bending vibration
1643	1639	ν_4 H-N-H bending vibration
1510		amine group

3.6.3 Ammonia adsorption on Pb-Na-X zeolites

In the following, each catalyst was given the following treatment (in the order listed) unless otherwise noted:

1) Activation at 773 K (10 K min^{-1}) for 2 h in vacuum.
2) Ammonia adsorption at 423 K subsequently at:
   a) 10^{-4} mbar, 60 min
   b) 10^{-3} mbar, 30 min
   c) 10^{-2} mbar, 30 min
   d) 10^{-1} mbar, 30 min
   e) 10^{0} mbar, 30 min
3) Evacuation of the cell; 15 minutes on a rotary pump followed by 15 minutes on a turbomolecular pump.

In Figure 3.6-1, which shows ammonia adsorbed on Pb-Na-X zeolites, at a pressure of 1 mbar and at 423 K, several peaks can be seen in the 3800 – 3100 cm^{-1} region. Following Gilles et al, the following peaks are assigned on Pb(9)-Na(96)-X:

Table 3.6-4: Reported band positions by Gilles *et al.* [84] regarding ammonia adsorption on Faujasites.

Peak	Identification
3399	ν_3 asymmetric N-H stretching vibration
3367	ν_3 asymmetric N-H stretching vibration
3317	ν_1 symmetric N-H stretching vibration
3253	ν_4 H-N-H bending vibration
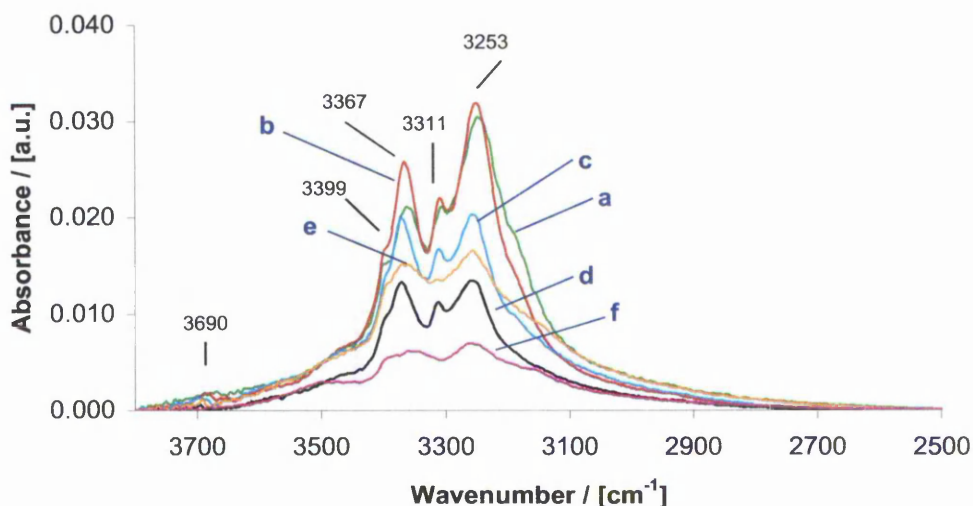
Figure 3.6-1: Normalised FTIR spectra of ammonia adsorbed on Pb-Na-X zeolites, at a pressure of 1 mbar, showing bands between 3800 and 2500 cm^{-1}. All spectra shown are difference spectra with respect to the activated catalyst. Legend: a) Na-X (parent zeolite); b) Pb(9)-Na(96)-X; c) Pb(34)-Na(76)-X; d) Pb(43)-Na(61)-X; e) Pb(63)-Na(27)-X; f) Pb(131)-X

In the 1800 – 1300 cm^{-1} region, a broad feature was found on all Pb-Na-X samples. Identification of species is not straightforward, as a result of overlapping peaks. At a lead loading of 16.9 wt% or greater, the broad feature between 1700 and 1500 cm^{-1} changed shape, and only one peak could be discovered.
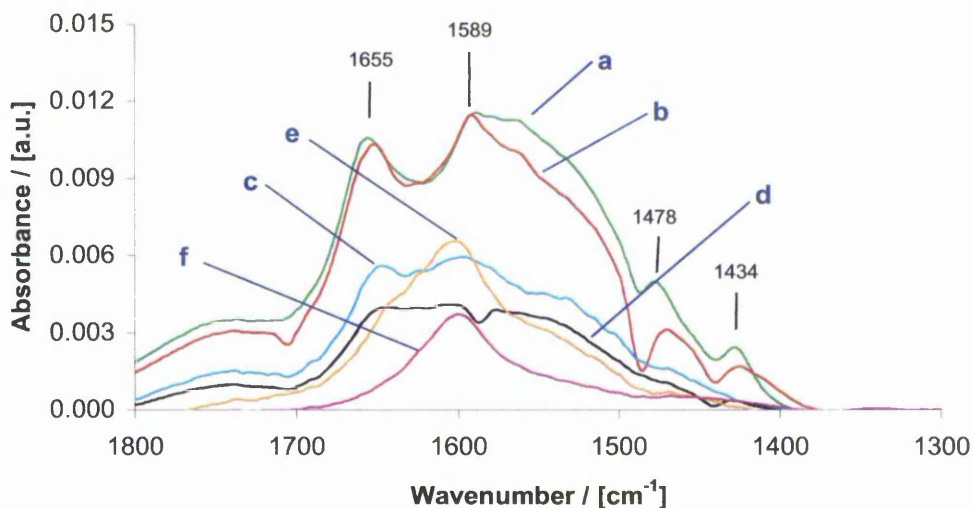
Figure 3.6-2: Normalised FTIR spectra of ammonia adsorbed on Pb-Na-X zeolites, at a pressure of 1 mbar, showing bands in the 1800 – 1300 cm^{-1} region. All spectra shown are difference spectra with respect to the activated catalyst. Legend: a) Na-X (parent zeolite); b) Pb(9)-Na(96)-X; c) Pb(34)-Na(76)-X; d) Pb(43)-Na(61)-X; e) Pb(63)-Na(27)-X; f) Pb(131)-Na-X

After evacuation of the cell, it was evident that most ammonia disappeared from the catalysts, indicating it was weakly held. Some species remained. Hydroxyl groups were seen at 3690 cm^{-1}. A stretching band of N-H was seen at ~3367 cm^{-1}, and a H-N-H bending vibration was evident at ~3253 cm^{-1}. From desorption experiments, the integral peak area in the 3500 – 3000 cm^{-1} region was found to decrease over the entire temperature range of the experiments. Non-specific peaks belonging to ammonia adsorbed on the surface (possibly bound through hydrogen bonding) caused the broad feature in this region. Thus, the complete range is not deemed suitable to investigate as a measure for the strength of the ammonia-zeolite interaction. No relation between lead loading and desorption temperature could be discovered, but this was undoubtedly due to the noisy quality of the spectra. High noise levels hinted that rather small quantities of ammonia adsorbed on the Pb-Na-X samples.
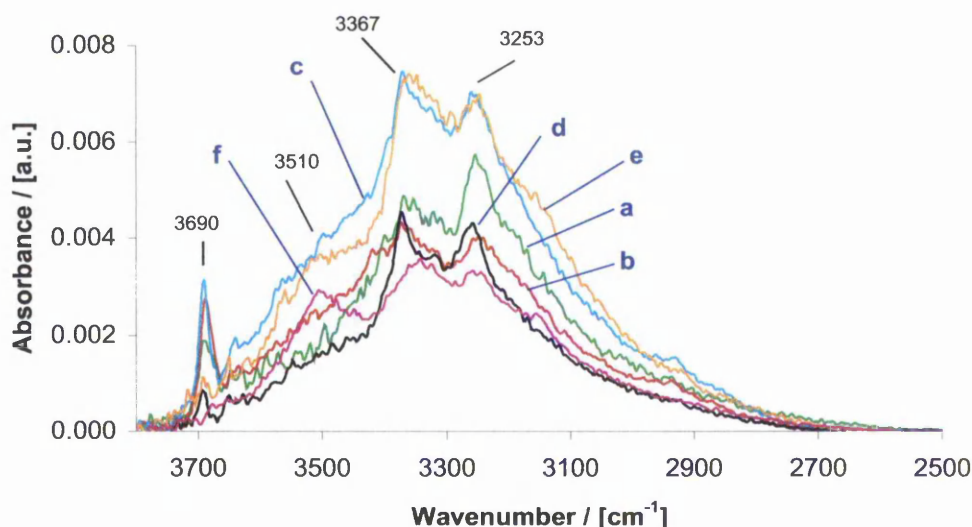
Figure 3.6-3: Normalised FTIR spectra of ammonia adsorbed on Pb-Na-X zeolites, after evacuation of the cell, showing bands between 3800 and 2500 cm^{-1}. All spectra shown are difference spectra with respect to the activated catalyst. Legend: a) Na-X (parent zeolite); b) Pb(9)-Na(96)-X; c) Pb(34)-Na(76)-X; d) Pb(43)-Na(61)-X; e) Pb(63)-Na(27)-X; f) Pb(131)-X

In the 1800 – 1300 cm^{-1} region, several features could be distinguished after evacuation of the cell (*vide* Figure 3.6-4). A fine structure was seen on samples with lead loading smaller than 24.1 wt%. Tentatively, the peak at ~1655 cm^{-1} was assigned to ammonia adsorbed on Lewis sites, whereas the peak at ~1434 cm^{-1} was assigned to ammonia adsorbed on Brønsted acid sites. Once again, assessment of desorption experiments proved to be rather complex, due to the

amount of adsorbed ammonia being rather small. No clear indication could be found with respect to the desorption temperature of ammonia from Pb-Na-X samples. Thus, it can be concluded that hardly any Brønsted acid sites existed on Pb-Na-X samples.
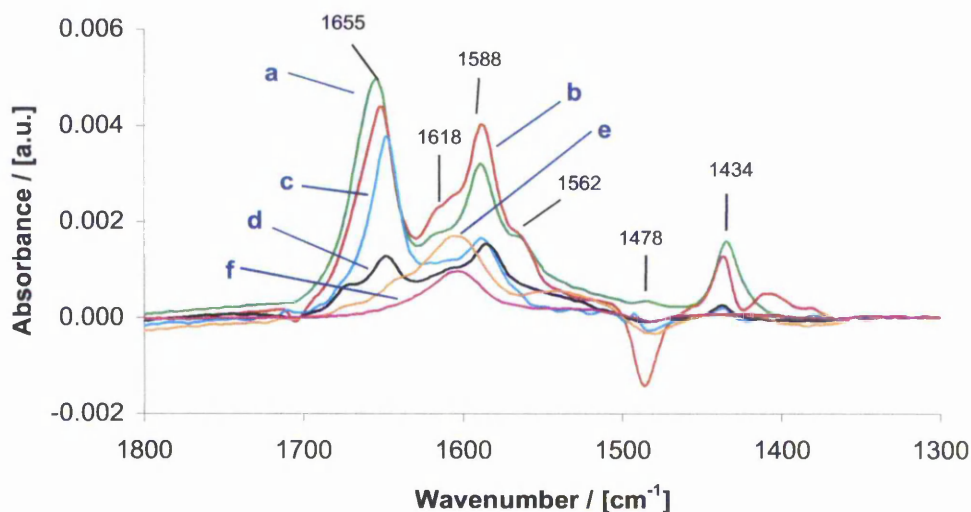
Figure 3.6-4: FTIR spectra of ammonia adsorbed on Pb-Na-X zeolites, after evacuation of the cell showing bands in the $1800 - 1300 \text{ cm}^{-1}$ region. All spectra shown are difference spectra with respect to the activated catalyst. Legend: a) Na-X (parent zeolite); b) Pb(9)-Na(96)-X; c) Pb(34)-Na(76)-X; f) Pb(43)-Na(61)-X; e) Pb(63)-Na(27)-X; f) Pb(131)-X

3.6.4 Ammonia adsorption on K-Na-Y zeolites

On Y zeolites, adsorption of ammonia on K-Na-Y is compared to adsorption of ammonia on H-Y. The H-Y sample was prepared by heating an NH_4-Y sample in vacuum. In Figure 3.6-5, it can be seen that about one order of magnitude more ammonia adsorbed on H-Y in comparison to K-Na-Y zeolites. Ammonia adsorbed on both high frequency (HF) and low frequency (LF) hydroxyl groups on H-Y, as was evident from peaks at ~3637 and 3563 cm^{-1} respectively. Only the HF band could be discovered on K(70)-Y, a catalyst which was prepared using three exchanges of Na-Y with potassium acetate, followed by a wash with distilled water.
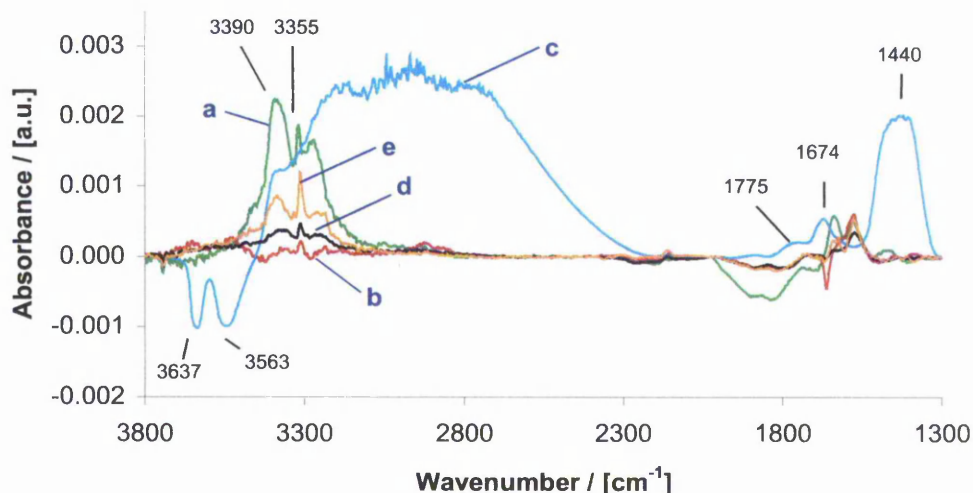
Figure 3.6-5: Normalised FTIR spectra of ammonia adsorbed on K-Na-Y zeolites, at a pressure of 1 mbar. All spectra are difference spectra with respect to the activated catalyst (except H-Y: normalised to 30 times overtone integral intensity in order to show the spectrum on the same scale as the other spectra). Legend: a) Na-Y (parent zeolite); b) K(87)-Y; c) H-Y; d) K(72)-Y; e) K(69)-Na-(15)-Y

After evacuation of the cell, on H-Y clearly it could be seen that ammonia was still adsorbed, judging from bands at 3637 and 3563 cm^{-1}. On H-Y, peaks at 1674 and 1440 were assigned to ammonia adsorbed on Lewis and Brønsted acid sites respectively. On K(87)-Y a feature at ~2945 and 2868 cm^{-1}. This appeared directly after opening of the rotary pump to evacuate the cell, and is probably due to a contamination in the rotary pump line (*vide* Figure 3.6-6). It is not visible on the ammonia admission spectra in Figure 3.6-5, and is in a different spectral range as the absorptions band of adsorbed ammonia.
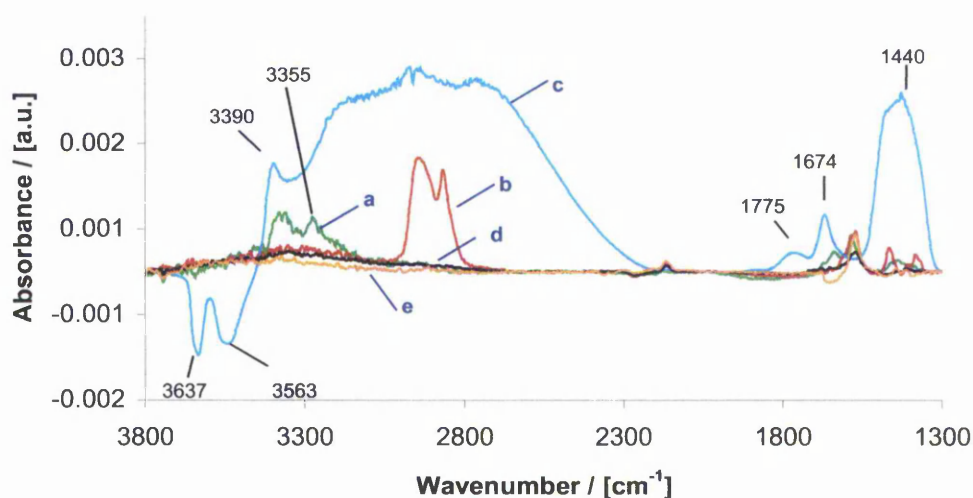
Figure 3.6-6: Normalised FTIR spectra of ammonia adsorbed on K-Na-Y zeolites, after evacuation of the cell (pressure < 10^{-6} mbar). All spectra are difference spectra with respect to the activated catalyst (except NH4-Y: normalised to 30 times overtone integral intensity in order to fit on the same scale as the other spectra). Legend: a) Na-Y (parent zeolite); b) K(87)-Y; c) H-Y; d) K(72)-Y; e) K(69)-Na-(15)-Y

Desorption experiments were not analysed further, as the amount adsorbed on K-Na-Y samples was not enough to obtain reliable information regarding desorption temperatures.

3.6.5 Ammonia adsorption on K-Na-X zeolites

Ammonia was adsorbed on two K-Na-X samples. Results can be seen in Figure 3.6-7. The amount of ammonia adsorbed decreased dramatically upon exchange of Na-X with potassium. Relatively little difference is seen between potassium exchanged Na-X samples. The broad feature at 1700 – 1500 cm^{-1} that was seen with ammonia adsorption on Pb-Na-X samples is seen as well on K-Na-X samples.
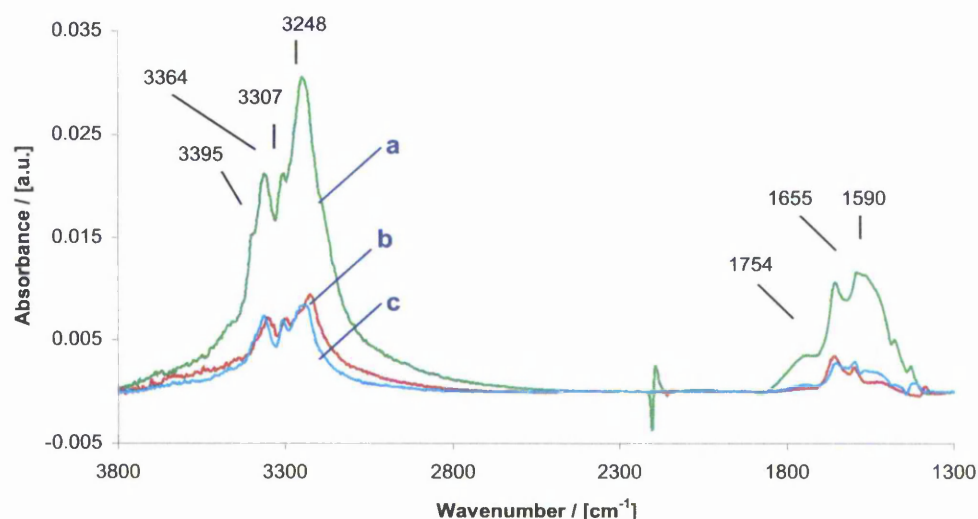
Figure 3.6-7: Normalised FTIR spectra of ammonia adsorbed on K-Na-X zeolites, at a pressure of 1 mbar in the cell. All spectra shown are difference spectra with respect to the activated catalyst. Legend: a) Na-X (parent zeolite); b) K(27)-Na(67)-X; c) K(100)-X

After evacuation of the cell, the peaks seen between 3800 and 2800 cm^{-1} at one mbar of ammonia pressure (*vide* Figure 3.6-7) disappeared from potassium-exchanged samples, whereas on Na-X peaks were still visible. Instead, a broad feature was seen on K-Na-X samples. A sharp feature around 2190 cm^{-1} was not clearly identified and was thought to have arisen as a result of background correction.

In the 1800 – 1300 cm^{-1} region, several peaks could be seen after evacuation of the cell. Analogues with Pb-Na-X samples, the peak at 1655 cm^{-1} was thought to be ammonia adsorbed on Lewis acid sites, whereas a minor contribution at ~1434 cm^{-1} was interpreted to be ammonia adsorbed on Brønsted acid sites.
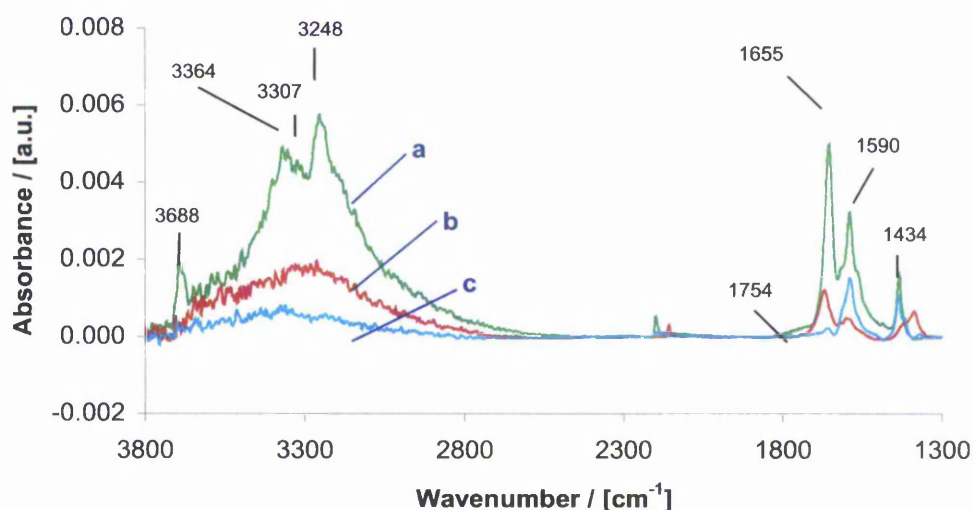
Figure 3.6-8: Normalised FTIR spectra of ammonia adsorbed on K-Na-X zeolites, after evacuation of the cell. All spectra shown are difference spectra with respect to the activated catalyst. Legend: a) Na-X (parent zeolite); b) K(27)-Na(67)-X; c) K(100)-X

Desorption experiments were not analysed further, as the amount adsorbed on K-Na-X samples was not enough to obtain reliable information regarding desorption temperatures.

3.6.6 Discussion and conclusion

From ammonia adsorption experiments it is clear that for K-Na-Y samples, a clear difference exists between the amount of ammonia on H-Y and K-Na-Y samples. This difference can be interpreted as a consequence of the decrease of acidity when a proton is substituted for a sodium or a potassium cation. Interestingly, on potassium exchanged X and Y samples Brønsted sites were still found, evident by a peak at ~1440 cm^{-1}.

With ammonia adsorption identification of Brønsted and Lewis acid sites is of particularly concern. Infrared bands of weakly bound ammonia are present in the same region as ammonia bands chemisorbed on Brønsted and Lewis acid sites [86, 87]. Adsorption at elevated temperatures is required when adsorbing ammonia. As a consequence, weak Brønsted or Lewis sites cannot be easily identified using ammonia adsorption. Further, Tsyganenko et al. recognised that

the mechanism of ammonia adsorption on solids is dependant on the hydroxylation of the surface [83]. Interaction of ammonia with the surface hydroxyl groups leads to formation of hydrogen bridges. It is difficult to distinguish adsorbed ammonia species from surface hydroxyl bands in the region between 3700 and 3000 cm^{-1}.

Interaction of ammonia adsorbed on a Lewis acid site with a Lewis base site leads to perturbation of an ammonia N-H v_3 band at ~3370 cm^{-1} according to Gilles et al. [84]. However, within a series of alkali exchanges X faujasites the trend in Gilles' data is not so clear [84]. In any case, interaction of ammonia with the Lewis acid site itself (i.e. the cation) is the dominant factor in the location of this band. Substituting for example Pb^{2+} for Na^+ would have the most dramatic effect on the position of the v_3 vibration bands of ammonia. Further, due to the noisy character of the spectra, exact determination of peak positions was not unambiguous.

On Y samples, the difference observed between the H-Y sample and alkali-exchanged samples can be explained by the decrease of Brønsted acidity when a proton is substituted for an alkali metal. The peak seen at ~1440 cm^{-1} on ammonia adsorbed on H-Y is reduced greatly on alkali-exchanged samples. This would then be incorporated into explanation of the difference in reactivity between H-Y and alkali-Y in the isopropyl alcohol (IPA) decomposition experiments with these samples. Whereas H-Y is only able to catalyse IPA to propene, K-Y samples have been seen to catalyse IPA to acetone. However, ammonia adsorption results are not able to explain differences in reactivity in the IPA reaction observed for K-Na-Y samples of roughly the same potassium loading.

3.7 Zeolite basicity: nitromethane adsorption

3.7.1 Abstract

Nitromethane adsorption on various solids has been studied by a number of research groups. During adsorption, the development of covalent and ionic isocyanate species (-NCO) during thermal desorption of nitromethane was seen as indicative of acidic and basic sites, respectively. Next to isocyanate species, researchers found cyanide species (-CN) during thermal desorption as well. Infrared spectroscopy can be used as a tool for monitoring the thermal desorption of nitromethane.

On Pb-Na-X catalysts used in this work, two bands in the infrared spectrum of nitromethane adsorbed at room temperature were assigned to isocyanate species. A further band was found to evolve during thermal desorption, which was most likely due to a conjugate double band. This band were also seen to develop during thermal desorption of nitromethane adsorbed on potassium, caesium and sodium X zeolites. On potassium exchanged Y zeolites a qualitative correlation was seen between this species evolving during thermal desorption of nitromethane and results seen in the dehydrogenation of isopropyl alcohol. Notably, no evidence was found for isocyanate species at the band positions reported in literature.

3.7.2 Background

The fundamental frequencies of free nitromethane (NM) in the liquid phase have been investigated by Hill *et al.* [88]. The bands seen between 3800 and 1300 cm^{-1} are quoted here:

Table 3.7-1: Fundamental infrared band positions of nitromethane reported by Hill *et al.* [88].

Mode	Band(s) / [cm^{-1}]	Intensity[a]
$\nu_a(CH_3)$	3045	w
$\nu_s(CH_3)$	2980	w
$\nu_a(NO_2) + \nu_s(NO_2)$	2955	w
$\nu_a(NO_2) + \delta_s(CH_3)$	2932	m
$2 \times \nu_s(NO_2)$	2802	w
$\nu(CN) + \nu_a(NO_2)$	2465	w
$\nu(CN) + \delta_s(CH_3)$	2285	w
$\delta(NO_2) + \delta_s(CH_3)$	2035	w
$2 \times \nu(CN)$	1830	w
$\nu_a(NO_2)$	1560	vs
$\delta_a(CH_3)$	1423	s
$\nu_s(NO_2)$	1404	s
$\delta_s(CH_3)$	1378	s
$2 \times \delta(NO_2)$	1313	w

a) w = weak, m = medium, s = strong, vs = very strong

It has been mentioned in §1.3.5.4 that adsorbed isocyanate species are infrared active [89, 90]. Nesterenko argued that the decomposition products of nitromethane, which develop when heating nitromethane adsorbed on a surface, could be used as a tool for characterisation of basic sites on a solid. Covalently bound isocyanate (NCO) was found at ~2280 cm^{-1} on ultra-stable Y (*i.e.* USY; a dealuminated zeolite Y), and on ~2220 cm^{-1} on MgO [91]. Ionic NCO was found at ~ 2190 cm^{-1} on MgO and was not found on USY. Ukisu *et al.* adsorbed NO and subsequently C_3H_6 on supported Cu-oxides, monitored by FTIR. They observed a band at 2240cm^{-1} which they assigned to surface isocyanate species [92]. The species developed upon heating the sample between 473 K (2240cm^{-1}) and 673 K (2234cm^{-1}), and was stable even at 673 K. Yamaguchi adsorbed nitromethane at room temperature on γ-alumina, with subsequent desorption at 573K. He assigned the following peaks [93]:

Table 3.7-2: FTIR peaks belonging to nitromethane species on γ-alumina (573K). After Yamaguchi [93].

Peak / [cm⁻¹]	Assignment
2261	isocyanate (NCO)
2236	isocyanate (NCO⁻)
2126	cyanide (NC⁻)
3570	OH-stretching (result of deprotonation of NM)

Nitromethane is thought to be an intermediate in the selective catalytic reduction (SCR) of NO_x (under oxygen rich conditions) by several researchers, and thus a few studies involving nitromethane were done on catalysts active in this reaction [94-98]. Satsuma et al. have adsorbed nitromethane on Co-ZSM-5; they assigned peaks of adsorbed nitromethane as follows [95, 99]:

Table 3.7-3: FTIR peaks belonging to nitromethane species adsorbed on Co-ZSM-5. After Satsuma [95].

Peak / [cm⁻¹]	Assignment
2156	Co-CN
2172	Co-NCO
2260	Al^{3+}-NCO

Further, Solymosi and Bansagi adsorbed gaseous hydrogen isocyanate on Cu-ZSM-5. They found that the IR peak position of isocyanate species was found to depend on the oxidation state of the copper [100].

Table 3.7-4: FTIR peaks belonging to nitromethane species on Cu-ZSM-5. After Solimosi and Bansagi [100].

Peak / [cm⁻¹]	Assignment
2230-2240	Cu^0-NCO
2200-2210	Cu^+-NCO
2180-2185	Cu^{2+}-NCO

Solymosi and Bansagi also quoted the following fundamental infrared band positions for hydrogen isocyanate:

Table 3.7-5: Fundamental infrared bands belonging to HCNO. After Solimosi and Bansagi [100].

Peak / [cm^{-1}]	Assignment
3531	$\nu_1(a')$ H-CNO
2274	$\nu_2(a')$ HN=CO
1327	$\nu_3(a')$ HN=CO

Studies of nitromethane adsorbed on alkali-exchanged X zeolites have been done by Lima et al. [101], who investigated the usage of nitromethane as a probe molecule for basic catalysts. They found NMR evidence for the presence of aci-anion nitromethane (*vide* §1.3.5.4) at room temperature, which they argued, was stabilised by a basic function of alkali-exchanged zeolite X [101].

Further, some band positions for metal-isocyanate (M-NCO) compounds can be found in literature (*vide* Table 3.7-6). These compounds coordinate through their nitrogen atom to the metal.

Table 3.7-6: Reported band positions for cyanato complexes.

Compound	Band	Band position	Reference
K(NCO)	ν_a(NCO)	2155	[102]
Si(NCO)$_4$	ν_a(NCO)	2284	[103]
Si(NCO)$_4$	ν_s(NCO)	1482	[103]
[Co(CNO)$_4$]$^{2-}$	ν_a(NCO)	2217, 2179	[104]
[Co(CNO)$_4$]$^{2-}$	ν_s(NCO)	1325	[104]
[Fe(CNO)$_4$]$^-$	ν_a(NCO)	2208, 2171	[104]
[Fe(CNO)$_4$]$^-$	ν_s(NCO)	1370	[104]
[Pd(CNO)$_4$]$^-$	ν_a(NCO)	2200, 2190	[105]
[Pd(CNO)$_4$]$^-$	ν_s(NCO)	1319	[105]

Some band positions were reported for fulminato complexes, which are CNO$^-$, bound to the metal either through the oxygen atom (M-ONC) the carbon atom (M-CNO) or through both [106]. In [Zn(CNO)$_4$]$^{2-}$ two bands were assigned to ν(CN) at 2146 and 2130 cm^{-1}. In [Pt(CNO)$_4$]$^{2-}$, these bands were found at 2194 and 2189 cm^{-1} [106].

Next, the results will be presented of infrared spectra observed for nitromethane adsorption on zeolite X and zeolite Y samples. The catalysts were given the following treatment (in the order listed) unless otherwise noted:

1) Activation at 773 K (10 K min^{-1}) for 2 h in vacuum.

2) Nitromethane adsorption at room temperature subsequently at:

   a) 10^{-3} mbar, 45 min

   b) 10^{-2} mbar, 30 min

   c) 10^{-1} mbar, 30 min

   d) 10^{0} mbar, 30 min

3) Evacuation of the cell; 15 minutes on a rotary pump followed by 15 minutes on a turbomolecular pump.

3.7.3 Nitromethane adsorption on Pb-Na-X zeolites

When nitromethane was adsorbed on Pb-Na-X zeolites, bands evolved at various positions in the infrared spectrum, yielding a complicated spectrum (Figure 3.7-1). In light of what was mentioned in §3.7.2, the peak at ~3031 cm^{-1} was assigned to an asymmetric stretch of a CH$_3$ group. At ~2953 cm^{-1} the symmetric counterpart of this vibration was found. At ~2469 cm^{-1} a band was found which was tentatively assigned to a combination of a stretching vibration of cyanide and an anti-symmetric stretching-vibration of a nitro group (NO$_2$) (*vide* Table 3.7-1). Bands at ~2291 and 2257 cm^{-1} were interpreted to be belonging to isocyanate species. Remarkably, these bands formed during adsorption at room temperature, on all lead exchanged zeolites, except on Pb(131)-X. Nesterenko reported appearance of these peaks only during thermal desorption of adsorbed nitromethane, in a temperature range of ~473 – 673 K [91].
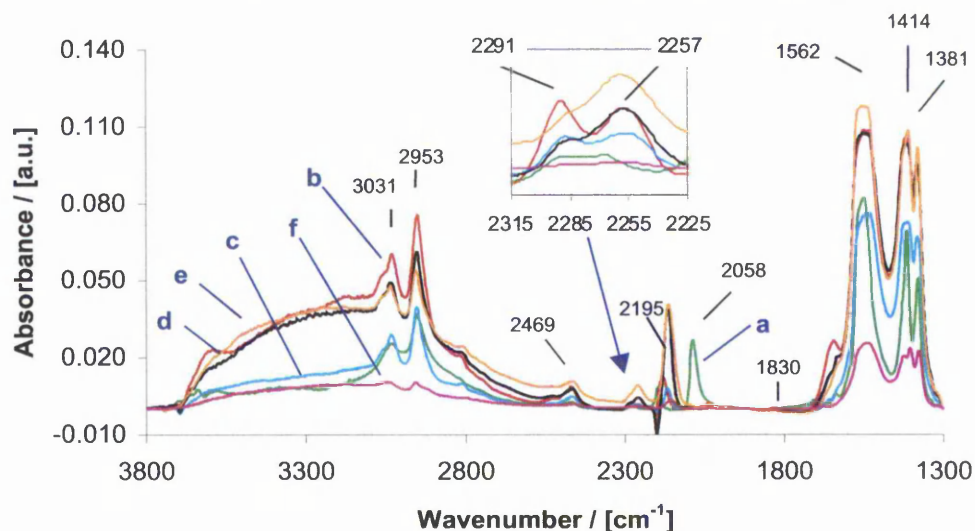
Figure 3.7-1: Normalised FTIR spectra of adsorbed nitromethane, showing results after evacuation of the cell (pressure < 10^{-5} mbar). All spectra shown are difference spectra with respect to the activated catalyst. Legend: a) Na-X (parent zeolite); b) Pb(9)-Na(96)-X; c) Pb(34)-Na(76)-X; d) Pb(43)-Na(61)-X; e) Pb(63)-Na(27)-X f) Pb(131)-X

An asymmetric stretching vibration of the -NO_2 group was found at ~1562 cm^{-1}. At ~1414 cm^{-1} a strong adsorption band was found. This peak was probably a composite of bands at ~1404 and ~1423 cm^{-1}, corresponding to a symmetric stretching vibration of -NO_2 and a bending vibration of a CH_3 group respectively. At ~1381 cm^{-1} a symmetric bending vibration of a CH_3 group was seen. This interpretation is deduced from Table 3.7-1.

No obvious relation between the amount of nitromethane adsorbed and lead loading was discovered when lead loading was plotted against normalised peak areas of adsorbed nitromethane (peak area of the NO_2 stretch at 1562 cm^{-1}; graph not shown).

A band was found during adsorption of nitromethane at ~2180 cm^{-1} on Pb(9)-Na(96)-X. The rise of this peak was accompanied by a very weak absorption at 1830 cm^{-1}. No sharp absorption band was seen around 3200 cm^{-1}. The variation of the peak position of the band at ~2180 cm^{-1} in relation to lead loading is plotted in Figure 3.7-2. The assignment of this peak is not without ambiguity. It could be assigned to a triple bond of C≡N, or to a cumulative stretching vibration of C=N=O.
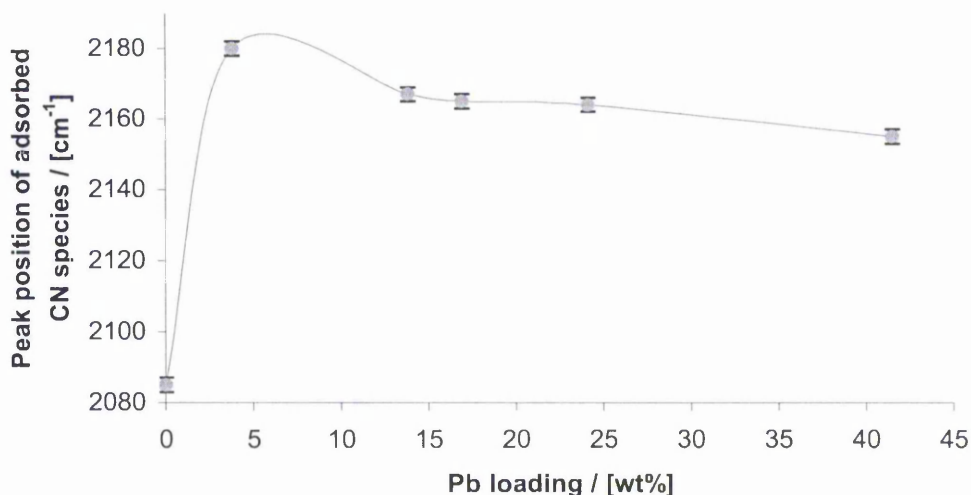
Figure 3.7-2: Peak position of a CN stretching vibration at in the FTIR spectra of adsorbed nitromethane at 1 mbar versus Pb loading. Line was added to highlight trends in the data. Resolution of the IR instrument is indicated as an error bar on the data points.

During thermal desorption of nitromethane from Pb(9)-Na(96)-X, the peak at ~2194 cm^{-1} was seen to increase in size with increasing temperature, as can be seen in Figure 3.7-3. The same effect was observed for Na-X and Pb(34)-Na(76)-X (spectra not shown). On Pb(43)-Na(61)-X, a peak at ~2165 cm^{-1} was seen to decrease with increasing desorption temperature, whilst a band at ~2188 cm^{-1} increased. On Pb(63)-Na(27)-X, a peak at 2163 cm^{-1} decreased, whilst a peak at 2246 cm^{-1} increased with increasing desorption temperature.
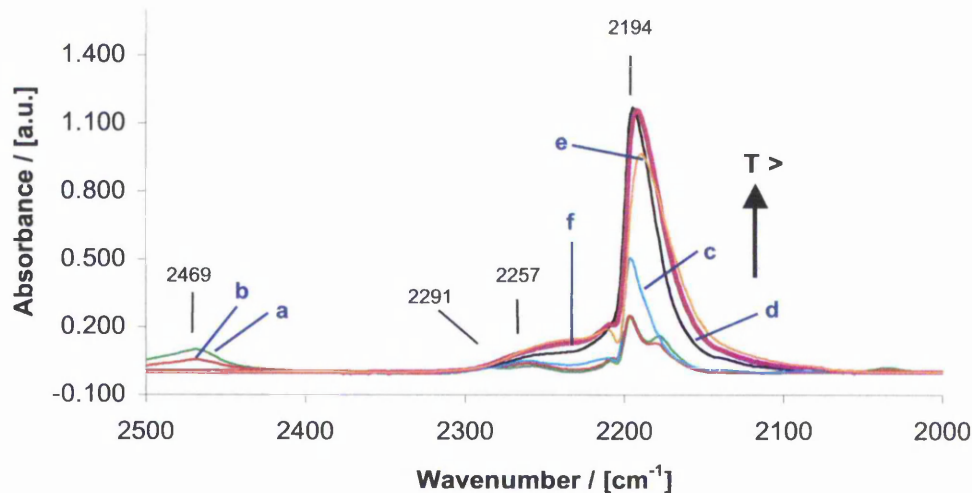
Figure 3.7-3: FTIR spectra of nitromethane desorbing from Pb(9)-Na(96)-X. All spectra shown are difference spectra with respect to the activated catalyst. Legend: a) RT; b) 373 K; c) 473 K; d) 573 K; e) 673 K; f) 773 K (thick line)

3.7.4 Nitromethane adsorption on various X zeolites

During adsorption of nitromethane on X zeolites, different cations gave rise to different features in the infrared spectrum. Cation loading was around 30% exchange for all samples in Figure 3.7-5, in which spectra of adsorbed nitromethane are shown. At an nitromethane pressure of 10^{-3} mbar, some differences could be observed between catalysts in the 1700 – 1300 cm^{-1} region. The amount of nitromethane adsorbed on the potassium exchanged zeolite was comparable to that adsorbed on the caesium exchanged sample. So were the amount adsorbed on the lead exchanged sample and on the parent zeolite.

The peak at 1490 cm^{-1} on Na-X, which could not be assigned to any vibration belonging to nitromethane, could not be seen on any of the exchanged catalysts. The peaks at 1409 and 1427 cm^{-1} are clearly separated on the caesium sample and the parent Na-X zeolite, whereas on the potassium and the lead exchanged sample, the peak at 1427cm^{-1} was a shoulder rather than a separated peak. At 1390 and 1381 cm^{-1}, two contributions can be seen on the

lead and on the parent Na-X zeolite, whereas a single peak was visible on the potassium and caesium exchanged samples.
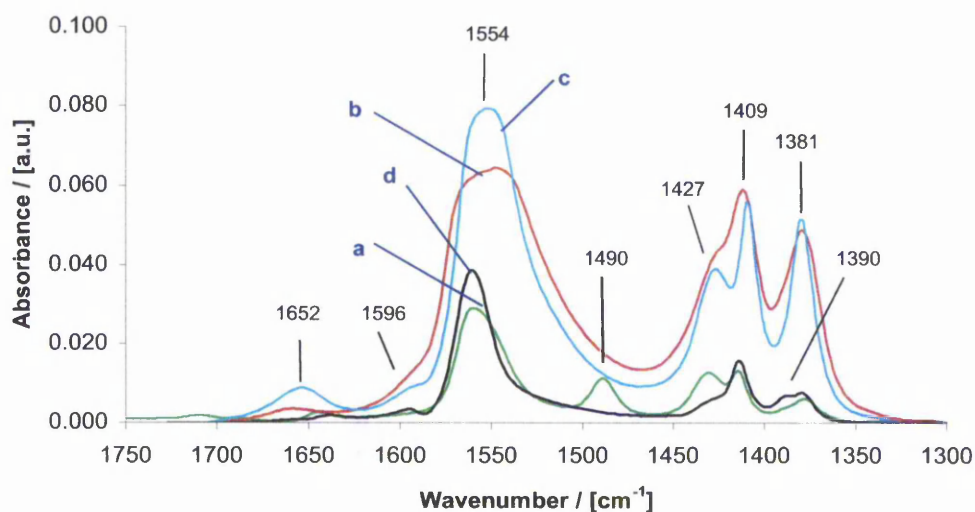
Figure 3.7-4: Normalised FTIR spectra of nitromethane adsorbed on X zeolites, at a pressure of 10^{-3} mbar in the cell. All spectra shown are difference spectra with respect to the activated catalyst. Legend: a) Na-X (parent zeolite); b) K(27)-Na(67)-X; c) Cs(22)-Na(75)-X; d) Pb(34)-Na(76)-X

When 1 mbar of nitromethane was adsorbed on the zeolite X samples, the lead exchanged sample again best resembled the carrier Na-X, whereas the caesium samples was similar to the potassium exchanged sample.
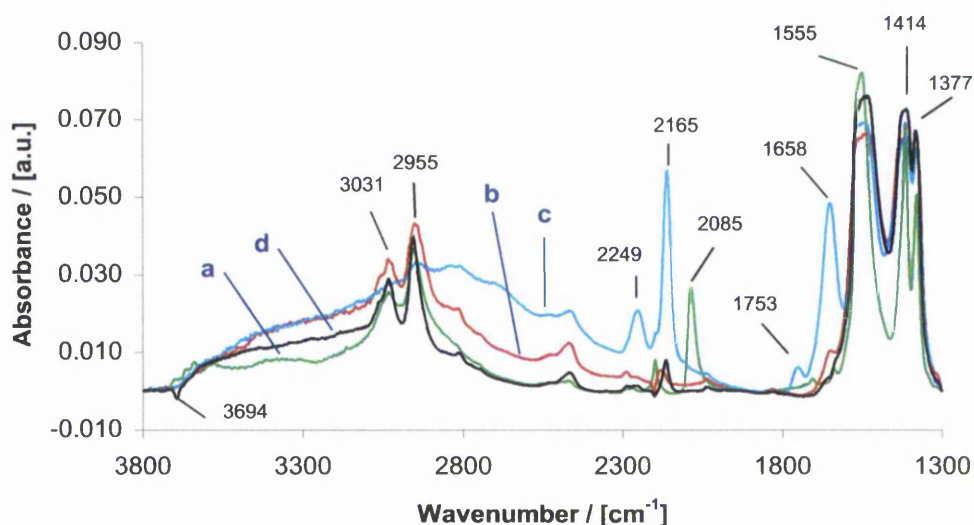
Figure 3.7-5: Normalised FTIR spectra of nitromethane adsorbed on X zeolites, at a pressure of 1 mbar in the cell. All spectra shown are difference spectra with respect to the activated catalyst. Legend: a) Na-X (parent zeolite); b) K(27)-Na(67)-X; c) Cs(22)-Na(75)-X; d) Pb(34)-Na(76)-X

After evacuation of the cell, the catalysts retained most of the adsorbed nitromethane (*vide* Figure 3.7-6).
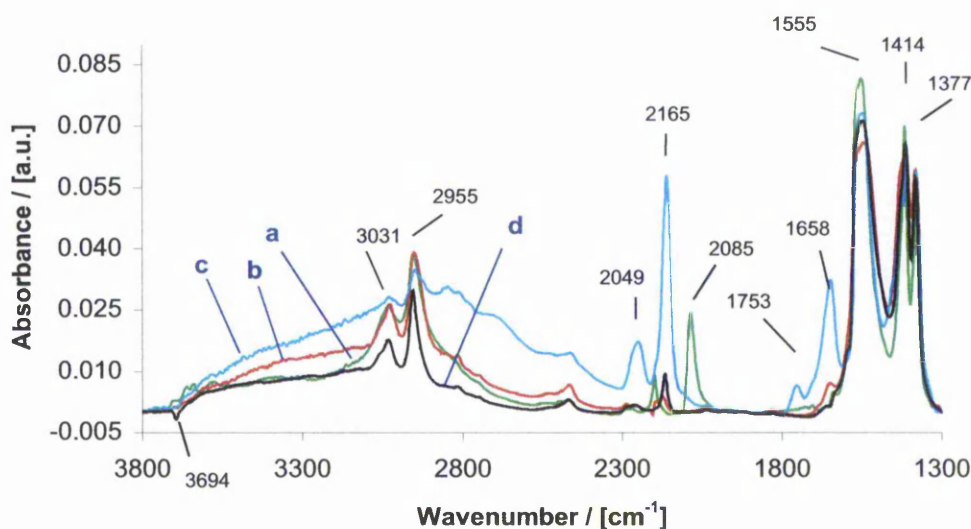
Figure 3.7-6: Normalised FTIR spectra of nitromethane adsorbed on X zeolites, at a pressure of 1 mbar in the cell. All spectra shown are difference spectra with respect to the activated catalyst. Legend: a) Na-X (parent zeolite); b) K(27)-Na(67)-X; c) Cs(22)-Na(75)-X; d) Pb(34)-Na(76)-X

For comparison, the bands that appeared during thermal desorption in the region between 2350 and 2000 cm^{-1} are shown in Figure 3.7-7 – Figure 3.7-10, for Na-X and three exchanged zeolite X samples. A peak at roughly 2190 cm^{-1}

was seen to rise with temperature on all samples except the caesium exchanged one. The maximum intensity of this peak was found at 673 K on the potassium and lead exchanged sample. On Na-X, the peak was still present at 773 K. Also on Na-X, another (minor) band was seen around 2240 cm^{-1} that rose in intensity with increasing temperature.
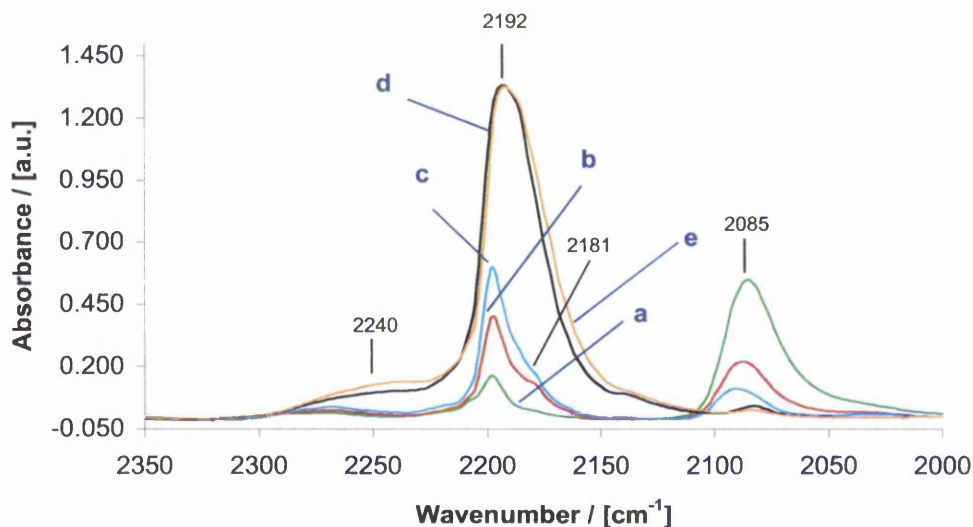
Figure 3.7-7: FTIR spectra of nitromethane desorption from Na-X. Legend: a) RT; b) 423 K; c) 523 K; d) 673 K; e) 773 K
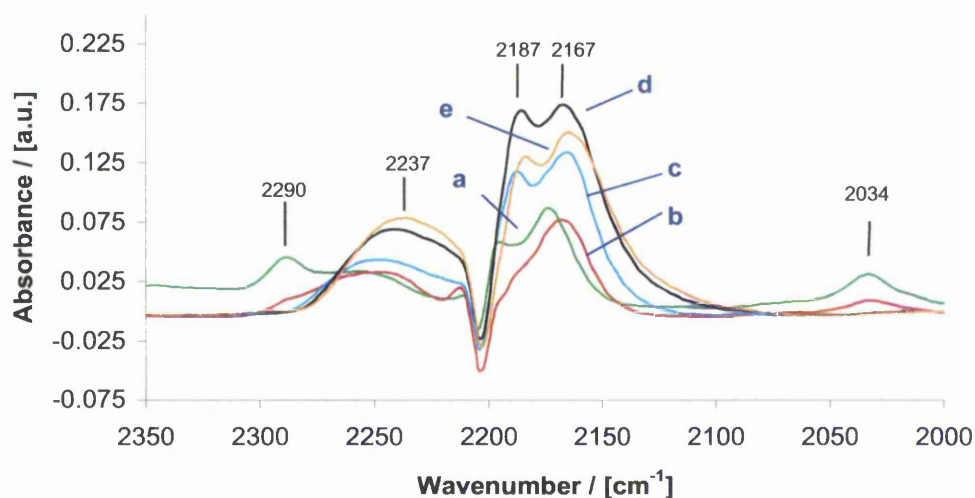
Figure 3.7-8: FTIR spectra of nitromethane desorption from K(27)-Na(67)-X. Legend: a) RT; b) 423 K; c) 523 K; d) 673 K; e) 773 K
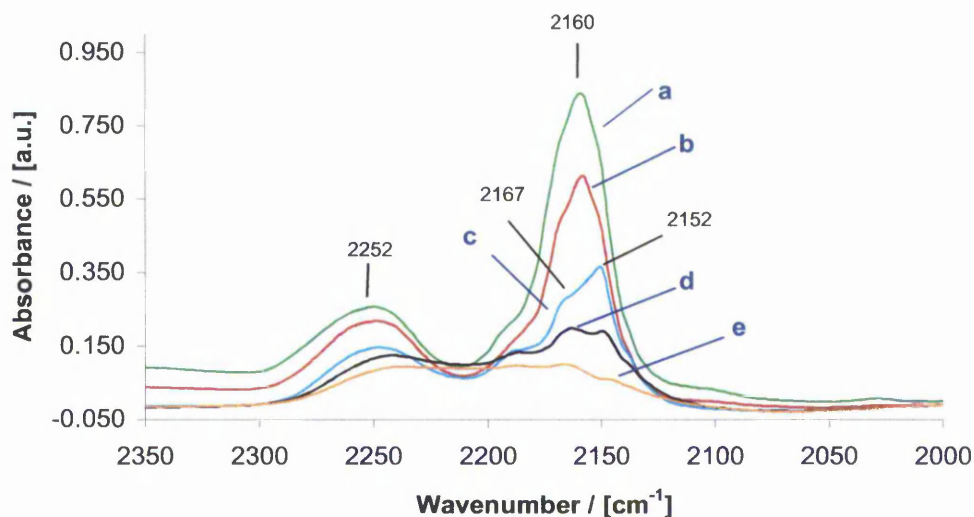
Figure 3.7-9: FTIR spectra of nitromethane desorption from Cs(22)-Na(75)-X. Legend: a) RT; b) 423 K; c) 523 K; d) 673 K; e) 773 K
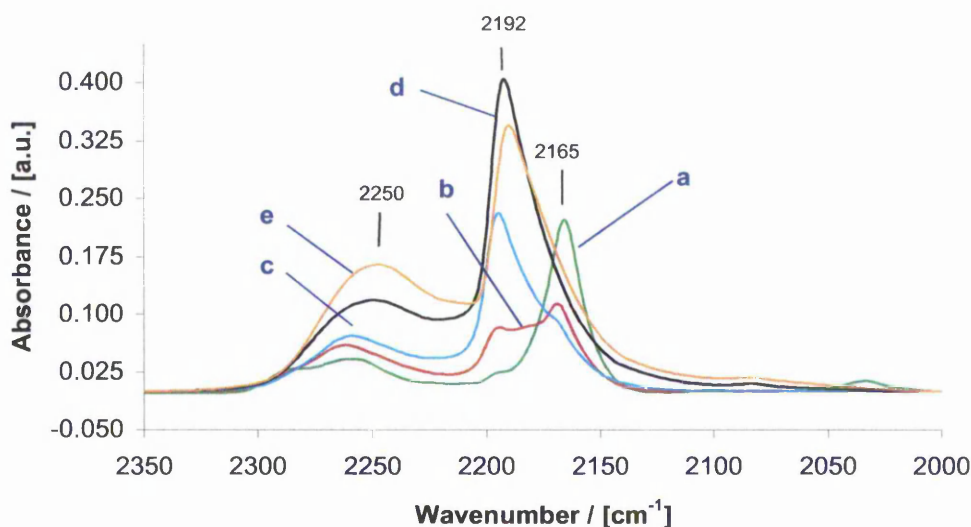
Figure 3.7-10: FTIR spectra of nitromethane desorption from Pb(34)-Na(67)-X. Legend: a) RT; b) 423 K; c) 523 K; d) 673 K; e) 773 K

3.7.5 Nitromethane adsorption on Y zeolites

On zeolite Y samples, spectra of adsorbed nitromethane were comparable to spectra seen of nitromethane on zeolite X samples. The integral intensity of nitromethane bands was highest on a H-Y sample compared to K-Na-Y samples.
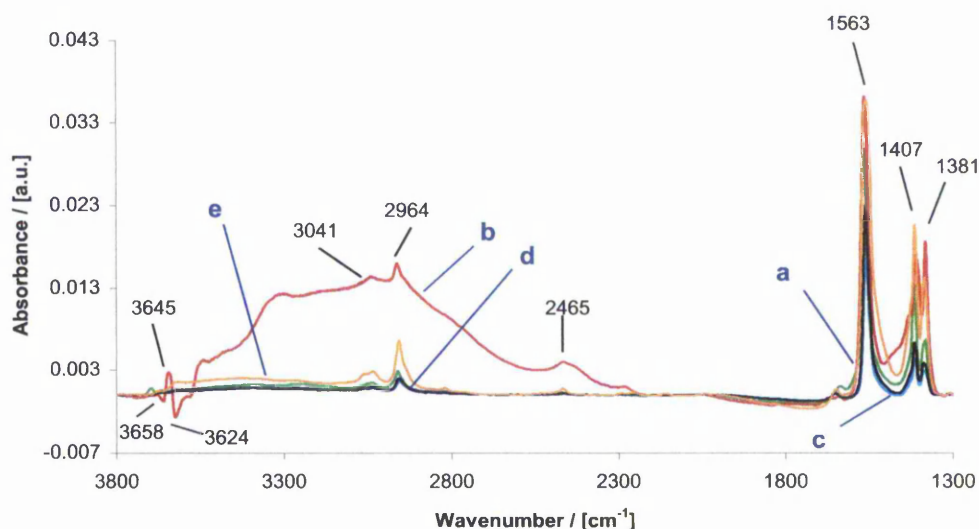
Figure 3.7-11: Normalised FTIR spectra of nitromethane adsorbed on K-Na-Y zeolites, at a pressure of 1 mbar in the cell. All spectra shown are difference spectra with respect to the activated catalyst. Legend: a) Na-Y (parent zeolite); b) H-Y; c) K(87)-Y; d) K(72)-Y; e) K(70)-Y

After evacuation of the cell, spectra appeared similar to the spectra recorded at one mbar pressure (*vide* Figure 3.7-12).
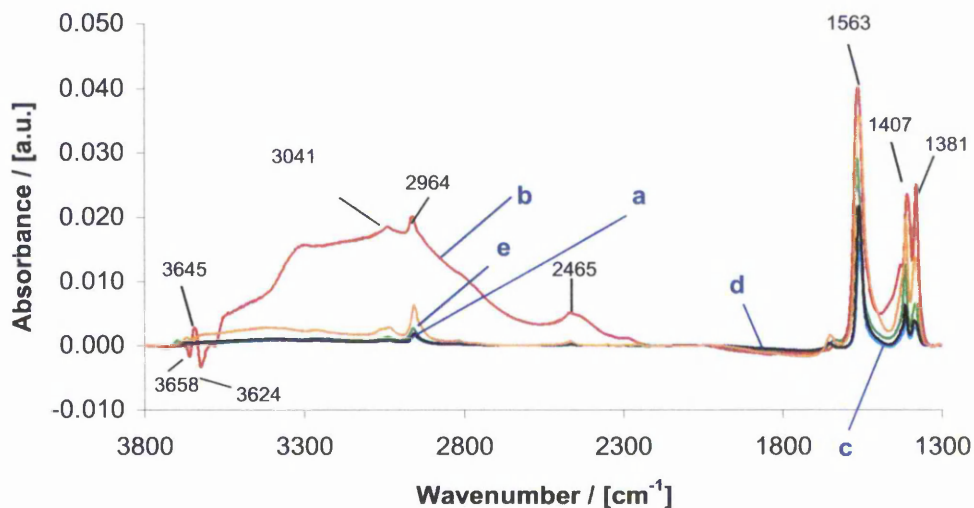
Figure 3.7-12: Normalised FTIR spectra of nitromethane adsorbed on K-Na-Y zeolites, after evacuation of the cell (pressure < 10^{-5} mbar). All spectra shown are difference spectra with respect to the activated catalyst. Legend: a) Na-Y (parent zeolite); b) NH_4-Y; c) K(87)-Y; d) K(72)-Y; e) K(70)-Y

During thermal desorption, a peak at ~2155 cm^{-1} was seen to increase with temperature on several K-Na-Y samples, in conjunction with a smaller feature at

~2250 cm^{-1}. In Table 3.7-7, behaviour of the peak at ~2155 cm^{-1} is summarised. The peak could in principle be assigned either to adsorbed cyanide (C≡N) or a cumulated C=N=O stretching vibration. Zinc oxide was used as a reference basic solid.

Table 3.7-7: Ion exchange conditions for Y zeolites in comparison with nitromethane desorption as monitored by infrared spectroscopy. Peak intensity was at a maximum at a temperature denoted by T_{max}. All exchanges performed at 343 K, in 250 ml water.

Sample	Exch. solution	Washing	C≡N / N=C=O band [cm^{-1}]	T_{max} [K]	IPA[b]
ZnO[a]	n.a.	n.a.	2196	673 K	+
NH$_4$-Y	n.a.	n.a.	n.a.	n.a.	-
Na-Y	n.a.	n.a.	2172	673 K	-
K(69)-Na(15)-Y	2 x 0.09 M KAc	n.a.	2167	673 K	+
K(70)-Y	3 x 0.09 M KAc	2 x H$_2$O	2154	RT	-
K(72)-Y	3 x 0.09 M KOH	2 x H$_2$O	2154	RT	-
K(87)-Y	3 x 0.09 M KAc	2 x 0.02 M KOH	2154	> 773 K	+

a) Prepared from precipitation of aqueous solutions of sodium carbonate and zinc nitrate
b) This column indicates if acetone was seen during the isopropyl alcohol decomposition (+).

In Figure 3.7-13 and Figure 3.7-14 the infrared spectra between 2000 and 2500 cm^{-1} of the thermal desorption of nitromethane on K(87)-Y and H-Y, respectively, are shown. On the potassium exchanged sample the species formed developed between ~473 and 873 K, whereas on H-Y the peak seen at 2275 cm^{-1} had a maximum area at ~473 K. On the H-Y sample, all species were desorbed at 873 K.
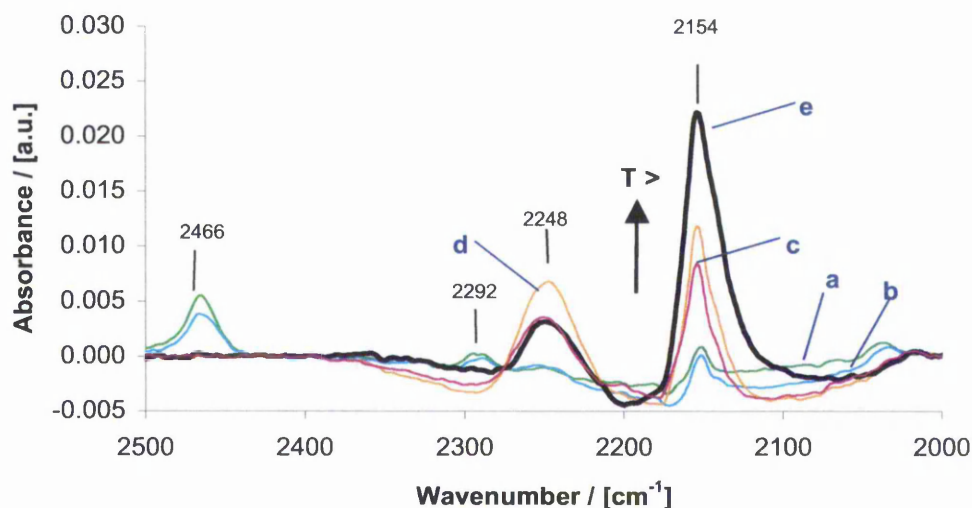
Figure 3.7-13: FTIR spectra of nitromethane desorbing from K(87)-Y. All spectra shown are difference spectra with respect to the activated catalyst. Legend: a) RT; b) 473 K; c) 673; d) 773 K; **e**) 873 K (thick line)

Figure 3.7-14: FTIR spectra of nitromethane desorbing from NH4-Y. All spectra shown are difference spectra with respect to the activated catalyst. Legend: a) RT; b) 473 K; c) 673 K; d) 773 K; e) 873 K (thick line)

3.7.6 Discussion and conclusion

As discussed in §3.7.2 and §1.3.5.4, the emergence of isocyanate species on the surface of solids during the thermal desorption of nitromethane was seen as evidence for basicity [91]. In Nesterenko's study, these species emerged

between 473 and 673 K [91]. However, on zeolite X and Y samples, no isocyanate bands were seen to increase during the thermal desorption (between 473 and 673 K) at the wavelengths mentioned by Nesterenko *et al.* [91]. Instead, a peak at was seen to develop during the thermal desorption of nitromethane between ~2155 and ~2190 cm^{-1} on zeolite X and Y samples. This band was assigned either to C≡N or N=C=O species adsorbed on (guest) cations. A reaction leading from adsorbed (aci-)nitromethane to an adsorbed N=C=O species seems more likely than one leading to C≡N species however. In the case of an N=C=O species, it is likely that the adsorption site was a guest cation, leading to species such as described in Table 3.7-3 and Table 3.7-4. Another possibility for an absorption band at these wavenumbers could in principle be an alkyne bond (C≡C) [89]. However, this possibility was ruled out, because of an absence of a peak at ~3200 cm^{-1}, which can be expected with an adsorbed alkyne [89].

Peaks at ~2250 cm^{-1} were found on Pb-Na-X samples at room temperature. These were assigned to isocyanate species. These species could arise from a basic decomposition route of nitromethane. Nesterenko suggested a relation between basicity and the band position of isocyanate species adsorbed on the oxygen atoms of the solid studied. However, it could not clearly be established which the adsorption site was in case of the isocyanate species. Further, no relation between lead loading and the band position of these isocyanate peaks observed on the Pb-Na-X samples could be discovered. In contrast, the band position of the C≡N or N=C=O band seen on Pb-Na-X increased initially with introduction of 3.8 wt% lead, to decrease when lead loading increased further. During the IPA dehydrogenation, selectivity to acetone had a maximum at 523 K when 3.8 wt% was loaded on Na-X. A further increase of lead loading leads to a decrease in selectivity to acetone.

3.8 References

1. Schmidt, W. and C. Weidenthaler, *Proceedings of the International Congress on Applied Mineralogy, 6th, Goettingen, Germany*, 241-244, (2000).

2. Barthomeuf, D., *Catalysis Reviews-Science and Engineering* **38**, 521-612, (1996).

3. Hattori, H., *Heterogeneous Catalysis and Fine Chemicals III* **78**, 35-49, (1993).

4. Hattori, H., *Chemical Reviews* **95**, 537-558, (1995).

5. Yagi, F., et al., *Acid-base catalysis II* **90**, 349-354, (1994).

6. Davidova, N., P. Kovacheva, and A.H. Weiss, *Catalysis Today* **13**, 625-626, (1992).

7. Kovacheva, P., N. Davidova, and A.H. Weiss, *Collection of Czechoslovak Chemical Communications* **57**, 2548-2552, (1992).

8. Kovacheva, P. and N. Davidova, *Studies in Surface Science and Catalysis* **98**, 194-5, (1995).

9. Stoecker, M., *Microporous Materials* **6**, 235-257, (1996).

10. Gruenert, W., et al., *Journal of Physical Chemistry* **98**, 10920-9, (1994).

11. Adnadjevic, B., et al., *Zeolites* **10**, 699-702, (1990).

12. Valcheva-Traykova, M.L. and N.P. Davidova, *Proceedings of the International Zeolite Conference, 12th, Baltimore, July 5-10, 1998* **2**, 981-987, (1999).

13. Kuehl, G.H. and A.E. Schweizer, *Journal of Catalysis* **38**, 469-76, (1975).

14. Kuehl, G.H., *Journal of Catalysis* **29**, 270-7, (1973).

15. Niemantsverdriet, J.W., *Spectroscopy in catalysis* (2nd ed.), Weinheim, 2000.

16. Sankar, G., J.M. Thomas, and C.R.A. Catlow, *Topics in catalysis* **10**, 255-264, (2000).

17. Breck, D.W., *Zeolite molecular sieves : structure, chemistry, and use* (1st ed.), Wiley-Interscience, London, 1974.

18. International Zeolite Association, http://www.iza-structure.org/databases/,

19. Savitsky and Golay, *Analytical Chemistry* **36**, 1627, (1964).

20.   Lide, D.R., *Handbook of chemistry and physics* (80th ed.), Boca Raton, 1999.

21.   Geremia, S., G. Nardin, and L. Randaccio, *Acta Chimica Slovenica* **43**, 357-363, (1996).

22.   Yeom, Y.H., Y. Kim, and K. Seff, *Journal of Physical Chemistry B* **101**, 5314-5318, (1997).

23.   Yeom, Y.H., Y. Kim, and K. Seff, *Microporous and Mesoporous Materials* **28**, 103-112, (1999).

24.   Holleman, A.F. and E. Wiberg, *Lehrbuch der Anorganischen Chemie* (33 ed.), Walter de Gruyter, Berlin, 1995.

25.   Sigma-Aldrich, *Material safety datasheet - product no. 467863*. 2003.

26.   Briggs, D. and M.P. Seah, *Practical surface analysis by Auger and X-ray photoelectron spectroscopy* (2nd ed.), London, 1983.

27.   Sanderson, R.T., *Chemical periodicity* (1st ed.), London, 1960.

28.   Wagner, C.D., et al., *Handbook of x-ray photoelectron spectroscopy* (1st ed.), Perkin-Elmer Corporation, Eden Prairie, 1979.

29.   Elliot, S., *The chemistry and physics of solids* (1st ed.), Chichester, 1997.

30.   Olson, D.H., C. Baerlocher, and W.M. Meier, *Atlas of zeolite framework types* (5th ed.), Amsterdam, 2001.

31.   International Centre for Diffraction Data, http://www.icdd.com, (1996).

32.   http://cds.dl.ac.uk,

33.   Zhu, L. and K. Seff, *Microporous and mesoporous materials* **46**, 111-113, (2001).

34.   Eulenberger, G.R., D.P. Shoemaker, and J.G. Keil, *J. Phys. Chem.* **71**, 1812-18, (1967).

35.   Zhu, L. and K. Seff, *Journal of physical chemistry B* **104**, 8946-8951, (2000).

36.   Nardin, G., L. Randaccio, and E. Zangrando, *Zeolites* **15**, 684-688, (1995).

37.   http://www.srs.ac.uk/srs/,

38.   Manceau, A., et al., *Environmental Science & Technology* **30**, 1540-1552, (1996).

39.   Sun, T. and K. Seff, *Journal of Physical Chemistry* **97**, 7719-7723, (1993).

40.   Boher, P., et al., *Journal of Solid State Chemistry* **57**, 343-350, (1985).

41.   Harada, H., Y. Sasa, and M. Uda, *Journal of Applied Crystallography* **14**, 141-142, (1981).

42.   Gavarri, J.R. and D. Weigel, *Journal of Solid State Chemistry* **13**, 252, (1975).

43.   Rajaram, R.K. and J.K.M. Rao, *Zeitschrift Fur Kristallographie* **160**, 225-233, (1982).

44.   Sherry, H.S., *Journal of physical chemistry* **70**, 1158-1168, (1966).

45.   Yuan, G., et al., *Journal of environmental science and health part a-Toxic/hazardous substances & environmental engineering* **34**, 625-648, (1999).

46.   O'Connor, J.F. and R.P. Townsend, *Zeolites* **5**, 158-164, (1985).

47.   Baur, W.H., *Am. Mineralogist* **49**, 697-704, (1964).

48.   Lipson, H. and H. Steeple, *Interpretation of x-ray powder diffraction patterns* (1st ed.), London, 1970.

49.   Joshi, U.D., et al., *Applied Catalysis, A: General* **239**, 209-220, (2003).

50.   Ambs, W.J. and W.H. Flank, *Journal of Catalysis* **14**, 118-125, (1969).

51.   Joshi, U.D., et al., *Thermochimica Acta* **387**, 121-130, (2002).

52.   Buskuhl, M. and E.H. Korte, *Analytical and Bioanalytical Chemistry* **374**, 672-675, (2002).

53.   Burgi, T., *Physical Chemistry Chemical Physics* **3**, 2124-2130, (2001).

54.   Zou, S.Z. and M.J. Weaver, *Analytical Chemistry* **70**, 2387-2395, (1998).

55.   Bauer, S., *American Journal of Physics* **60**, 257-261, (1992).

56.   Krauth, O., et al., *Journal of Chemical Physics* **113**, 6330-6333, (2000).

57.   Hathaway, P.E. and M.E. Davis, *Journal of Catalysis* **116**, 263-278, (1989).

58.   Davis, R.J., E.J. Doskocil, and S. Bordawekar, *Catalysis Today* **62**, 241-247, (2000).

59.   Doskocil, E.J. and R.J. Davis, *Journal of Catalysis* **188**, 353-364, (1999).

60.   Xu, J., A.Z. Yan, and Q.H. Xu, *Chinese journal of chemistry* **13**, 156-162, (1995).

61.   Weitkamp, J., et al., *11th International Congress on Catalysis - 40th Anniversary, Pts a and B* **101**, 731-740, (1996).

62.   Concepcion-Heydorn, P., et al., *Journal of Molecular Catalysis A - Chemical* **162**, 227-246, (2000).

63.   Yashima, T., H. Suzuki, and N. Hara, *Journal of Catalysis* **33**, 486-492, (1974).

64.   Smirniotis, P.G. and W.M. Zhang, *Applied Catalysis A - General* **176**, 63-73, (1999).

65.   Krylov, O.V., *Catalysis Today* **13**, 481-486, (1992).

66.   Li, C.Y. and L.V.C. Rees, *Reactive Polymers, Ion Exchangers, Sorbents* **7**, 89-99, (1988).

67.   Lahousse, C., et al., *Journal of Molecular Catalysis* **87**, 329-332, (1994).

68.   Kung, H.H., S. Akhter, and K. Lui, *Abstracts of Papers of the American Chemical Society* **188**, 209-INOR, (1984).

69.   Gervasini, A. and A. Auroux, *Journal of Catalysis* **131**, 190-198, (1991).

70.   Lavalley, J.C., *Catalysis today* **27**, 377-401, (1996).

71.   Di Cosimo, J.I., et al., *Journal of Catalysis* **178**, 499-510, (1998).

72.   Sivasanker, S., *Studies in Surface Science and Catalysis* **145**, 85-90, (2003).

73.   Jacobs, P.A., et al., *Journal of the Chemical Society, Faraday Transactions I* **69**, 1056-1068, (1973).

74.   Jacobs, P.A., F.H. Van Cauwelaert, and E.F. Vansant, *Journal of the Chemical Society, Faraday Transactions I* **69**, 2130-2139, (1973).

75.   Martra, G., et al., *Catalysis Today* **73**, 83-93, (2002).

76.   Rege, S.U. and R.T. Yang, *Chemical Engineering Science* **56**, 3781-3796, (2001).

77.   Garrone, E., et al., *Proceedings of the International Zeolite Conference, 12th, Baltimore, July 5-10, 1998* **4**, 2705-2710, (1999).

78.   van Bekkum, H., et al., *Introduction to Zeolite Science and Practice* (2nd ed.), Elsevier, Amsterdam, 2001.

79.   Skoog, D.A. and J.J. Leary, *Principles of instrumental analysis* (4th ed.), Fort Worth, 1992.

80.   Galactic, T., *Grams/32*, v. 5.10

81.   Laboratories, S.R., *The infrared spectra handbook of inorganic compounds* (1st ed.), Sadtler Research Laboratories, Philadelphia, 1984.

82.   Doskocil, E.J. and P.J. Mankidy, *Applied Catalysis A - General* **252**, 119-132, (2003).

83.   Tsyganenko, A.A., D.V. Pozdnyakov, and V.N. Filimonov, *Journal of molecular structure* **29**, 299-318, (1975).

84. Gilles, F., et al., *Studies in Surface Science and Catalysis* **142B**, 1687-1694, (2002).

85. Jacobs, W.P.J.H., *Spectroscopic studies of the proton-ammonia interaction in zeolite Y*, in *PhD thesis, Schuit institute of Catalysis*. 1993, Technische Universiteit Eindhoven: Eindhoven.

86. Zhang, W.M., et al., *Journal of Physical Chemistry B* **104**, 4122-4129, (2000).

87. Kustov, L.M., *Topics in catalysis* **4**, 131-144, (1997).

88. Hill, J.R., et al., *Journal of Physical Chemistry* **95**, 3037-3044, (1991).

89. Silverstein, R.M. and F.X. Webster, *Spectrometric identification of organic compounds* (6th ed.), New York, 1998.

90. van der Maas, J.H., *Basic infrared Spectroscopy* (2nd ed.), London, 1972.

91. Nesterenko, N., et al., *New Journal of Chemistry* **23**, 665-666, (1999).

92. Ukisu, Y., et al., *Catalysis Letters* **11**, 177-181, (1991).

93. Yamaguchi, M., *Journal of the Chemical Society-Faraday Transactions* **93**, 3581-3586, (1997).

94. Hayes, N.W., R.W. Joyner, and E.S. Shpiro, *Applied Catalysis, B: Environmental* **8**, 343-363, (1996).

95. Satsuma, A., et al., *Journal of Catalysis* **181**, 165-169, (1999).

96. Cant, N.W., et al., *Catalysis Today* **54**, 473-482, (1999).

97. Liu, I.O.Y., et al., *Journal of Catalysis* **203**, 487-494, (2001).

98. Lombardo, E.A., et al., *Journal of Catalysis* **173**, 440-449, (1998).

99. Lobree, L.J., et al., *Journal of Catalysis* **169**, 188-193, (1997).

100. Solymosi, F. and T. Bansagi, *Journal of Catalysis* **156**, 75-84, (1995).

101. Lima, E., et al., *Studies in Surface Science and Catalysis* **135**, 3662-3669, (2001).

102. Ellestad, O.H., et al., *Acta Chem. Scand.* **26**, 1721 -, (1972).

103. Miller, F.A. and G.L. Carlson, *Spectrochimica acta* **17**, 977 -, (1961).

104. Forster, D. and D.M.L. Goodgame, *J. Chem. Soc.*, 262-7, (1965).

105. Forster, D. and D.M.L. Goodgame, *J. Chem. Soc.*, 1286-9, (1965).

106. Nakamoto, K., *Infrared and Raman spectra of inorganic and coordination compounds* (3rd ed.), Wiley, New York, 1978.

4   Overall conclusion

For the investigation of basic character of zeolite catalysts, several experimental techniques are available. Any conclusions with regard to the relation between structure and activity of basic sites in a zeolite catalyst are strongly dependant on the experimental conditions opted for.

Ion exchange was chosen with the aim of modifying properties of zeolites X, Y and Beta. It was shown that crystalline materials were obtained after ion exchange, whose bulk composition deviated slightly from the surface composition for Pb-Na-X materials. Extended x-ray absorption fine structure studies showed that lead had a 2^+ oxidation state in Pb-Na-Y.

Activation of the zeolites requires elevation of temperature. From literature studies, it was suspected destructive structural changes might occur with zeolites of a low Si/Al ratio such as zeolite X when they are submitted to thermal treatment. Metallic lead was found when exchanged zeolite X was heated to 973 K in vacuum or in helium. High lead loadings, such as 42wt%, even led to the emergence of metallic lead during activation at 773 K. The zeolites remained crystalline after activation at 773 or 973 K.

From reactor data it is concluded that incorporation of small amounts of lead(II), in the order of ~4wt% results in the highest yield of acetone at 723 K. The activation temperature has little effect on the catalyst's performance. Small amount of lead (≤ 17wt%) have a marked positive effect on the selectivity for acetone compared to zeolite Na-X (measured between 473 and 773 K), whilst being resilient to thermal treatment up to 973 K. Further increase of lead loading did not yield a significant improvement of acetone selectivity or acetone yield. Catalysts with such increased lead loadings (24wt% or more) activated at 973 K yielded less acetone than when they were activated at 773 K. On the whole, reactor data suggests basic sites are indeed present in Pb-Na-X samples. The optimum reaction conditions found for best acetone yield were 723 K using a catalyst with ~4wt% lead. On Pb-Na-Y and Pb-H-Beta samples no significant selectivities to acetone were achieved.

In the probe molecule adsorption experiments, Pb-Na-X samples showed behaviour that has been associated with basicity in literature. Carbonate

structures were found on these samples when carbon dioxide was adsorbed. Some carbonates were strongly adsorbed, vacating the zeolite only at desorption temperatures of 573 K or above. Adsorption of a basic probe molecule, ammonia, yielded relatively weakly adsorbed species on Pb-Na-X samples. During adsorption of nitromethane isocyanate species were detected at room temperature. These species were seen in literature to appear on basic materials, during desorption of nitromethane between 473 and 673 K.

Known basic materials, such as potassium and caesium exchanged zeolites showed more conversion of isopropyl alcohol and selectivity to acetone in the isopropyl alcohol dehydrogenation at higher temperatures (> 523 K) when compared to Pb-Na-X samples. On K-Na-Y catalysts of similar potassium loading, it was noticed that washing the zeolite with water after the ion exchange procedure had a negative effect on the catalysts' isopropyl alcohol dehydrogenation ability. Carbon dioxide adsorption on was similar on the conventional basic zeolites (Cs-Na-X and K-Na-X) and Pb-Na-X samples of lead loadings < ~24wt%. Ammonia and nitromethane adsorption experiments showed that these Pb-Na-X samples and K-Na-X displayed similar behaviour.

Over H-Y, a known acidic material, no acetone is produced in the isopropyl alcohol reaction. Further, ammonia is more strongly bound on H-Y than on for example K-Na-Y zeolites.

It can be concluded that reactor data in combination with adsorption data have shown that basic sites are indeed present in Pb-Na-X samples.

5   Future work

Some suggestions for continuation of the research presented in the previous chapters are given in this chapter. They shall focus on three main aspects of this work: ion exchange, catalysis and probe molecule absorption.

Firstly, in the ion exchange experiments it is of interest to examine whether the lead introduced through ion exchange does indeed enter the cavities of zeolite X. Some evidence was presented in this work that sodium does indeed exit the zeolite after the initial exchange. If the lead ions have occupied exchange sites in zeolite X, it should in principle be possible to reverse the process, *i.e.* to back-exchange the lead for sodium ions. The amount of lead leaving the zeolite should be matched against the amount of sodium being re-introduced. Further extended x-ray absorption fine structure studies should be undertaken to examine the local structure around the lead Pb-Na-X. A possible link between local structure and catalysis would be worth investigating.

Secondly, since activity in the isopropanol dehydrogenation has been shown for Pb-Na-X, it would be feasible to try and test this catalyst in further basic reactions that are of more commercial interest, such as aldol condensation reactions. It would also be interesting to investigate whether a binary exchanged zeolite would be active in the isopropyl alcohol dehydrogenation. As Pb-X is active at lower temperatures, and K-X is active at higher temperatures, a novel Pb-K-X catalyst might provide the best of both worlds.

Lastly, the nitromethane adsorption experiments done for this work show very interesting results. However, peak identification in the infrared monitored adsorption studies remains very difficult, because of the complex modes of adsorption and the subsequently complex spectra. It would be worth undertaking experiments using radioactively labelled nitromethane (*e.g.* 13C-nitromethane). Peak shifts that arise as a result of the introduction of a heavier atom could be linked to the structure of the adsorbed species, by comparing with the unlabelled counterpart. Infrared monitored adsorption studies of the target molecule used for this work (isopropanol) are interesting with respect to the identification of a possible adsorption site.

Appendix A: Suppliers' information

Catal International,
PO BOX 507
Sheffield
S10 3YT
The United Kingdom
http://www.catal.co.uk/

CCLRC Daresbury Laboratory
Warrington
Cheshire
WA4 4AD
The United Kingdom
http://www.srs.ac.uk/srs/

Razel Scientific Instruments, Inc
100 Reasearch Drive
Stamford,
CT 06906
USA
http://www.razelscientific.com/

Süd-Chemie AG
Süd-Chemie Haus
Lenbachplatz 6
80333 München
Federal Republic of Germany
http://www.sud-chemie.com/

Viridian Partnership
PO Box 746
Woking
Surrey
GU24 0AZ
The United Kingdom

Zeolyst International
P.O. Box 830
Valley Forge, PA 19482
The United States of America
http://www.zeolyst.com/
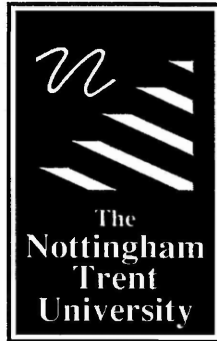
Libraries & Learning Resources

The Boots Library: 0115 848 6343
Clifton Campus Library: 0115 848 6612
Brackenhurst Library: 01636 817049